POLARIZED PARTON DISTRIBUTIONS MEASURED

AT THE HERMES EXPERIMENT

by

Jürgen Wendland

Master of Science (Simon Fraser University, 1999)

THESIS SUBMITTED IN PARTIAL FULFILLMENT

OF THE REQUIREMENTS FOR THE DEGREE OF

DOCTOR OF PHILOSOPHY

IN THE DEPARTMENT

OF

PHYSICS

APPROVAL

Name: Jürgen Wendland

Degree: Doctor of Philosophy

Title of Thesis: Polarized Parton Distributions Measured at the HERMES Experiment

Examining Committee: Dr. Mike Hayden (Chair)

Dr. Michel Vetterli, Professor, Senior Supervisor
Department of Physics, Simon Fraser University

Dr. David Boal, Professor
Department of Physics, Simon Fraser University

Dr. Christopher Oram, Senior Research Scientist
TRIUMF

Dr. Howard Trottier, Professor
Department of Physics, Simon Fraser University

Dr. Dugan O'Neil, Assistant Professor, Internal Examiner
Department of Physics, Simon Fraser University

Dr. Richard Keeler, Professor, External Examiner
Department of Physics, University of Victoria

Date Approved: September 16, 2003

PARTIAL COPYRIGHT LICENSE

I hereby grant to Simon Fraser University the right to lend my thesis, project or extended essay (the title of which is shown below) to users of the Simon Fraser University Library, and to make partial or single copies only for such users or in response to a request from the library of any other university, or other educational institution, on its own behalf or for one of its users. I further agree that permission for multiple copying of this work for scholarly purposes may be granted by me or the Dean of Graduate Studies. It is understood that copying or publication of this work for financial gain shall not be allowed without my written permission.

Title of Thesis/Project/Extended Essay

POLARIZED PARTON DISTRIBUTIONS

MEASURED AT THE HERMES

EXPERIMENT

Author:_
    (signature)/

JÜRGEN WENDLAND

(name)

22nd of September 2003

(date)

Abstract

The HERMES experiment at DESY, Germany was designed to carry out precision measurements of the proton spin structure using polarized deep-inelastic scattering. The experiment utilizes the 27.5 GeV electron or positron beam of the HERA accelerator which is longitudinally polarized at HERMES, in combination with a polarized internal gas target. For this work, data on longitudinally polarized hydrogen and deuterium targets were used to determine cross section asymmetries with respect to the alignment of the target and beam polarizations. Inclusive asymmetries on the proton and the deuteron, where only the scattered electron/positron is detected, were measured with high precision. In semi-inclusive deep-inelastic scattering, at least one final-state hadron is detected in coincidence. Semi-inclusive asymmetries of pions on the proton and pion and kaon asymmetries on the deuteron were measured for the first time by the HERMES collaboration. The measured asymmetries include detector effects and effects of higher-order processes in quantum electrodynamics. A new unfolding procedure that takes into account the correlations between kinematic bins was implemented to correct for these effects.

The polarized parton densities of the up, down, and sea flavours were obtained from the unfolded inclusive and semi-inclusive asymmetries in a probabilistic analysis based on leading-order quantum chromodynamics. In the case of the up quark and the down quark, the polarized densities were determined to be positive and negative, respectively. The polarized densities of the sea flavours, decomposed for the first time into the densities of the anti-up, anti-down, and strange quarks, were found to be compatible with zero. Moments of the polarized parton densities were computed. The Bjørken sum rule was verified and the total spin carried by the quark spins was determined to be $(38.0 \pm 8.0)\,\%$. This latter result is larger than earlier measurements but still smaller than $\sim 60\,\%$ predicted in relativistic models of the proton.

Acknowledgements

Contents

List of Tables

List of Figures

Chapter 1

Introduction

The investigation of the structure of protons and neutrons is of great importance for the understanding of all matter, as these two particles, collectively known as nucleons, and the electron make up essentially all of the visible mass in the universe. The structure of nucleons is described in the Standard Model, the theory of the strong and electro-weak interactions. In this model, the electron is one of six elementary leptons — the electron, the muon, the tau and three corresponding neutral neutrinos. The nucleons are composite particles of quarks. There are six different types of quarks or quark flavours — up (u), down (d), strange (s), charm (c), bottom (b), and top (t). Leptons and quarks and their corresponding anti-particles are fermions, they interact through the exchange of gauge bosons. Charged leptons interact electro-magnetically via the photon and weakly via the W, and Z-bosons. Neutrinos only interact weakly. Quarks are subject to the electro-weak interaction and the strong interaction that is mediated by the gluon. Nucleons are composed of three valence-quarks (proton: uud, neutron: udd) which exchange gluons that can fluctuate into quark/anti-quark pairs, the sea-quarks.

The interplay of quarks and gluons is modeled in the theory of the strong interaction, quantum chromodynamics (QCD). The high-energy or equivalently small distance behaviour of quarks and gluons can be described with perturbative expansions in QCD, because the running coupling constant is small and becomes zero in the limit of zero distance. However, at small energies or large distances the running coupling becomes large and solutions in perturbative QCD diverge. The former limit leads to asymptotic freedom, *i.e.* the strong force vanishes and quarks move quasi-freely. The latter limit results in confinement of quarks inside hadrons. The theoretical description of nucleon structure therefore involves non-perturbative QCD making quantitative predictions difficult,

1

at best. Experiments are consequently crucial tools to investigate nucleon structure.

Point-like leptons are an ideal probe for such experiments. Early elastic scattering experiments produced results on nucleon form-factors, that describe the extended charge distribution and the magnetization density in the nucleon. Inelastic scattering experiments measured the distribution of excited nucleon states — the resonances. Since the advent of deep-inelastic scattering experiments — the hard scattering of leptons off the quarks in the nucleon — in the 1950's, a wealth of data has been collected on the behaviour of the quarks and the gluons in the nucleon. First experiments that investigated the spin structure of the nucleon were carried out at SLAC [1], verifying theoretical expectations in principle. However, the subsequent CERN experiment (EMC) measured the contribution by the quark spins to the nucleon spin to be close to zero [2], contrary to the (very) naive model expectation that the spin of the nucleon is carried by the spins of the valence quarks. This result became known as the "proton spin crisis". Relativistic quark models attribute the nucleon spin to the total spin of the valence and sea-quarks, $\Delta\Sigma$, the spin of the gluons, ΔG, and the orbital angular momentum of the quarks and the gluons, L_q and L_g respectively:

$$\frac{1}{2} = \frac{1}{2}\Delta\Sigma + \Delta G + L_q + L_g.$$

These models predict a quark spin contribution around 60 % [3] compared to later measurements that yielded $\lesssim$ 30 % (see Ref. [4] and references therein).

The HERMES experiment is a second generation experiment designed to investigate the spin of the quarks in the nucleon in detail [5]. It uses the polarized electron beam of the HERA collider at the DESY laboratory in combination with an internal polarized gas target. This thesis presents a determination of the polarizations and polarized parton densities of the u, d, $\bar{u}$, $\bar{d}$, and the s quarks in the nucleon. The analysis is based on cross section asymmetries with respect to the orientation of the beam and target polarizations which were measured with the HERMES experiment in the years 1996 to 2000. A review of the theory of the structure of the nucleon with emphasis on the spin structure is given in the first chapter. The HERMES experiment is described in the following part. Chapters 4 and 5 describe the data selection and the identification of electrons, pions, and kaons. The measurement of the asymmetries is discussed in Ch. 6 and the asymmetries corrected for detector effects and radiative processes are presented in Ch. 7. The quark polarizations and a comparison with model predictions are given in Ch. 8, followed by a summary.

Chapter 2

Deep-Inelastic Scattering

This chapter reviews the relevant theory of electron-nucleon scattering. After an introductory review of elastic and inelastic scattering, the chapter focuses on electron-nucleon scattering in the deep-inelastic regime. Special attention is paid to the nucleon spin. The parton model is introduced and theoretical predictions of nucleon structure in terms of sum rules are given. The final sections of this chapter are devoted to the experimental determination of the polarized parton densities in inclusive and semi-inclusive deep-inelastic scattering. This chapter makes use of Refs. [6, 7, 8, 9]. Additional references are given throughout the text.

2.1 Elastic and Inelastic Electron-Nucleon Scattering

Scattering of electrons off a nucleon is kinematically described by the initial and final four-momenta of the electron $k = (E, \vec{k})$ and $k' = (E', \vec{k'})$ respectively and the initial momentum of the nucleon $P = (E_P, \vec{P})$. The negative squared four-momentum transfer to the nucleon mediated by a (virtual) photon is given by

$$-Q^2 \equiv q^2 \equiv (k - k')^2 \overset{\text{lab}}{=} -4 E E' \sin^2 \frac{\theta}{2} \qquad (2.1)$$

where θ is the electron scattering angle in the laboratory frame with the nucleon initially at rest. In elastic scattering, the nucleon remains intact with momentum $P' = (E'_P, \vec{P'})$ and Q^2 is the only independent variable. The energy transfer,

$$\nu \overset{\text{lab}}{=} E - E', \qquad (2.2)$$

3

is related to Q^2 through $\nu = Q^2/(2M)$. Under the assumption that the nucleon is a point-like spin-1/2 particle with Dirac magnetic moment, the elastic scattering cross section is given by

$$\frac{d\sigma}{d\Omega} = \left(\frac{d\sigma}{d\Omega}\right)_{\text{Mott}} \left[1 + \frac{Q^2}{4M^2} \cdot 2\tan^2\frac{\theta}{2}\right]. \tag{2.3}$$

Here M is the nucleon's mass and the Mott cross section describes the scattering off a spin-less point-like particle,

$$\left(\frac{d\sigma}{d\Omega}\right)_{\text{Mott}} = \frac{\alpha^2}{4\,E^2\sin^4\frac{\theta}{2}}\,\frac{E'}{E}\cos^2\frac{\theta}{2}, \tag{2.4}$$

where $\alpha = e^2/(4\pi)$ is the fine structure constant. Eqs. (2.3) and (2.4) are given in the one-photon approximation, accurate to about 1%. Deviations of the electron-proton cross section from these elastic cross sections were first reported in 1955 [10, 11]. McAllister, Hofstadter and their collaborators measured the cross section of scattering electrons with an energy of 188 MeV off protons. Their result, shown in Fig. 2.1, is a clear indication that the proton exhibits sub-structure. The
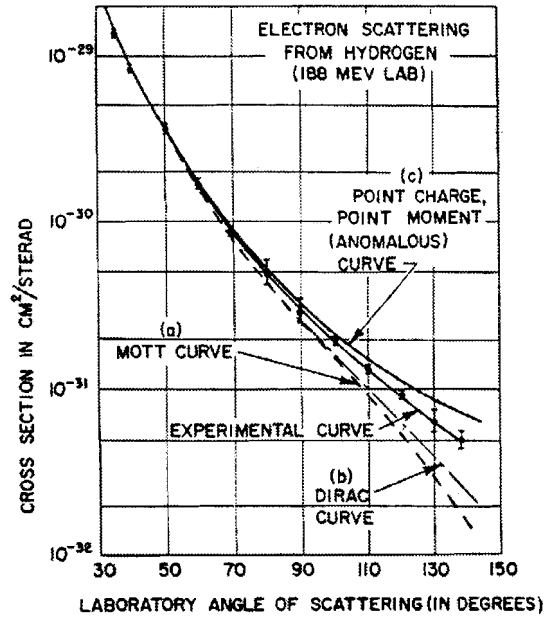
Figure 2.1: The electron-proton cross section measured by McAllister and Hofstadter [11]. For comparison, the Mott cross section (a), the Dirac cross section, Eq. (2.3), (b) and the cross section expected for a point-like proton with anomalous magnetic moment (c) are also shown.

extended structure of the nucleon is accounted for in the Rosenbluth cross section [12],

$$\frac{d\sigma}{d\Omega} = \left(\frac{d\sigma}{d\Omega}\right)_{\text{Mott}} \left(\frac{G_E^2(Q^2) + \frac{Q^2}{4M^2}G_M^2(Q^2)}{1 + \frac{Q^2}{4M^2}} + \frac{Q^2}{2M^2}G_M^2(Q^2)\tan^2\frac{\theta}{2}\right), \qquad (2.5)$$

where G_E and G_M are the electric and magnetic form factors. The three-dimensional Fourier transforms of the form factors in the electron-nucleon center-of-mass frame where $Q^2 = \vec{q}^2$,

$$\int \frac{d^3q}{(2\pi)^3} e^{-i\vec{q}\cdot\vec{r}} \frac{M}{E(\vec{q})} G_{E,M}(\vec{q}^2), \qquad (2.6)$$

describe the charge distribution and the magnetization density in the nucleon. The Q^2 dependence of the proton form factors, which is due to the extended nucleon structure,[1] is shown in Fig. 2.2.
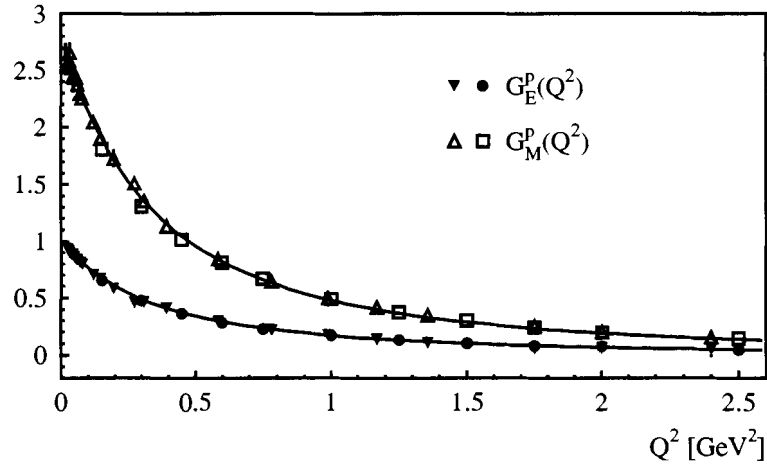
Figure 2.2: The electric and magnetic form factors of the proton in the range $0 < Q^2 < 2.5\,\text{GeV}^2$. Shown are typical data [13, 14], and a dipole fit, $G_M^p/\mu_p = G_E^p = [1 + Q^2/(0.71\,\text{GeV}^2)]^{-2}$ (solid curves).

Based on an expansion of Eq. (2.6), the form factors can be used to calculate the mean squared charge, $\langle r_E^2 \rangle$, and magnetic, $\langle r_M^2 \rangle$, radii. They are for the proton [8]

$$\sqrt{\langle r_E^2 \rangle}_{\text{proton}} = (0.86 \pm 0.01)\,\text{fm}, \qquad \sqrt{\langle r_M^2 \rangle}_{\text{proton}} = (0.86 \pm 0.06)\,\text{fm}. \qquad (2.7)$$

At larger energy transfers the electron can also scatter inelastically off the nucleon, exciting the nucleon into a resonant state. In the case of the proton, the first resonance is the $\Delta(1232)$. The

---

[1]In the case of a point-like spin 1/2 particle with Dirac magnetic moment, the form factors reduce to $G_E = G_M = 1$.

spectrum of resonances that occurs in the range $W = 1 \ldots 2\,\mathrm{GeV}$ is shown in Fig. 2.3, where W is the total mass in the hadronic final state,

$$W^2 = (P + q)^2 = M^2 + 2\,P \cdot q - Q^2 \overset{\mathrm{lab}}{=} M^2 + 2\,M\,\nu - Q^2. \tag{2.8}$$

The first excitation is followed by the $N^*(1440)$, the $N^*(1520)$ and the $N^*(1535)$ in the second
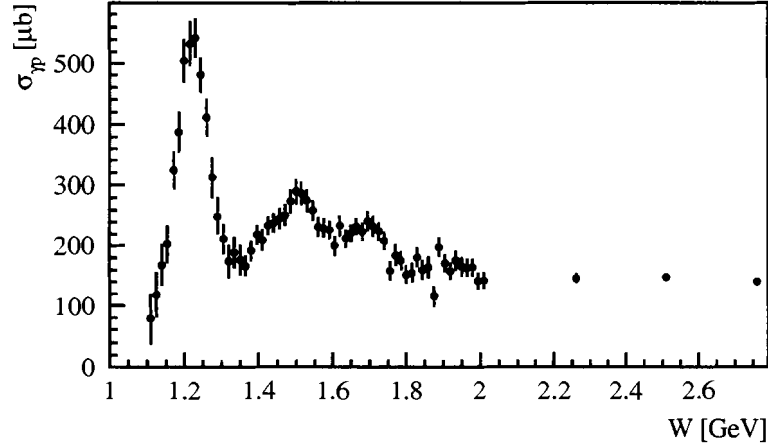
Figure 2.3: The inelastic photon-proton scattering cross section. The data were measured in the reaction $e + p \rightarrow e + X$, where X denotes any final state. The cross section was extrapolated to $Q^2 = 0$, where the electron-proton cross section is directly related to the photon-nucleon cross section [15].

resonance region. The $N^*(1680)$ resonance dominates the cross section in the third peak. The spectrum of these resonances, which primarily decay into a nucleon and a pion, is further evidence for the composite structure of the nucleon.

The cross section for inelastic electron-nucleon scattering depends on two independent variables, because unlike in elastic scattering mass is not conserved. A common choice for these independent variables is ν and Q^2. The cross section for unpolarized inelastic inclusive scattering, when only the scattered electron is detected, is given by (see Sec. 2.2.2 for more details)

$$\frac{d^2\sigma}{d\Omega\,dE'} = \frac{4\,\alpha^2\,E'^2}{Q^4}\left(W_2(\nu, Q^2)\cos^2\frac{\theta}{2} + 2\,W_1(\nu, Q^2)\sin^2\frac{\theta}{2}\right). \tag{2.9}$$

The response functions W_1 and W_2 describe the composite structure of the nucleon. In the limit of

elastic scattering ($\nu \to Q^2/(2M)$), the response functions are related to the nucleon form factors:

$$W_1(\nu, Q^2) = \frac{Q^2}{4\,M^2} G_M^2(Q^2)\, \delta\left(\nu - \frac{Q^2}{2\,M}\right)$$

$$W_2(\nu, Q^2) = \frac{G_E^2(Q^2) + \frac{Q^2}{4\,M^2} G_M^2(Q^2)}{1 + \frac{Q^2}{4\,M^2}}\, \delta\left(\nu - \frac{Q^2}{2\,M}\right).$$

(2.10)

At larger invariant masses $W \gtrsim 2\,\mathrm{GeV}$ the cross section becomes smooth. The reaction cannot be attributed to exciting a specific resonance, because the scattering process results in a complicated multi-particle state. In this region which is treated in detail in the following sections, the quarks in the nucleon may be probed in deep-inelastic scattering.

2.2 Deep-Inelastic Scattering

2.2.1 Kinematics of the Scattering Reaction

At squared momentum transfers $Q^2 > 1 \ldots 2\,\mathrm{GeV}$ the wavelength, $\lambda \simeq 1/\sqrt{Q^2}$, of the photon that mediates the scattering process, becomes sufficiently small to probe the constituents of the nucleon. In this region, elastic and inelastic scattering still occur at invariant masses $W = M \equiv 0.938\,\mathrm{GeV}$ and $W = M_R$ respectively, where M_R is the mass of a given resonance. However, by requiring invariant masses $W \gtrsim 2\,\mathrm{GeV}$ or equivalently $\nu > 1 \ldots 2\,\mathrm{GeV}$, the scattering process enters the deep-inelastic scattering domain, where both Q^2 and ν are large, but their ratio is not. In this domain, the reaction may be described as scattering off individual quarks in the nucleon which breaks apart and forms a hadronic final state X.

Deep-inelastic scattering (DIS) of charged leptons off the nucleon is mediated by the exchange of a virtual photon, γ^*, or a virtual Z-boson. At energies such as those of the HERMES experiment where the energy transfer ν is small compared to the Z-boson mass, the contributions due to the weak interaction can be neglected. The following discussion is restricted to the scattering of electrons or positrons, referred to here collectively as electrons in the following, with initial and final state energies such that their mass m can be neglected. A schematic diagram of the DIS process in the one photon exchange approximation is shown in Fig. 2.4. An electron with momentum $k = (E, \vec{k})$ and spin s scatters off a nucleon with momentum P and spin S. The nucleon is considered to be initially at rest, $P = (M, 0)$.
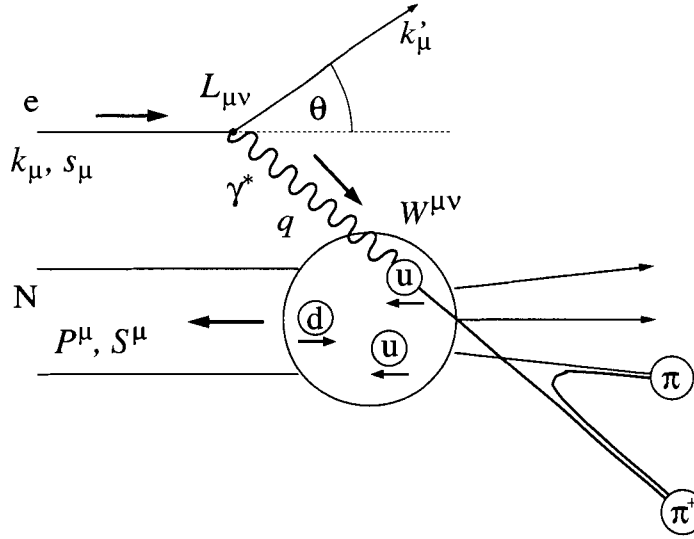
Figure 2.4: Diagram of the polarized deep-inelastic scattering process. The arrows represent the spins of the corresponding particles.

The energy E' and the scattering angle θ of the final state electron determine the energy ν and the negative squared four-momentum Q^2 of the virtual photon. The total invariant mass of the hadronic final state is related to ν and Q^2 by Eq. (2.8). The inelasticity of the scattering process is given by the Bjørken scaling variable $x \overset{\text{lab}}{=} Q^2/(2M\nu)$. The Bjørken scaling variable can be interpreted as the fraction of the nucleon momentum carried by the struck quark, see Sec. 2.3. Instead of the photon energy or equivalently the energy transfer to the nucleon, ν, the fractional energy transfer $y \overset{\text{lab}}{=} \nu/E$ is often used. In the limit of elastic scattering, the Bjørken scaling variable is unity, and $y \overset{\text{lab}}{=} Q^2/(2ME)$, see Sec. 2.1. A summary of the relevant kinematic variables is given in Tab. 2.1.

A DIS experiment in which only the final state electron is detected is referred to as inclusive and denoted

$$e + N \to e + X.$$

Additional information becomes available in semi-inclusive DIS (SIDIS), where a final state hadron h is detected in coincidence,

$$e + N \to e + h + X.$$

The kinematics of the final state hadron are described by its fractional energy z with respect to the energy transfer ν and the Feynman variable $x_F \overset{\text{lab}}{\simeq} 2p^{\|}_{CM}/W$, where $p^{\|}_{CM}$ is the hadron's

longitudinal momentum with respect to the photon momentum in the photon-nucleon center-of-mass system. The hadron that contains the struck quark carries a large energy fraction z and has positive x-Feynman, as it travels in the forward direction with respect to the photon. Hadrons that contain the struck quark or that are part of the "jet" that contains the struck quark are called the current fragments, whereas hadrons in the final state that are formed from the spectator quarks are the target fragments.

2.2.2 The Deep-Inelastic Scattering Cross Section

The inclusive deep-inelastic scattering cross section in a solid angle $d\Omega$ and energy interval $[E', E' + dE']$ is most generally given as a contraction of the leptonic tensor $L_{\mu\nu}$ and the hadronic tensor $W^{\mu\nu}$,

$$\frac{d^2\sigma}{dE'\,d\Omega} = \frac{\alpha^2}{Q^4} \frac{E'}{E} L_{\mu\nu}\,W^{\mu\nu}. \tag{2.11}$$

The tensor of the point-like lepton can be calculated in quantum electrodynamics. It is given to first order by

$$L_{\mu\nu} = L_{\mu\nu}^S + L_{\mu\nu}^A = 2\left[k_\mu k_\nu' + k_\nu k_\mu' - g_{\mu\nu}\,k\cdot k' + i\,\epsilon_{\mu\nu\alpha\beta}\,s^\alpha q^\beta\right], \tag{2.12}$$

where $g_{\mu\nu}$ is the Minkowski metric and $\epsilon_{\mu\nu\alpha\beta}$ the totally anti-symmetric Levi-Civita tensor. The term $(g_{\mu\nu}m)$ accounting for the electron mass m was neglected. The first three terms are symmetric and define $L_{\mu\nu}^S$. The last term is the anti-symmetric part $L_{\mu\nu}^A$ of the leptonic tensor which vanishes in unpolarized scattering.

The hadronic tensor that describes the composite structure of the nucleon cannot be calculated exactly. However, Lorentz invariance, gauge invariance, and parity conservation of the electromagnetic interaction lead to the general form of the hadronic tensor $W_{\mu\nu} = W_{\mu\nu}^S + W_{\mu\nu}^A$,

$$\begin{aligned}
W_{\mu\nu} =& \left(-g_{\mu\nu} - \frac{q_\mu q_\nu}{Q^2}\right)\frac{F_1(x,Q^2)}{M} + \left(P_\mu + \frac{P\cdot q}{Q^2}q_\mu\right)\left(P_\nu + \frac{P\cdot q}{Q^2}q_\nu\right)\frac{F_2(x,Q^2)}{M(P\cdot q)} \\
&+ i\epsilon_{\mu\nu\alpha\beta}\,q^\alpha\,\frac{1}{P\cdot q}\left[S^\beta\,g_1(x,Q^2) + \left(S^\beta - \frac{S\cdot q}{P\cdot q}P^\beta\right)g_2(x,Q^2)\right],
\end{aligned} \tag{2.13}$$

The structure functions $F_1(x,Q^2)$ and $F_2(x,Q^2)$ account for the spin-independent nucleon structure. These terms comprise the symmetric tensor $W_{\mu\nu}^S$. The structure functions are equivalent to the response functions defined in Eqs. (2.10); they are related via

$$F_1(x,Q^2) = M\,W_1(\nu,Q^2), \qquad F_2(x,Q^2) = \nu\,W_2(\nu,Q^2). \tag{2.14}$$

Table 2.1: The kinematics of polarized inclusive and semi-inclusive deep-inelastic scattering. The kinematics are given in the limit that the mass of the lepton can be neglected.

$k = (E, \vec{k})$, $k' = (E', \vec{k'})$	4-momenta of the initial and final state electrons
$s = 2\lambda \left(\lvert\vec{k}\rvert, E\, \vec{k}/\lvert\vec{k}\rvert \right)$	Spin 4-vector of the initial state electron with helicity $\lambda = \pm\frac{1}{2}$
θ, ϕ	Polar angle and azimuthal angle of the scattered electron
$P \overset{\text{lab}}{=} (M, 0)$	4-momentum of the initial target nucleon
$S = (0, \vec{S})$, $S^2 = -1$,	Spin 4-vector of the initial state nucleon
$q = (\nu, \vec{q})$	4-momentum of the virtual photon
$Q^2 = -q^2 \overset{\text{lab}}{=} 4EE' \sin^2 \dfrac{\theta}{2}$	Negative squared 4-momentum transfer
$\nu = \dfrac{1}{M} P \cdot q \overset{\text{lab}}{=} E - E'$	Energy of the virtual photon
$x = \dfrac{Q^2}{2\, P \cdot q} \overset{\text{lab}}{=} \dfrac{Q^2}{2\, M\nu}$	Bjørken scaling variable
$y = \dfrac{P \cdot q}{P \cdot k} \overset{\text{lab}}{=} \dfrac{\nu}{E}$	Fractional energy of the virtual photon
$W^2 = (P + q)^2 \overset{\text{lab}}{=} M^2 + 2M\nu - Q^2$	Squared invariant mass of the hadronic final state
$p = (E_h, \vec{p})$	4-momentum of a hadron in the final state
$z = \dfrac{P \cdot p}{P \cdot q} \overset{\text{lab}}{=} \dfrac{E_h}{\nu}$	Fractional energy of the final state hadron, $0 < z < 1$
$p^{\parallel}_{CM} = \dfrac{\vec{p} \cdot \vec{q}}{\lvert\vec{q}\rvert} \bigg\rvert_{\gamma^* - N}$	Projection of the hadron momentum onto the photon momentum $\vec{q}$ in the photon-nucleon center-of-mass frame
$x_F = \dfrac{p^{\parallel}_{CM}}{\lvert\vec{q}\rvert} \overset{\text{lab}}{\simeq} \dfrac{2 p^{\parallel}_{CM}}{W}$	Feynman variable, $-1 < x_F < 1$

The spin-dependent nucleon structure is contained in the functions $g_1(x, Q^2)$ and $g_2(x, Q^2)$. The two corresponding terms in Eq. (2.13) make up the anti-symmetric tensor $W_{\mu\nu}^A$.

The Unpolarized Cross Section. The anti-symmetric lepton tensor cancels, if $L_{\mu\nu}$ is averaged over the initial electron spin states, that is, if the electron beam is unpolarized. Such an experiment is only sensitive to the unpolarized structure functions F_1 and F_2, because the cross section reduces to

$$\frac{d^2\sigma}{dE'\,d\Omega} = \frac{\alpha^2}{Q^4}\frac{E'}{E}\,L_{\mu\nu}^S\,(W^{\mu\nu,S} + W^{\mu\nu,A}) = \frac{\alpha^2}{Q^4}\frac{E'}{E}\,L_{\mu\nu}^S\,W^{\mu\nu,S}. \tag{2.15}$$

The cross section in the intervals $[x, dx + x]$ and $[Q^2, Q^2 + dQ^2]$ is related to this expression by

$$\frac{d^2\sigma}{dx\,dQ^2} = \frac{2\pi M\nu}{E'\,x\,((P+k)^2 - M^2)}\frac{d^2\sigma}{dE'\,d\Omega}.$$

In terms of the Mott cross section (Eq. (2.4)), the unpolarized cross section of inclusive deep-inelastic scattering is therefore

$$\frac{d^2\sigma}{dx\,dQ^2} = \left(\frac{d\sigma}{d\Omega}\right)_{\text{Mott}}\frac{\pi}{E'^2\,x}\left(\frac{1}{\nu}\,F_2(x, Q^2) + \frac{2}{M}\,F_1(x, Q^2)\tan^2\frac{\theta}{2}\right). \tag{2.16}$$

The cross section for unpolarized inelastic scattering given in Eq. (2.9) is analogous to this cross section and follows from equivalent symmetry considerations of the hadronic tensor.

The DIS process can also be interpreted as a virtual photo-absorption by the nucleon, with the electron being the source of the virtual photon. The photon with invariant mass $-Q^2 < 0$ and energy ν has components of longitudinal and transverse polarization. The respective photo-absorption cross sections $\sigma_L(x, Q^2)$ and $\sigma_T(x, Q^2)$ can be combined in the total cross section,

$$\frac{d^2\sigma}{dx\,dQ^2} = \Gamma\left[\sigma_T(x, Q^2) + \epsilon\,\sigma_L(x, Q^2)\right], \tag{2.17}$$

where the kinematic factor Γ is

$$\Gamma = \frac{\alpha}{2\pi^2 Q^2}\frac{\nu^2(1-x)}{E^2\,x}\frac{1}{1-\epsilon}. \tag{2.18}$$

The factor ϵ is the ratio of longitudinal to transverse polarization of the virtual photon:

$$\epsilon = \left[1 + \frac{2\,\vec{q}^2}{Q^2}\tan^2\frac{\theta}{2}\right]^{-1} = \frac{1 - y - \frac{1}{4}\gamma^2 y^2}{1 - y + \frac{1}{4}y^2\,(\gamma^2 + 2)}, \tag{2.19}$$

where $\gamma^2 \equiv Q^2/\nu^2$. The ratio of the absorption cross sections, $R = \sigma_L/\sigma_T$, is related to the unpolarized nucleon structure functions by

$$R(x, Q^2) \equiv \frac{\sigma_L}{\sigma_T} = \frac{(1+\gamma^2)F_2(x, Q^2) - 2xF_1(x, Q^2)}{2xF_1(x, Q^2)}, \qquad (2.20)$$

where the numerator is the longitudinal structure function $F_L \equiv (1+\gamma^2)F_2 - 2xF_1$. A parameteri-
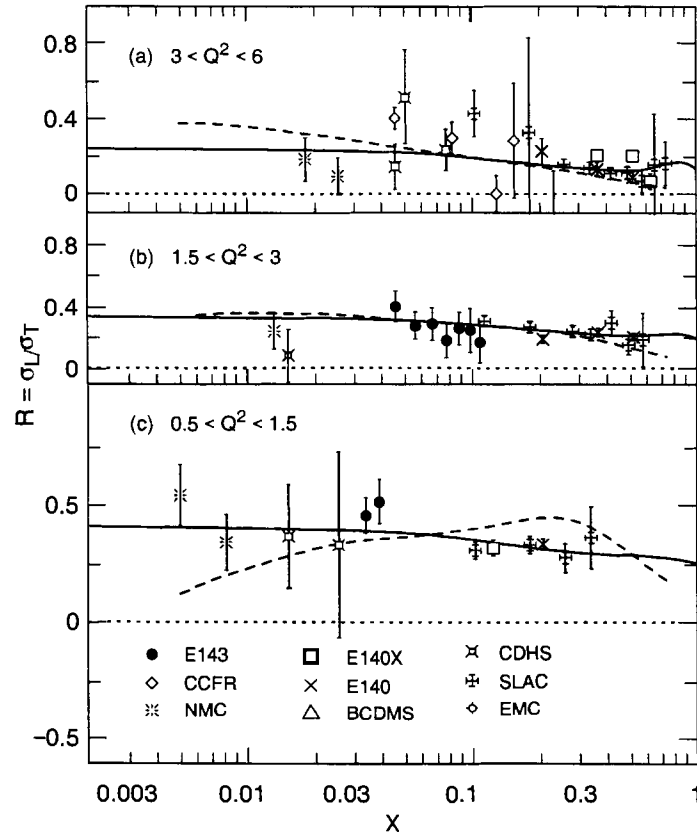
Figure 2.5: The ratio of longitudinal and transverse cross sections $R = \sigma_L/\sigma_T$ as a function of x in three ranges of Q^2. The solid line shows the parameterization R1998 [16]. Also shown are measurements from various experiments. The dashed lines show the results of a next-to-next-to-leading order calculation in perturbative QCD. The figure is reproduced from Ref. [16].

zation of R [16] and available data are shown in Fig. 2.5. In the Q^2-range relevant for the HERMES experiment, the precise data available from a number of experiments provide tight constraints on the parameterization.

It follows from Eq. (2.20) that the structure function F_1 is related to F_2 via

$$F_1(x, Q^2) = \frac{1 + \gamma^2}{2x\left(1 + R(x, Q^2)\right)} F_2(x, Q^2). \tag{2.21}$$

In the limit $Q^2 \to \infty$ and $\nu \to \infty$ with $x = Q^2/(2M\nu)$ finite, which is known as the Bjørken limit, the longitudinal absorption cross section vanishes, because of helicity conservation at the photon-parton vertex. In this limit, Eq. (2.21) simplifies to the Callan-Gross relation [17],

$$F_2(x) = 2x\, F_1(x). \tag{2.22}$$

The structure function F_2 has been measured over six orders of magnitude in Q^2 and five orders in x. The data — shown in Fig. 2.6 — were collected by various fixed target experiments at SLAC and CERN [19, 20, 21, 22], and colliding beam experiments at DESY [23, 24, 25]. For values of $x \gtrsim 0.13$, the structure is largely independent of Q^2. This scaling behaviour, suggested by Bjørken in 1967 [26], was first observed at SLAC — the corresponding data are included in the $x = 0.25$ bin in Fig. 2.6. Bjørken scaling is explained in the simple parton model, whereas scaling violations observed at smaller values of x can be explained within the QCD improved parton model. Both models are discussed in Sec. 2.3.

The Polarized Cross Section. The cross section becomes sensitive to the anti-symmetric part of the hadronic tensor, if the leptonic and hadronic tensors are not averaged over the spin-states, i.e. if the electron beam and the target are polarized. The polarized structure functions g_1 and g_2 can be isolated by considering the difference in cross section upon reversal of the target spin orientation. The two most useful configurations are a longitudinally polarized electron beam, denoted by $\to$ and a longitudinally or transversely polarized target, denoted by $\Rightarrow$ and $\Leftarrow$ for the parallel and anti-parallel longitudinal orientation, or $\Uparrow$ and $\Downarrow$ for the two transverse orientations. The cross section differences for these two experiments are

$$\frac{d^2\sigma^{\to\Leftarrow}}{dx\,dQ^2} - \frac{d^2\sigma^{\to\Rightarrow}}{dx\,dQ^2} = \frac{4\pi\alpha^2}{ME^2Q^2x}\left[(E + E'\cos\theta)\, g_1(x, Q^2) + 2Mx\, g_2(x, Q^2)\right], \tag{2.23}$$

$$\frac{d^2\sigma^{\to\Uparrow}}{dx\,dQ^2} - \frac{d^2\sigma^{\to\Downarrow}}{dx\,dQ^2} = \frac{4\pi\alpha^2}{ME^2Q^2x}\sin\theta\cos\phi\left[g_1(x, Q^2) + \frac{2E}{\nu}\, g_2(x, Q^2)\right]. \tag{2.24}$$

Here θ is the polar angle and ϕ the azimuthal angle of the scattered electron as defined in Fig. 2.7. The longitudinal cross section (Eq. (2.23)) is independent of the azimuthal angle, while the cross
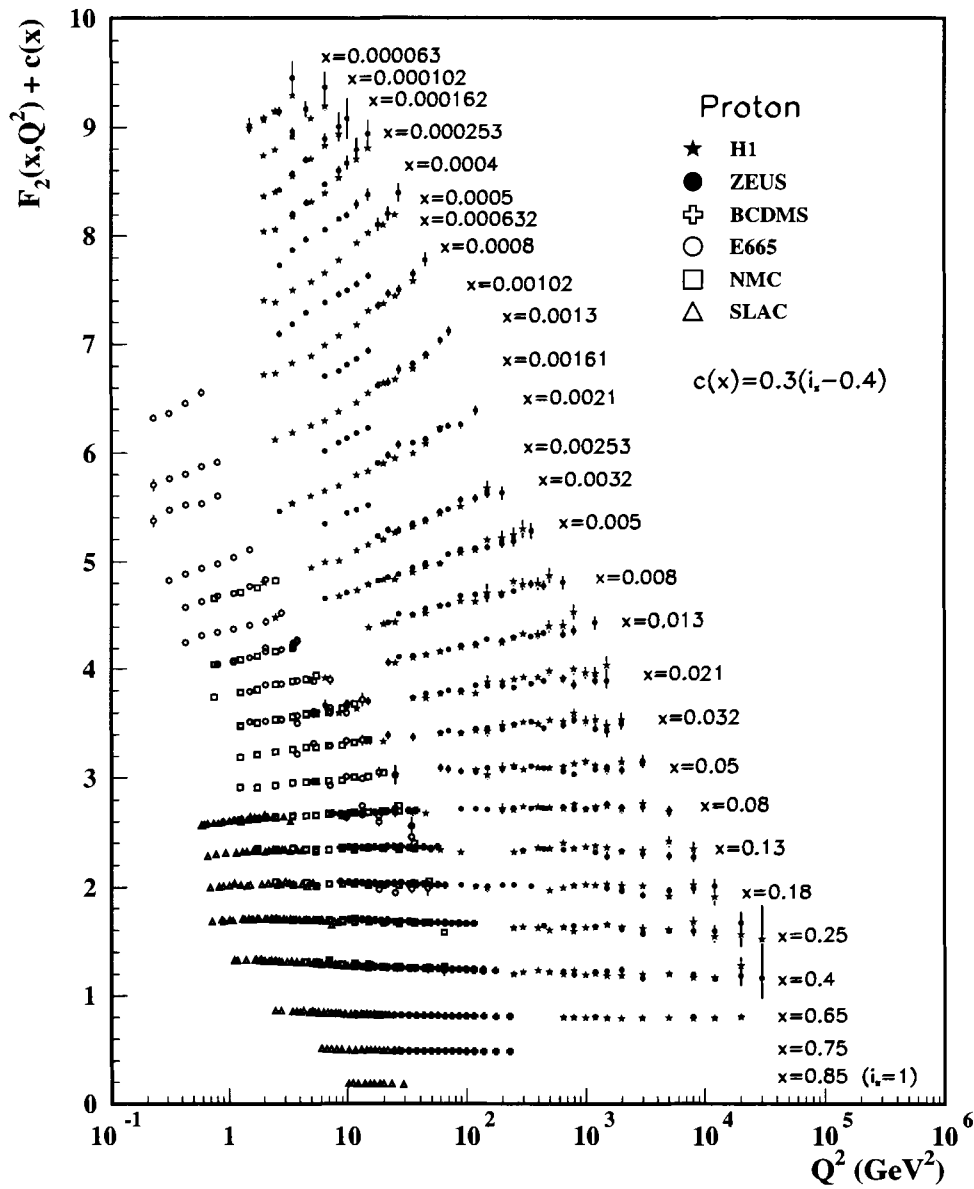
Figure 2.6: The unpolarized proton structure function $F_2(x, Q^2)$ in electromagnetic scattering of positrons, electrons, or muons off protons. The error bars represent the statistical and systematic uncertainties. For better representation, the data were offset by a constant $c(x) = 0.3(i_x - 0.4)$, where i_x is the x-bin number. The plot is reproduced from Ref. [18].
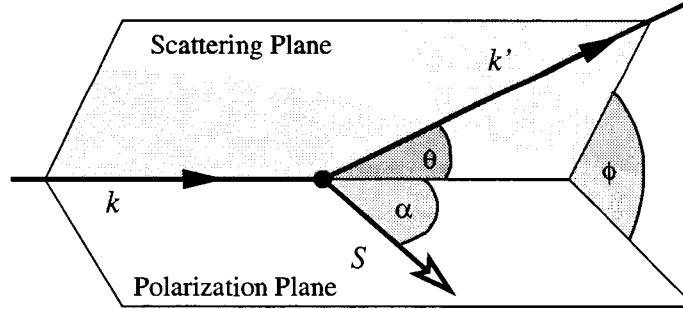
Figure 2.7: Angle definitions in the laboratory frame used in polarized deep-inelastic scattering. Here, k, k', and S are the three-vectors of the incoming and outgoing lepton and of a target spin respectively. The angle α vanishes for the longitudinally polarized target, and $\alpha = 90°$ in the case of a transversely polarized target. In the former case, the azimuthal angle ϕ is undefined.

section for a transversely polarized target is modulated by $\cos \phi$. The former cross section is largely sensitive to g_1 because the contribution by g_2 is suppressed by M/E ($E \gg M$), and similarly the latter cross section is sensitive to g_2. Measurements of g_1 and g_2 utilizing both processes were carried out recently at SLAC [27, 28, 29].

Measurements of the spin structure function g_1 are presented on the proton, the deuteron, and the neutron in Fig. 2.8. The data, presented as function of x, were collected by fixed target experiments at SLAC [30, 31, 28, 32, 4], CERN [33, 34, 35], and at DESY [36, 37]. Naturally the experiments were carried out with varying setups and therefore the Q^2 values vary by orders of magnitude for any given value of x. In the Figure, the data collected by EMC and E155 were evolved to $Q^2 = 10.7\,\text{GeV}^2$ and $Q^2 = 5\,\text{GeV}^2$; all other data are presented at the measured Q^2. The data shown in Fig. 2.8 extend over a range $0.01 \ldots 100\,\text{GeV}^2$ in Q^2 at moderate x. In particular, a comparison of the HERMES data with the results by the SMC collaboration which were collected at $Q^2 \sim 0.8 \ldots 20\text{GeV}^2$ and $Q^2 \sim 0.01 \ldots 100\text{GeV}^2$ respectively, shows that scaling violations in the measured ranges are small as expected from the unpolarized measurements in the corresponding kinematic range.

The spin structure functions g_2 on the proton, the deuteron, and the neutron are shown in Fig. 2.9. Precise measurements by the E155 collaboration show that the spin structure function on the proton and the deuteron is essentially compatible with zero. In the determination of the quark polarizations presented in Ch. 8, contributions due to g_2 were neglected and an uncertainty was included in the systematic error.
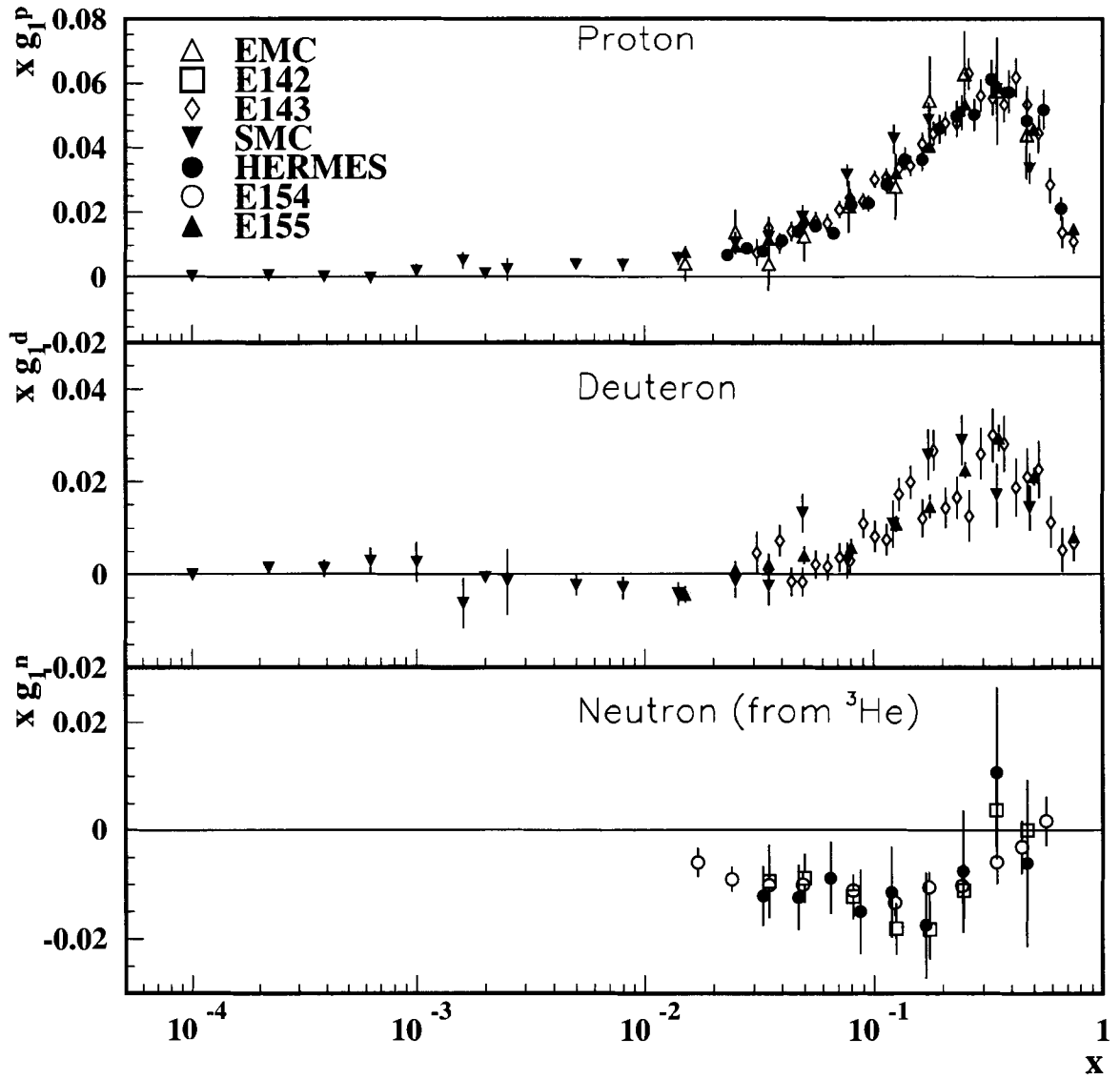
Figure 2.8: The polarized structure function $xg_1(x, Q^2)$ on the proton, the deuteron, and the neutron. See the text for details. The plot is reproduced from Ref. [18].
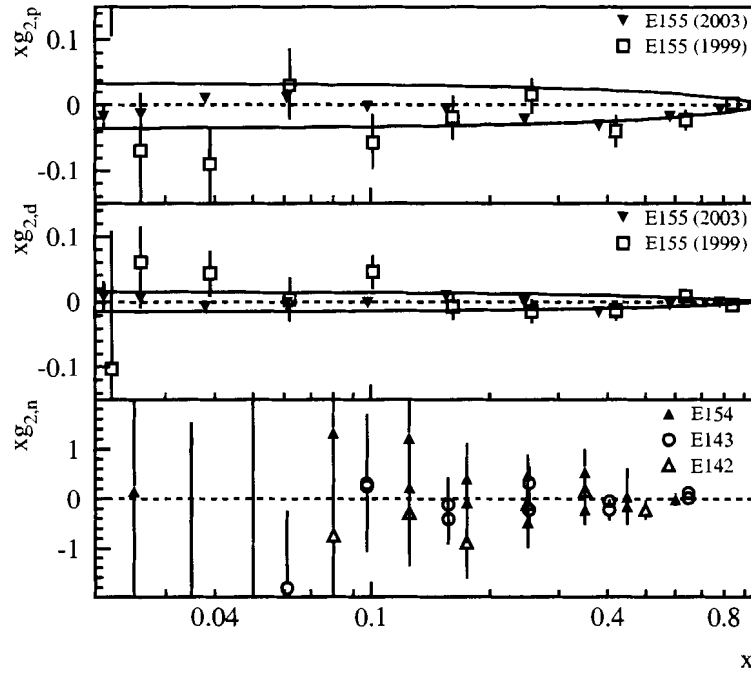
Figure 2.9: The polarized structure function $xg_2(x, Q^2)$ on the proton, the deuteron, and the neutron. All data were collected at SLAC with the experiments E155 [38, 29], E154 [39], E143 [40], and E142 [30]. Compatible measurements of $g_{2,p}$ and $g_{2,d}$ with large statistical uncertainties by the E143 collaboration [31] are omitted.

2.3 The Parton Model

2.3.1 The Simple Parton Model

The observation of Bjørken scaling at SLAC (see above) provided experimental verification of Feynman's parton model [41]. In this model, the nucleon is viewed as being comprised of point-like non-interacting constituents, the partons, which absorb the virtual photon in the deep-inelastic scattering reaction.

The parton model is formulated in an infinite momentum frame, in which the nucleon is moving with very high momentum $\tilde{P}$ in the positive z-direction. Lorentz invariance of the structure functions ensures that their description in this reference frame is valid in any other frame. The photon momentum $\tilde{q}$ in this frame is fixed by Lorentz invariance to be $-\tilde{Q}^2 = -Q^2 \overset{\text{lab}}{=} -2xM\nu$ and $\tilde{P} \cdot \tilde{q} = P \cdot q \overset{\text{lab}}{=} M\nu$. Furthermore the masses of the partons can be neglected relative to the nu-

cleon momentum and they can be viewed as free on the time-scale of the photon-parton interaction [26]. The struck parton remains free after the interaction, as it receives a large momentum from the photon. Therefore it is on mass shell and its 4-momentum vanishes:

$$(\zeta \tilde{P} + \tilde{q})^2 = \zeta^2 M^2 + 2\zeta \tilde{P} \cdot \tilde{q} - Q^2 \approx 0, \tag{2.25}$$

where ζ is the fraction of the nucleon momentum carried by the struck quark. It follows that the scaling variable x equals the momentum fraction ζ in the limit that the term $\zeta^2 M^2$ is negligible compared to $\tilde{Q}^2$ and $\tilde{P} \cdot \tilde{q} = 2M\nu$, which is equivalent to the Bjørken limit introduced in the previous section.

In this limit, the cross section for scattering off the nucleon reduces to the incoherent sum of the cross sections for scattering off the partons in the nucleon. The structure functions for a point-like particle with mass m are given by Eqs. (2.10) with the replacement $M \to m$ and $G_E = G_M \equiv 1$. The nucleon structure functions are in terms of these functions weighted by the parton number density $q(x)$ and their squared charges in units of e:

$$F_1(x, Q^2) \longrightarrow F_1(x) = \frac{1}{2} \sum_q \int d\zeta \, \frac{x}{\zeta} \, e_q^2 \, q(\zeta) \, \delta(\zeta - x) \qquad = \frac{1}{2} \sum_q e_q^2 \, q(x) \tag{2.26}$$

$$F_2(x, Q^2) \longrightarrow F_2(x) = \sum_q \int d\zeta \, \zeta \, e_q^2 \, q(\zeta) \, \delta(\zeta - x) \qquad = x \sum_q e_q^2 \, q(x), \tag{2.27}$$

where the identification of $\zeta = x$ is explicitly contained in the δ-functions stemming from Eqs. (2.10). The parton model thus implies that the nucleon structure functions scale — they are independent of Q^2 at a given value of x, if the nucleon consists of point-like constituents. In this limit, the Callan-Gross relation (Eq. (2.22)) is trivially satisfied.
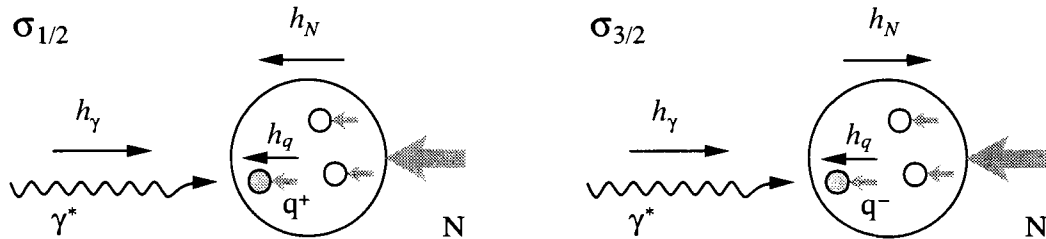
Figure 2.10: Spin-dependent deep-inelastic scattering in the Breit frame. The helicities of the photon γ^*, the struck parton q, and the nucleon N are indicated by the arrows labeled $h_{\gamma,q,N}$. The shaded arrows indicate the momenta of the particles.

The unpolarized picture of the nucleon can be extended to include the polarized nucleon structure. In a reference frame, known as the Breit frame, in which the struck parton recoils with its momentum reversed, $\vec{p}_f = -\vec{p}_i$, the photon is absorbed by the parton in a head-on collision. Assuming the partons have spin $1/2$, angular momentum conservation requires that the spin-1 photon is absorbed by partons with the same helicity, so that the final state parton has spin $1/2$. The photon probes partons with the same helicity as the nucleon if the photon and nucleon helicities are the same. The corresponding parton number densities are labeled q^+ and the cross section $\sigma_{1/2}$. If the nucleon and the photon have opposite helicity, partons with helicity opposite to that of the nucleon are probed. The cross section and the parton densities for this process are $\sigma_{3/2}$ and q^- respectively. The two processes are illustrated in Fig. 2.10.

The difference of the two cross sections, $\sigma_{1/2} - \sigma_{3/2}$, is proportional to g_1, while the sum is proportional to F_1. Analogously to the unpolarized structure function F_1, the structure function g_1 can therefore be expressed as the incoherent sum of helicity dependent or polarized parton densities:

$$g_1(x) = \frac{1}{2} \sum_q e_q^2 \left(q^+(x) - q^-(x) \right) = \frac{1}{2} \sum_q e_q^2 \, \Delta q(x), \qquad (2.28)$$

where $\Delta q(x) \equiv q^+(x) - q^-(x)$ defines the polarized parton density. Clearly the unpolarized densities are given in terms of the polarized parton densities by $q(x) = q^+(x) + q^-(x)$. Unlike g_1, the function g_2 has no interpretation in the simple parton model, in which it vanishes,

$$g_2(x) = 0. \qquad (2.29)$$

An interpretation of g_2 that is related to transverse spin, see Eq. (2.24), is only possible in models that incorporate massive off-shell partons and transverse momentum $p_\perp$.

While the parton model was proposed before the advent of QCD, extensive theoretical and experimental work showed that the charged partons that interact electromagnetically are the quarks of QCD. The sums in Eqs. (2.26) and (2.27) run over all quark flavours (u, d, s, c, b, t) and their corresponding anti-quarks. However, in practice only the four lightest flavours contribute to the structure functions. At the energies of the HERMES experiment where contributions from the charm quark are also negligible, the sum reduces to the flavours u, d, s, and $\bar{u}$, $\bar{d}$, and $\bar{s}$. The structure functions

of the proton are therefore given by

$$F_{1p}(x) = \frac{1}{2}\left[\frac{4}{9}\left(u(x) + \bar{u}(x)\right) + \frac{1}{9}\left(d(x) + \bar{d}(x)\right) + \frac{1}{9}\left(s(x) + \bar{s}(x)\right)\right], \tag{2.30}$$

$$g_{1p}(x) = \frac{1}{2}\left[\frac{4}{9}\left(\Delta u(x) + \Delta\bar{u}(x)\right) + \frac{1}{9}\left(\Delta d(x) + \Delta\bar{d}(x)\right) + \frac{1}{9}\left(\Delta s(x) + \Delta\bar{s}(x)\right)\right]. \tag{2.31}$$

The neutron structure functions are written in terms of the parton densities for the proton using isospin symmetry, $u_n \to d_p \equiv d$, $d_n \to u_p \equiv u$, $\bar{u}_n \to \bar{d}_p \equiv \bar{d}$, and $\bar{d}_n \to \bar{u}_p \equiv \bar{u}$,

$$F_{1n}(x) = \frac{1}{2}\left[\frac{4}{9}\left(d(x) + \bar{d}(x)\right) + \frac{1}{9}\left(u(x) + \bar{u}(x)\right) + \frac{1}{9}\left(s(x) + \bar{s}(x)\right)\right], \tag{2.32}$$

$$g_{1n}(x) = \frac{1}{2}\left[\frac{4}{9}\left(\Delta d(x) + \Delta\bar{d}(x)\right) + \frac{1}{9}\left(\Delta u(x) + \Delta\bar{u}(x)\right) + \frac{1}{9}\left(\Delta s(x) + \Delta\bar{s}(x)\right)\right]. \tag{2.33}$$

In the following, the sum over all quark flavours, $\sum_q$, is understood to run over these six quark and anti-quark flavours only.

The densities of the three valence quarks in the nucleon (cf. Ch. 1) that carry its electric charge and baryon quantum number are similarly expressed in terms of these parton distributions,

$$u_V(x) \equiv u(x) - \bar{u}(x), \qquad \Delta u_V(x) \equiv \Delta u(x) - \Delta\bar{u}(x),$$
$$\tag{2.34}$$
$$d_V(x) \equiv d(x) - \bar{d}(x), \qquad \Delta d_V(x) \equiv \Delta d(x) - \Delta\bar{d}(x).$$

Here, symmetry in the infinite sea of quark/anti-quark pairs surrounding the valence quarks allowed the identification $u_{\text{sea}}(x) \equiv \bar{u}(x)$, $\Delta u_{\text{sea}}(x) \equiv \Delta\bar{u}(x)$, and analogously $d_{\text{sea}}(x) \equiv \bar{d}(x)$ and $\Delta d_{\text{sea}}(x) \equiv \Delta\bar{d}(x)$.

2.3.2 The Parton Model and Quantum Chromodynamics

The data displayed in Fig. 2.6 show that Bjørken scaling is violated at small and large x. The structure function F_2 increases with increasing Q^2 at small x and slowly decreases at large x. These observations can be explained if interactions among the partons are introduced in the model, which are assumed to be negligible in the simple parton model during the time that the partons are probed by the lepton. The interactions of the charged partons (or quarks) can be modeled in the framework of quantum chromodynamics (QCD).

QCD is a local gauge theory based on an internal non-Abelian symmetry of the quarks known as colour, or $SU(3)_c$. All hadrons existing in nature are colour singlets. The basic singlet states are the
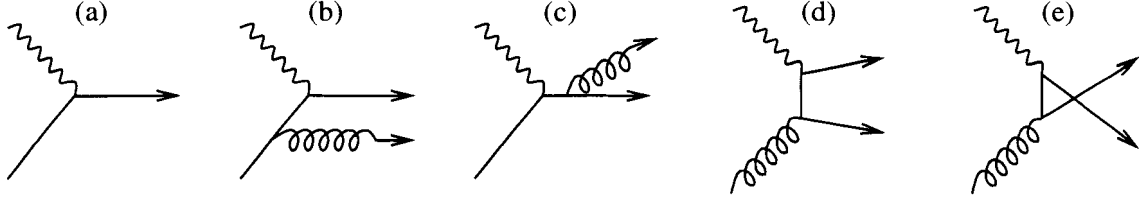
Figure 2.11: The leading $O(\alpha)$ contribution (a), and the $O(\alpha\alpha_s)$ QCD radiative corrections to the DIS cross section: Gluon bremsstrahlung, (b) and (c), and gluon-initiated scattering or photon-gluon fusion, (d) and (e).

mesons $q_a\bar{q}^a$, and the baryons $\epsilon^{abc}q_aq_bq_c$. Here, ϵ^{abc} is the totally anti-symmetric tensor. The quarks q_a, $a = R, B, G$ (for red, blue, green) are elements of the fundamental representation of the group of colour transformations $SU(3)_c$. The anti-quarks $\bar{q}_a$ are elements of the corresponding complex conjugate representation.

Quarks couple to gluons that mediate the strong interaction. The strength of the coupling $g_s^2 = 4\pi\alpha_s$ (α_s is defined analogously to the fine structure constant of QED) is given to leading order in perturbation theory by

$$\alpha_s(\mu^2) = \frac{1}{b\,\log\,(\mu^2/\Lambda^2)} \qquad \text{with} \qquad b = \frac{33 - 2\,n_f}{12\pi}, \tag{2.35}$$

where μ is the mass scale introduced in the renormalization of the coupling. In DIS, the mass scale is usually set equal to Q^2. The number of energetically allowed quark flavours given by n_f depends on this mass scale, because of the large range of masses of the quarks. The parameter Λ represents the scale at which perturbation theory breaks down and the coupling diverges. The value of Λ is about $200 - 300\,\text{GeV}$ depending on the renormalization scheme and the number of quark flavours n_f. The coupling constant vanishes, if the mass scale becomes large. In this limit, the quarks do not interact, a phenomenon known as asymptotic freedom. The simple parton model is recovered in this limit. The coupling strength becomes large as μ approaches Λ. This is evidence for the confinement of quarks in hadrons.

The interaction of the quarks in the proton gives rise to corrections to the DIS cross section. The contributions to order $O(\alpha\alpha_s)$ are shown in Fig. 2.11. These corrections and the scale dependence of the coupling strength lead to the scaling violations in the nucleon structure functions. The quark densities are said to evolve with Q^2. The Q^2 evolution can be calculated in perturbation theory based on the leading order graphs shown in Fig. 2.11 and higher orders as necessary. The results are

summarized in the DGLAP equations [42, 43, 44],

$$
Q^2 \frac{\partial}{\partial Q^2} \begin{pmatrix} q(x, Q^2) \\ g(x, Q^2) \end{pmatrix} = \frac{\alpha_s(Q^2)}{2\pi} \sum_{q'} \int_x^1 \frac{d\xi}{\xi} \begin{pmatrix} P_{qq'}\left(\frac{x}{\xi}\right) & P_{qg}\left(\frac{x}{\xi}\right) \\ P_{gq'}\left(\frac{x}{\xi}\right) & P_{gg}\left(\frac{x}{\xi}\right) \end{pmatrix} \begin{pmatrix} q'(\xi, Q^2) \\ g(\xi, Q^2) \end{pmatrix}, \quad (2.36)
$$

where $q(x, Q^2)$ and $g(x, Q^2)$ are the quark and gluon densities in an interval $[x, x + dx]$ at a resolution given by Q^2. The functions P_{ab} are the splitting functions. In leading order, $\alpha_s P_{qq}(x/\xi)$ is the probability that a quark with momentum fraction ξ will radiate a gluon and leave a quark with momentum fraction x. Similarly $\alpha_s P_{gq}(x/\xi)$ is the probability that a gluon will create a $q\bar{q}$ pair, where the quark carries the momentum fraction x. The evolution of the gluon density is based on the splitting functions P_{gq} and P_{gg}. The former is equivalent to P_{qg} and the latter describes the splitting of a gluon into a gluon pair. The DGLAP evolution equations allow to calculate the parton densities at any scale Q^2 where perturbation theory applies, provided the densities are known at some scale Q_0^2. The evolution of the polarized parton densities $\Delta q(x, Q^2)$ is analogous to the unpolarized case with the replacements $q \to \Delta q$, $g \to \Delta g$, and $P_{ab} \to \Delta P_{ab}$. The evolution of the polarized densities is in general different from the unpolarized densities because the polarized and unpolarized splitting functions are different, except for $\Delta P_{qq}(x) = P_{qq}$ [45, 46]. In the kinematic region where the valence quarks dominate the parton densities, the difference of the splitting functions is expected to be small [47]. Therefore the ratio of the polarized and unpolarized quark densities and the structure function ratio g_1/F_1 is expected to be approximately Q^2 independent at moderate x. While the splitting functions can be calculated in perturbative QCD, the parton densities $q(x, Q^2)$, $g(x, Q^2)$, $\Delta q(x, Q^2)$, and $\Delta g(x, Q^2)$ cannot be calculated perturbatively from first principles, because they depend on non-perturbative (long-distance) parts of the strong interaction.

In terms of the effective parton densities at scale Q^2, the unpolarized and polarized structure

functions F_1 and g_1 of the nucleon become,

$$F_1(x, Q^2) = \frac{1}{2} \sum_q e_q^2 \left\{ q(x, Q^2) \right.$$

$$\left. + \frac{\alpha_s(Q^2)}{2\pi} \int_x^1 \frac{d\xi}{\xi} \left[C_q\left(\frac{x}{\xi}\right) q(\xi, Q^2) + C_g\left(\frac{x}{\xi}\right) g(\xi, Q^2) \right] \right\} \qquad (2.37)$$

$$g_1(x, Q^2) = \frac{1}{2} \sum_q e_q^2 \left\{ \Delta q(x, Q^2) \right.$$

$$\left. + \frac{\alpha_s(Q^2)}{2\pi} \int_x^1 \frac{d\xi}{\xi} \left[\Delta C_q\left(\frac{x}{\xi}\right) \Delta q(\xi, Q^2) + \Delta C_g\left(\frac{x}{\xi}\right) \Delta g(\xi, Q^2) \right] \right\} \qquad (2.38)$$

The renormalization scheme-dependent coefficient functions $C_{q,g}$ and $\Delta C_{q,g}$ are related to the short-distance photon-quark and photon-gluon cross sections shown in Fig. 2.11. In leading order of α_s, the coefficient functions vanish and the structure functions are

$$F_1(x, Q^2) = \frac{1}{2} \sum_q e_q^2 \, q(x, Q^2), \qquad g_1(x, Q^2) = \frac{1}{2} \sum_q e_q^2 \, \Delta q(x, Q^2). \qquad (2.39)$$

These expressions are analogous to Eqs. (2.26), (2.27) and (2.28), modified for the scale dependence of the parton distributions given by the DGLAP equations. To this order the parton densities are universal, *i.e.* they appear in any hard reaction involving the nucleon.

The scale dependence of the structure functions can be given a physical interpretation through the resolution of the photon probe given by Q^2. At low Q^2 the photon resolves only little of the internal nucleon structure. It probes predominantly the valence quarks that carry large fractions of the momentum. The number of resolved quarks and gluons that share the momentum increases with Q^2. Thus at large Q^2 the photon probes predominantly partons with small momentum fractions x. The data shown in Fig. 2.6 confirm this picture: At small x the parton densities increase with Q^2 and they decrease slowly with Q^2 at large x.

2.4 Sum Rules

Integrated over the range in momentum fraction x, the parton number densities have to reproduce the quantum numbers of the nucleon. The simplest integrals, or sum rules, are the first moments of the unpolarized densities that for the proton give baryon number one, charge one and strangeness

zero,

$$\int_0^1 dx \; u_V(x, Q^2) \equiv \int_0^1 dx \; \left(u(x, Q^2) - \bar{u}(x, Q^2)\right) = 2, \tag{2.40}$$

$$\int_0^1 dx \; d_V(x, Q^2) \equiv \int_0^1 dx \; \left(d(x, Q^2) - \bar{d}(x, Q^2)\right) = 1, \tag{2.41}$$

$$\int_0^1 dx \; \left(s(x, Q^2) - \bar{s}(x, Q^2)\right) = 0. \tag{2.42}$$

The Gottfried sum rule [48] involves the proton and neutron structure functions F_{2p} and F_{2n} respectively:

$$\int_0^1 \frac{dx}{x} \left(F_{2p}(x, Q^2) - F_{2n}(x, Q^2)\right) = \frac{1}{3} \tag{2.43}$$

This sum rule follows in the simple parton model, with the assumptions of isospin symmetry and of a symmetric light quark sea, $\bar{u}(x, Q^2) \equiv \bar{d}(x, Q^2)$. Perturbative QCD corrections to the right hand side of Eq. (2.43) were found to be small [49]. Clear evidence of a deviation from the Gottfried sum rule was found at CERN in 1990 [50], showing that the symmetry of the light quark sea is violated.

Sum rules involving the polarized structure function g_1 provide insight into the nucleon spin structure. The integral of the proton and neutron structure functions $g_{1p(n)}$ can be written as [45]

$$\Gamma_{1p(n)} \equiv \int_0^1 dx \; g_{1p(n)}(x, Q^2) = \frac{1}{12} \left(\pm a_3 + \frac{a_8}{3}\right) \Delta C_{NS}(Q^2) + \frac{a_0}{9} \Delta C_S(Q^2), \tag{2.44}$$

where the minus sign is for the neutron structure function. $\Delta C_S(Q^2)$ and $\Delta C_{NS}(Q^2)$ are the singlet and non-singlet coefficient functions respectively. In the $\overline{\text{MS}}$-renormalization scheme, they are for three quark flavours to second (third) order in α_s [51]:

$$\Delta C_S(Q^2) = 1 - \frac{\alpha_s(Q^2)}{\pi} - 1.096 \left(\frac{\alpha_s(Q^2)}{\pi}\right)^2, \tag{2.45}$$

$$\Delta C_{NS}(Q^2) = 1 - \frac{\alpha_s(Q^2)}{\pi} - 3.583 \left(\frac{\alpha_s(Q^2)}{\pi}\right)^2 - 20.215 \left(\frac{\alpha_s(Q^2)}{\pi}\right)^3. \tag{2.46}$$

The quantities a_0, a_3, and a_8 measure the proton matrix elements of the flavour singlet, triplet, and octet vector currents:

$$\langle P, S | J_{5\mu}^0 | P, S \rangle = 2M a_0 \, S_\mu \tag{2.47}$$

$$\langle P, S | J_{5\mu}^3 | P, S \rangle = M a_3 \, S_\mu \tag{2.48}$$

$$\langle P, S | J_{5\mu}^8 | P, S \rangle = M a_8 \, S_\mu \tag{2.49}$$

where $J^0_{5\mu}$ is the flavour singlet current, and $J^3_{5\mu}$ and $J^8_{5\mu}$ are the non-singlet axial-vector currents. The triplet current matrix element is equal to the axial charge of the nucleon,

$$g_a = |g_A/g_V| = 1.2670 \pm 0.0030 \qquad (2.50)$$

(see Ref. [18]) which can be measured in neutron β-decay. The matrix element of the octet current is similarly measured in hyperon β-decays. A recent analysis [52] reports a value of

$$a_8 = 0.585 \pm 0.025. \qquad (2.51)$$

However, the determination of a_8 requires the assumption of $SU(3)$ flavour symmetry. The effects of symmetry breaking in hyperon β-decay were estimated to be on the order of 10 % [53]. The singlet current $J^0_{5\mu}$ is not related to any measurable quantities, other than the moments $\Gamma_{1p(n)}$.

2.4.1 The Bjørken Sum Rule

The Bjørken sum rule [54] is the most fundamental test of QCD in polarized DIS. Derived long before the introduction of QCD from current algebra and $SU(2)$ isospin symmetry, it relates the moments Γ_{1p} and Γ_{1n} of the proton and the neutron given in Eq. (2.44) to the axial charge of the nucleon, Eq. (2.50),

$$\Gamma_{1p} - \Gamma_{1n} = \int_0^1 dx \left[g_{1p}(x, Q^2) - g_{1n}(x, Q^2) \right] = \frac{1}{6} \left| \frac{g_A}{g_V} \right| \Delta C_{NS}(Q^2), \qquad (2.52)$$

while the singlet and octet matrix elements a_0 and a_8 cancel in the difference. The analysis of all available data on g_{1p} and g_{1n} in next-to-leading order perturbative QCD [4] yielded a value of $\Gamma_{1p} - \Gamma_{1n} = 0.176 \pm 0.003(\text{stat}) \pm 0.007(\text{syst})$ at a scale $Q^2 = 5\,\text{GeV}^2$. This experimental result agrees within the uncertainties with the Bjørken sum rule prediction of 0.183 ± 0.002 at this scale.

2.4.2 The Ellis-Jaffe Sum Rule

While the Bjørken sum rule relates the difference of the proton and neutron polarized structure functions to the isotriplet matrix element a_3, a sum rule can be derived for the moments Γ_{1p} and Γ_{1n} individually, if the polarized densities of the strange quarks and the gluon are assumed to vanish, $\Delta s + \Delta \bar{s} \equiv \Delta g \equiv 0$. Under this assumption it follows that $a_0 = a_8$ and Eq. (2.44) reduces to the Ellis-Jaffe sum rule [55],

$$\Gamma_{1p(n)} = \frac{1}{12} \left(\pm a_3 + \frac{a_8}{3} \right) \Delta C_{NS}(Q^2) + \frac{a_8}{9} \Delta C_S(Q^2). \qquad (2.53)$$

In the same next-to-leading order analysis cited in the previous section, the moments of the proton and neutron spin structure functions are $\Gamma_{1p} = 0.118 \pm 0.004(\text{stat}) \pm 0.007(\text{syst})$ and $\Gamma_{1n} = -0.058 \pm 0.005(\text{stat}) \pm 0.008(\text{syst})$ at $Q^2 = 5\,\text{GeV}^2$. The Ellis-Jaffe predictions at this scale are $\Gamma_{1p} = 0.170 \pm 0.005$ and $\Gamma_{1n} = -0.014 \pm 0.005$. The violation of the Ellis-Jaffe sum rule is evidence that the polarized strange quark and anti-quark densities and the polarized gluon densities do not vanish or that the assumption of $SU(3)$ symmetry in the calculation of a_8 is not valid.

2.4.3 The Spin Carried by the Quarks

In the simple parton model of non-interacting quarks, the singlet and non-singlet proton matrix elements can be expressed in terms of the first moments $\Delta q \equiv \int_0^1 dx\, q(x, Q^2)$ of the polarized parton densities,

$$a_3 = \Delta q_3 \equiv \Delta u + \Delta \bar{u} - (\Delta d + \Delta \bar{d}), \tag{2.54}$$

$$a_8 = \Delta q_8 \equiv \Delta u + \Delta \bar{u} + \Delta d + \Delta \bar{d} - 2(\Delta s + \Delta \bar{s}), \tag{2.55}$$

$$a_0 = \Delta q_0 \equiv \Delta u + \Delta \bar{u} + \Delta d + \Delta \bar{d} + \Delta s + \Delta \bar{s}. \tag{2.56}$$

In this model, the singlet matrix element measures the contributions of the quark spins to the nucleon spin, $\Delta \Sigma = \Delta q_0$. A measurement of the moment of the structure function g_{1p} in combination with Eqs. (2.44), (2.50) and (2.51) can therefore be used to determine $\Delta \Sigma$. The first such measurement [2] gave a value compatible with zero, $\Delta \Sigma = 0.006 \pm 0.058(\text{stat}) \pm 0.117(\text{syst})$, leading to the "proton spin crisis" (see Ch. 1). Recent measurements in inclusive DIS constrain a_0 to the range $0.2 \le a_0 \le 0.3$ at scales $Q^2 < 10\,\text{GeV}^2$; *e.g.* the E155 collaboration measured a value of $a_0 = 0.23 \pm 0.04(\text{stat}) \pm 0.06(\text{syst})$ at $Q^2 = 5\,\text{GeV}^2$ (see Ref. [4] and references therein).

In the framework of QCD, the nucleon spin is composed of the fraction carried by the quark spins $\Delta \Sigma$, by the orbital angular momentum of the quarks L_q, by the gluon spins ΔG, and by the orbital angular momentum of the gluons L_G that also includes a term from the quark-gluon interactions [3, 56],

$$\frac{1}{2} = \frac{1}{2}\Delta\Sigma(\mu^2) + L_q(\mu^2) + \Delta G(\mu^2) + L_G(\mu^2). \tag{2.57}$$

The operators depend on the renormalization scale μ^2 which is also the scale at which the nucleon is probed, $\mu^2 = Q^2$.

Predictions of the spin carried by the quark spins have been made in a number of models. In the $SU(6) \supset SU(3)_{flavour} \otimes SU(2)_{spin}$ quark model [57], the nucleon wave-function is constructed

from the non-relativistic flavour and spin wave functions of the three constituent quarks. In this model, the nucleon spin is thus due to the spins of the constituent quarks only, $\Delta\Sigma = 1$, because binding forces and interactions are neglected.

In another simple approach, the spin content is predicted using the assumptions leading to the Ellis-Jaffe sum rule. In this case, the spin is related to the octet current matrix element measured in hyperon β-decay, $\Delta\Sigma = a_0 = a_8 = 0.585 \pm 0.025$ (see Eqs. (2.51) and (2.56)).

In bag models, the nucleon is composed of relativistic quarks that are confined by boundary conditions (the bag) [3]. In these models the quark spins carry about 65 % of the nucleon spin. The remaining spin is accounted for by the quark orbital angular momentum.

The chiral quark soliton model (χQSM) [58] is based on the chiral Lagrangian of massless quarks. The quarks acquire dynamic mass via spontaneous symmetry breaking of the chiral symmetry. Baryons are soliton solutions of the chiral Lagrangian in the limit of infinite quark colours (large N_c). Within the framework of this model the contribution of the quark spins was recently predicted to be $\Delta\Sigma = 0.56$ at a scale of $5\,\text{GeV}^2$, while the remaining nucleon spin is carried by orbital angular momentum [59].

In a QCD sum rule approach, that successfully predicts the fractions of the nucleon momentum carried by the quarks and gluons [60, 61], the spin carried by the gluons was calculated in Refs. [56, 62]. The total contribution carried by the spins of the gluons and the gluon orbital angular momentum is found to be $(\Delta G + L_G) \approx 0.35 \pm 0.13$ and thus $(1/2\,\Delta\Sigma + L_q) \approx 0.15 \pm 0.13$ or $\Delta\Sigma \lesssim 0.3 \pm 0.26$ at a scale of $1\,\text{GeV}^2$.

The various models therefore favour values around $\Delta\Sigma \approx 0.6$. Nevertheless, there exist predictions of smaller values that are consistent with measurements in inclusive deep-inelastic scattering. More precise measurements of the nucleon spin content are consequently essential to resolve the "proton spin crisis".

In inclusive measurements of $\Delta\Sigma$, an additional complication arises. The values of $\Delta\Sigma$ given above were obtained using the relation $\Delta\Sigma = a_0$. While this identification holds in the simple parton model, it is not valid in the QCD improved parton model. In QCD, the axial anomaly [45, 63] leads to a non-zero gluon polarization. As a consequence the singlet proton matrix element becomes in terms of $\Delta\Sigma$ and the spin carried by the gluons ΔG:

$$a_0 = \Delta\Sigma - n_f \frac{\alpha_s(Q^2)}{2\pi}\Delta G. \qquad (2.58)$$

The small values of a_0 can therefore be explained by a sizable gluon polarization. Yet, the value of

ΔG would have to be substantially larger than one, in order to explain the discrepancy between the inclusive measurements and a value of $\Delta\Sigma \approx 0.6$. Based on this value of $\Delta\Sigma$ and on the measured range of a_0 given above, the gluon polarization would be in the range $\Delta G \approx 2\ldots 3$.

The contribution of the quark spins to the nucleon spin is more directly accessed in semi-inclusive DIS, where the additional information on the hadronic final state allows to determine the polarized parton densities individually. This technique is introduced in the following section.

2.5 Semi-Inclusive Deep-Inelastic Scattering

As outlined in the previous section, a determination of the contribution of the quark spins to the nucleon spin from inclusive DIS data is only possible in combination with neutron and hyperon decay data. Polarized inclusive DIS data permit a determination of the sum of the polarized quark and anti-quark densities $\Delta q(x, Q^2) + \Delta\bar{q}(x, Q^2)$ only, because the virtual photon couples to the squared fractional charges of the quarks. The individual polarized quark densities are computed from inclusive data by imposing additional constraints. For example, in the standard scenario of the GRSV2000 parameterization [64], the sea is assumed $SU(3)$ flavour symmetric:

$$\Delta\bar{u}(x, Q^2) = \Delta u_{\text{sea}}(x, Q^2) = \Delta\bar{d}(x, Q^2) = \Delta d_{\text{sea}}(x, Q^2) = \Delta\bar{s}(x, Q^2) = \Delta s(x, Q^2). \quad (2.59)$$

Furthermore the Bjørken sum rule is assumed and the octet matrix element Δq_8 is assumed to agree with the value obtained from hyperon decays.

Another way to access $\Delta\Sigma$ and the polarized parton densities is semi-inclusive DIS, where as outlined in Sec. 2.2.1 and illustrated in Fig. 2.4, a final state hadron is detected in coincidence with the scattered lepton. In the parton model, the struck quark absorbs all of the energy of the virtual photon and is knocked out of the nucleon. Due to confinement the quark hadronizes into a colour-singlet state of hadrons, the current fragments. Analogously the target remnant containing the spectator quarks hadronizes into a second colour-singlet state, the target fragments. The hadronization process is also called fragmentation.

The semi-inclusive DIS cross section is modified with respect to the inclusive cross section to account for the production of the hadron. In leading order QCD, the structure functions g_1 and F_1

given in Eq. (2.39) are rewritten to include this modification,

$$F_1^h(x, Q^2, z) = \frac{1}{2} \sum_q e_q^2 \, q(x, Q^2) \, D_q^h(Q^2, z), \tag{2.60}$$

$$g_1^h(x, Q^2, z) = \frac{1}{2} \sum_q e_q^2 \, \Delta q(x, Q^2) \, D_q^h(Q^2, z). \tag{2.61}$$

Here the fragmentation functions $D_q^h(Q^2, z)$ describe the probability that a quark of flavour q will fragment (hadronize) into a hadron of type h that carries an energy fraction $z = E_h/\nu$ of the virtual photon energy. The structure functions given here rely on the assumption that the hard scattering off the quark and the fragmentation process factorize. In the case of the polarized structure function g_1^h, Eq. (2.61) holds under the additional assumption that the fragmentation process is independent of the relative helicities of the struck quark and the nucleon. This assumption is well-founded for the production of pseudo-scalar (spin-0) mesons, like pions and kaons, that dominate the fragmentation. Nevertheless the existence of a sizable contribution by spin-dependent fragmentation was recently suggested [65], but no evidence was found, as discussed in Sec. 7.7.2.

In order to determine the quark densities $\Delta q(x, Q^2)$ from semi-inclusive measurements (see Sec. 8.4), knowledge of the fragmentation functions is required. Since the fragmentation process inherently involves long-range interactions, it is not possible to calculate fragmentation functions perturbatively. For this work, the LUND string fragmentation model [66] implemented in the JETSET Monte Carlo generator [67] was used. The LUND string model describes the linear confinement of quarks at large distances. The gluon field between a quark/anti-quark pair is modeled as a flux-tube or simply a string between the two particles. The field energy density $\kappa \approx 1$ GeV/fm measured in hadron spectroscopy provides the scale for the linear potential $V(r) = \kappa r$ of the $q\bar{q}$-pair separated by a distance r. When the potential between the two quarks exceeds the invariant mass of a $q\bar{q}$-pair, the string breaks apart and forms another quark/anti-quark pair. A given quark/anti-quark pair is removed from this process and forms a colour singlet hadron when it is close to the corresponding mass shell. Baryons are produced in the so-called popcorn mechanism [68] in which for example an initial $q\bar{q}$-pair combines with two successively produced pairs to form a baryon and an anti-baryon.

The LUND string fragmentation model conserves all quantum numbers and is Lorentz invariant. The implementation in the JETSET program allows to tune a number of parameters, for example the width of the Gaussian distribution of the transverse momentum of the produced hadron and the suppression of strange quarks with respect to the up and down quarks. The fragmentation model

used for the analysis presented in this thesis that was tuned using hadron multiplicities measured at the HERMES experiment is documented in Ref. [69].

The determination of the polarized parton densities using semi-inclusive DIS trades the assumptions used in the analysis of inclusive DIS data for the modeling of the fragmentation process and the assumption of factorization. Subject to these assumptions semi-inclusive DIS provides a more direct method to access the individual polarized parton densities based on the measurement of spin-dependent asymmetries which are defined in the following section.

2.6 Asymmetries

From an experimental point of view it is advantageous to calculate asymmetries of cross sections instead of the cross sections directly, because an asymmetry measurement does not require to measure absolute cross sections and in addition instrumental effects and other systematic effects usually cancel in the asymmetry. To access the spin structure functions $g_1(x, Q^2)$ and $g_2(x, Q^2)$ the relevant asymmetries that are related to the cross section differences defined in Eqs. (2.23) and (2.24) are

$$A_{||}(x, Q^2) = \frac{\frac{d^2\sigma^{\rightleftarrows}}{dx\,dQ^2} - \frac{d^2\sigma^{\rightrightarrows}}{dx\,dQ^2}}{\frac{d^2\sigma^{\rightleftarrows}}{dx\,dQ^2} + \frac{d^2\sigma^{\rightrightarrows}}{dx\,dQ^2}}, \qquad A_\perp(x, Q^2) = \frac{\frac{d^2\sigma^{\rightarrow\Uparrow}}{dx\,dQ^2} - \frac{d^2\sigma^{\rightarrow\Downarrow}}{dx\,dQ^2}}{\frac{d^2\sigma^{\rightarrow\Uparrow}}{dx\,dQ^2} + \frac{d^2\sigma^{\rightarrow\Downarrow}}{dx\,dQ^2}}. \tag{2.62}$$

The asymmetries $A_{||}$ and $A_\perp$ measure the cross section difference with respect to the relative orientations of the lepton and the nucleon spin. However, the fundamental process in DIS is the interaction of the virtual photon with the target nucleon, as illustrated in Fig. 2.10 for the longitudinal case. The asymmetries of virtual photo-absorption on the nucleon are

$$A_1 = \frac{\sigma_{1/2} - \sigma_{3/2}}{\sigma_{1/2} + \sigma_{3/2}} = \frac{g_1 - \gamma^2 g_2}{F_1}, \qquad A_2 = \frac{2\,\sigma_{TL}}{\sigma_{1/2} + \sigma_{3/2}} = \frac{\gamma(g_1 + g_2)}{F_1}, \tag{2.63}$$

where the relations to the nucleon structure functions are also given and dependencies on x and Q^2 and the differentials $d^2/(dx\,dQ^2)$ are omitted. The cross sections $\sigma_{1/2}$ and $\sigma_{3/2}$ were already defined in Sec. 2.3. The cross section σ_{TL} measures the interference of longitudinal and transverse photo absorption amplitudes. These asymmetries are related to the experimentally accessible asymmetries $A_{||}$ and $A_\perp$ via [5]

$$A_{||} = D\,(A_1 + \eta A_2), \qquad A_\perp = D\,(-\frac{\eta}{\xi}A_1 + \xi A_2), \tag{2.64}$$

where $\gamma \equiv Q^2/\nu^2$, $\eta \equiv \epsilon\gamma y/[1 - (1 - y)\epsilon]$, and $\xi \equiv \sqrt{2\epsilon/(1 + \epsilon)}$ are kinematic factors. The depolarization factor $D \equiv D(x, Q^2)$ accounts for the depolarization of the virtual photon with respect to the polarization of the lepton,

$$D = \frac{1 - (1 - y)\epsilon}{1 + \epsilon R},$$ (2.65)

where $R = \sigma_L/\sigma_T$ and ϵ are defined in Eqs. (2.20) and (2.19), respectively. The virtual photon-nucleon asymmetry A_1 given in Eq. (2.63) can be written in terms of the lepton-nucleon asymmetry $A_{\parallel}$ only, if the structure function g_2 is assumed to be small:

$$A_1 = \frac{1}{(1 + \eta\gamma)D} A_{\parallel} - \frac{\eta\gamma(1 + \gamma^2)}{1 + \eta\gamma} \frac{g_2}{F_1} \stackrel{g_2 \approx 0}{=} \frac{1}{(1 + \eta\gamma)D} A_{\parallel}.$$ (2.66)

The small size of g_2 with respect to g_1 is evident from Fig. 2.8 and 2.9. The contribution of g_2 in Eq. (2.66) is further reduced by the small size of the kinematic factor $\eta\gamma$ which is $1.4 \cdot 10^{-3} < \eta\gamma < 0.6$ in the kinematic range covered by the HERMES data presented in this thesis. A measurement of the longitudinal asymmetry $A_{\parallel}$ therefore allows to measure the photon-nucleon asymmetry A_1.

In semi-inclusive DIS, the corresponding asymmetry A_1^h is analogously related to the structure functions g_1^h and F_1^h,

$$A_1^h(x, Q^2) \stackrel{g_2 \approx 0}{=} \frac{\int_{z_1}^{z_2} dz\, g_1^h(x, Q^2, z)}{\int_{z_1}^{z_2} dz\, F_1^h(x, Q^2, z)},$$ (2.67)

where the integration runs over the range in z that is used in the identification of hadrons that are part of the current fragments.

In leading order, the inclusive asymmetry A_1 and the semi-inclusive asymmetries A_1^h can be written in terms of the polarized and unpolarized parton number densities $(\Delta)q(x, Q^2)$ and the fragmentation functions $D_q^h(Q^2, z)$:

$$A_1(x, Q^2) = \frac{\sum_q e_q^2 \Delta q(x, Q^2)}{\sum_{q'} e_{q'}^2 q'(x, Q^2)},$$ (2.68)

$$A_1^h(x, Q^2) = \frac{\sum_q e_q^2 \Delta q(x, Q^2) \int_{z_1}^{z_2} dz\, D_q^h(Q^2, z)}{\sum_{q'} e_{q'}^2 q'(x, Q^2) \int_{z_1}^{z_2} dz\, D_{q'}^h(Q^2, z)}.$$ (2.69)

The extraction of the polarized parton densities from the measured inclusive and semi-inclusive asymmetries presented in Ch. 8 is based on these relations.

Chapter 3

The HERMES Experiment at HERA

The HERMES experiment (HERA measurement of spin) is carried out at the DESY (Deutsches Elektronen-Synchrotron) laboratory in Hamburg, Germany. The laboratory was founded in 1959 and the first synchrotron (DESY) was built from 1960 to 1964. Experiments using the positron-electron collider PETRA (built in 1976–1978) lead to the discovery of the gluon in 1979. The HERA (Hadron-Elektron-Ring-Anlage) positron-proton collider was completed in 1990. The two experiments H1 and ZEUS have been running since 1992. Both experiments analyze collisions of the proton and the positron beam to perform precision measurements of unpolarized nucleon structure. The fourth experiment, HERA-B, was in operation from 2000 until early 2003. It used the proton beam with a fixed target to investigate charmed and bottom meson production. The HERMES experiment commissioned in 1995 uses the positron beam with a fixed gaseous target that is internal to the positron ring. This chapter describes the components of the HERA accelerator relevant to the HERMES experiment, the HERMES target, and the HERMES spectrometer and data acquisition system. For more details on the DESY laboratory, the reader is referred to Ref. [70].

3.1 The Polarized Positron Beam of the HERA Storage Ring

The HERA facility is a high-energy particle accelerator with a circumference of 6.3 km. Two storage rings provide a proton beam with a momentum of 920 GeV and a positron beam with 27.6 GeV. The beams are brought into collision at two interaction points where the experiments ZEUS and H1 are located. A diagram is shown in Fig. 3.1.

32
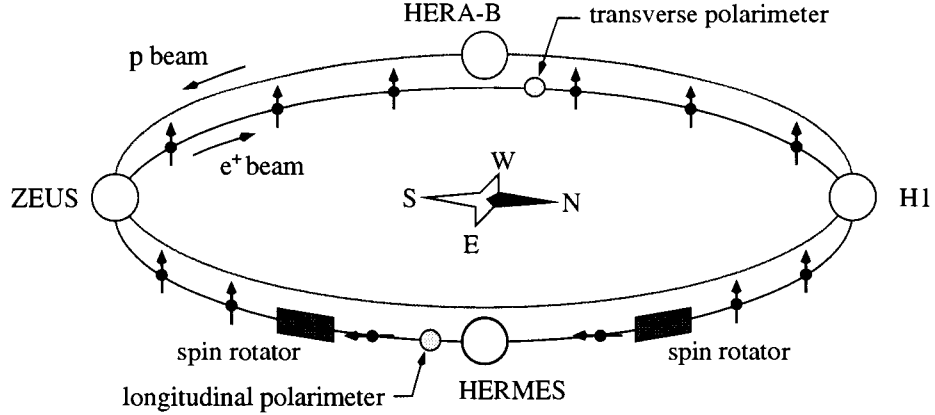
Figure 3.1: Schematic diagram of the HERA collider at DESY.

The positron beam[1] is arranged in bunches each being 27 ps long. The machine provides 220 positions for positron bunches in 96 ns intervals. A positron fill occupies 189 bunches that are arranged in three trains. The first and second trains are followed by seven vacant positions, leaving 17 empty positions after the last train. Every eleventh bunch is not brought into collision with the proton beam. These pilot bunches are used to monitor and tune the beam.

The positron beam is initially unpolarized. The positron spins align with the vertical magnetic field of the bending magnets in the curved sections of HERA. The transverse polarization of the beam given by

$$P_B = \frac{N_\downarrow - N_\uparrow}{N_\downarrow + N_\uparrow}, \tag{3.1}$$

where $N_{\uparrow(\downarrow)}$ is the number of positrons (anti-)aligned with the magnetic field, builds up by the Sokolov-Ternov (ST) mechanism [71]. This mechanism exploits a small asymmetry in the spin-flip probability during the emission of synchrotron radiation in the aligned and the anti-aligned spin-state with respect to the magnetic field. The anti-aligned state is populated on a time-scale that is large compared to other dynamical phenomena in storage rings, because only very few synchrotron radiation events cause a spin-flip. The polarization increases according to

$$P_B(t) = P_{\max}(1 - \exp(-t/\tau)), \tag{3.2}$$

where τ is the characteristic polarization time and $P_{\max}$ is the maximum achievable polarization. In a perfectly flat storage ring, in which the magnetic field is perpendicular to the positron orbit, the

---

[1] In 1998, electrons were used instead of positrons. The analysis reported in this thesis is not affected by this choice, except for the luminosity measurement that uses different physical processes (see Sec. 3.4).

maximum polarization is $P_{ST} = 8/(5\sqrt{3}) = 92.4\%$ [71]. In this case, the characteristic time τ_{ST} depends on the beam energy and the radius of curvature in the magnets only. In an ideal synchrotron of the size of the HERA positron ring, τ_{ST} is 36.5 min.

In practice, P_{max} is reduced by depolarizing effects, which are mainly caused by the stochastic motion of the positrons when synchrotron radiation is emitted. These oscillations about the ideal orbit give rise to non-vertical magnetic field components that decrease the maximum polarization. Additional depolarizing factors are magnet misalignments and Coulomb interactions during collision with the proton beam. The depolarizing effects may be combined in a time constant τ_{dep} that reduces the characteristic time τ and the maximum polarization P_{max} with respect to τ_{ST} and P_{ST},

$$P_{max} = P_{ST} \frac{\tau_{dep}}{\tau_{ST} + \tau_{dep}}, \qquad \tau = \tau_{ST} \frac{\tau_{dep}}{\tau_{ST} + \tau_{dep}}. \tag{3.3}$$

The maximum polarization routinely achieved at HERA is about 60% with characteristic times of 20 to 24 minutes.

The transverse polarization of the positrons is rotated into the longitudinal direction upstream of the HERMES experiment and it is rotated back downstream of the experiment. The spin rotation is accomplished by an arrangement of vertical and horizontal bends in the beam-line [72]. During data-taking periods the helicity of the longitudinally polarized beam was reversed every few months by re-arranging the spin rotators. A summary of the average beam polarizations and the charge of the beam during the five data-taking years analyzed is given in Tab. 3.1.

Table 3.1: Beam polarization and HERA lepton beam charge for each year of HERMES running. The numbers are weighted by the luminosity so that the value at the beginning of the fill dominates. Polarization values were larger at the end of the fill. The fractional uncertainties are used in the data analysis. They arise from the systematic uncertainties on the measurements by the two polarimeters weighted by the time periods each polarimeter was in use.

Year	Beam charge	Beam Polarization ($\langle P_B \rangle$)	Fractional Uncertainty ($\langle \sigma(P_B)/P_B \rangle$)
1996	e^+	52.8%	3.4%
1997	e^+	53.1%	3.4%
1998	e^-	52.1%	3.4%
1999	e^+	53.3%	1.8%
2000	e^+	53.3%	1.9%

3.2 Beam Polarimetry

Precise knowledge of the beam polarization is indispensable to compute the spin asymmetries discussed in Ch. 2, but also necessary to decrease the depolarizing effects by tuning the orbit of the positron beam. The polarization is measured in two locations as shown in Fig. 3.1.

3.2.1 The Transverse Polarimeter

The transverse polarimeter (TPOL) [73, 74] in the West straight section uses a spatial asymmetry in the polarized Compton scattering cross section to determine the beam polarization. A continuous laser of circularly polarized light is Compton back-scattered off positron bunches into a position sensitive calorimeter. The TPOL operates in single-photon mode, *i.e.* the intensity of the laser is chosen such that the probability to back-scatter more than one photon in a positron bunch is smaller than 1 %. In the calorimeter, the energy and position of each photon is measured as a function of the helicity of the light, which is flipped at a rate of 90 Hz. The observed spatial asymmetry under reversal of the laser helicity is proportional to the positron beam polarization. The systematic uncertainties on the polarization measurement with the TPOL arise mainly from the calibration using the rise-time curve and the maximal polarization. The fractional uncertainty due to this source is $(\sigma\,(P_B)\,/P_B)_{\text{rise}} = 3.3\,\%$ [75]. Additional uncertainties of 0.9 % arise from corrections to the raw polarization measurement. The total systematic uncertainty of 3.4 % is the quadratic sum of these sources. The first observation of transverse polarization at HERA in November 1991 was a prerequisite for the approval of the HERMES experiment.

3.2.2 The Longitudinal Polarimeter

The longitudinal polarimeter (LPOL) [76] located downstream of the HERMES experiment was commissioned in the Fall of 1996. It provides an independent measurement of the polarization in the longitudinally polarized section of the positron ring. The measurement employs an energy asymmetry in the Compton scattering cross section of circularly polarized laser light off the longitudinally polarized beam positrons. The observed asymmetry in the energy deposited in the LPOL calorimeter with respect to the helicity of the incident laser light is proportional to the longitudinal polarization of the positron beam. The laser is pulsed with close to 100 Hz and the helicity is reversed with every pulse. The high backgrounds of bremsstrahlung photons from the HERMES target and synchrotron radiation from the bending magnet upstream of the LPOL do not allow to

operate the LPOL in single-photon mode. Instead the LPOL is operated in multi-photon mode. In a laser pulse interaction with a positron bunch, the LPOL thus measures the total energy deposited in the calorimeter by many scattered Compton photons. This mode allows to measure the polarization of a single bunch with high statistical precision of an absolute 1 %. The polarization of each electron bunch is provided every minute as the time-average of the observed asymmetry. The overall beam polarization is the bunch current weighted average of the individual bunch polarizations. The LPOL provides an absolute measurement of the beam polarization that in contrast to the TPOL does not rely on rise-time curve calibrations. The fractional systematic uncertainty of 1.6 % is mainly due to the energy calibration of the LPOL calorimeter.

3.3 The HERMES Target

The HERMES experiment uses a fixed gaseous target that is internal to the positron beam pipe. Data were collected with targets of polarized helium-3 (1995), polarized atomic hydrogen (1996 and 1997), and polarized atomic deuterium (1998 through 2000). In addition, data were taken using unpolarized targets of H_2, D_2, N_2, Ne, and Kr. As opposed to the solid targets used in most competing experiments, that suffer from high dilutions and polarizations smaller than 50 %, a gas target is pure and high polarization can be achieved ($P_T > 80\%$). The polarization can be flipped in milliseconds, compared to hours in the case of a solid target.

3.3.1 The Storage Cell

A disadvantage of a gaseous target is its low areal density. In an atomic polarized jet, the density is typically smaller than 2×10^{11} atoms/cm^2, whereas densities up to 10^{25} atoms/cm^2 can be reached with a solid target. A storage cell [77] in the beam pipe confines the target atoms to a small volume and thus increases the gas density. Typical areal densities were more than two orders of magnitude greater than for a jet — 7.6×10^{13} atoms/cm^2 in the case of hydrogen and 2.1×10^{14} atoms/cm^2 in the case of deuterium.

The storage cell walls are made from 75 μm thick 95.5 % pure aluminum. The elliptical profile with principal axes 29.8 × 9.8 mm^2 (21.0 × 8.9 mm^2 in 2000) matches that of the positron beam pipe. The cell has a total length of 547 mm of which only the upstream 400 mm are used to hold the target gas due to the limited spectrometer acceptance. The final 147 mm warrants that all scattered
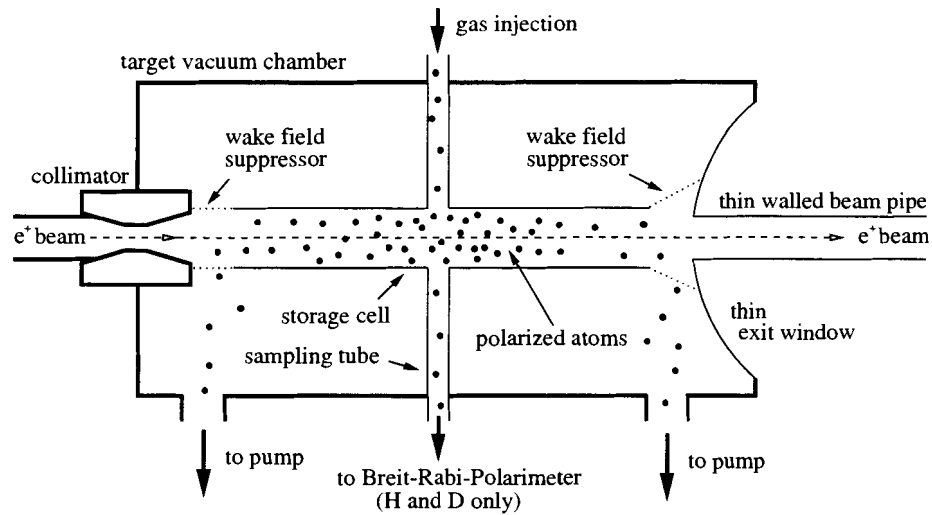
Figure 3.2: Diagram of the target chamber. The figure omits to show the asymmetric design of the target cell, see text for details. The diagram is not to scale.

particles pass through the same amount of material. The cell walls are coated with dri-film[2] to minimize recombination and inhibit the depolarization of atoms in the target gas. A layer of ice (H_2O, D_2O) forms in the first weeks of operation as the Dri-film is damaged. The ice layer was observed to improve the surface quality. The cell was cooled to 100 K in 1996 through 1999 and to 60 K in 2000 to reduce the gas flow and thus to increase the areal density and to decrease the number of wall collisions. A longitudinal magnetic holding field maintains the polarization of the target gas.

The target gas is injected in the middle of the cell. Atoms undergo several hundred collisions with the cell walls before they are removed by a turbo-molecular pump at the ends of the utilized cell volume. A diagram of the target chamber containing the storage cell is shown in Fig. 3.2. A collimator protects the storage cell from synchrotron radiation and the beam halo. Thin metal strips at the ends of the target cell provide electrical contact and a smooth transition between the beam pipe and the cell. These wake field suppressors reduce the electromagnetic fields (wake fields) that are induced in the target cell by the bunch structure of the positron beam. A thin-walled exit window at the downstream end of the target chamber is installed to minimize the interaction of the produced particles with the chamber.

---

[2]Dri-film, a hydrophobic silicon based polymer, was chosen for its radiation hardness [77].

3.3.2 The Polarized Target

The polarized hydrogen or deuterium gas injected into the target cell is prepared in an atomic beam source (ABS). A sample of the gas in the cell is analyzed in the target gas analyzer (TGA) and a Breit-Rabi-Polarimeter (BRP). The diagram in Fig. 3.3 illustrates the setup of the polarized target. The polarized helium-3 gas was prepared in an optically pumped target [78]. A description of this target is omitted, because the helium data were not used in the analysis reported in this thesis.
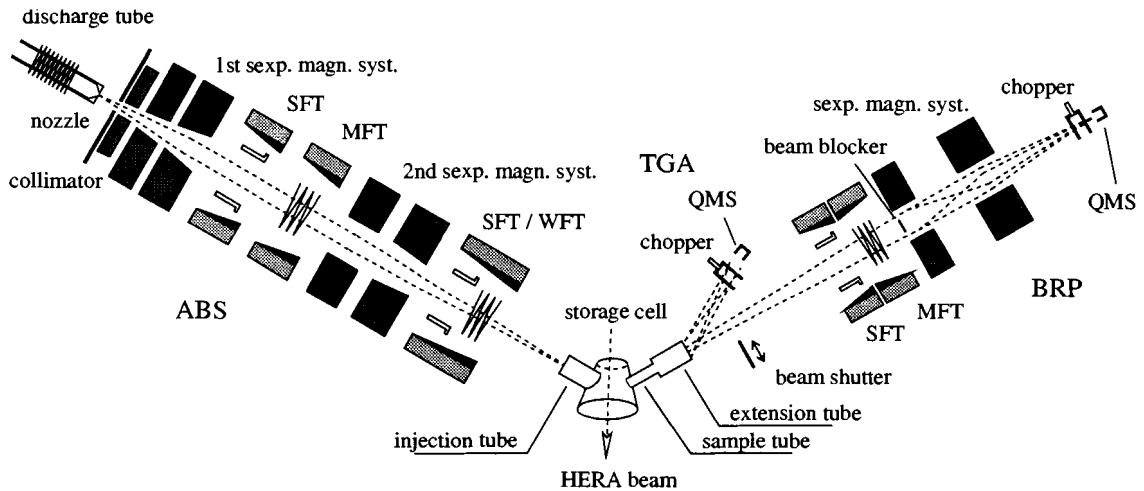
Figure 3.3: Diagram of the HERMES polarized target. Shown is the atomic beam source (ABS) that provides polarized hydrogen or deuterium, the target gas analyzer (TGA) and the Breit-Rabi-Polarimeter (BRP). SFT, MFT, and WFT label the strong, medium, and weak field transitions in the ABS and the BRP.

The Atomic Beam Source. The atomic beam source uses a radio frequency discharge to dissociate molecular hydrogen or deuterium. The atoms are then injected into a sextupole magnet system through a cooling nozzle and a differential pumping system. The sextupole system uses the Stern-Gerlach mechanism to select hyperfine states with electron spin projection $m_S = +1/2$ or $m_S = -1/2$. The population of the hyperfine states can be manipulated in a series of adiabatic high frequency transitions. A second sextupole is followed by another set of high frequency transitions. A complete description of state preparation is given in Ref. [79]. As an example the preparation of the P_z^+ state of atomic deuterium, i.e. $m_I = +1$, is described in the following. The deuterium

hyperfine states $|m_I, m_S\rangle$ of nuclear projection m_I for $m_S = +1/2$ are customarily labeled

$$|1\rangle = |1, \frac{1}{2}\rangle, \quad |2\rangle = |0, \frac{1}{2}\rangle, \quad \text{and} \quad |3\rangle = |-1, \frac{1}{2}\rangle,$$

and similarly for the states $|4\rangle$, $|5\rangle$, and $|6\rangle$ of electron spin projection $m_S = -1/2$ (see right hand panel in Fig. 3.4). The first sextupole is used to select the states $|1\rangle$, $|2\rangle$, and $|3\rangle$. A strong field
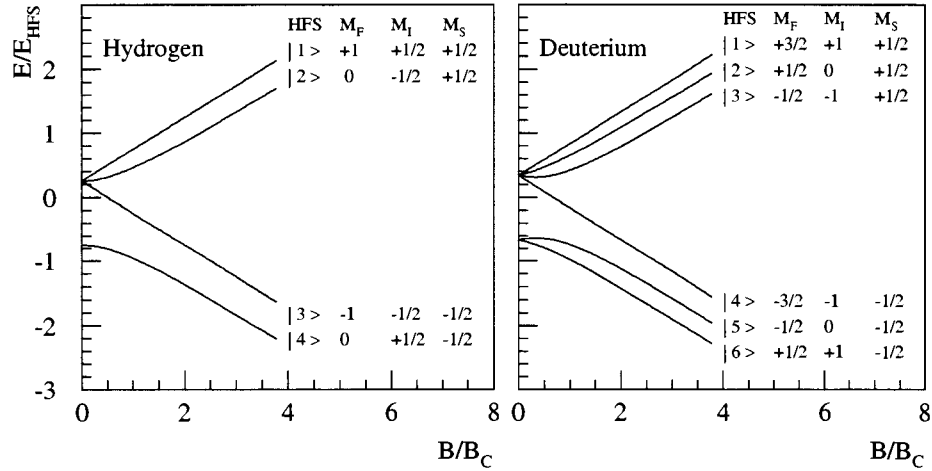
Figure 3.4: Hyperfine energy levels of hydrogen and deuterium as function of the magnetic holding field. The magnetic field is shown normalized to the critical field B_C and the energy is scaled with the hyperfine energy E_{HFS} [79].

transition induces the transition $|3\rangle \rightarrow |5\rangle$. In the following sextupole, the state $|5\rangle$ ($m_S = -1/2$) is eliminated. The final strong field transition, $|2\rangle \rightarrow |6\rangle$ leaves only the states $|1\rangle$ and $|6\rangle$ (both $m_I = +1$) in the gas that is injected into the storage cell. In practice, atomic polarizations of the injected gas were larger than 97 % in the case of hydrogen and above 91 % in the case of deuterium.

The Breit-Rabi-Polarimeter and the Target Gas Analyzer. The polarization of the gas inside the storage cell is sampled with a Breit-Rabi-Polarimeter (BRP) that is mounted off-axis to the ABS as shown in Fig. 3.3. A small sample of target gas enters the sampling tube and is subsequently analyzed by the BRP or the target gas analyzer (TGA). The BRP [80] essentially works in reverse to the ABS. High frequency transitions and a sextupole system are used to select a particular hyperfine state. The polarization is then deduced from the relative populations of the various states, which are measured in a quadrupole mass spectrometer (QMS).

The TGA [81, 82] is used to measure the amount of molecular and atomic gas in the target cell with another QMS. A chopper in front of the QMS allows to measure the count rate from background gases. Typical fractions of atomic hydrogen (deuterium) in the target cell are 95 % (93 %) [83].

The effective polarizations of the target gas that take into account the atomic fraction, and the atomic and molecular polarizations are summarized in Tab. 3.2 for the data-taking periods 1996 through 2000.

Table 3.2: Effective polarizations and systematic uncertainties of the target gas [84, 85].

Year	Target Gas	Target Polarization $(P_{z\pm})$	Fractional Uncertainty $(\langle\sigma(P_z)\rangle/\langle P_z\rangle)$
1996	H	$\pm 0.759 \pm 0.042$	5.5 %
1997	H	$\pm 0.850 \pm 0.032$	3.8 %
1998	D	$\pm 0.856 \pm 0.064$	7.5 %
1999	D	$\pm 0.832 \pm 0.058$	7.0 %
2000	D	$+0.851 \pm 0.031$ -0.840 ± 0.028	3.5 %

The Unpolarized Target. In addition to the polarized targets, unpolarized targets of H_2, D_2, ^3He, $^{14}N_2$, ^{20}Ne, and ^{84}Kr were used during the data-taking period 1995 through 2000. These gases were injected into the target cell with the Unpolarized Gas Feed System (UGFS). The density of the unpolarized gas was usually one to two orders of magnitude higher than the density of the polarized gas. In 2000, data were collected with even higher densities at the end of selected fills. The high statistics available made possible precise measurements of unpolarized processes, e.g. the flavour asymmetry in the light quark sea [86], pion multiplicities in deep-inelastic scattering [87], and the spin transfer in Λ_0-production [88]. In this thesis pion and kaon multiplicities extracted from unpolarized hydrogen data collected in 2000 were used to compute the nuclear mixing in the deuteron (see Sec. 8.2).

3.4 The Luminosity Monitor

The luminosity is determined by measuring well-known cross sections of scattering processes of the beam positrons/electrons with the atomic electrons in the target gas. Bhabha scattering ($e^+e^- \to e^+e^-$) and pair annihilation ($e^+e^- \to \gamma\gamma$) were measured when a positron beam was used (1996,

1997, 1999–2000) and Møller scattering ($e^- e^- \rightarrow e^- e^-$) was measured when HERA was run with electrons (1998). The cross sections of all three processes are known to high order in QED. The luminosity $\mathcal{L}$ follows from the measured rate of events normalized to the cross section integrated over the acceptance of the luminosity monitor and corrected for its efficiency.

The luminosity monitor [89] is located close to the beam pipe 7.2 m downstream of the target cell inside of the calorimeter as shown in Fig. 3.5. The monitor consists of two calorimeters on either side of the storage ring. Each calorimeter is made from a matrix of 3 × 4 radiation hard $\mathrm{NaBi(WO_4)_2}$ crystals with a total size of $66 \times 88 \times 200 \ \mathrm{mm}^3$. The crystals are read out by individual photomultiplier tubes. Subject to spatial requirements, the size and position of the calorimeters were optimized with respect to the 6.1 mrad opening angle in the laboratory system of the scattered $e^+ e^-$-pair for a 27.5 GeV beam.

The luminosity monitor measures the rate of coincident events with an energy deposition of at least 4.5 GeV in each calorimeter. This requirement reduces the rate of background events that typically deposit a high amount of energy in only one of the calorimeters. The measurement of the relative luminosity has an associated uncertainty of 0.9–1.5 % which is uncorrelated between measurements. The uncertainty on the integrated relative luminosity needed in the measurement of the asymmetries (see Ch. 6) is therefore negligble.

3.5 The HERMES Spectrometer

The HERMES spectrometer [90] was designed with an open forward geometry to measure DIS and SIDIS events. The spectrometer consists of two identical halves below and above the positron beam pipe (see Fig. 3.5). The coordinate system used is defined with the z-axis pointing in the direction of the beam pipe, the y-axis pointing upwards and the x-axis pointing inwards with respect to the ring. The proton beam passes through the spectrometer in between the halves parallel to the positron beam at a distance of 71 cm. Both beams are shielded from the field of the spectrometer magnet with a steel plate. The plate limits the acceptance to polar angles larger than $|\theta_y| > 40\,\mathrm{mrad}$ in the vertical direction. The upper limits are $|\theta_y| < 140\,\mathrm{mrad}$ in the vertical direction and $|\theta_x| < 180\,\mathrm{mrad}$ in the horizontal direction. Particle tracking is accomplished with a set of tracking chambers in front of and behind the spectrometer magnet. The deflection of the charged particles in the magnetic field of the magnet is used to determine the momentum of charged tracks. The particle identification detectors provide excellent electron/positron versus hadron identification. In addition, a threshold Čerenkov
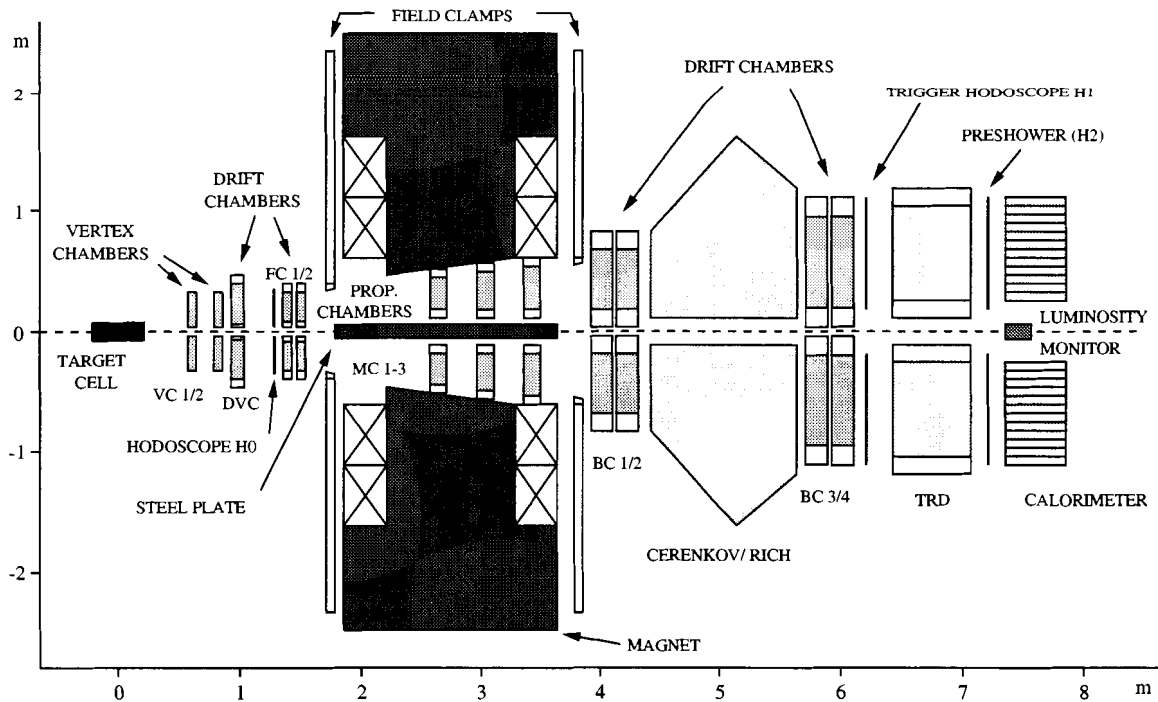
Figure 3.5: The HERMES spectrometer. The schematic shows the main detector components. Additional components not shown include the silicon detector, the wide angle muon hodoscopes, and the muon wall.

counter which was upgraded to a ring-imaging Čerenkov detector (RICH) in 1998 allows for the identification of pions (and kaons and protons in the case of the RICH) in the hadron sample. In the following, the components of the upper spectrometer are described. The bottom half is constructed in complete analogy. The description omits upgrades that were not relevant for this thesis, e.g. the silicon vertex detectors [91], the wide angle muon hodoscopes, and the muon wall.

3.5.1   The Particle Tracking System

The front-tracking system.   The front-tracking system is used to determine the event vertex (see below) and the angles of the emerging charged tracks with respect to the positron beam. Two silicon gas micro-strip detectors (VC 1/2) [92] and two drift chambers (FC 1/2) [93] were initially installed. The VC's were operational only in 1997, and they were uninstalled in 1999 because of technical difficulties. In the analysis for this thesis, the VC's were not used for tracking. An additional drift chamber, called the drift vertex chamber (DVC) was added in 1997 to provide redundancy in the

front-tracking system that solely relied on the FC's in 1996.

All tracking chambers in the spectrometer have planes with wires arranged in the vertical direction (X), and wire-planes tilted by $\pm 30°$ with respect to the vertical (U and V). Additionally planes offset by half a cell size (X', U', and V') are used to resolve left-right ambiguities.

The uniformity of this setup simplifies and accelerates the tracking algorithm described below. The drift vertex chamber, located at $z = 1.1$ m downstream of the target cell, is a conventional drift chamber with six planes ($XX'UU'VV'$). The drift cell size is 6 mm. The DVC achieves a spatial resolution of 220 μm in each plane. The FC's are mounted at about $z = 1.6$ m on the front face of the spectrometer magnet. With a drift cell size of 7 mm, they provide a resolution of 225 μm in each of the planes that are arranged in the same $XX'UU'VV'$ configuration as the DVC.

The magnet. The spectrometer magnet is used to determine the momentum of charged tracks. The tracks are bent horizontally in the vertical magnetic dipole field with an integrated field strength of $\int dlB = 1.3$ Tm.[3] The magnetic field is inhomogeneous in the entire volume because of the pole faces that diverge to match the vertical acceptance of the spectrometer. Field clamps shield the spectrometer from fringe fields in front of and behind the magnet. The beam pipes are shielded from the magnetic field with the steel plate mentioned above. The magnetic field map was determined with model calculations and measured with a 3D-Hall-probe. The calculations agree with the measurements within a few percent. The detailed field map was incorporated into the tracking algorithm.

Three multi-wire proportional chambers (MC 1–3) [94] are installed in the gap inside of the magnet. The chambers have a cell size of 2 mm. Each of the three chambers has three planes in the UXV configuration. The resolution of each plane is about 700 μm. The MC's are mostly used to determine the momentum of low energy particles that are deflected out of the acceptance of the back-tracking system by the magnetic field.

The back-tracking system. The back-tracking system is used to reconstruct the tracks of charged particles that pass through the magnet. The reconstructed back-tracks are matched with front-tracks to determine the particle momenta. In addition, the position information of the back chambers is used to associate signals in the particle identification detectors with particle tracks.

---

[3]The magnet is capable of providing a field strength of 1.5 Tm, but it is operated at 1.3 Tm to reduce power consumption.

Two pairs of drift chambers (BC 1/2 and BC 3/4) [95, 96] are installed in front of and behind the Čerenkov detector. Each of the chambers has six planes in the $UU'XX'VV'$ configuration. The drift cell size of 15 mm provides a resolution of 275 μm and 300 μm per plane for BC 1/2 and BC 3/4 respectively.

The track reconstruction algorithm. Particle tracks were reconstructed using the pattern of hits in the front and back-tracking systems [97]. In the first step of this procedure, the partial front and back-tracks, which are to a good approximation assumed to be straight lines, are reconstructed separately in each of the U, V, and X orientations. The algorithm is based on a fast tree search. For each orientation, the algorithm begins by considering the entire plane and successively doubles the resolution by discarding the halves without a hit. In each step, the combined patterns of all planes in a given orientation are compared to a database of physically possible tracks and only corresponding patterns are kept. After about 11 steps the search reaches a resolution that is sufficient for track finding. The projections in the three planes are then combined to form the partial tracks in the front and the back respectively.
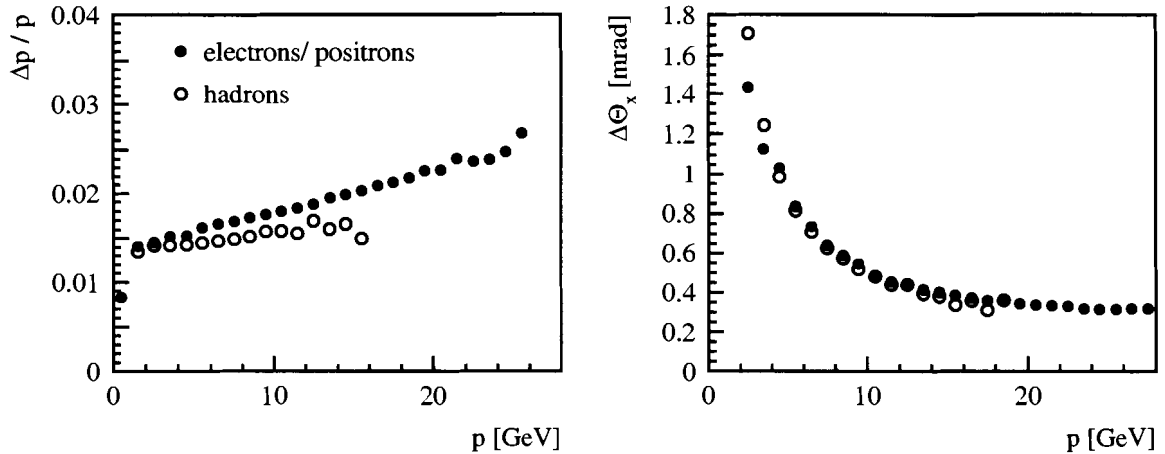
Figure 3.6: Resolution of the tracking system for electron/ positron tracks and hadron tracks. In the left hand panel, the relative momentum resolution is shown, the right hand panel shows the resolution in the horizontal scattering angle θ_x, both as a function of the track momentum p.

The front and back-tracks are associated by matching pairs that intersect in the center of the magnet within a given tolerance. For each associated pair, the front-track is forced to agree with the magnet mid-point of the back-track, and the front-track is recomputed accordingly. This procedure

improves the resolution of the front-tracking system, that relies on the DVC chambers and the FC chambers only (except for 1996 when the DVC's were not yet installed). The particle momentum is determined using another database of $520,000$ tracks which contains the momentum as a function of the front and back-track parameters. The intrinsic momentum resolution is improved to better than $\Delta p/p = 0.005$ by applying interpolation techniques. Multiple scattering in the spectrometer material leads to somewhat reduced resolutions for the reconstructed track momenta and scattering angles. Fig. 3.6 shows the resolutions for the deuterium data sample as obtained from a Monte Carlo simulation of the entire spectrometer [98]. The resolution for the hydrogen dataset is up to a factor of two better, because of the shorter radiation length of the threshold Čerenkov counter compared to the ring-imaging Čerenkov detector, see below.

3.5.2   The Particle Identification Detectors

The HERMES particle identification (PID) system consists of a calorimeter, two scintillator ho-doscopes (H0 and H1), a lead-scintillator hodoscope H2 (the preshower detector), a threshold Čer-enkov counter (a ring-imaging Čerenkov detector since 1998), and a transition radiation detector. Typical detector responses of the detectors used in offline PID are shown in Fig. 3.7. In the discussion of electron/positron discrimination from hadrons, electrons and positrons are referred to collectively as leptons. The algorithms used for PID are discussed in Ch. 5.

The calorimeter.   The electromagnetic calorimeter [99] allows for the identification of leptons by their large energy deposition. The measurement of photons from neutral particle decays permits the identification of π^0's and η's. In addition, the calorimeter response is used in the first-level trigger (*cf.* Sec. 3.6).

Each half of the calorimeter is constructed from 420 radiation hard F101 lead-glass blocks, arranged in 10 rows and 42 columns. Each block is coupled to a photomultiplier tube (PMT). A schematic drawing of the preshower detector (see below) and the calorimeter is shown in Fig. 3.8. A block has a cross-sectional area of $9 \times 9\,\mathrm{cm}^2$ and a length of $50\,\mathrm{cm}$ or 18 radiation lengths. About $90\,\%$ of the shower of a lepton axially incident in the z-direction is contained in a block.

Test beam measurements with a 3×3 array of blocks showed a linear energy response for electrons within $1\,\%$ in the range from 1 to $30\,\mathrm{GeV}$ and an energy resolution of $\sigma(E)/E = (5.1 \pm 1.1)/\sqrt{E[\mathrm{GeV}]} + (1.5 \pm 0.5)$ [100]. The resolution during operation in the spectrometer was found
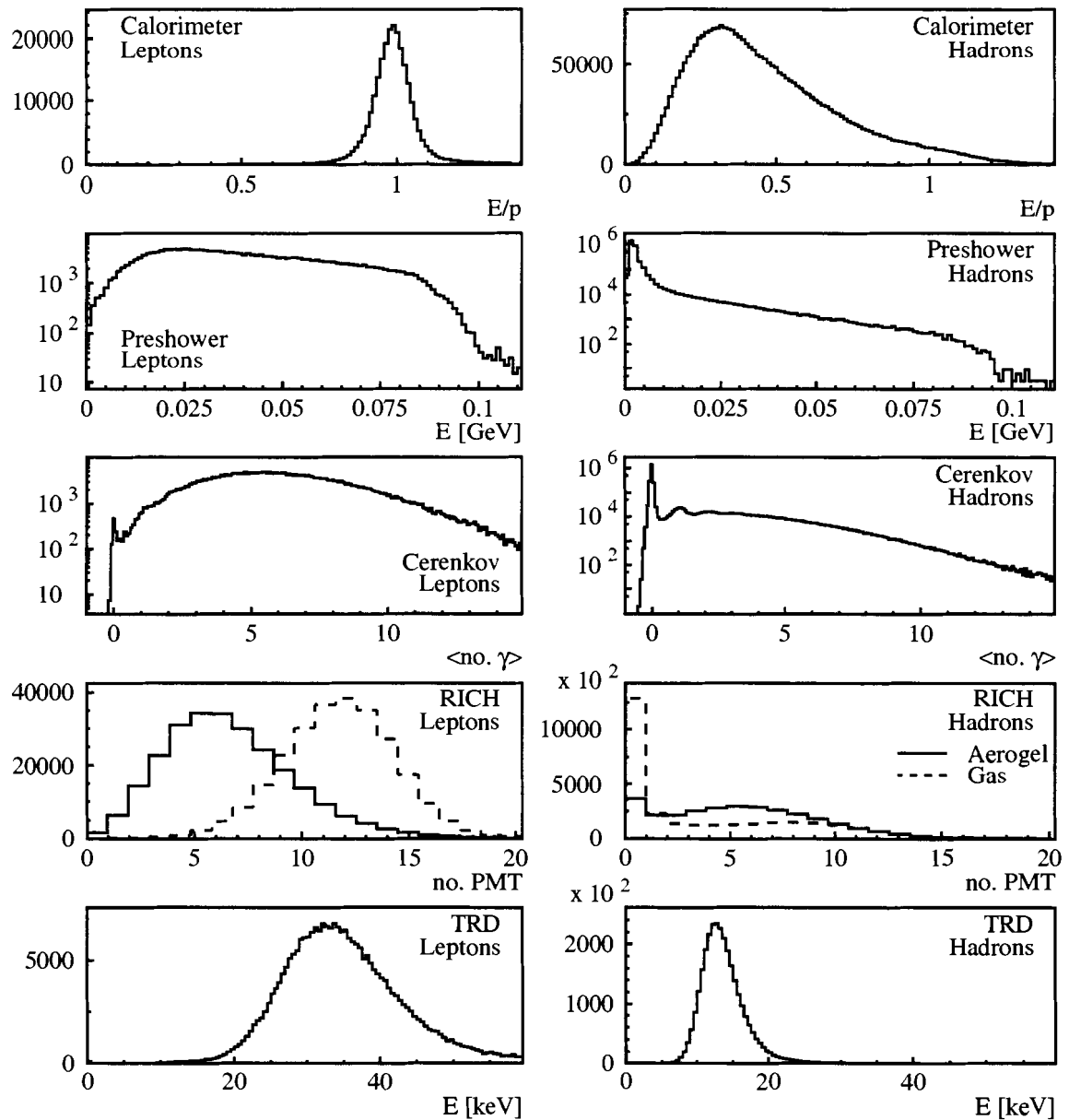
Figure 3.7: The PID detector responses for leptons and hadrons. For these plots, hadrons and leptons were identified with cuts on the responses of the other PID detectors, see Ch. 5. All histograms were computed from a dataset collected in 2000, except for the threshold Čerenkov histograms which were extracted from a 1997 dataset. The histograms are normalized and scaled to the 2000 and 1997 flux factors in order to eliminate bias due to different efficiencies of the hadron and lepton cuts.
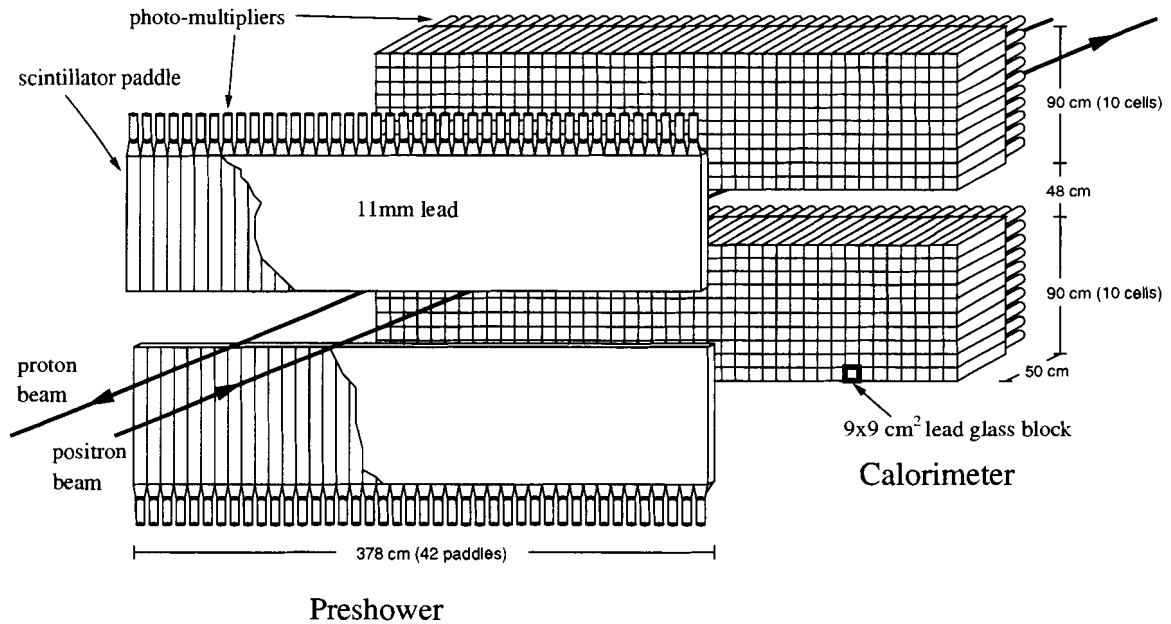
Figure 3.8: The upper half of the preshower detector and the calorimeter.

to be slightly worse because of the preshower detector and imperfections in the gain matching of the lead-glass block/PMT modules.

The calorimeter halves are moved away from the beam pipe during injection to prevent radiation damage. The effects of long-term radiation damage and the long term stability in general are monitored by comparing the momentum of leptons as measured by the tracking system and the energy deposited in the calorimeter. The ratio was found to be stable within 1 % during a one year period of operation. Additional monitor calorimeter modules mounted near the beam-pipe verified these results.

Typical lepton and hadron responses of the calorimeter are shown in Fig. 3.7. The respective panels show the ratio of deposited energy and momentum E/p. Leptons lose all of their energy in an electromagnetic shower that is completely contained in the calorimeter. Their distribution is thus peaked at $E/p = 1$. Hadrons deposit only a fraction of their kinetic energy through ionization energy loss. The observed depletion of low energy hadrons is due to the minimum ionization energy of 0.8 GeV and a trigger threshold effect that suppresses hadrons with low energy deposition in the calorimeter (see Sec. 3.6).

The hodoscopes. Three hodoscopes [90] are installed in the HERMES spectrometer. The scintillator hodoscope H1 and the lead-scintillator H2 (the preshower detector) are constructed from 42 vertical panels of scintillator. Each panel is 1 cm thick and has an area of $9.3 \times 91 \text{cm}^2$. The modules overlap by 2–3 mm to avoid any holes in the acceptance. Both hodoscopes are used to provide fast signals for the first-level trigger. The preshower detector is additionally used for particle identification. For this purpose, an 11 mm (2 radiation length) sheet of lead sandwiched between two 1.3 mm steel sheets is installed in front of the scintillator (see Fig. 3.8).

The front hodoscope, H0, located directly in front of the drift chamber FC1 is constructed from a single sheet of 3.2 mm thick plastic scintillator corresponding to 0.7 % radiation length. The sole use of H0 is backward particle discrimination in the trigger. The low rate of about 1 MHz does not require segmentation.

The hadron and lepton responses of the preshower detector are shown in Fig. 3.7. The larger energy deposited by leptons in an electromagnetic shower makes possible the discrimination from hadrons that only interact by nuclear ionization. Due to the short radiation length leptons are not absorbed in the preshower and the initiated electromagnetic shower often carries through into the calorimeter.

The transition radiation detector. The transition radiation detector (TRD) [90] plays a vital role in the particle identification system. Transition radiation is emitted when a relativistic charged particle traverses two media with different dielectric constants. In each medium, the particle induces a different Coulomb field. These fields do not match at the boundary. The required continuity at the boundary gives rise to an additional field — the transition radiation [101, 102]. The total energy emitted as transition radiation is given by

$$E = \frac{2}{3} \alpha \, \omega_p \, \gamma, \tag{3.4}$$

where α is the fine structure constant, ω_p the plasma frequency of the medium, and γ the usual Lorentz factor. Transition radiation is emitted in a cone about the particle track with an opening angle $\theta \simeq 1/\gamma$. At high energies the radiation, mainly consisting of X-rays, is therefore emitted almost collinear to the particle trajectory. Many material interfaces are needed for a practical detector, because the emission of transition radiation has a small probability.

The HERMES transition radiation detector (*cf.* Fig. 3.9) is built from six consecutive modules. Each module with an active area of $72.4 \times 325 \text{cm}^2$ is essentially an independent detector. The
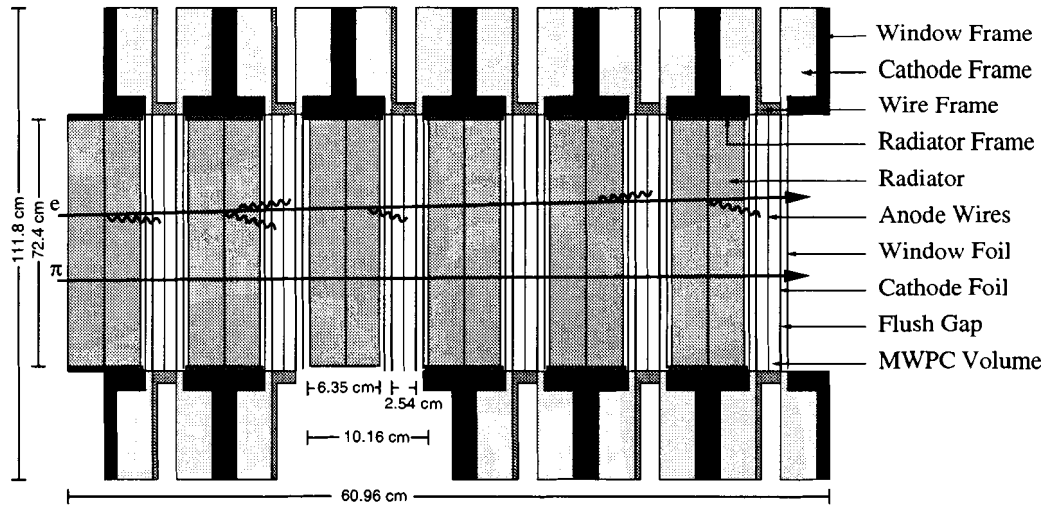
Figure 3.9: The upper half of the transition radiation detector. The opening angles of the transition radiation photons are exaggerated.

modules consist of a radiator that initiates the transition radiation and a multi-wire proportional chamber (MWPC) to measure the TR photons and to provide a coarse position measurement. The radiator material is a predominantly two-dimensional matrix of fibers with 17–20 μm diameter. Each radiator is 6.35 cm thick and thus has approximately 267 dielectric layers.

Each MWPC is 2.54 cm thick and has 256 vertical wires with a separation of 1.27 cm. The chamber gas is a mix of 90 % Xe and 10 % CH_4 which was chosen because it efficiently absorbs X-rays.

At HERMES energies only leptons emit a significant amount of transition radiation, because of the linear energy dependence of the total energy emitted on the Lorentz factor.[4] In addition, every charged particle deposits ionization energy in the chamber gas. At high energies, it is impossible to distinguish transition radiation from the ionization energy because of the small opening angle of the former. Leptons are thus simply distinguished from hadrons by their larger average energy deposition in the MWPC's.

Typical TRD responses to hadrons and leptons are shown in two panels in Fig. 3.7. The panels show the truncated mean of the six modules instead of the response of a single module. The truncated mean is the average of the five smallest signals. In this average, the high-energy tail of the hadronic response that is generated by the rare production of knock-on electrons is significantly reduced,

---

[4]The Lorentz factor of a 10 GeV lepton is about 20, 000 and that of a 10 GeV pion about 70.

but the mean of the lepton signals remains virtually unchanged. The lepton distribution is broad and located at higher values than the hadron peak centered near the minimum ionization energy of 11 keV (5 GeV pion).

The threshold Čerenkov counter. The threshold Čerenkov counter [90] is used to identify pions in the hadron sample. In addition, it aids in the separation of leptons and hadrons. For pion identification, the counter makes use of the Čerenkov effect. Particles with velocities larger than the phase velocity of light in the material the particles pass through (the radiator) emit Čerenkov radiation at a characteristic angle θ_c given by [101]

$$\cos \theta_c = \frac{1}{\beta n},\qquad (3.5)$$

where βc_0 is the velocity of the particle, c_0 the speed of light in vacuum, and n the refractive index of the material. No light is emitted, if

$$\beta < \beta_{\text{thresh}} = 1/n \qquad \text{or} \qquad p < p_{\text{thresh}} = \frac{m\,c_0}{\sqrt{n^2 - 1}},\qquad (3.6)$$

where p is the momentum of the particle, and m its mass.

The counter shown in Fig. 3.10 was located between BC 1/2 and BC 3/4. The support structure was constructed from aluminum with entrance and exit windows made out of double walled thin foils. Nitrogen flowed in between the foils to reduce diffusion of atmospheric gases into the active volume. A set of 20 spherical mirrors and corresponding photo-multipliers were used to collect and measure the emitted Čerenkov photons. The radiator gas and the detector structure constituted only 0.35 % of a radiation length. Particle tracking with BC 3/4 was thus virtually un-affected by multiple scattering in the Čerenkov counter.

In 1996 and 1997, the radiator gas was 70 % vol. N_2 and 30 % vol. C_4F_{10} with refractive index $n = 1.000629$. The threshold momenta for pions, kaons, and protons follow from Eq. (3.6) to be 3.8, 13.9, and 25.8 GeV. Thus only pions emit Čerenkov radiation for particle momenta between 3.8 and 13.9 GeV.

The mean number of photons measured in the Čerenkov counter is shown for leptons and hadrons in Fig. 3.7. All leptons observed in the Čerenkov detector are above threshold and thus radiate. The small peak at zero is due to detector inefficiencies. Hadrons with momenta below the respective thresholds do not emit Čerenkov radiation giving rise to the large peak at zero. This is followed by the one-photon peak at one and a broad distribution at higher values.
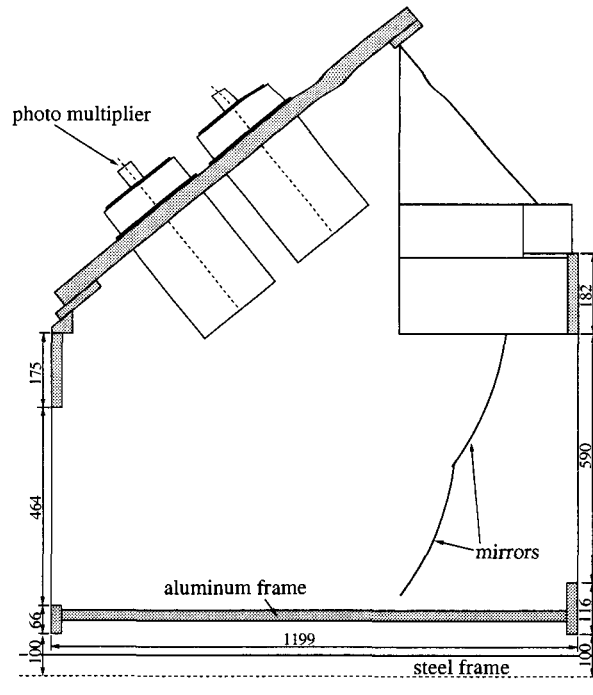
Figure 3.10: The upper half of the threshold Čerenkov counter.

The ring-imaging Čerenkov detector. During the shutdown in the Spring of 1998, the threshold Čerenkov counter was replaced by a ring-imaging Čerenkov detector (RICH) [103]. The detector measures the pattern of Čerenkov photons, that are emitted in a cone around the particle trajectory with characteristic angle θ_c as outlined in the previous section. Measurement of the opening angle permits the identification of pions, kaons, and protons in the hadron sample. Similar to the threshold Čerenkov counter the RICH responses also provide information for the separation of hadrons and leptons.

The RICH detector was built using the support structure of the Čerenkov counter. A schematic cut-away view of the upper half of the RICH detector is shown in Fig. 3.11. The RICH detector uses two radiator materials. A 5.5 cm thick wall of five rows of aerogel tiles is installed directly behind the entrance window. Aerogel is a type of foam consisting of colloidal silica particles. The second radiator is a heavy gas, C_4F_{10}, that fills the void in the detector. The refractive indices and the corresponding momentum thresholds are listed in Tab. 3.3. In the relevant momentum range of 2 to 15 GeV, the Čerenkov radiation emitted in the aerogel complements that emitted in the gas radiator for the identification of hadron types.
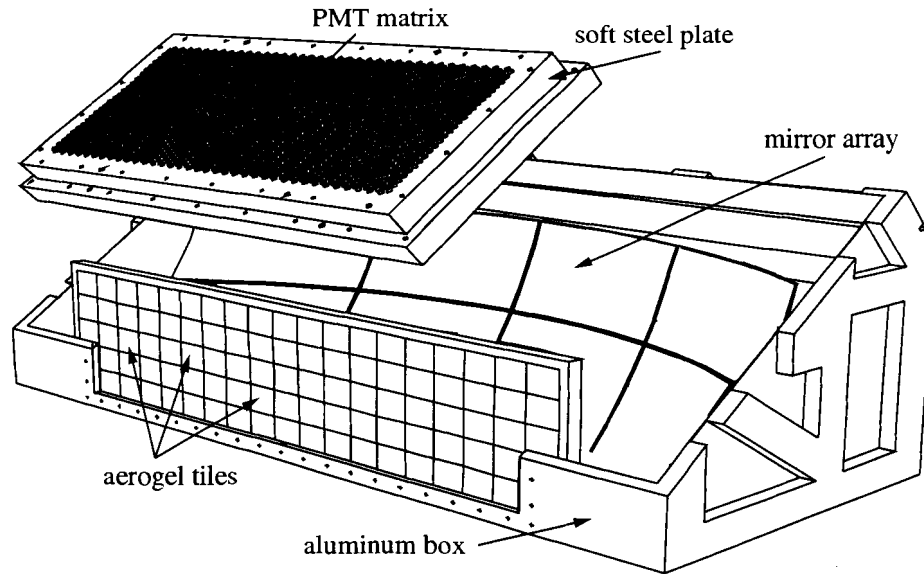
Figure 3.11: Schematic of the upper half of the RICH detector.

Table 3.3: Refractive indices and Čerenkov light thresholds of the ring-imaging Čerenkov detector.

	n	p^{π}_{thresh}	p^{K}_{thresh}	p^{p}_{thresh}
Aerogel	1.0304	0.6 GeV	2.0 GeV	3.8 GeV
C_4F_{10}	1.00137	2.7 GeV	9.4 GeV	17.9 GeV

The Čerenkov radiation emitted in the two radiator materials is imaged by a spherical mirror array onto a focal plane above the gas radiator. In the focal plane, an array of 1934 photo-multiplier tubes measures the projections of the Čerenkov cones. The photo-multipliers are arranged in a hexagonal closed packed matrix and each photo-multiplier is surrounded by an aluminized plastic foil funnel to maximize the light collection. A typical event is shown in Fig. 3.12.

The increased total radiation length with respect to the threshold Čerenkov detector of more than a factor of 20 led to a decreased momentum resolution of the particle tracking algorithm.

For the identification of hadrons and leptons, the RICH is used in the same way as the threshold Čerenkov. The distributions shown in Fig. 3.7 are explained analogously. In the case of the gas, more PMT signals are observed on average, because more photons are emitted in the greater radiation length of the gas and the higher density of photons in the (smaller) gas-rings causes a PMT to fire with higher probability [104].
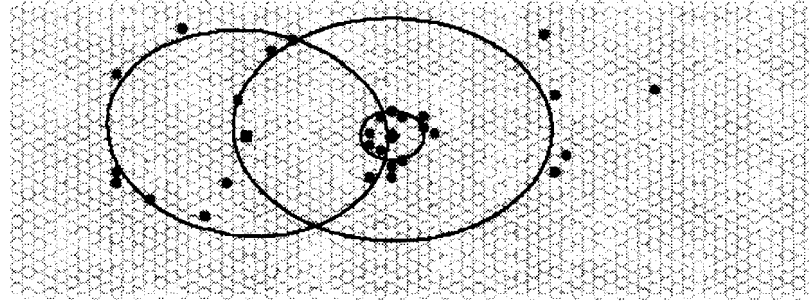
Figure 3.12: A 1.5 GeV π^- (left) and a 14.6 GeV electron (right) observed on the photo-multiplier matrix of the bottom RICH detector [103]. The pion only radiates in the aerogel, whereas the electron radiates in both materials and thus generates two Čerenkov cones, the smaller ring being the gas ring. The solid rings were reconstructed with the inverse ray tracing algorithm described in Sec. 5.2.2.

3.6 The Trigger

The trigger selects interesting events and suppresses background events [90]. For the former type of events, the trigger initiates the digitization and the readout of the detector signals. Events with signatures of DIS events or photo-production processes (with no electron in the acceptance) are recorded. Additional triggers are used for detector calibrations and monitoring. Several trigger levels up to time scales $\lesssim 1$ ms are possible. However, the HERMES experiment only uses a first-level trigger decision which is made within about 400 ns. The following explanation focuses on the DIS trigger (trigger 21).

Positron events are selected by requiring hits in the three hodoscopes and an energy deposition in two adjacent columns in the calorimeter. The signals are required to be in coincidence with the HERA accelerator bunch signal. The hodoscope signals suppress neutral particle background. The front hodoscope H0 eliminates events due to showers generated by the proton beam by distinguishing backward and forward going particles. DIS events are discriminated from charged background events by requiring a signal larger than the minimum ionizing energy of 0.8 GeV in the sum of two adjacent columns in the calorimeter. A threshold of 3.5 GeV used for unpolarized data-taking suppresses the hadron background rate by more than a factor of 10. The threshold corresponds to a range in y of $y \leq 0.85$. In the case of polarized running the calorimeter threshold is set to 1.4 GeV

which increases the accessible range in y to $y \leq 0.95^5$. The average rate of the DIS trigger was about 58 Hz in the 2000 data-taking period. Approximately 4–6 % of these events are identified as DIS events in offline analysis.

3.7 Data Acquisition and Data Storage

An event is recorded, when a trigger signal is generated. The digitization electronics are located in the HERMES electronics trailer close to the experiment. The drift chamber signals are read out by LeCroy 1877 Multihit FastBus TDC's (Time to Digital Converters). The magnet chambers and the RICH use the LeCroy PCOS4 readout system. The photomultiplier tubes and the TRD channels are digitized with LeCroy 1881M FastBus ADC's (Analog to Digital Converters).

Additional information from for example the luminosity monitor, the polarimeters, and information on detector supply voltages, temperatures, gas pressures etc. is read out independent of the triggered events. These so-called slow control data are typically read on a time scale of 10 seconds.

The collected information is processed by an event builder module and send to a DEC Alpha Cluster (a Linux cluster since 2002) over a fast optical link. Here the raw data are buffered on hard disks in EPIO (Experimental Physics Input Output Package [105]) format. At the end of each fill the data are transferred to a taping robot at the DESY main site via an FDDI (Fiber Distributed Data Interface) link. In addition, the data are backed up locally on data tapes.

The raw detector hit and timing information is processed in several steps before it is ready for physics analysis. In the first step, the raw data are decoded by HDC (the HERMES decoder). The decoder uses mapping, geometry and calibration from separate databases to associate the recorded TDC, ADC etc. signals with the detector components. The HERMES reconstruction code (HRC) then finds tracks in the spectrometer (see Sec. 3.5.1). These event data are stored in so-called HRC files. The event data are synchronized with the slow control data using a timing signal that is written to both data streams during data-taking. The synchronized data are stored in μDST files, which contain data that are useful for physics analysis, but exclude information that is only needed for expert studies of the experimental components. In the HDC, HRC, slow control, and μDST files the data are arranged in entity-relationship databases [106].

Time intervals labeled fill, run, burst, and event are defined in the HERMES data. A *fill* is the longest interval. It comprises all data collected during a HERA positron fill. A typical fill is 8

---

[5]In 1996, polarized data were initially collected with the 3.5 GeV threshold.

hours long. A *run* is defined by its size of about 450 MB of raw EPIO data. At high intensities, a run can be as short as 10 minutes. Runs are frequently terminated manually, when the experimental conditions are changed, for example when switching from polarized to unpolarized running. A *burst* is defined by the time scale at which slow control data are read out. A burst is approximately 10 s long. An *event* is the shortest interval. It contains all reconstructed tracks in the spectrometer that are observed when a trigger is generated.

Chapter 4

Data Selection

The analysis presented in this thesis is based on data collected with polarized hydrogen and deuterium targets in the years 1996 through 2000. This chapter discusses the selection of the high quality data that were used for physics analysis with emphasis on the polarized data. In the first part, the data production scheme is reviewed with regard to data quality. Then the tools used to monitor, document, and check the integrity of the μDST data (see Sec. 3.7) are introduced. This is followed by a discussion of the general running conditions during the various periods of polarized data-taking.

4.1 Data Collection and Processing

During data collection the status of the spectrometer, the polarimeters, and the target is continuously monitored by the shift crew. In addition to the usual checks of supply voltages, temperatures, leakage currents, wire voltages *etc.*, crude physics analyses, for example a determination of the rate of DIS events, are performed online using a fraction of the data. The shift crew records information on the overall conditions and the running mode (*e.g.* polarized running or beam polarimeter calibrations) in an electronic and in a paper logbook.

In offline analysis, the data are initially available in two data streams, the event data and the slow control data (see Sec. 3.7). The data are initially stored in the "*A*"-productions of each running period. In this production, the detector signals are calibrated based on the calibrations of the previous data-taking period. Detailed detector calibrations are subsequently carried out and the resulting data are stored in the "*B*"-productions. Additional corrections to the detector responses that rely on proper

calibrations, *e.g.* the TRD x and y correction [107], are applied in the "*C*"-productions. For each experimental component, information on its status is included, usually in the form of a bit-pattern. This information is available for each burst, although the components are generally monitored on longer time scales. The data of these main productions are analyzed with the same physics analysis package that is used for the online physics monitoring. The results archived on a web page [108] are used to verify the data integrity. The data quality applied to the final μDST data which contain the synchronized event and slow data, is discussed in the next section.

4.2 μDST Data Quality

All μDST productions are thoroughly checked for inconsistencies with a web-based analysis package. The software analyzes a given μDST production and provides a set of web pages that displays graphs of relevant quantities for each experimental component. These data quality plots are archived in the μDST section on the data quality web pages [108]. The plots are arranged in groups that cover the target, the beam polarization, current and luminosity, the tracking detectors, the PID detectors, high voltage trips, the trigger system and the data acquisition. The data are displayed in one and two-dimensional histograms for sets for 500 runs, the latter as a function of the run-number. As an example the beam polarization measured by the TPOL, the LPOL, and the best value chosen for analysis are shown in Fig. 4.1. The figure shows plots of the three quantities for a fraction of the runs as they are shown on the web pages. Periods during which the TPOL or the LPOL was selected to provide the best measurement are easily identified. Moreover periods where the wrong choice was made can be found based on these graphs. Similarly plots of the other relevant quantities for the components listed above are included on the web page. The HRC, slow or μDST data are redone for any periods where problems are found and a reanalysis of the data is possible and reasonable. The data are marked as not analyzable if the problems are severe or a reanalysis is not done.

The data quality information collected during these checks and the quality information provided for the various experimental components in the slow control and HRC data are summarized in a bit-pattern for each burst. In this pattern, a given bit identifies whether the condition of a particular part of the experiment was satisfactory for physics analysis. Generally bursts were discarded from the analysis, if
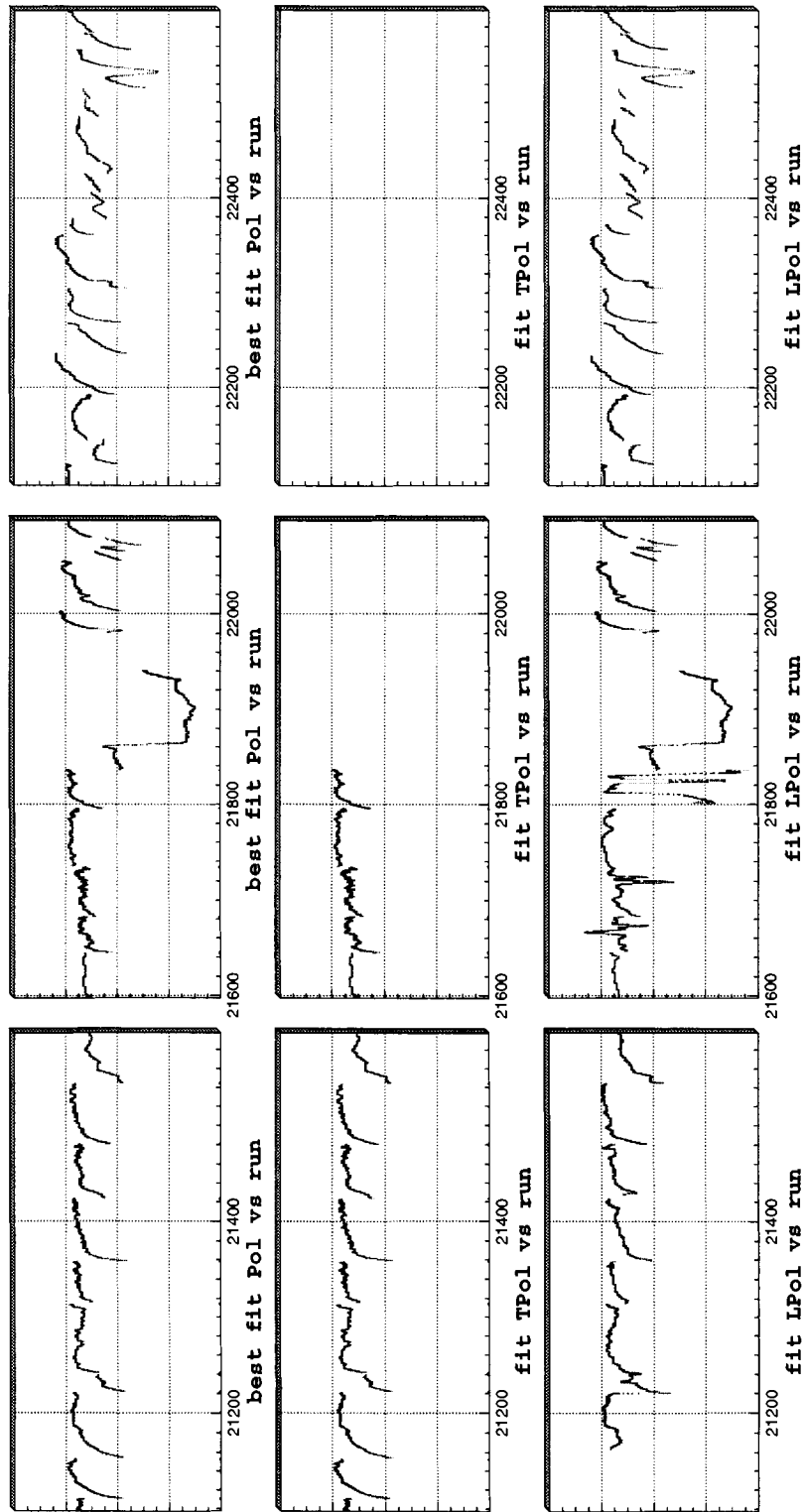
Figure 4.1: Example of the data quality plots. The fitted beam polarization for 1500 runs in the 1997 data versus the run-number. See text for details. The shown data were collected in a time period of about a month.

[Beam polarization] the beam polarization was low ($< 30\%$), or the measurement was unreliable;

[Luminosity] the luminosity was low ($< 5\,\mathrm{Hz}$), or the measurement was unreliable;

[Target] the target was not in polarized running mode, the target was not in a definitive polarization state, or the target was otherwise malfunctioning;

[DAQ] the DAQ was not working properly or the data processing failed;

[Logbook] problems were reported in the electronic or in the paper logbook by the shift crew;

[PID] the PID detectors were malfunctioning;

[HV trips] there were high voltage trips in the wire chambers.

Details of the bit-pattern of 32 bits are given in the appendix in Tab. A.1 for the 2000 data production as an example. The bit-patterns for the other data productions are defined similarly [108]. The patterns for all bursts in a data production are provided in a burst list that is available on the data quality web page.

The data quality scheme outlined here expands on previously used methods. Data quality and detailed documentation is provided consistently for all μDST productions in the new section of the data quality web pages.

Table 4.1: The bursts and fractional luminosities collected in each experimental running mode for data collected from 1996 through 2000. The 97c1 production does not contain polarized data.

	Total	Polarized		Unpolarized		Studies	
Prod.	Bursts	Bursts	Fract. lumi	Bursts	Fract. lumi	Bursts	Fract. lumi
96c2	478 837	301 772	20.8 %	85 828	59.8 %	99 237	19.4 %
97b4	811 232	639 776	33.6 %	123 226	64.3 %	48 230	2.1 %
97c1	623 948	578 727	93.8 %	n/a	n/a	45 221	6.2 %
98c1	559 081	326 047	28.9 %	77 941	62.2 %	155 093	8.9 %
99b2	535 731	437 254	42.3 %	24 853	47.8 %	73 624	9.9 %
00c1	968 627	783 881	24.1 %	87 143	72.4 %	97 603	3.5 %

4.3 Data Productions

The polarized and unpolarized data collected from 1996 through 2000 are made available in the μDST productions 96c2, 97c1, 98c1, 99b2, and 00c1 respectively. In this coding, the first two digits identify the data-taking year, the letter labels the production. The final digit is the version of the μDST production, where the version 1 is usually suitable for physics analysis, but re-productions are sometimes necessary. The 97c1 production includes only the polarized data, contrary to the other productions. Thus the 97b4 production that comprises all data recorded in 1997 is included in the discussion for completeness.

The data are generally collected in three distinct running modes. The target is run with polarized or unpolarized gas and data are recorded for calibrations and detector studies. The total number of bursts of each production and the number of bursts in the respective running modes are tabulated in Tab. 4.1. For each running mode, the fractional luminosity is also listed. The fractions of the running modes vary only little over the five years. The largest amount of time ($\sim$ bursts) was dedicated to polarized running. In 1996 and 1997, the polarized data were collected with a hydrogen target, while in 1998, 1999, and 2000 a deuterium target was used (see Sec. 3.3). A significant amount of data was collected with unpolarized targets in short time periods in all years. In this case, more fractional luminosity was recorded for the same number of bursts, because of the larger target density. Finally in each year, time was devoted to experimental studies and detector calibrations.

As mentioned above the quality of the data is determined with the aid of a bit-pattern that defines the quality criteria for each production. In the case of polarized running, all criteria are required, whereas for unpolarized running, bits regarding polarization are dropped. The fractions of good polarized and good unpolarized data with respect to all collected polarized and unpolarized data respectively are summarized in Tab. 4.2. In the following sections, the running conditions during the polarized data-taking periods are discussed in more detail.

4.3.1 The Polarized Hydrogen Data

The quality of the polarized hydrogen data comprising the 96c2 and the 97c1 productions is summarized in Tab. 4.3. The table shows the fractions of bad luminosity for each of the components listed in Sec. 4.2. Additionally the table contains the fractions of bad luminosity when two experimental components were bad at the same time. For example, 25.3 % of the bad data were discarded because the beam polarization was bad and 2.7 % were discarded because both the beam polarization and

Table 4.2: Fractions of good polarized and good unpolarized data for the years 1996 through 2000. The last two rows summarize the polarized data on hydrogen (96c2 and 97c1) and the polarized data on deuterium (98c1, 99b2, and 00c1). The 97c1 production does not contain unpolarized data.

Prod.	Polarized			Unpolarized		
	Good bursts		Good lumi	Good bursts		Good lumi
96c2	152 136	(50.4 %)	56.0 %	55 389	(64.5 %)	81.5 %
97b4	386 896	(60.5 %)	68.2 %	100 467	(81.5 %)	84.5 %
97c1	417 448	(72.1 %)	79.3 %	n/a		n/a
98c1	260 334	(79.8 %)	86.6 %	65 177	(83.6 %)	84.6 %
99b2	317 900	(72.7 %)	78.8 %	19 388	(78.0 %)	87.1 %
00c1	601 504	(76.7 %)	83.0 %	58 441	(67.1 %)	84.1 %
$\vec{H}$	569 584	(64.7 %)	71.4 %			
$\vec{D}$	1 179 738	(76.3 %)	83.0 %			

the luminosity were bad. In the row labeled 'exclusive', the fraction of bad luminosity is listed that was discarded because only the corresponding component was malfunctioning. For example, 18 % of the bad luminosity was discarded because only the beam polarization was bad.

The largest part of the data was rejected because of problems with the beam polarization and the target, and because of problems reported in the logbook. The beam polarization often dropped below the acceptable limit of 0.3 during a fill and intermittent difficulties to provide a current measurement also caused data to be rejected.

In the case of the target, high molecular recombination rates in the target cell lead to long periods in 1996 that were rejected from the analysis. In 1997, a beam dump in the target cell in July resulted in damage to the cell and consequently in low atomic fractions in the target gas. In addition, problems with low target magnet currents caused target polarizations too small for analysis. The target and logbook data quality are correlated because the target problems were often recorded in the logbook. Data were marked unanalyzable in the logbook for an extended period in 1996 because of an extraneous vertex chamber cover plate in the bottom half of the spectrometer. The total discarded data in the polarized running mode amount to 28.6 % of the luminosity.

Table 4.3: Data quality matrix of the polarized hydrogen data collected in 1996 and 1997. The diagonal elements are the percentage of bad luminosity lost due to the corresponding component. (28.6 % of the total polarized luminosity was marked bad, see Tab. 4.2.) The off-diagonal elements are the percentages of bad luminosity when both corresponding components were bad. The 'exclusive' row lists the amount of bad luminosity when only the corresponding component was bad. The quoted bit-pattern lists the bits of the data quality bit-pattern for each component in hexadecimal format.

Component	Bit-pattern	1	2	3	4	5	6	7
1 Beam Pol	10000002x	25.3	2.7	1.9	1.5	2.2	1.7	0.2
2 Lumi	00000030x		14.0	1.8	1.3	1.9	0.9	0.2
3 Target	A9A08001x			31.6	4.2	9.8	1.4	0.6
4 DAQ	400001CCx				18.1	3.9	0.8	0.4
5 Logbook	00007E00x					28.7	2.6	1.3
6 PID	020E0000x						11.6	1.0
7 HV Trips	00100000x							3.9
Exclusive		18.0	8.7	17.1	9.5	12.9	6.3	1.8

4.3.2 The Polarized Deuterium Data

The polarized deuterium data correspond to the 98c1, the 99b2, and the 00c1 productions. After the shutdown in the first half of 1998, HERA did not deliver high polarizations so that polarized data were not collected until 1999. The 98c1 polarized dataset was recorded in the spring of 1999 and the 99b2 production represents data from the second half of 1999.[1] The quality of the data is summarized in Tab. 4.4. Most of the bad luminosity was rejected because of problems with the beam polarization, the target, the DAQ, and the PID system. In the case of the beam polarization, most data were discarded in the Spring of 1999 (98c1) when periods with low polarization were frequent after the long shutdown. Target problems dominated the data-taking in the second half of 1999 (99b2), when frequent problems affected the target performance. In September, two holes were found in the target cell at the wake-field suppressors which had compromised the target operation. Recurring dead blocks in the calorimeter affected the PID system in the 2000 data-taking period. In principle, these data could be recovered, because the dead blocks lay near the edges of

---

[1]In the following, the 98c1 polarized dataset is often referred to as the 1998 data and the 99b2 dataset as the 1999 data.

Table 4.4: Data quality matrix of the polarized deuterium data collected in 1999 and 2000. (17 % of the polarized deuterium data were marked unanalyzable, see Tab. 4.2.) See Tab. 4.3 for more details.

Component	Bit-pattern	1	2	3	4	5	6	7
1 Beam Pol	10000002x	18.9	0.5	1.8	1.1	1.7	0.7	0.2
2 Lumi	00000030x		5.4	2.7	1.1	0.5	0.7	0.4
3 Target	AD818001x			32.7	3.0	0.9	1.7	0.4
4 DAQ	400001CCx				22.5	0.9	1.7	0.4
5 Logbook	00007E00x					8.6	1.1	0.3
6 PID	022E0000x						27.0	0.6
7 HV Trips	00500000x							2.4
Exclusive		14.5	1.7	24.7	16.7	4.6	22.6	1.2

the acceptance. However, the large statistics of the deuterium dataset rendered this time-consuming procedure unnecessary. The apparent large amount of DAQ problems is of the same absolute size as in the hydrogen data. In both datasets, the first burst of each run is discarded because of synchronization difficulties of slow and event data at the beginning of a run. The general high quality of the data in 2000 emphasizes this fixed fraction of bad data. The total discarded data in the polarized running mode amount to 17 % of the luminosity.

Chapter 5

Particle Identification

The identification of the scattered lepton is crucial in any deep-inelastic scattering experiment. In a semi-inclusive analysis, hadrons in the final state have to be identified as well. The HERMES spectrometer includes four particle identification (PID) detectors, as described in Sec. 3.5, which distinguish leptons[1] and hadrons with small contaminations and high efficiencies. In addition, the Čerenkov detector makes possible the identification of pions in the hadron sample and since the RICH detector upgrade in 1998 kaons can also be identified. Some of the work reported here was already described in Ref. [109] and is only included for completeness. The technical details of the software are documented in Refs. [110, 111].

5.1 Lepton-Hadron Discrimination

The identification of leptons and hadrons is based on the detector responses of the calorimeter, the preshower detector, the Čerenkov detector (the RICH since 1998), and the transition radiation detector. The detector responses of hadrons and leptons are discussed in Sec. 3.5.

5.1.1 Formalism

The detector responses are combined in an algorithm based on Bayesian statistics to calculate conditional probabilities $P(H_{l(h)}|E, p, \theta)$ for the hypothesis that a track is a lepton or a hadron given the track momentum p, its polar angle θ and an energy deposition E in the chosen detector. By means

---

[1]In analogy to Sec. 3.5.2, electrons and positrons are collectively referred to as leptons.

of Bayes' Theorem, these probabilities may be written as

$$P(H_{l(h)}|E,p,\theta) = \frac{P(H_{l(h)}|p,\theta)\ P(E|H_{l(h)},p)}{\sum_{i=l,h} P(H_i|p,\theta)\ P(E|H_i,p)}.\tag{5.1}$$

The hadron and lepton probabilities can thus be computed from the probabilities (the *parent distributions*) $P(E|H_{l(h)},p)$ that a lepton (hadron) with momentum p will deposit an energy E in the detector and the prior probability (the *particle fluxes*) $P(H_{l(h)}|p,\theta)$ that a track with momentum p and polar angle θ is a lepton (hadron). Here the detector responses are assumed to be uniform within the detector's acceptance and thus independent of θ.[2] The computation of the parent distributions and the fluxes from data is described below.

The probabilities $P(H_l|E,p)$ and $P(H_h|E,p)$ are combined into a logarithmic ratio PID,

$$\text{PID} \equiv \log_{10} \frac{P(H_l|E,p,\theta)}{P(H_h|E,p,\theta)}.\tag{5.2}$$

In terms of the parent distributions and the flux factors, this quantity becomes

$$\text{PID} = \log_{10} \frac{P(E|H_l,p)\ P(H_l|p,\theta)}{P(E|H_h,p)\ P(H_h|p,\theta)} = \text{PID}_{det} - \log_{10}\Phi,\tag{5.3}$$

where

$$\text{PID}_{det} \equiv \log_{10} \frac{P(E|H_l,p)}{P(E|H_h,p)} \qquad \text{and} \qquad \Phi \equiv \frac{\phi_h}{\phi_l} \equiv \frac{P(H_h|p,\theta)}{P(H_l|p,\theta)}.\tag{5.4}$$

The information of all PID detectors is taken into account in the sum of the PID-values for each detector:

$$\text{PID}_{cal} + \text{PID}_{pre} + \text{PID}_{cer(ric)} + \text{PID}_{trd},\tag{5.5}$$

where $\text{PID}_{ric} = \sum_{i=g,a} \text{PID}_{ric,i}$ is the sum of the ratios for the gas and the aerogel response, and $\text{PID}_{trd} = \sum_{i=1}^{6} \text{PID}_{trd,i}$ is the sum over the six TRD modules. PID values commonly defined are,

$$\text{PID2} \equiv \text{PID}_{cal} + \text{PID}_{pre}$$

$$\text{PID3} \equiv \text{PID}_{cal} + \text{PID}_{pre} + \text{PID}_{cer(ric)}\tag{5.6}$$

$$\text{PID5} \equiv \text{PID}_{trd}.$$

The full capabilities of the PID system are thus exploited in the combination

$$\text{PID} = \text{PID3} + \text{PID5} - \log_{10}\Phi.\tag{5.7}$$

---

[2]Note that the transition radiation detector response was observed to depend on the position of the track in the TRD modules. This dependence is corrected for in the μDST productions [107], before the algorithm discussed here is applied.

5.1.2   Formation of the Parent Distributions

The parent distributions $P(E|H_{l(h)}, p)$ are an intrinsic property of a PID detector that can be calculated through normalizing the appropriate particle counts as a function of the detector response. In principle, the count numbers can be determined at test-beam facilities with appropriate lepton and hadron beams. At HERMES, parent distributions derived from such test-beam data were used initially. For the datasets discussed here, a different approach is used. The parent distributions are extracted from the data collected during normal operation of the experiment. As opposed to using a test-beam facility this method has the advantage that the parent distributions take into account aging effects, varying detector conditions and calibrations during the respective data-taking periods.

The parent distributions are calculated for each year separately from the corresponding μDST production. Only appropriate good quality data are used by rejecting bursts that fail the data-quality-bits $(421E13DC)$x in case of the 96c2 and 97c1 productions, and the bits $(427E13DC)$x for the 98c1, 99b2, and 00c1 productions (see also Ch. 4 and App. A). Tracks are discarded, if they are not part of trigger 21 events, if they originate from vertices outside the target cell, or if they are not fully inside the acceptance of the HERMES spectrometer.

In the final data-sample, hadrons and leptons for the parent distribution of a given detector are identified by imposing cuts on the responses of the other PID detectors. For example, to generate lepton parent distributions for the calorimeter[3], cuts are imposed on the responses of the preshower, the Čerenkov/RICH, and the TRD. This method relies on the assumption that the PID detector responses of a given particle type used for identification are uncorrelated. In order to test this assumption, the detector correlations were estimated for leptons and hadrons in 3 GeV momentum intervals with the usual estimator for correlations of two variables x and y in N measurements [112]:

$$\rho = \frac{\overline{xy} - \overline{x}\,\overline{y}}{\sigma_x \sigma_y} \pm \frac{1}{\sqrt{N-1}}(1 - \rho^2). \tag{5.8}$$

Two sample scatter-plots of detector responses are given in Fig. 5.1 for the momentum interval $3\,\text{GeV} < p < 6\,\text{GeV}$. The preshower and calorimeter responses for leptons are highly correlated $(\rho \simeq 0.5)$, whereas the hadron response of the TRD is uncorrelated with the calorimeter response. The correlations for all detectors averaged over the momentum intervals are presented in Fig. 5.2. In the case of the lepton responses, the preshower detector is significantly correlated with the calorimeter and to a smaller extent with the TRD modules. The negative correlation with the calorimeter

---

[3]In the case of the calorimeter, the ratio of response E and track momentum p is used instead of the response.
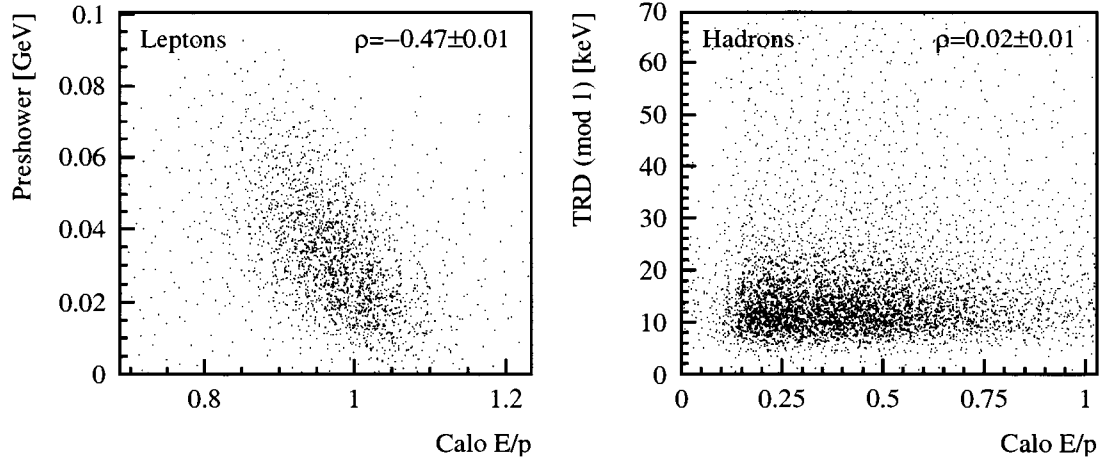
Figure 5.1: Example scatter-plots of detector correlations. The left hand plot shows the preshower detector versus the calorimeter response (E/p) for leptons in the momentum interval $3\,\text{GeV} < p < 6\,\text{GeV}$. The right hand plot presents the TRD module 1 response versus the calorimeter response (E/p) for hadrons in the same momentum interval.

arises because the energy lost in the preshower detector is missing in the formation of E_{calo}/p. Thus large energy loss in the preshower causes small E_{calo}/p and vice versa. The small positive correlation with the TRD is due to electromagnetic showers that develop in the lead in front of the TRD[4] and that propagate into the preshower detector.

The two RICH radiator materials are slightly correlated because of electromagnetic showers in the aerogel or the gas that lead to an increased number of hit photo-multipliers in both the aerogel ring and the gas ring (see Fig. 3.12). There is also a small correlation among the TRD modules, which is largest for neighbouring modules. It is caused by a small probability that transition radiation leaks into the following modules.

Consequently only a loose cut on the preshower was chosen in the case of the calorimeter parent distributions and no cuts were imposed among the RICH radiator materials or among the TRD modules. In all other cases, stringent cuts were found not to bias the parent distributions despite non-vanishing correlations.

In the case of the hadron responses, only the Čerenkov/RICH detector has sizable correlations with the other detectors. The response of both detectors depends on the hadron's momentum. At momenta above the pion threshold for example, a cut on the maximum Čerenkov response rejects

---

[4]A thin lead sheet shields the TRD from synchrotron radiation generated upstream of the experiment.
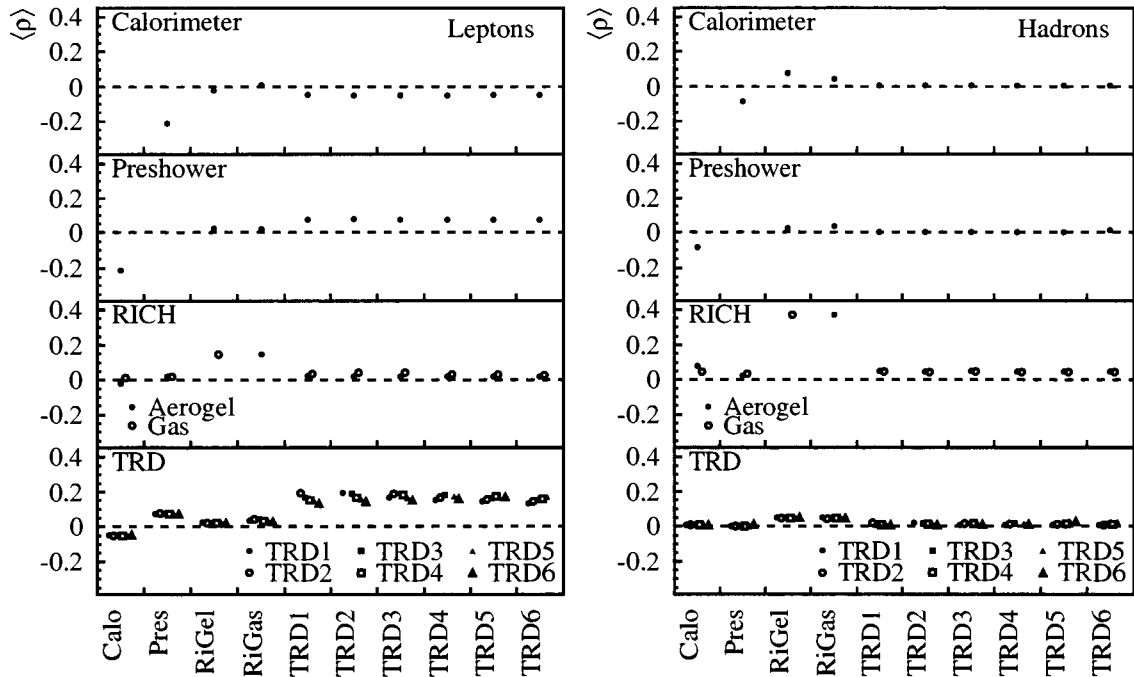
Figure 5.2: PID detector correlations averaged over 3 GeV momentum intervals. Left hand side: Leptons; right hand side: Hadrons. Correlations of a detector or module with itself are 1 and not shown. Correlations with the Čerenkov detector are similar to those of the RICH aerogel radiator and not shown.

more pions than kaons or protons thereby biasing the hadron sample. The RICH radiators are also found to be highly correlated with each other, because as before the responses are similar for a given hadron type in the hadron sample.

Therefore no cuts were imposed on the Čerenkov/RICH detector to identify hadrons for the other PID detectors. No cuts were imposed among the radiator materials. For consistency with the lepton case, no cuts were applied among the TRD modules.

The final cuts, summarized in Tab. 5.1, were chosen such that the particle samples are sufficiently clean while ensuring a reasonable number of tracks in each parent distribution. Restrictive cuts were chosen for the large 1998 to 2000 datasets, whereas fairly loose cuts were used in case of the smaller 1996 and 1997 datasets.

The parent distributions are arranged in a number of momentum intervals, in order to account for the momentum dependence of the detector responses [109]. The intervals were chosen such

Table 5.1: Detector cuts to identify leptons and hadrons for generating parent distributions. In case of the calorimeter, parent distributions a less stringent cut on the preshower response is used to identify leptons. See text for details.

		1996/ 1997	1998 – 2000
Calorimeter	leptons	$0.92 < E/p < 1.10$	$0.92 < E/p < 1.05$
	hadrons	$0.01 < E/p < 0.80$	$0.01 < E/p < 0.50$
preshower [GeV]	leptons	$0.025 < E$ (Calo: 0.01)	$0.030 < E$ (Calo: 0.01)
	hadrons	$0 < E < 0.004$	$0 < E < 0.003$
Čerenkov	leptons	$1.4 < \langle no.\gamma \rangle$	–
	hadrons	–	–
RICH Aerogel	leptons	–	$1 < N_{PMT}$
	hadrons	–	–
RICH Gas	leptons	–	$4 < N_{PMT}$
	hadrons	–	–
TRD [keV]	leptons	$26.0 < E$	$26.0 < E$
	hadrons	$0.1 < E < 14.0$	$0.1 < E < 13.0$

that the response of the detector within the interval was sufficiently constant. At the same time the number of intervals was chosen as small as possible in order to minimize the required memory. The bins were optimized separately for the two calorimeter thresholds, 1.4 GeV and 3.5 GeV, used in the trigger. The momentum bins are listed in table 5.2.

The algorithms to calculate the parent distributions were implemented in the program xparent. The determination of the PID-ratios for a given track is done with the library PIDlib. A detailed description of both software packages is given in Ref. [110].

5.1.3 Fluxes

The identification of leptons and hadrons can be improved, if a sensible estimate of the particle flux factors $\phi_{l(h)} = P(H_{l(h)}|p, \theta)$ as defined in Eq. (5.4) is available. In terms of the number of incident

Table 5.2: Momentum binning of the parent distributions.

Calorimeter threshold 1.4 GeV			
		Bins	Intervals [GeV]
Calor.	lept.	6	0., 2.5, 3.5, 4.5, 6.5, 8.5, 30.0
	hadr.	8	0., 1.0, 1.5, 2.0, 4.0, 5.0, 7.0, 10.0, 30.0
Presh.	lept.	9	0., 1.5, 2.0, 2.5, 3.0, 4.0, 6.0, 8.5, 12.0, 30.0
	hadr.	4	0., 2.5, 6.0, 9.0, 30.0
Čer.	lept.	4	0., 4.4, 10.0, 17.0, 30.0
	hadr.	10	0., 1.0, 4.0, 4.4, 5.0, 6.0, 8.0, 10.0, 12.5, 15.0, 30.0
RICH	lept.	10	0., 1.5, 2.0, 2.5, 3.0, 3.5, 4.0, 5.0, 6.0, 7.0, 30.0
	hadr.	10	0., 1.5, 2.0, 2.5, 3.0, 3.5, 4.0, 5.0, 6.0, 7.0, 30.0
TRD	lept.	5	0., 6.0, 12.0, 18.0, 23.0, 30.0
	hadr.	6	0., 2.0, 4.0, 6.0, 8.0, 10.0, 30.0

Calorimeter threshold 3.5 GeV			
		Bins	Intervals [GeV]
Calor.	lept.	6	0., 2.0, 3.0, 5.0, 7.0, 10.0, 30.0
	hadr.	13	0., 1.0, 1.5, 2.0, 3.0, 3.5, 4.0, 4.5, 5.0, 6.0 7.0, 8.0, 9.0, 30.0
Presh.	lept.	9	0., 1.5, 2.0, 2.5, 3.0, 4.0, 6.0, 8.5, 12.0, 30.0
	hadr.	3	0., 3.0, 8.5, 30.0
Čer.	lept.	4	0., 4.4, 10.0, 17.0, 30.0
	hadr.	10	0., 1.0, 4.0, 4.4, 5.0, 6.0, 8.0, 10.0, 12.5, 15.0, 30.0
RICH	lept.	10	0., 1.5, 2.0, 2.5, 3.0, 3.5, 4.0, 5.0, 6.0, 7.0, 30.0
	hadr.	10	0., 1.5, 2.0, 2.5, 3.0, 3.5, 4.0, 5.0, 6.0, 7.0, 30.0
TRD	lept.	5	0., 6.0, 12.0, 18.0, 23.0, 30.0
	hadr.	6	0., 2.0, 4.0, 6.0, 8.0, 10.0, 30.0

particles, the flux ratio can be written as

$$\Phi(p, \theta) = \frac{(\text{number of incident hadrons } (p, \theta))}{(\text{number of incident leptons } (p, \theta))}.$$ (5.9)

In practice, the flux ratio is calculated in a number of bins in momentum and polar angle. The bins are given in Tab. 5.3. The flux ratio cannot be calculated exactly because particle identification, a

Table 5.3: The momentum and polar angle bins for the calculation of the flux ratio.

	Bins	Ranges
p [GeV]	27	0., 1.4, 2.4, 3., 4., 5., 6., 7., 8., 9., 10., 11., 12., 13., 14.,15., 16., 17., 18., 19., 20., 21., 22., 23., 24., 25., 26., 30.
θ	6	0.040, 0.075, 0.100, 0.125, 0.150, 0.175, 0.300

necessary input, depends directly on this ratio (see Eq. (5.7)). Instead, it is estimated in an iterative procedure [113]. Initially the flux ratio is taken to be uniform,

$$\Phi_0(p, \theta) \equiv 1,$$ (5.10)

which corresponds to equal probabilities to detect a hadron or a lepton. The data are then analyzed and the flux ratios

$$\Phi_1(p, \theta) = \frac{(\text{number of tracks with PID} < 0 \ (p, \theta))}{(\text{number of tracks with PID} > 0 \ (p, \theta))}$$ (5.11)

are calculated for each p-θ-bin. These ratios are used in the next iterative step to calculate PID and the flux ratio Φ_2. The iteration is continued until convergence, which is typically reached in less than five steps. The flux factors for the polarized deuterium data are shown in Fig. 5.3. The distributions are virtually identical to those for the polarized hydrogen data.

The difference between the quantities PID3 + PID5 and PID3 + PID5 − $\log_{10} \Phi$ is presented in Fig. 5.4. The plots illustrate that the inclusion of the flux factor centers the PID distributions about the cuts at PID < 0 and PID > 1 to identify hadrons and leptons respectively. However, it is noted that the impact of the flux factors on the hadron and lepton count numbers is small and that therefore an analysis without flux factors is a good approximation.

5.1.4 Contaminations and Efficiencies of the DIS and SIDIS Samples

The contamination and the identification efficiency of a given particle type depend on the data sample that is selected for analysis. In this section, the contaminations and efficiencies of the DIS
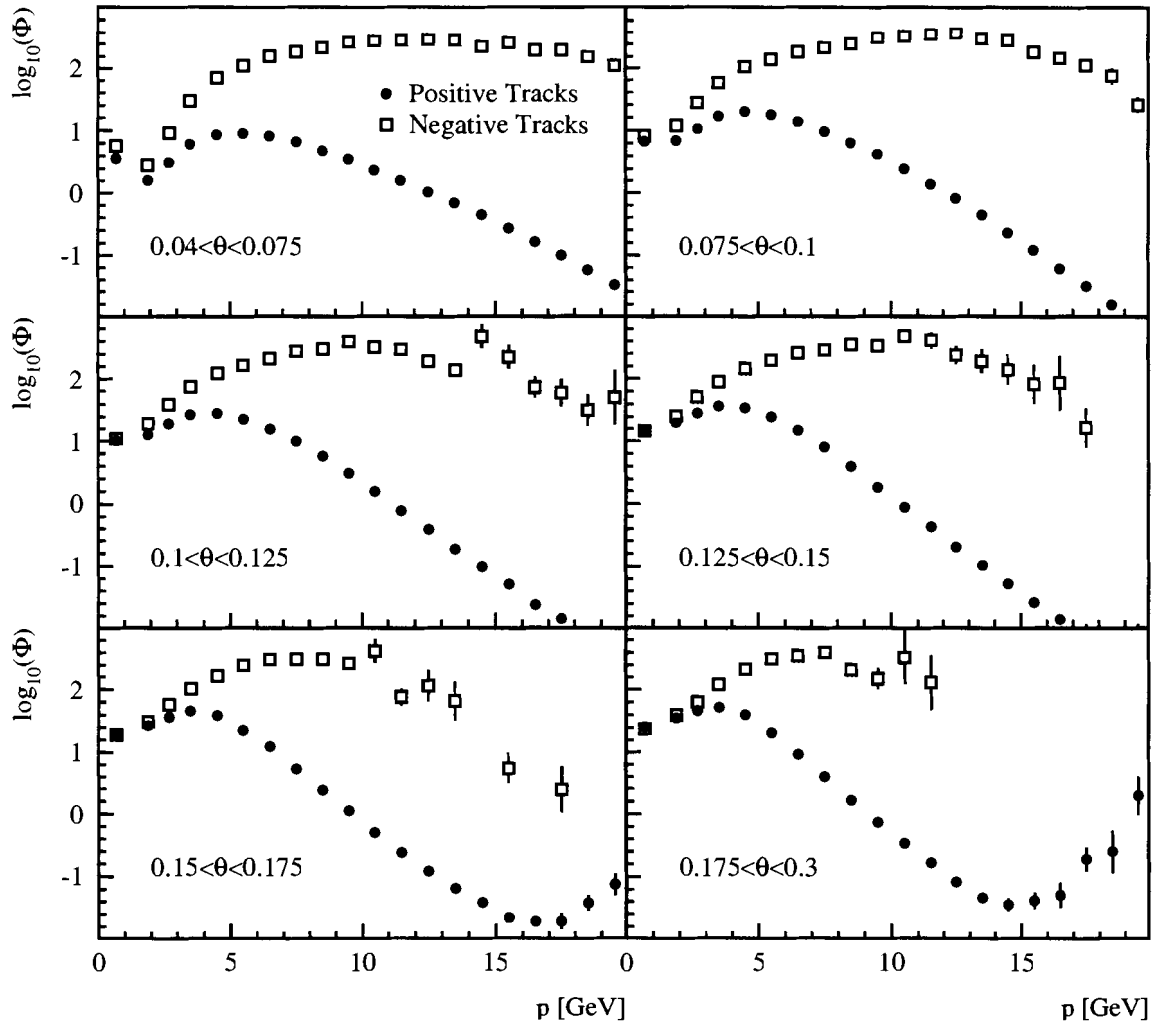
Figure 5.3: The logarithm of the flux ratio $\log_{10} \Phi = \log_{10} \phi_h/\phi_l$ as a function of momentum in six bins of polar angle. The fluxes presented were extracted from polarized deuteron data collected in 2000 with the 1.4 GeV calorimeter threshold. The open squares show the flux ratio for positive tracks and the solid circles the ratio for negative tracks. The kink at low momentum is due to the calorimeter threshold in the trigger that does not fire for single electrons below 1.4 GeV. At large polar angles only few DIS electrons are observed and thus the threshold effect is negligible. At large momentum and large polar angle the negative particle flux was often not calculable, because no electrons were observed. In the analysis, $\log_{10} \Phi = 0$ was assumed in these kinematic bins.
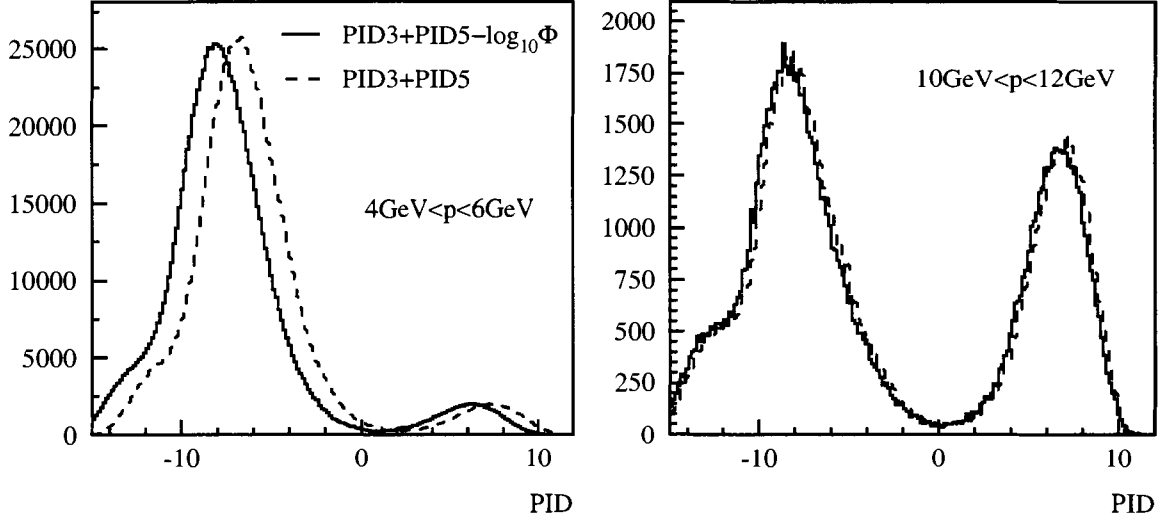
Figure 5.4: PID distributions for positive tracks with and without fluxes. Left: $4\,\mathrm{GeV} < p < 6\,\mathrm{GeV}$, right: $10\,\mathrm{GeV} < p < 12\,\mathrm{GeV}$. The solid line shows the PID distribution with flux correction, and the dashed line the PID distribution without flux correction. The shoulder at large negative PID values is caused by the RICH PID, that improves the hadron identification for hadrons that do not emit Čerenkov radiation.

electron and the SIDIS hadron sample are discussed. The cuts used to define these samples are listed in Sec. 6.1.

For this study, the PID cut for the DIS sample was removed. For the SIDIS sample, the DIS electron was identified using the PID cut PID > 1 and the sample of coincident tracks was studied without the PID cut. The PID distributions for these two samples are shown in Fig. 5.5.

The contamination and efficiency of the lepton sample for a given PID cut, PID_l, is given by

$$\mathrm{Con}(\mathrm{PID}_l) = \frac{\int_{\mathrm{PID}_l} d\mathrm{PID}\; N_h}{\int_{\mathrm{PID}_l} d\mathrm{PID}\; (N_l + N_h)} = \frac{\int_{\mathrm{PID}_l} d\mathrm{PID}\; P(H_h|\mathcal{E},p,\theta)}{\int_{\mathrm{PID}_l} d\mathrm{PID}\; (P(H_l|\mathcal{E},p,\theta) + P(H_h|\mathcal{E},p,\theta))}, \quad (5.12)$$

$$\mathrm{Eff}(\mathrm{PID}_l) = \frac{\int_{\mathrm{PID}_l} d\mathrm{PID}\; N_l}{\int d\mathrm{PID}\; N_l} = \frac{\int_{\mathrm{PID}_l} d\mathrm{PID}\; P(H_l|\mathcal{E},p,\theta)}{\int d\mathrm{PID}\; P(H_l|\mathcal{E},p,\theta)}, \quad (5.13)$$

where the probabilities are defined by Eq. (5.1) and the response $\mathcal{E}$ represents the combined responses of all PID detectors, $P(H_{l(h)}|\mathcal{E},p,\theta) \equiv \prod_i P(H_{l(h)}|E_i,p,\theta)$. The contamination and efficiency of the hadron sample may be defined in a similar way. The probabilities $P(H_{l(h)}|\mathcal{E},p,\theta)$
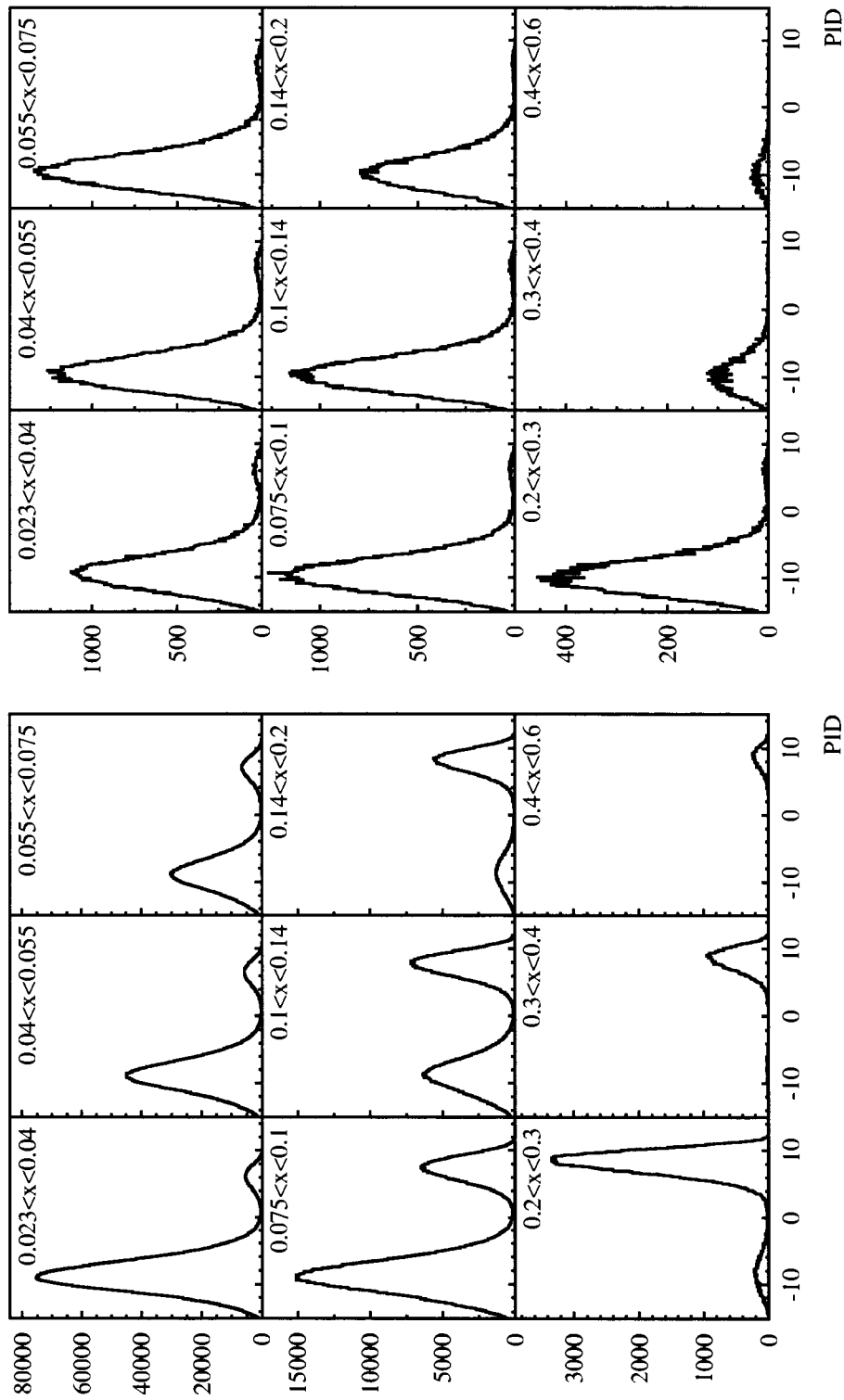
Figure 5.5: PID distributions of DIS (left) and SIDIS (right) candidates with full flux correction. The distributions are shown in the nine bins of x used in the asymmetry analysis discussed in the following chapter. The plots are based on the polarized proton data collected in 1996 and 1997.

were calculated using the probability method as described in Refs. [109, 114],

$$P(H_l|\mathcal{E},p,\theta) = \frac{10^{\text{PID}}}{1 + 10^{\text{PID}}} \quad \text{and} \quad P(H_h|\mathcal{E},p,\theta) = \frac{1}{1 + 10^{\text{PID}}}. \tag{5.14}$$

The contaminations and efficiencies of the DIS lepton sample are shown in Fig. 5.6 for three PID
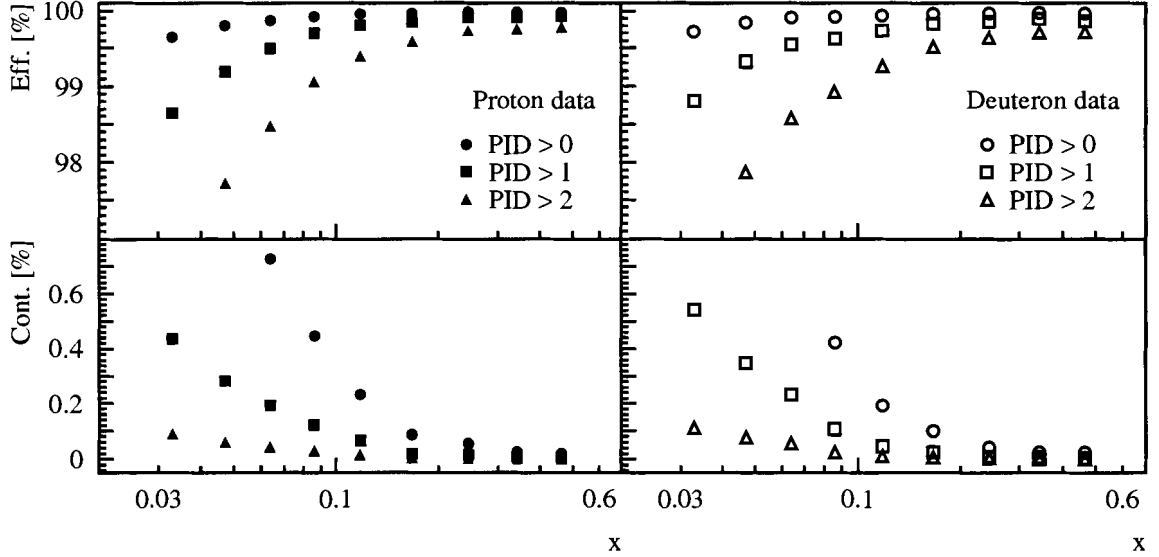
Figure 5.6: Contamination and Efficiency of the DIS lepton sample as a function of x-Bjørken. Shown are the distributions for three PID cuts.

cuts. Both quantities are similar for the proton and the deuteron data. The efficiency is larger than 98 % for PID > 1 over the entire range in x with contaminations smaller than 0.6 %. The identification of leptons is worse at low x where hadrons dominate the data sample (see Fig. 5.5). Based on this analysis the cut PID > 1 was selected for the identification of DIS leptons.

The contamination and efficiency of the coincident SIDIS hadron sample was estimated analogously. The contamination is negligible (< 0.1 %) over the entire x-range because of the small number of leptons in the sample as evident in Fig. 5.5. The selected cut PID < 0 is virtually 100% efficient.

5.2 Hadron Identification

5.2.1 Pion Identification with the Threshold Čerenkov Detector

Čerenkov detectors allow the identification of hadron types in the hadron sample. The threshold of the Čerenkov detector in operation until 1998 was set such that pions with momenta above 3.8 GeV and kaons with momenta above 13.6 GeV emit Čerenkov radiation (see Sect. 3.5.2). A hadron track was thus identified as a pion if its momentum was between 4 and 13.8 GeV and the number of detected photo-electrons was above the noise level ($\langle \text{no}.\gamma \rangle > 0.25$). The contamination of the pion sample is negligible, because the lepton contamination is negligible as shown in the previous section and pions dominate the hadron sample.

5.2.2 Pion, Kaon, and Proton Identification with the RICH detector

The RICH detector allowed the identification of pions, kaons, and protons in the momentum range $2\,\text{GeV} < p < 15\,\text{GeV}$. In the semi-inclusive analysis, a momentum range of $4\,\text{GeV} < p < 13.8\,\text{GeV}$ was used for consistency with the threshold Čerenkov detector. The pattern of Čerenkov photons emitted by tracks passing through the aerogel and the gas radiators, on the photomultiplier matrix was associated with tracks using an inverse ray tracing algorithm [115]. For a given track, the algorithm compares the measured Čerenkov angles with the theoretically expected angles. For each hadron type hypothesis $h = \pi$, K, p, the theoretical emission angle of photons $\theta_{\text{th};h}^{a,g}$ is computed assuming that the photon was emitted in the aerogel, a, and the gas, g, respectively. The average Čerenkov angle $\langle \theta \rangle_h^{a,g}$ for the hadron hypothesis h is calculated for each radiator by including only photons with emission angles within $\pm 2\,\sigma_\theta$ of the theoretically expected emission angle. Here $\sigma_\theta \simeq 8\,\text{mrad}$ is the single photon resolution of the RICH. This procedure rejects background photons, and photons due to other tracks or the other radiator. Fig. 5.7 shows the distribution of average angles in the two radiators as a function of the particle momentum.

The computed average angles are used to calculate the likelihood for each hadron type hypothesis

$$\mathcal{L}_h^{a,g} = \exp\left[\frac{-1}{2\,\sigma_{\langle\theta\rangle_h^{a,g}}^2} \left(\theta_{\text{th};h}^{a,g} - \langle\theta\rangle_h^{a,g} \right)^2 \right], \qquad h = \pi, K, p. \tag{5.15}$$

A track is assigned the particle hypothesis with the largest total likelihood $\mathcal{L}_h^{\text{tot}} = \mathcal{L}_h^a \cdot \mathcal{L}_h^g$. The confidence of the hadron identification is quantified in the rQp factor, which is the logarithmic ratio of the likelihood of the most probable particle hypothesis to the likelihood of the second most
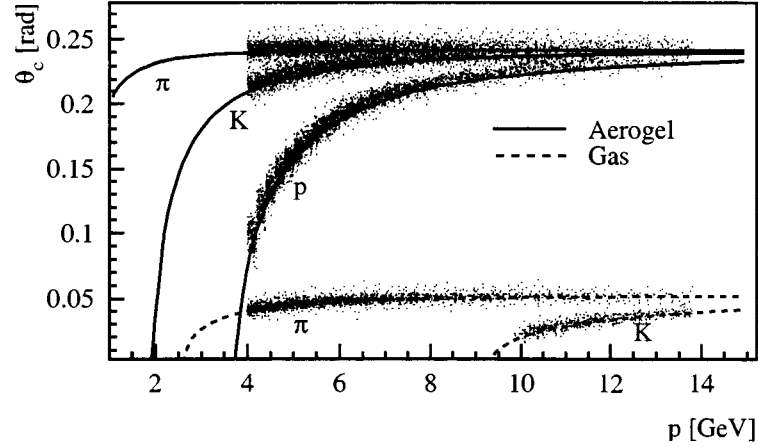
Figure 5.7: Characteristic Čerenkov angle versus momentum for the three hadron hypotheses and the two radiators.

probable hypothesis,

$$\mathrm{rQp} = \log_{10} \frac{\mathcal{L}_{h_1}^{\mathrm{tot}}}{\mathcal{L}_{h_2}^{\mathrm{tot}}}. \tag{5.16}$$

In the analysis, the rQp factor is required to be larger than zero, in order to ensure that the RICH hadron identification system found a most likely particle.

The contamination and efficiency of the RICH hadron identification was estimated with a Monte Carlo simulation and with pion and kaon tracks from experimentally reconstructed ρ^0, ϕ, K_s^0, and Λ particle decays [116]. In the latter case, the hadron types are deduced by restricting the invariant mass of two charged tracks in an event to the ρ^0-mass, for example. The two tracks are then identified with pions. This analysis provides probabilities $P(h_i|h_t)$ that a given hadron of true type h_t is identified as hadron of type h_i. Note that $P(h_i|h_t)$ with $h_i = h_t$ is the efficiency of the system, but $P(h_i|h_t)$ with $h_i \neq h_t$ does not describe the contamination of the sample of type h_i, because the relative hadron fluxes are not taken into account. The conditional probabilities are combined in a matrix,

$$\mathcal{P} = \begin{pmatrix} P(\pi_i|\pi_t) & P(\pi_i|K_t) & P(\pi_i|p_t) \\ P(K_i|\pi_t) & P(K_i|K_t) & P(K_i|p_t) \\ P(p_i|\pi_t) & P(p_i|K_t) & P(p_i|p_t) \end{pmatrix}. \tag{5.17}$$

The $\mathcal{P}$-matrix depends on the track momentum and the topology of rings on the photomultiplier matrix. The $\mathcal{P}$-matrix is thus computed in 1 GeV momentum bins and the topology is accounted for by taking the track multiplicity in the given detector half into account. The flux of identified hadrons,
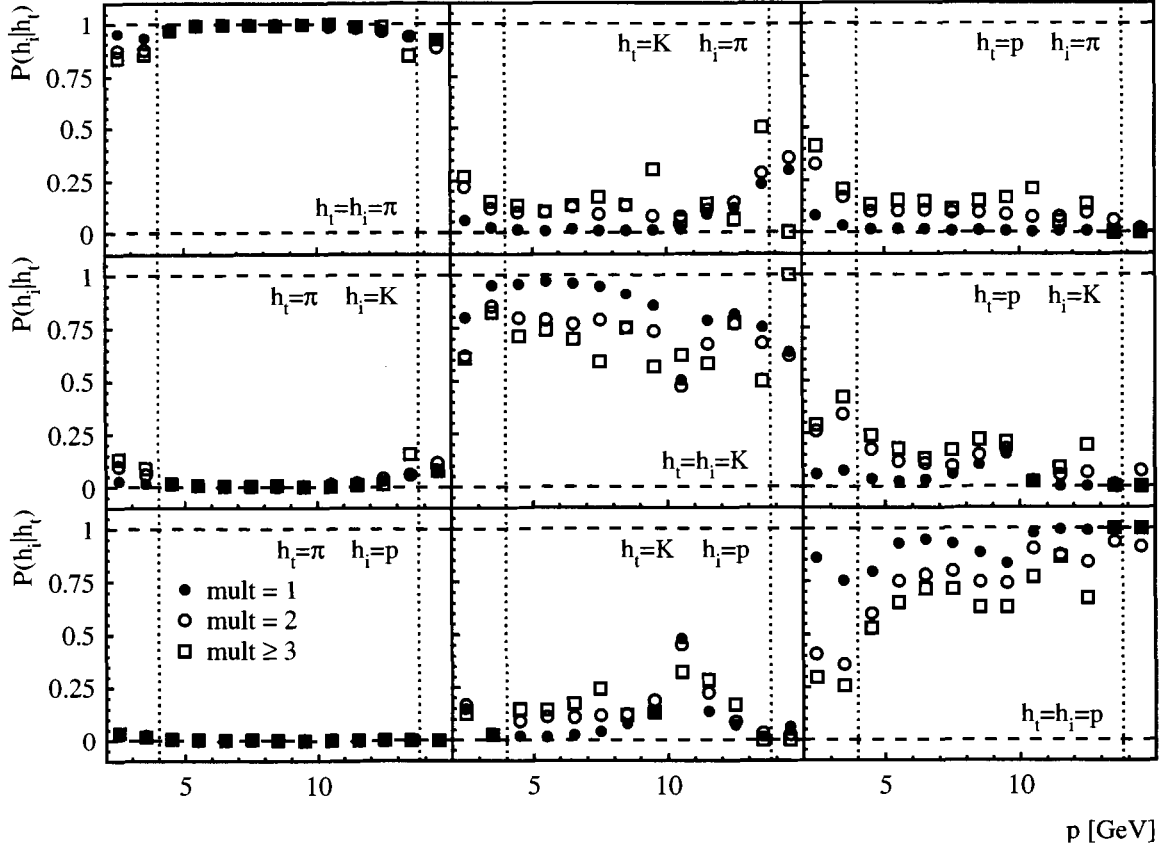
Figure 5.8: The $\mathcal{P}$-matrix elements of the RICH PID system. The elements are arranged in the same way as the $\mathcal{P}$-matrix in Eq. (5.17). Shown are the probabilities as a function of momentum for the track multiplicities one, two, and three or more. The dotted lines indicate the lower and upper boundaries of the momentum range used in the semi-inclusive analysis.

$\vec{I} = (N_\pi^i, N_K^i, N_p^i)$, is related the flux of true hadrons, $\vec{N} = (N_\pi^t, N_K^t, N_p^t)$, by $\vec{I} = \mathcal{P} \cdot \vec{N}$. The true flux follows by inversion of the $\mathcal{P}$-matrix,

$$\vec{N} = \mathcal{P}^{-1} \cdot \vec{I}. \tag{5.18}$$

The elements in the inverse $\mathcal{P}$-matrix do not represent probabilities. In fact, some of the off-diagonal elements of the $\mathcal{P}^{-1}$-matrix are negative. The elements are meaningful and lead to the fluxes of true hadrons only in combination with the identified hadron fluxes (see App. A.2).

In the semi-inclusive analysis, each pion, kaon, and proton track was assigned a weight according to the inverse $\mathcal{P}$-matrix. For example, a track identified as a pion was weighted with the element

$(\mathcal{P}^{-1})_{\pi_t,\pi_i}$ in the true pion count rate and with $(\mathcal{P}^{-1})_{K_t,\pi_i}$ in the true kaon count rate. The count numbers of true hadrons are computed as the sums of these weights,

$$N_h^t \equiv N_{h_t} = \sum_j (\mathcal{P}^{-1})_{h_t,(h_i)_j} \qquad h_t = \pi, \, K, \, p, \tag{5.19}$$

where the sum runs over all hadron tracks and $(h_i)_j$ labels the identified hadron type of track j.

The numerical values of the $\mathcal{P}$-matrix are provided in Ref. [117] and presented in Fig. 5.8. For all hadron-types, the identification worsens with increasing multiplicity in the corresponding detector half, because overlapping Čerenkov rings in the PMT matrix of the RICH make the association of single photons with the rings ambiguous. However, the ratio of DIS events with one, two, and three or more tracks in a given detector half is 1 : 0.15 : 0.01. The identification of pions is highly efficient and the probability of identifying a kaon or a proton to be a pion is small. The identification of kaons has a larger momentum dependence that is discontinuous at the kaon momentum threshold of the gas radiator. Similarly protons are identified with efficiencies larger than 75 % in events with track multiplicity one. The count numbers of SIDIS hadrons are listed in Tab. 6.2.

Chapter 6

The Observed Double Spin Asymmetries

In this chapter, the determination of the cross section asymmetries discussed in Sec. 2.6 is described. In the first part, the criteria to identify inclusive and semi-inclusive DIS events are presented. Then the asymmetry formalism is given followed by results. The chapter concludes with a discussion of various systematic studies. The asymmetries shown in this chapter were not corrected for instrumental effects or for higher order QED effects. The correction algorithm and the corrected asymmetries are given in the following chapter.

6.1   Selection of Deep-Inelastic Scattering Events

6.1.1   Geometrical and Kinematic Requirements

Deep-inelastic scattering events were selected from the data that remained after all data quality criteria described in Ch. 4 were applied. The DIS trigger described in Sec. 3.6 preselects events that are likely to be deep-inelastic. Tracks that are part of these events are subjected to further cuts in order to ensure that they are fully inside of the spectrometer acceptance and to identify the DIS positron[1] and coincident semi-inclusive hadrons.

Tracks were required to originate from vertices that lay within the target cell. This requirement ensured that the tracks selected stemmed from interactions of the beam with the target gas. For example, the cut in the longitudinal direction rejected tracks from beam interactions with the collimator in front of the target cell. The scattering angles of the tracks were required to be in the range

---

[1]As shown in Tab. 3.1 the HERA accelerator was run with electrons in 1998. The analysis discussed here for the case of DIS positrons also holds for the data taken in 1998.

Table 6.1: Geometric and kinematic requirements for the identification of DIS and SIDIS tracks. See text for details.

Geometry cuts	
Vertex Position	$D_{\text{vert}} < 0.75\,\text{cm}, \quad -18\,\text{cm} < Z_{\text{vert}} < 18\,\text{cm}$
Scattering angle	$\theta_x < 170\,\text{mrad}, \quad 40\,\text{mrad} < \theta_y < 140\,\text{mrad}$
Calorimeter cluster position	$x_{\text{calo}} < 175\,\text{cm}, \quad 30\,\text{cm} < y_{\text{calo}} < 100\,\text{cm}$
Track momentum	$p > 0.5\,\text{GeV}$
Kinematic cuts (DIS positron)	
PID	$\text{PID} \equiv \text{PID3} + \text{PID5} - \Phi > 1$
Calorimeter energy	$E_{\text{calo}} > 3.5\,\text{GeV}$
Scale	$Q^2 > 1\,\text{GeV}^2$
Invariant mass of the hadronic final state	$W^2 > 10\,\text{GeV}^2$
Energy transfer	$y < 0.85$
Kinematic cuts (SIDIS hadrons)	
PID	$\text{PID} \equiv \text{PID3} + \text{PID5} - \Phi < 0$
Fractional energy	$0.2 < z < 0.8$
Feynman scaling variable	$0.1 < x_F < 1$
Pion (threshold Čerenkov)	$4\,\text{GeV} < p < 13.8\,\text{GeV}, \quad \langle \text{no}.\gamma \rangle > 0.25$
Pion (RICH)	$4\,\text{GeV} < p < 13.8\,\text{GeV}, \quad \text{rQp} > 0, \quad \text{weight } \omega^\pi$
Kaon (RICH)	$4\,\text{GeV} < p < 13.8\,\text{GeV}, \quad \text{rQp} > 0, \quad \text{weight } \omega^K$

corresponding to the opening of the spectrometer magnet. In the back of the spectrometer, a cut on the position of the calorimeter cluster associated with each track rejected tracks with clusters that were not fully contained in the calorimeter and more generally tracks that were not fully inside of the acceptance of the rear part of the spectrometer. Tracks with very small momentum were discarded.

From the remaining sample of tracks, positrons were identified in each event by requiring that $\text{PID} > 1$ as described in Ch. 5. The scattered DIS positron in each event was selected from these positrons by a set of kinematic cuts: A cut on the calorimeter energy $E_{\text{calo}} > 3.5\,\text{GeV}$ was used to match the trigger threshold of $3.5\,\text{GeV}$ used in the first period of 1996. The requirement that $Q^2 > 1\,\text{GeV}^2$ selected events from the deep-inelastic scattering region. A large invariant mass of the hadronic final state $W^2 > 10\,\text{GeV}^2$ further rejected events from the resonance region ($W \lesssim 2\,\text{GeV}$). This cut additionally improved the separation of the target and current fragments for the

identification of semi-inclusive hadrons. Finally the requirement $y < 0.85$ rejected DIS events in a region where the contribution by higher order QED effects to the cross section is large. Note that this cut essentially supersedes the cut on E_{calo}, because in the case of positrons E_{calo} is approximately equal to the positron energy. The positron with the highest momentum was identified with the DIS positron, if more than one positron remained after all the cuts listed.

In the sample of tracks coincident with the DIS positron, hadrons were identified with PID < 0. Semi-inclusive hadrons were selected from this data sample with a cut on the fractional energy of the hadron, $0.2 < z < 0.8$, and a cut on x-Feynman, $x_F > 0.1$. The lower boundaries of both cuts in combination lead to a large probability that the hadron is part of the current fragments that contain the struck quark [118, 119]. The upper boundary on z discarded hadrons from exclusive events such as diffractive vector meson production, where the virtual photon fluctuates into an (off-shell) $q\bar{q}$ pair which is scattered onto the mass shell by diffractive interaction with the target [120]. Pions were identified up to 1998 with the threshold Čerenkov counter and pions and kaons with the RICH since 1998 as described in Sec. 5.2. All hadrons in an event that fulfilled these conditions were included in the corresponding count rates. The multiplicity of SIDIS hadrons is shown in Fig. 6.1. The average multiplicities of positive and negative SIDIS hadrons are 0.16 and 0.10 respectively for both targets.
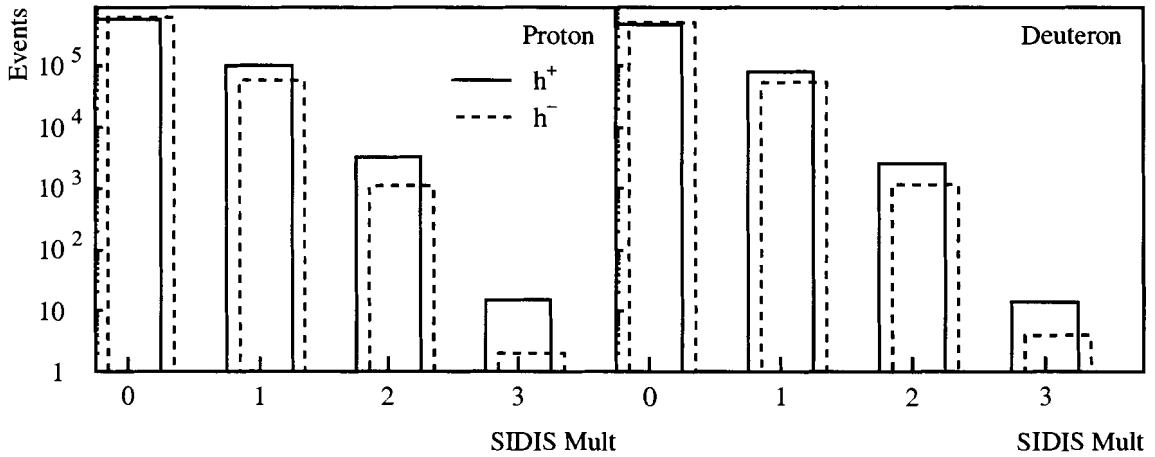
Figure 6.1: The number of DIS events as a function of the SIDIS multiplicity. The plots are based on subsets of the proton and the deuteron data.

The requirements imposed for the identification of DIS and SIDIS events are summarized in Tab. 6.1. The phase space in x and Q^2 defined by the cuts on the DIS positron is shown in Fig. 6.2.
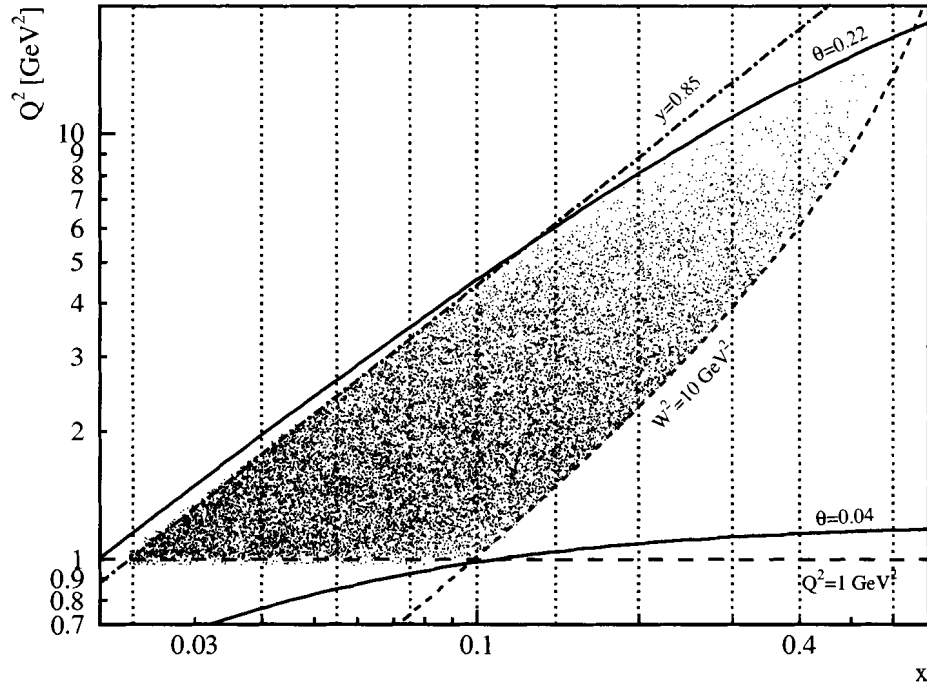
Figure 6.2: The kinematic plane. The graph shows the kinematic range in x and Q^2 defined by the HERMES spectrometer and the cuts applied to identify DIS events. The dotted vertical lines indicate the x-binning used in the analysis. A typical set of DIS events was super-imposed.

The superimposed scatter-plot of a typical set of DIS events illustrates the statistical distribution of the events that decreases with Q^2 as expected in Eq. (2.11).

6.1.2 Correction for Charge Symmetric Background

The particle count rates were corrected for charge symmetric background processes (*e.g.* $\gamma \rightarrow e^+ + e^-$). The rate for this process was estimated by considering lepton tracks with a charge opposite to the beam charge that passed the DIS cuts. It was assumed that these leptons stemmed from pair production processes and that the associated anti-lepton was not detected. The rate for the charge symmetric process (where the particle is detected with the same charge as the beam but originating from pair production) is the same. The number of events with an opposite sign lepton is therefore an estimate of the number of charge symmetric events that masquerade as DIS events. This number was subtracted from the inclusive DIS count rate.

Hadrons coincident with the background DIS track, that passed the SIDIS cuts, were also sub-

tracted from the corresponding SIDIS hadron sample. The DIS background rate was $\sim 6\%$ with respect to the total DIS rate in the smallest x-bin and decreased rapidly with increasing x. The overall background fraction from this source was only 1.4 %.

6.1.3 The Particle Count Numbers

The particle count numbers for the data-productions analyzed are summarized in Tab. 6.2. The numbers are presented in terms of equivalent numbers of events N_{eq} and they were summed over the two orientations of target and beam polarization. The equivalent count number is the number of unweighted events with the same relative error as the sum of weighted events N,

$$\frac{\sigma(N_{eq})}{N_{eq}} \equiv \frac{\sqrt{N_{eq}}}{N_{eq}} = \frac{\sqrt{\sum_i (\omega_i)^2}}{\sum_{i'} \omega_{i'}} \equiv \frac{\sigma(N)}{N}. \tag{6.1}$$

The uncertainty on the counts,

$$\sigma(N) = \sqrt{\sum_i \omega_i^2}, \tag{6.2}$$

is a consequence of the Poisson distribution of the events. The weights ω_i are defined in Sec. 5.2 for hadrons identified by the RICH detector in semi-inclusive events. For pions identified by the threshold Čerenkov counter, for undifferentiated hadrons, and for inclusive DIS events the weight is unity, $\omega_i = 1$. An additional weight of ± 1 is applied according to their classification as signal or charge-symmetric background.

Table 6.2: Equivalent count numbers of DIS positrons and SIDIS hadrons for the hydrogen and the deuterium data.

	96c2	97c1	**Total H**	98c1	99b2	00c1	**Total D**
DIS $e^{\pm}$	482,058	1,234,813	1,716,866	737,418	925,835	5,011,256	6,674,475
h^+	77,210	202,222	279,432	115,544	143,433	795,501	1,054,477
h^-	44,629	115,973	160,602	75,039	95,499	524,243	694,779
π^+	32,171	85,662	117,833	52,122	64,342	356,858	490,641
π^-	22,457	59,605	82,062	41,787	52,919	290,744	385,450
K^+				8,163	10,488	57,057	75,707
K^-				3,305	4,399	23,801	33,284

6.2 The Observed Asymmetries

6.2.1 Formation of the Asymmetries

The cross section asymmetry $A_{\parallel}$ given in Eq. (2.62) can be related to the measured number of counts in two configurations of beam and target polarization. The number of inclusive events $N^{\rightleftarrows(\Rightarrow)}$ and of semi-inclusive hadrons $N_h^{\rightleftarrows(\Rightarrow)}$ in the anti-aligned (aligned) configuration of beam and target polarizations is given by

$$N_{(h)}^{\rightleftarrows(\Rightarrow)} = \int_{\rightleftarrows(\Rightarrow)} dt\, \sigma_0\, \mathcal{A}(t)\, \mathcal{L}(t) \left(1 \pm P_T(t)\, P_B(t)\, A_{\parallel}^{(h)}\right), \qquad (6.3)$$

where the negative sign is for the parallel configuration. The luminosity in the time interval $[t, t+dt]$ is given by $\mathcal{L}(t)$, while the beam and target polarizations are given by $P_B(t)$ and $P_T(t)$ respectively. The unpolarized cross section σ_0 and the asymmetry $A_{\parallel}^{(h)}$ are time-independent. In the analysis, the acceptance of the spectrometer, $\mathcal{A}(t)$, which includes any DAQ inefficiencies is assumed to be constant for each data-taking period, $\mathcal{A}(t) \equiv \mathcal{A}$. Eq. (6.3) can be solved for $A_{\parallel}$, eliminating the unpolarized cross section σ_0 and the acceptance $\mathcal{A}$. In terms of the number of counts, the asymmetry is then given by

$$A_{\parallel}^{(h)} = \frac{N_{(h)}^{\rightleftarrows} L^{\Rightarrow} - N_{(h)}^{\Rightarrow} L^{\rightleftarrows}}{N_{(h)}^{\rightleftarrows} L_P^{\Rightarrow} + N_{(h)}^{\Rightarrow} L_P^{\rightleftarrows}} \qquad (6.4)$$

for the inclusive asymmetry $A_{\parallel}$ and the semi-inclusive asymmetries $A_{\parallel}^h$ of the various types of hadrons, $h = h^{\pm}, \pi^{\pm}, K^{\pm}$. The counts are normalized by the integrated luminosities $L^{\Rightarrow}$ and $L^{\rightleftarrows}$,

$$L^{\rightleftarrows(\Rightarrow)} = \int_{\rightleftarrows(\Rightarrow)} dt\, \mathcal{L}(t), \qquad (6.5)$$

where the integral is understood to run over the time periods where the beam and target polarizations were anti-aligned (aligned). Similarly $L_P^{\Rightarrow}$ and $L_P^{\rightleftarrows}$ are the luminosities weighted by the target polarization $P_T(t)$ and the beam polarization $P_B(t)$ and integrated over time t,

$$L_P^{\rightleftarrows(\Rightarrow)} = \int_{\rightleftarrows(\Rightarrow)} dt\, P_T(t)\, P_B(t)\, \mathcal{L}(t). \qquad (6.6)$$

The luminosity and the beam and target polarizations are measured in intervals of the order of one minute. Eqs. (6.5) and (6.6) therefore rely on the assumption that these values are approximately constant between measurements.

Note that Eq. (6.4) holds for polarized gaseous hydrogen and deuterium targets only. For other targets, the measured asymmetry of counts on the right hand side of Eq. (6.4) is reduced by the target

dilution factor f_D. This factor is the cross section fraction that is due to polarizable nucleons in the target. It is 1 for pure hydrogen and deuterium targets, $\sim 1/3$ for a pure helium target and usually much smaller for solid state targets.[2]

6.2.2 Azimuthal Acceptance Correction

The measured semi-inclusive asymmetries were corrected for acceptance effects due to the asymmetric azimuthal acceptance of the spectrometer. In the formalism described in Sec. 2.6, the semi-inclusive asymmetry of hadron type h was written in terms of the structure functions F_1^h and g_1^h given in Eqs. (2.60) and (2.61). This expression has to be modified, when non-zero transverse parton momenta with respect to the virtual photon momentum are taken into account. Non-zero intrinsic transverse momentum leads to a non-trivial azimuthal dependence of the hadron production cross sections (see e.g. [122, 123]). The relevant azimuthal angle ϕ^h is the angle between the plane defined by the initial and final state electron and the plane defined by the virtual photon and the final state hadron. Azimuthal dependencies were measured by various groups, for example the azimuthal dependence of semi-inclusive single-spin asymmetries on deuterium with respect to the target polarization was recently measured by the HERMES collaboration [124]. The semi-inclusive (double-spin) asymmetries computed in this work were integrated over the azimuthal angle ϕ^h. In the integrated asymmetry, the azimuthal dependence of the semi-inclusive cross sections result in a dependence on the non-trivial azimuthal acceptance of the spectrometer [125, 126],

$$A_{\parallel}^h = \frac{\int d\Phi \int d\phi^h \, \Delta\sigma^h(\phi^h) \, \epsilon(\Phi, \phi^h)}{\int d\Phi \int d\phi^h \, \sigma^h(\phi^h) \, \epsilon(\Phi, \phi^h)}. \tag{6.7}$$

Here $\Delta\sigma^h(\phi^h)$ is the polarized semi-inclusive cross section for longitudinal beam and target polarization and $\sigma^h(\phi^h)$ is the corresponding unpolarized cross section. The function $\epsilon(\Phi, \phi^h)$ parameterizes the detector acceptance, where Φ is azimuthal angle of the scattered electron in the spectrometer reference frame. In other words, the asymmetric acceptance affects the acceptance for final state hadrons depending on the azimuthal angle of the scattered electron with respect to the spectrometer.

The measured semi-inclusive asymmetries were corrected for this azimuthal acceptance effect. The acceptance correction was parameterized [127] as a function of x and z based on an analysis of

---

[2]Recently, [6]LiD solid state targets became available. This material has a target dilution factor of 1/3 [121].

HERMES data [128],

$$C_\phi^h(x) = 1 + \left(\log_{10}(x) - \log_{10}(x_0^h)\right)\left[a_0^h + a_1^h \, \log_{10}(x) + a_2^h \, \log_{10}^2(x) + a_3^h \, \log_{10}^3(x)\right], \quad (6.8)$$

$$C_\phi^h(z) = b_0^h + b_1^h \, z + b_2^h \, z^2 + b_3^h \, z^3. \qquad (6.9)$$

The coefficients a_i^h, b_i^h, and the values x_0^h are given in Tabs. B.1 and B.2 in App. B. The correction was applied to the measured asymmetries given in Eq. (6.4),

$$A_\parallel^h = C_\phi^h \, \frac{N_h^{\rightleftarrows} L^{\rightrightarrows} - N_h^{\rightrightarrows} L^{\rightleftarrows}}{N_h^{\rightleftarrows} L_P^{\rightrightarrows} + N_h^{\rightrightarrows} L_P^{\rightleftarrows}}. \qquad (6.10)$$

The correction factor $C_\phi^h(x)$ is largest for $x < 0.1$, where the factor is about 1.1, leading to a 10 % correction. In the entire kinematic range, the absolute correction of the asymmetry is small, because of the small size of the asymmetry at low x (see below) and because the correction is small at $x > 0.1$. The correction as function of z is about 10 % at small z and becomes smaller at larger z. It was applied in a z-dependence study of the Born asymmetries (see Sec. 7.7.2).

6.2.3 Statistical Uncertainties and Correlations

The statistical uncertainties shown as the error bars arise from the uncertainties on the particle counts. The uncertainty on the asymmetries follow via the usual error propagation,

$$\sigma\left(A_\parallel^{(h)}\right) = |C_\phi| \, \frac{\left|L^{\rightrightarrows} L_P^{\rightleftarrows} - L^{\rightleftarrows} L_P^{\rightrightarrows}\right|}{\left[N_{(h)}^{\rightleftarrows} L_P^{\rightrightarrows} + N_{(h)}^{\rightrightarrows} L_P^{\rightleftarrows}\right]^2} \, \sqrt{\left[N_{(h)}^{\rightrightarrows} \sigma\left(N_{(h)}^{\rightleftarrows}\right)\right]^2 + \left[N_{(h)}^{\rightleftarrows} \sigma\left(N_{(h)}^{\rightrightarrows}\right)\right]^2}, \quad (6.11)$$

where the factor $|C_\phi|$ arises from the azimuthal acceptance correction and the uncertainties on the count numbers are given by Eq. (6.2). The uncertainties on the photon-nucleon asymmetries are scaled with respect to $\sigma\left(A_\parallel^{(h)}\right)$ due to the depolarization factor,

$$\sigma\left(A_1^{(h)}\right) = \left|\frac{1}{(1 + \eta\gamma)D}\right| \sigma\left(A_\parallel^{(h)}\right). \qquad (6.12)$$

The inclusive asymmetry is correlated with the semi-inclusive asymmetries, which are also correlated with each other. The correlation can be estimated using the average hadron multiplicities [129, 130],

$$\rho\left(A_\parallel^{h_\alpha}, A_\parallel^{h_\beta}\right) = \frac{\langle n^{h_\alpha} \, n^{h_\beta}\rangle}{\sqrt{\langle(n^{h_\alpha})^2\rangle \, \langle(n^{h_\beta})^2\rangle}}, \qquad (6.13)$$

where the inclusive "multiplicity" is by definition $n^e = 1$. The hadron multiplicities are

$$\langle n^{h_\alpha} \rangle = \frac{\sum_{\text{evts}} N^{\text{evt}}_{h_\alpha}}{N_{\text{evts}}}, \qquad \langle n^{h_\alpha} n^{h_\beta} \rangle = \frac{\sum_{\text{evts}} N^{\text{evt}}_{h_\alpha} N^{\text{evt}}_{h_\beta}}{N_{\text{evts}}}, \tag{6.14}$$

where the sum runs over all DIS events, $N^{\text{evt}}_{h_\alpha}$ is the weighted number of hadrons of type h_α in a given event, and N_{evts} is the total number of DIS events. The correlations of the measured asymmetries are listed in Tabs. B.7 and B.8 in App. B.

6.2.4 Results

The measured asymmetries $A^{(h)}_\parallel$ on the proton and the deuteron are shown in Figs. 6.3 and 6.4. The numerical values are tabulated in Tabs. B.3 and B.4 in App. B. The proton asymmetries are the averages of the 1996 and 1997 running periods weighted by the corresponding statistical uncertainties,

$$A^{(h)}_{\parallel p} = \sum_{i=96,97} \frac{A^{(h)}_{\parallel p,i}}{\left(\sigma(A^{(h)}_{\parallel p,i})\right)^2} \left[\sum_{i=96,97} \frac{1}{\left(\sigma(A^{(h)}_{\parallel p,i})\right)^2} \right]^{-1} \tag{6.15}$$

The deuteron asymmetries are analogously the averages of the 1998 through 2000 running periods. The figures also show the photon-nucleon asymmetries $A^{(h)}_1$ that follow from $A^{(h)}_\parallel$ via Eq. (2.66). The asymmetries are shown as a function of x at the measured Q^2. The bins in x that were used in the data analysis are tabulated in Tab. 6.3. The differences between $A^{(h)}_\parallel$ and $A^{(h)}_1$ are a consequence of the depolarization of the virtual photon with respect to the positron (see Eq. (2.65)).

Table 6.3: The bins in x used in the analysis.

bin	1	2	3	4	5	6	7	8	9
x_{low}	0.023	0.040	0.055	0.075	0.1	0.14	0.2	0.3	0.4
x_{up}	0.040	0.055	0.075	0.1	0.14	0.2	0.3	0.4	0.6

A discussion of the final asymmetries is given in Sec. 7.6. The asymmetries shown here are not corrected for detector smearing and QED radiative effects — they are merely intermediate results.

6.2.5 Systematic Uncertainties on the Asymmetries

The systematic uncertainties, shown as the error bands in Figs. 6.3 and 6.4, arise from various sources related to the measurement, the parameterization for R and the assumption $g_2 \approx 0$.
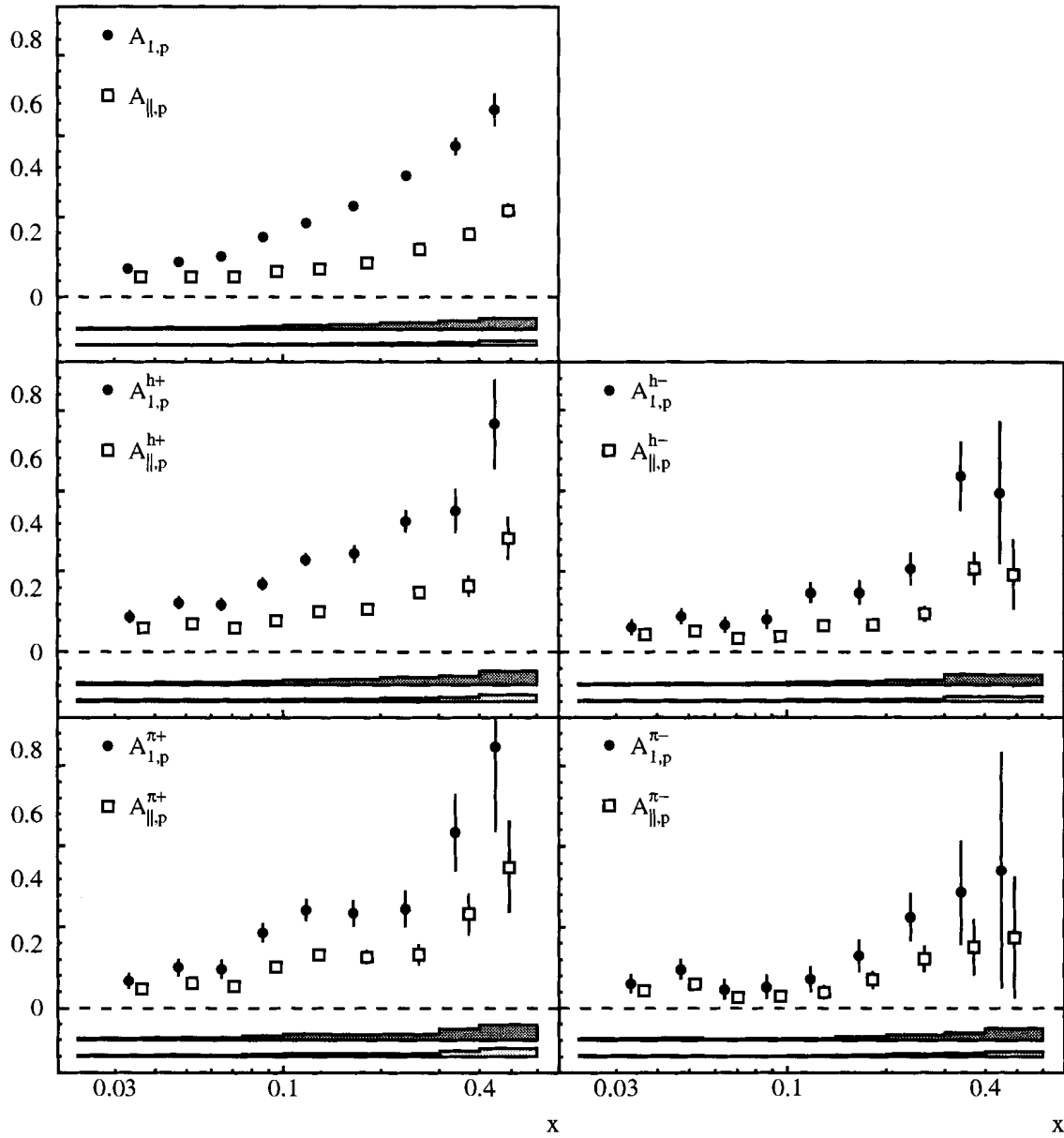
Figure 6.3: The measured positron-nucleon and photon-nucleon asymmetries $A_{\parallel}^{(h)}$ and $A_1^{(h)}$ on the proton. The error bars represent the statistical uncertainties. The shaded band is the systematic uncertainty on $A_{\parallel}^{(h)}$ and the open band is that on $A_1^{(h)}$. The asymmetries $A_{\parallel}^{(h)}$ are offset in x for presentation.
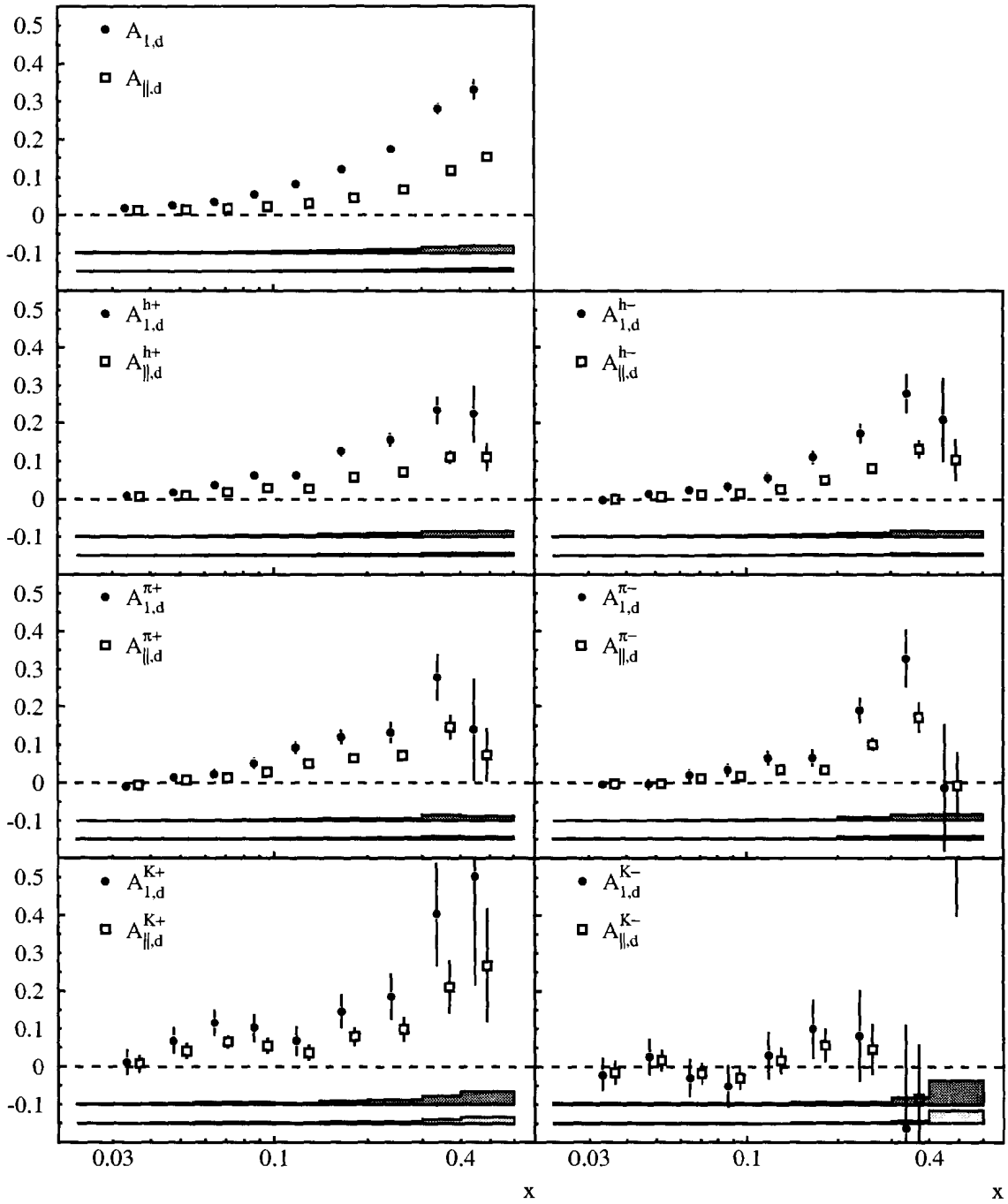
Figure 6.4: The measured positron-nucleon and photon-nucleon asymmetries $A_{\parallel}^{(h)}$ and $A_1^{(h)}$ on the deuteron. See Fig. 6.3 for explanations.

Target polarization. The determination of the target polarization makes use of measurements of the polarization of the atomic fraction in the target gas, the degree of molecular recombination and various other factors [84, 131]. In the case of the target polarizations, for the data-taking periods 1996, and 1998 and 1999, the polarizations were determined in a normalization of the inclusive asymmetry to the asymmetry measured in 1997 and in 2000 respectively [85]. The target polarizations and their uncertainties are summarized in Tab. 3.2. The associated uncertainty on the asymmetries is given by

$$\sigma_{P_T}\left(A^{(h)}_{\|,1}\right) = \left| \frac{\langle \sigma\left(P_z\right)\rangle}{\langle P_z\rangle} A^{(h)}_{\|,1} \right|. \tag{6.16}$$

Due to the normalization procedure, the determination of the target polarization is 100 % correlated for the same target types. The uncertainty on the target polarization applies to $A^{(h)}_{\|}$ and $A^{(h)}_1$.

Beam polarization. The beam polarization was measured with the transverse polarimeter (TPOL) in 1996 through 1998. Since 1997 the measurement of the longitudinal polarimeter (LPOL) was used during time-periods when a reliable measurement by the TPOL was not available. The relative systematic uncertainty on the measurement by the TPOL is 3.4 %. This uncertainty was assigned to the data collected in 1996 through 1998. It was assumed to be 100 % correlated between years because of the full correlation of the uncertainty on the calibration of the TPOL which is the main source of uncertainty (see Sec. 3.2.1).

Since 1999 the LPOL is mainly used for the beam polarization measurement. The associated systematic uncertainty is $\sigma\left(P_B\right)/P_B = 1.6\%$ [76]. The total uncertainty weighted for the time periods when the LPOL or the TPOL were used amounts to $\sigma(P_B)/P_B = 1.8\%$ in 1999 and $\sigma(P_B)/P_B = 1.9\%$ in 2000 (see Tab. 3.1). The uncertainty was assumed to be maximally correlated for 1999 and 2000.

Analogously to the target polarization measurement, the uncertainty on the asymmetries due to the beam polarization measurement is

$$\sigma_{P_B}\left(A^{(h)}_{\|,1}\right) = \left| \frac{\sigma(P_B)}{P_B} A^{(h)}_{\|,1} \right|. \tag{6.17}$$

This uncertainty applies to $A^{(h)}_{\|}$ and $A^{(h)}_1$.

Particle identification. Systematic uncertainties on the counts of positrons/electrons, unclassified hadrons, pions, and kaons in principle lead to a systematic uncertainty on the asymmetries. In the

case of the identification of leptons and hadrons, the inclusive and semi-inclusive asymmetries were found to be very stable with respect to changes, for example the omission of flux factors (Fig. 5.4). Variations in the asymmetries were also found to be small when older particle identification schemes (see *e.g.* [132]) or simply the detector cuts defined in Tab. 5.1 were used in the analysis. The broad minimum between the hadron and the lepton peak in the PID distributions, *cf.* Fig. 5.5, suggests that any systematic effects leading to a shift in the distribution have negligible impact on the particle counts, which further reduces in the asymmetries. As shown in Ch. 5 contaminations of the hadron and lepton samples are also negligible. A systematic uncertainty on the asymmetries due to the lepton-hadron discrimination was therefore neglected.

Uncertainties on the pion asymmetries measured with the help of the threshold Čerenkov were neglected for similar reasons. Small mis-calibrations of the detector leave the separation of hadrons into those that generate a signal in the detector (pions) and other hadrons in the given momentum range virtually unaffected. Contaminations of the pion sample are negligible.

A systematic uncertainty on the pion and kaon asymmetries extracted with the help of the RICH was also not included. The uncertainty on the RICH hadron identification was estimated to be small with little impact on the semi-inclusive asymmetries (see Sec. 6.3.3). As described in Sec. 5.2 contaminations and efficiencies were explicitly included in the particle count numbers through the weighting with the inverse $\mathcal{P}$-matrix elements.

Azimuthal acceptance correction. The azimuthal acceptance correction discussed in Sec. 6.2.2 is based on an analysis of HERMES data. The functional form of the parameterizations fitted to the data is motivated by the effective theory given in Ref. [126]. The systematic uncertainty was estimated to be $\sigma(C_\phi^h) = 2\%$ [127]. The corresponding uncertainty on the asymmetries is

$$\sigma_\phi\left(A_{\parallel,1}^h\right) = \left|\sigma(C_\phi^h)\, A_{\parallel,1}^h\right| \tag{6.18}$$

This uncertainty applies to the semi-inclusive asymmetries $A_\parallel^h$ and A_1^h only. It was assumed to be uncorrelated between the various types of semi-inclusive asymmetries.

The ratio $R = \sigma_L/\sigma_T$. In the calculation of the photon-nucleon asymmetries $A_1^{(h)}$, uncertainties arise from the parameterization of the ratio $R = \sigma_L/\sigma_T$ which is used in the calculation of the depolarization factor D. The parameterization and the data from which it was derived are shown in Fig. 2.5. The uncertainty on the parameterization given in Ref. [16] is about 6\% in the kinematic

range covered in this analysis. The uncertainty on the asymmetries $A_1^{(h)}$ follows from Eq. (2.64) and Eq. (2.65):

$$\sigma_R\left(A_1^{(h)}\right) = \left| \frac{\epsilon}{1 + \epsilon R} \sigma(R) \, A_1^{(h)} \right| \tag{6.19}$$

It is 100 % correlated between all data-taking years.

The structure function g_2. As described in Sec. 2.6 the structure function g_2 is assumed to be zero in this analysis. Upper limits on the systematic uncertainty of this assumption are shown as the solid lines in Fig. 2.9 for the proton and the deuteron. These simple functions of the form $\hat{g}_{2p}(x) = \pm 0.035 \, x^{-1} \, (1-x)^{0.7}$ and $\hat{g}_{2d}(x) = \pm 0.015 \, x^{-1} \, (1-x)^{0.9}$ are a limiting estimate for the deviation from $g_2 = 0$. They envelop the available data which were measured at a Q^2-scale similar to that of the HERMES experiment, $1.3 \, \mathrm{GeV}^2 < Q^2 < 10 \, \mathrm{GeV}^2$ (E143) and $1.0 \, \mathrm{GeV}^2 < Q^2 < 30 \, \mathrm{GeV}^2$ (E155).

From Eqs. (2.62) and (2.63) the asymmetries $A_1^{(h)}$ and the ratio $g_1^{(h)}/F_1^{(h)}$ for non-vanishing g_2 are:

$$A_1^{(h)} = \frac{1}{(1 + \eta\gamma) \, D} \, A_\parallel^{(h)} - \frac{\eta\gamma \, (1 + \gamma^2)}{1 + \eta\gamma} \, \frac{g_2^{(h)}}{F_1^{(h)}} \,, \tag{6.20}$$

$$\frac{g_1^{(h)}}{F_1^{(h)}} = \frac{1}{(1 + \eta\gamma) \, D} \, A_\parallel^{(h)} + \frac{\gamma \, (\gamma - \eta)}{1 + \eta\gamma} \, \frac{g_2^{(h)}}{F_1^{(h)}} \,. \tag{6.21}$$

Therefore the uncertainty for the asymmetries $A_1^{(h)}$ with $\sigma\left(g_2^{(h)}(x)\right) = |\hat{g}_2(x)|$ is

$$\sigma_{g_2}\left(A_1^{(h)}\right) = \left| \frac{\eta\gamma \, (1 + \gamma^2)}{1 + \eta\gamma} \, \frac{\hat{g}_2(x)}{F_1(x)} \right| \,, \tag{6.22}$$

where F_1 is computed with the parameterization of F_2 given in Ref. [133] via Eq. (2.21). This uncertainty was assigned to the observed asymmetries shown in Figs. 6.3, 6.4 and the Born asymmetries shown in Figs. 7.8, 7.9. However, in the determination of the polarized quark densities presented in Ch. 8 the relevant quantities are the ratios $g_1^{(h)}/F_1^{(h)}$. The uncertainty due to g_2 for this ratio follows from Eq. (6.21),

$$\sigma_{g_2}\left(g_1^{(h)}/F_1^{(h)}\right) = \left| \frac{\gamma \, (\gamma - \eta)}{1 + \eta\gamma} \, \frac{\hat{g}_2(x)}{F_1(x)} \right| \,. \tag{6.23}$$

The kinematic factor $\gamma \, (\gamma - \eta)$ reduces the uncertainty on this latter ratio by a factor between $0.002 \ldots 0.021$, while the uncertainty on the asymmetry is only scaled by a factor $0.001 \ldots 0.167$.

The same uncertainty is assigned to the inclusive asymmetries A_1 and the semi-inclusive asymmetries A_1^h, because measurements of the structure function g_2^h are not available. The uncertainty due to g_2 is maximally correlated between all years.

Total systematic uncertainty. The systematic uncertainties arising from the various sources were added in quadrature to yield the total systematic uncertainty,

$$\sigma_{tot}^{sys}\left(A_{\parallel,1}^{(h)}\right) = \sqrt{\sum_i \left[\sigma_i\left(A_{\parallel,1}^{(h)}\right)\right]^2}. \tag{6.24}$$

As noted above the systematic uncertainty on $A_\parallel$ is due to the uncertainties of the beam and target polarization measurements only. The systematic uncertainty on the semi-inclusive asymmetries $A_\parallel^h$ includes additionally the uncertainty due to the determination of the azimuthal acceptance correction.

6.3 Systematic Studies

6.3.1 Compatibility of Data-Taking Periods
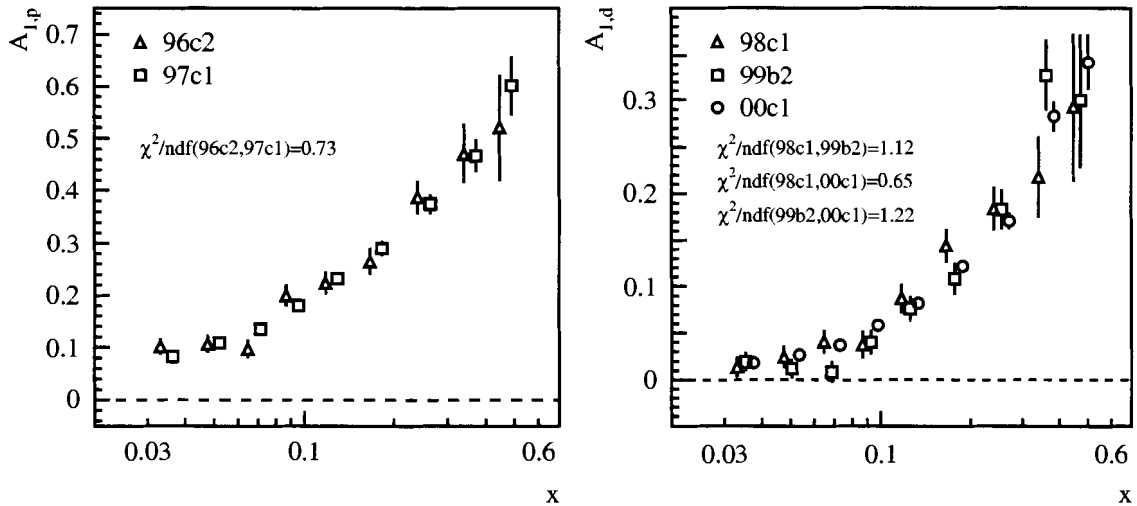
Figure 6.5: Left: The inclusive proton asymmetries computed from the 96c2 and 97c1 productions. Right: The inclusive deuteron asymmetries of the 98c1, 99b2, and 00c1 productions. The asymmetries of the 96c2, 99b2, and the 00c1 productions are offset in x for presentation.

$\chi^2/(ndf = 9)$	97c1	99b2	00c1
96c2 A_{1p}	0.73		
96c2 $A_{1p}^{\pi^+}$	0.40		
96c2 $A_{1p}^{\pi^-}$	0.50		
98c1 A_{1d}		1.12	0.65
98c1 $A_{1d}^{\pi^+}$		1.14	0.66
98c1 $A_{1d}^{\pi^-}$		0.64	1.02
98c1 $A_{1d}^{K^+}$		0.60	0.81
98c1 $A_{1d}^{K^-}$		0.58	0.69
99b2 A_{1d}			1.22
99b2 $A_{1d}^{\pi^+}$			0.93
99b2 $A_{1d}^{\pi^-}$			1.07
99b2 $A_{1d}^{K^+}$			0.70
99b2 $A_{1d}^{K^-}$			0.51
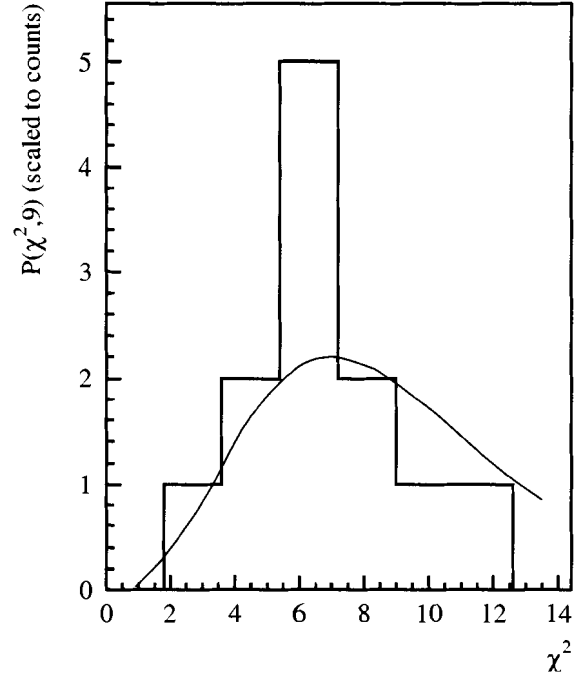
Figure 6.6: The χ^2 values of all asymmetries of the data productions. The table lists the reduced values χ^2/ndf with $ndf = 9$ for asymmetries of the same target and type. The plot shows a histogram of the χ^2 values compared to the expected χ^2 distribution for 9 degrees of freedom. The distribution was scaled to the histogram entries. The χ^2 values for the comparison of the asymmetries in 98c1 and 99b2 were not included in the histogram to avoid double counting.

As mentioned, the proton asymmetries stem from the data productions 96c2 and 97c1 of 1996 and 1997, and the deuteron asymmetries from the data productions of 98c1, 99b2, and 00c1 of 1998 through 2000. Variations in the experimental setup and the pre-processing of the data can in principle introduce bias in the asymmetries. Fig. 6.5 compares the inclusive asymmetries A_{1p} and A_{1d} determined from the respective data productions. The χ^2 values for the inclusive asymmetries as well as for the various semi-inclusive asymmetries are listed in Fig. 6.6. They are in the expected range. A histogram of the χ^2 values also shown in the figure is superimposed with a scaled χ^2 distribution for $ndf = 9$ degrees of freedom, which follows from the number of x-bins. The distribution is in good agreement with the histogram. The observed fluctuations in the asymmetries are therefore statistical. Note that, due to the almost complete correlation of the systematics on the asymmetries for the same target (see Sec. 6.2.5), the systematic uncertainties were not included in this study.

6.3.2 Beam Helicity Dependence of the Asymmetries

The beam helicity of the HERA positron ring was reversed several times during the five years of data-taking. The helicity was reversed after the 1996 running period, twice in 1997 and routinely about once a month in 1999 and 2000.

The asymmetries averaged over the measured range $0.023 < x < 0.6$ are shown in Fig. 6.7. The averaged asymmetries were fitted with a constant as indicated by the solid line. The reduced χ^2 values of these fits which are also given in the figure, are within the expectation. There is therefore no indication of a dependence of the asymmetries on the beam helicity due to instrumental effects or unexpected physical mechanisms. Furthermore there is no indication of a time-dependence of the measured asymmetries.

6.3.3 Hadron Identification with the RICH

For the semi-inclusive deuteron asymmetries, pions and kaons were identified using the ring imaging Čerenkov detector. Contaminations and efficiencies of the identification scheme were included in the $\mathcal{P}$-matrix, as outlined in the Sec. 5.2. The asymmetries calculated using the inverse $\mathcal{P}$-matrix are compared with asymmetries without the $\mathcal{P}^{-1}$-weighting in Fig. 6.8. The positive and negative pion asymmetries are virtually unaffected, because the RICH is highly efficient in the identification of pions. The differences in the kaon asymmetries are also small compared to the statistical uncertainties. The neglection of the efficiencies and contaminations by disregarding the $\mathcal{P}$-matrix represents an upper estimate of the potential variation in the $\mathcal{P}$-matrix elements due to systematic effects. As a more precise estimate of the uncertainties was not available at the time of this thesis, no systematic uncertainties due to the RICH identification were included in the uncertainties on the asymmetries.
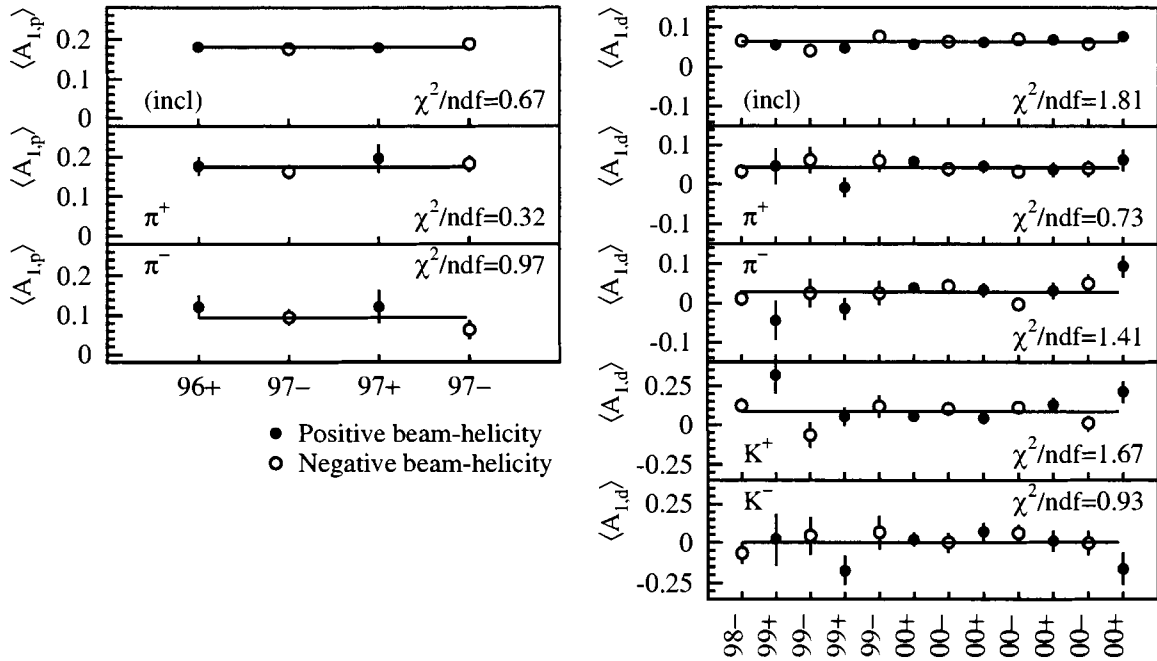
Figure 6.7: Proton and deuteron asymmetries integrated over $0.023 < x < 0.6$ for periods with one beam helicity state. The '+' and '−' signs indicate the positive and negative beam helicity of the respective periods. The data are presented as a function of time. The error bars shown are statistical.
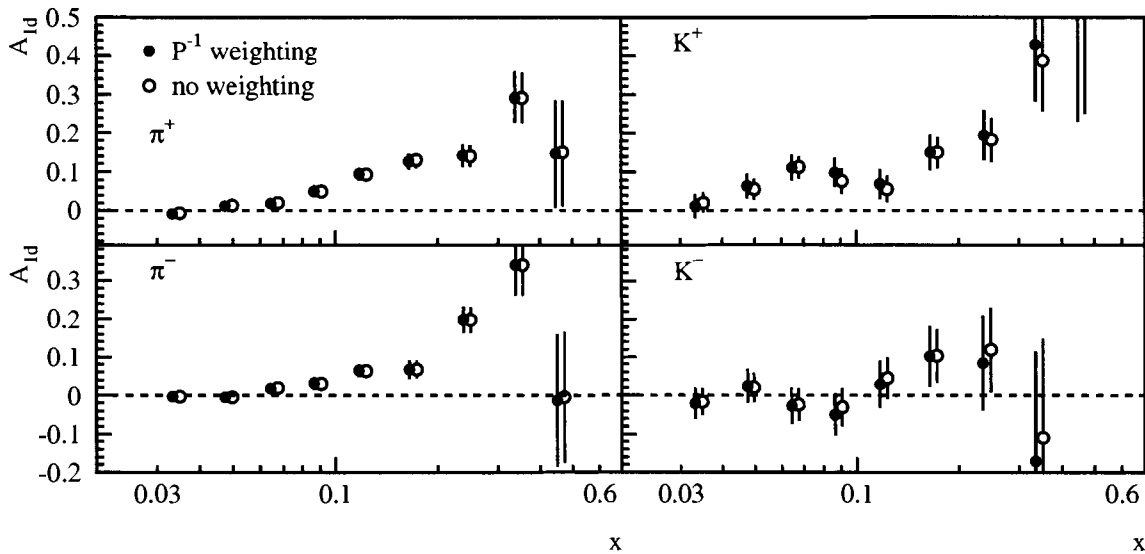
Figure 6.8: Pion and kaon asymmetries on the deuteron with and without $\mathcal{P}^{-1}$-matrix weighting. The latter asymmetries are offset in x for presentation. Systematic uncertainties are not shown.

Chapter 7

The Born Asymmetries

The asymmetries presented in the previous chapter are subject to instrumental and QED processes beyond lowest order in α. The physical quantities of interest, however, are the asymmetries of the two DIS processes shown in Fig. 2.10. The measured asymmetries therefore have to be corrected in order to find these lowest order or Born asymmetries. This chapter first discusses the two sources for which corrections are applied, namely higher-order QED effects and detector smearing effects. In the second part, the unfolding algorithm that was used to correct the asymmetries is introduced, followed by a presentation of the Born asymmetries.

7.1 QED Radiative Effects

The cross section expressions discussed in Ch. 2 are based on first-order QED, which is commonly referred to as the Born level. However, in the measured inclusive and semi-inclusive asymmetries higher order QED processes also contribute. The mediation of the scattering reaction through a Z–boson is not relevant at HERMES energies. Fig. 7.1 shows the three second-order Feynman diagrams that change the lowest order process, which is also shown. Figs. 7.1a and 7.1b are the diagrams of initial and final state bremsstrahlung that change the kinematics of the initial and the final state electron, respectively. The vertex correction shown in Fig. 7.1c alters the anomalous magnetic moment, whereas the vacuum polarization diagram depicted in Fig. 7.1d reduces the total cross section.

While the latter two diagrams affect the overall normalization of the cross section, the bremsstrahlung processes affect the direct connection of the measured kinematics of the initial and scat-
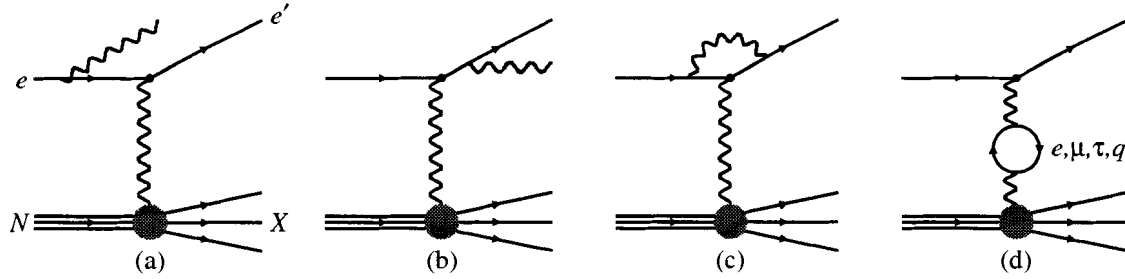
Figure 7.1: Second order QED radiative corrections for the deep-inelastic scattering process.

tered electron with the kinematics of the virtual photon at the hadronic vertex. This effect is illustrated in Fig. 7.2 for final state bremsstrahlung. The scattered electron emits a photon and conse-

Measured		Born
$\nu_X = (E - E')$	$\geq$	$\nu_B = (E - (E' + \omega_0))$
$Q_X^2 = 4EE' \sin^2 \dfrac{\theta_X}{2}$	$\leq$	$Q_B^2 = 4E(E' + \omega_0) \sin^2 \dfrac{\theta_B}{2}$
$x_X = \dfrac{Q_X^2}{2M\nu_X}$	$\leq$	$x_B = \dfrac{Q_B^2}{2M\nu_B}$
$W_X^2 = M^2 + 2M\nu_X - Q_X^2$		$W_B^2 = M^2 + 2M\nu_B - Q_B^2$
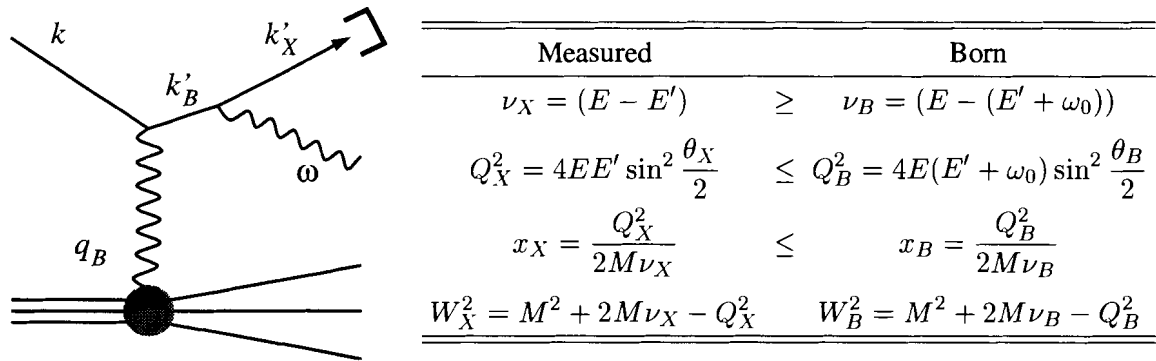
Figure 7.2: Diagram and kinematics of final state bremsstrahlung. The diagram illustrates the emission of an undetected photon with 4–momentum ω before the detection of the scattered electron. The table on the right hand side lists the kinematics calculated from the observed electron (labelled X) and the kinematics of the virtual photon, *i.e.* the Born kinematics (labelled B). These expressions are similar in the case of initial state bremsstrahlung.

quently the measured kinematics merely allow to calculate the experimental kinematics ν_X, Q_X^2 etc. The connection of these kinematics to the Born kinematics, *i.e.* those of the virtual photon, or those of a Born process with a virtual photon with the same energy are given in the table of Fig. 7.2. The measured value of the energy transfer ν_X is larger than the energy of the virtual photon ν_B. Q_X^2 and x_X are smaller than their Born counterparts. There is no such inequality for W^2. This discussion is analogous for initial state bremsstrahlung and the expressions for the measured and the Born kinematics are identical except for $Q_B^2 = 4(E - \omega_0)E' \sin^2(\theta_B/2)$.

The event kinematics derived from the initial and the scattered electron therefore differ in general

from the kinematics of the virtual photon with which the nucleon structure is probed. In fact, through the emission of bremsstrahlung photons an elastic or inelastic scattering event can appear to be a deep-inelastic scattering event by the measured kinematics. The contributions of these events to the measured scattering cross section are referred to as elastic and inelastic tails. The total cross section of the DIS process including higher order QED effects is therefore

$$\sigma_X = \sigma_{elas} + \sigma_{qela} + \sigma_{inel},$$ (7.1)

where σ_{elas} is the elastic tail and σ_{qela} the quasi-elastic tail that describes scattering off a nucleon in a nucleus with more than one nucleon[1]. The cross section σ_{inel} is the inelastic cross section that includes the deep-inelastic contribution. Contributions from vacuum polarization and vertex corrections are also included in σ_{inel}. To second order these corrections do not arise in σ_{elas} and σ_{qela}.

In the case of semi-inclusive events, the detection of a final state hadron eliminates the elastic and quasi-elastic tails from the measured cross section, because no hadrons are produced in these processes. Radiative corrections to the semi-inclusive cross section are therefore smaller, although the measurement is still subject to bremsstrahlung and loop corrections of the inelastic cross section σ_{inel}.

The higher order QED effects shown in Fig. 7.1 are independent of the spin of the electron or the target nucleon. However, the radiative corrections become spin-dependent through the spin-dependence of the elastic, quasi-elastic, and inelastic cross sections. The asymmetries of these subprocesses at the measured kinematics are presented in Sec. 7.5.

The radiative corrections discussed here are implemented in POLRAD [134, 135], a program that calculates radiative corrections to inclusive and semi-inclusive polarized DIS cross section. The Monte Carlo generator RADGEN [136] which is based on POLRAD, is used in the HERMES Monte Carlo simulation [137]. A description of the algorithm used in RADGEN is included in the discussion of the HERMES Monte Carlo simulation below.

7.2   Detector Effects

The second class of corrections to the Born cross section arises from interactions of the final state particles with material in the target and the spectrometer. A track passing through any material

---

[1]In the case of hydrogen, $\sigma_{qela} = 0$

undergoes multiple scattering. This effect causes the front and back-tracks to deviate from the straight lines that are assumed in the tracking algorithm. In the case of the front-track, multiple scattering impacts the determination of the scattering angle. In combination with the back-track, the determination of the track momentum through matching the two partial tracks is also compromised. In addition, imperfect calibrations and deviations in the alignment of the tracking detectors lead to systematic bias in the measured track parameters with respect to the true values. While QED radiative effects lead to a larger energy transfer ν_X with respect to ν_B, detector smearing effects frequently result in a larger measured energy of the scattered electron and thus a smaller ν_X. Hence, the inequalities given in Fig. 7.2 hold only approximately when both QED radiative effects and detector smearing effects are taken into account.

Detector effects are simulated in a Monte Carlo simulation of the entire detector using the GEANT toolkit [138]. GEANT (geometry and tracking) is a comprehensive software package that simulates the passage of particles through matter using Monte Carlo techniques. The simulation of the HERMES target and the spectrometer based on GEANT is included in the HERMES Monte Carlo simulation.

7.3 Finite Bin Size Effects

A secondary effect that is a result of detector smearing and QED radiative processes is due to the finite bin size of the measurement (see Tab. 6.3). Differences in the distribution of Born events within a bin with respect to the distribution of the measured events lead to different average values of x_B and x_X within a given x-bin. Analogously, the average Q^2-values and the other kinematic quantities are affected by these differences in the cross sections.

7.4 Unfolding Kinematic Migration

The detector smearing and QED radiative effects were corrected using an unfolding algorithm [139]. The principal idea is to correct the measured asymmetries for the kinematic migration and cross section renormalization in the parallel $(+)$ and the anti-parallel $(-)$ state based on matrices

$$\mathcal{S}_\pm(i,j) \equiv \frac{\partial \sigma_\pm^X(i)}{\partial \sigma_\pm^B(j)}, \qquad i = 1, \ldots N_X, \; j = 1, \ldots N_B. \tag{7.2}$$

that give the contribution to the measured cross section in a given bin $i = 1, \ldots N_X$ by the Born cross section in bin $j = 1, \ldots N_B$, where N_X and N_B are the number of experimental and Born bins, respectively. Eq. (7.2) holds under the assumption that higher order derivatives involving amplitudes are negligible. Additional contributions to the measured asymmetries that arise from background processes are simply subtracted.

The unfolding procedure relies on two sets of Monte Carlo data — a dataset (the Born dataset) that stems from a simulation of the Born process only and a dataset (the tracked data) that includes higher order QED processes, the detector simulation, and the tracking algorithm. In the latter case, the kinematics of the underlying Born process in each event have to be available as well. Based on the tracked Monte Carlo data, $N_X \times (N_B + 1)$ matrices $n_\pm(i, j)$ can be constructed for the parallel and anti-parallel spin state, that describe the count rates that fall in both bin j of Born kinematics and bin i of experimental kinematics. The bins $j = 1, \ldots N_B$ describe the migration of DIS events, where both the experimental and the Born kinematics are within the acceptance. Here, acceptance refers to both the geometrical acceptance of the spectrometer and the phase space defined by the DIS and SIDIS cuts. The additional bin $j = 0$ contains background rates that feed into the experimental bins through QED radiative and detector smearing effects. For example, in the case of the inclusive data sample on the proton, the background stems from elastic and inelastic scattering events that are radiated (through QED effects) or smeared (by interactions in the detector) into the acceptance. The experimental rates in the parallel and anti-parallel spin state in bin i as estimated by the Monte Carlo are given by the sum

$$n_\pm^X(i) = \sum_{j=0}^{N_B} n_\pm(i, j), \qquad i = 1, \ldots N_X. \tag{7.3}$$

The corresponding Born rates, $n_\pm^B(j)$, in each spin state and bin $j \neq 0$ can be calculated from the Born Monte Carlo data. The Born rates cannot be obtained from $n_\pm(i, j)$ by summing over the experimental bins i, because QED radiative processes change the normalization of the cross section and because of Born events that are radiated out of the acceptance or are undetected due to detector inefficiencies. Note that the Born rates and the experimental rates have to be normalized such that they represent cross sections in order to incorporate them in the algorithm described in the following.

The Monte Carlo rates $n_\pm(i, j)$ and $n_\pm^B(j)$ allow to estimate the event migration defined in Eq. (7.2),

$$\mathcal{S}_\pm(i, j) = \frac{n_\pm(i, j)}{n_\pm^B(j)}, \qquad i = 1, \ldots N_X, \; j = 1, \ldots N_B. \tag{7.4}$$

These matrices do not bias the asymmetry measurement by the Monte Carlo model for the Born distributions, because both the numerator and the denominator scale with the relative number of Born events generated in each bin j.

The measured asymmetries presented in Ch. 6 have the simple form

$$A_{\parallel}^X(i) = \frac{X_-(i) - X_+(i)}{X_-(i) + X_+(i)}, \qquad i = 1, \ldots N_X, \tag{7.5}$$

where $X_\pm(i)$ represent the effective rates normalized for luminosity and polarization in the (anti-) parallel orientation as measured in the experiment. The sought-after Born asymmetry $A_{\parallel}^B$ is similarly given by

$$A_{\parallel}^B(j) = \frac{B_-(j) - B_+(j)}{B_-(j) + B_+(j)} = \frac{B_-(j) - B_+(j)}{n_-^B(j) + n_+^B(j)}, \qquad j = 1, \ldots N_B, \tag{7.6}$$

where $B_\pm(j)$ are the rates of the Born distributions that give rise to the measured rates $X_\pm(i)$. The last expression in Eq. (7.6) holds under the assumption that the Monte Carlo simulation correctly reproduces the unpolarized Born cross section,

$$B_u(j) \equiv B_+(j) + B_-(j) = n_+^B(j) + n_-^B(j) \equiv n_u^B(j), \qquad j = 1, \ldots N_B. \tag{7.7}$$

The experimental asymmetry $A_{\parallel}^X$ can be rewritten in terms of the Born rates, the migration matrices, the unpolarized experimental rates, and the polarized background $n_p(i,0) \equiv n_-(i,0) - n_+(i,0)$,

$$A_{\parallel}^X(i) = \frac{k(i) \sum_{j=1}^{N_B} \left[S_-(i,j) B_-(j) - S_+(i,j) B_+(j) \right]}{k(i) \, n_u^X(i)} + \frac{k(i) \, n_p(i,0)}{k(i) \, n_u^X(i)}, \qquad i = 1, \ldots N_X. \tag{7.8}$$

The additional factor $k(i)$ is a normalization constant that takes into account unsimulated detector inefficiencies and other polarization and j-independent effects not incorporated in the Monte Carlo simulation. The second term in Eq. (7.8) represents the background asymmetry estimated by the simulation.

An expression for the Born asymmetry is found by eliminating the rate $B_+(j)$ in favour of $B_-(j)$ and $B_u(j)$ and rearranging Eq. (7.8),

$$\sum_{j=1}^{n_B} \left[S_-(i,j) + S_+(i,j) \right] B_-(j) =$$

$$A_{\parallel}^X(i) \, n_u^X(i) - n_p(i,0) + \sum_{j=1}^{N_B} S_+(i,j) \, n_u^B(j), \qquad i = 1, \ldots N_X. \tag{7.9}$$

The Born asymmetry given by $A_{\parallel}^{B}(j) = [2B_-(j) - B_u(j)]/B_u(j)$, is then

$$A_{\parallel}^{B}(j) = -1 + \frac{2}{n_u^{B}(j)} \sum_{i=1}^{N_X} [\mathcal{S}]^{-1}(j,i) \times$$

$$\left[A_{\parallel}^{X}(i)\, n_u^{X}(i) - n_p(i,0) + \sum_{k=1}^{N_B} \mathcal{S}_+(i,k)\, n_u^{B}(k) \right], \qquad j = 1,\ldots N_B, \tag{7.10}$$

where $n_u^{B}(j) \equiv n_-^{B}(j) + n_+^{B}(j)$ and $\mathcal{S}(i,j) \equiv \mathcal{S}_-(i,j) + \mathcal{S}_+(i,j)$. This expression holds for the inclusive and the semi-inclusive asymmetries presented in Ch. 6. It can be used for any kind of kinematic binning. However, Eq. (7.10) is restricted to $N_X = N_B$ due to the matrix inversion.

The statistical covariance matrix of the Born asymmetry follows from Eq. (7.10) with the statistical uncertainties on $A_{\parallel}^{X}$ given by Eq. (6.11),

$$V\left(A_{\parallel}^{B}(j), A_{\parallel}^{B}(k) \right) = \sum_{i=1}^{N_X} \mathcal{D}(j,i)\mathcal{D}(k,i)\, \sigma^2\left(A_{\parallel}^{X}(i) \right), \tag{7.11}$$

where $\mathcal{D}(j,i)$ is the dilution matrix,

$$\mathcal{D}(j,i) \equiv \frac{\partial A_{\parallel}^{B}(j)}{\partial A_{\parallel}^{X}(i)} = \frac{2\mathcal{S}^{-1}(j,i)\, n_u^{X}(i)}{n_u^{B}(j)}. \tag{7.12}$$

The inclusive and semi-inclusive asymmetries are correlated with each other, as shown in Eq. (6.13). The covariance for two types of asymmetries is augmented with the corresponding correlation:

$$V\left(A_{\parallel}^{B,\alpha}(j), A_{\parallel}^{B,\beta}(k) \right) = \sum_{i=1}^{N_X} \mathcal{D}(j,i)\mathcal{D}(k,i)\, V\left(A_{\parallel}^{X,\alpha}(i), A_{\parallel}^{X,\beta}(i) \right), \tag{7.13}$$

where α and β label the respective inclusive and semi-inclusive asymmetries. The covariance on the measured asymmetries follows from the correlation in Eq. (6.13) and the respective uncertainties given by Eq. (6.11).

The Born asymmetry A_1^{B} follows from $A_{\parallel}^{B}$ by Eq. (2.66):

$$A_1^{B}(j) = \frac{1}{[(1 + \eta\gamma)D]_j}\, A_{\parallel}^{B}(j). \tag{7.14}$$

Similarly the covariance is

$$V\left(A_1^{B,\alpha}(j), A_1^{B,\beta}(k) \right) = \left| \frac{1}{[(1+\eta\gamma)D]_j} \frac{1}{[(1+\eta\gamma)D]_k} \right| V\left(A_{\parallel}^{B,\alpha}(j), A_{\parallel}^{B,\beta}(k) \right). \tag{7.15}$$

In both expressions the factors η, γ, and D are calculated at the Born kinematics x_B and y_B in bin j and in the case of the covariance also in bin k. The Born kinematics are related to the measured kinematics through a bin-centering-correction to account for the finite bin size effect mentioned in Sec. 7.3. The correction based on an estimate using the HERMES Monte Carlo simulation is given by,

$$x_B = \frac{x_B^{MC}}{x_X^{MC}} \, x_X, \qquad y_B = \frac{y_B^{MC}}{y_X^{MC}} \, y_X, \tag{7.16}$$

where MC labels the average values determined from the Born Monte Carlo data (x_B^{MC} and y_B^{MC}) and the tracked Monte Carlo data (x_X^{MC} and y_X^{MC}). The other kinematic variables follow from these two independent quantities. In the case of the semi-inclusive measurements, z_B and $x_{F,B}$ are obtained in the same way.

7.5 The HERMES Monte Carlo Simulation

7.5.1 The Algorithm

The Born Monte Carlo data and the tracked Monte Carlo data that are needed as input to the unfolding algorithm were generated with the HERMES Monte Carlo simulation. The simulation consists of three main parts: the generation of semi-inclusive DIS events, the generation of higher order QED processes and the simulation of the particle interactions with the spectrometer. In a final step, the detector signals are processed by the same tracking algorithm used in the experiment (cf. Sec. 3.5.1).

The tracked Monte Carlo simulation. A DIS event is simulated by first randomly generating a (ν, Q^2) pair with a weight ω_B that reflects the Born cross section σ_B. The (ν, Q^2) pair is used in RADGEN to calculate the ratio of the cross section as given in Eq. (7.1) integrated over the loops and the bremsstrahlung photons to the Born cross section. The ratio is applied to ω_B to obtain a weight ω that reflects the experimental cross section.

Based on the cross section for the emission of bremsstrahlung, RADGEN randomly generates a bremsstrahlung photon and the kinematics of the virtual photon (ν_B, Q_B^2) are recalculated accordingly. The generated bremsstrahlung photon determines the type of event that follows from the kinematics of the virtual photon (ν_B, Q_B^2). The event is elastic, if $x_B = 1$, quasi-elastic (in the case of the deuteron) if $x_B = 2$, and inelastic or deep-inelastic, if $0 < x_B < 1$. JETSET generates

hadrons in the final state, if the process mediated by the virtual photon is inelastic or deep-inelastic. The event generation described so far is carried out in the Monte Carlo generator gmc_disNG.

The parameters of the final state particles are then passed to HMC, the GEANT simulation of the HERMES target and spectrometer. GEANT generates the particle interactions with the target and spectrometer materials and creates appropriate signals in the tracking and PID detectors. The simulated signals are finally used in the tracking algorithm. The tracked data are stored in files similar to the μDST's that hold the experimental data.

The Born Monte Carlo simulation. In this case, only the lowest order DIS process without detector effects has to be simulated. A generated (ν, Q^2) pair with weight ω_B is passed directly to JETSET for the generation of the final state hadrons.

The calculation of the inclusive Born count rate n_B from the tracked Monte Carlo data is in principle possible using the initial (ν, Q^2) pair and the weight ω_B. However, the semi-inclusive count rate of for example positive pions $n_B^{\pi^+}$ cannot be extracted from the tracked Monte Carlo data, because hadrons are generated using the kinematics (ν_B, Q_B^2) which are only indirectly related to ω_B and (ν, Q^2) through the kinematics of the bremsstrahlung photon and the ratio ω_X/ω_B. Therefore the weight that correctly describes the Born cross section at (ν_B, Q_B^2) is not available. In addition, the use of two independent Monte Carlo datasets for the Born and the tracked data guarantees the statistical independence of $n_B(j)$ and $n(i, j)$.

7.5.2 The Monte Carlo Datasets

Tracked Monte Carlo data and Born Monte Carlo data were generated for the hydrogen and the deuterium targets. The Monte Carlo parameters, specifically the LUND fragmentation parameters, were tuned to match the kinematics of the HERMES experiment [69]. The GRSV2000 parameterization [64] was used as input for the polarized parton densities.

The final Monte Carlo datasets for each target comprised an equivalent number of 3×10^6 fully tracked DIS events and 5×10^6 equivalent Born DIS events. The statistics were found to be sufficient to render the statistical uncertainties on the simulated migration matrices and background rates negligible.

A comparison of kinematic distributions normalized to the total number of DIS events is shown in Fig. 7.3. The inclusive Monte Carlo distributions are in good agreement with the data. In the

case of the invariant mass W^2 of semi-inclusive events, the agreement is not as good. The Monte Carlo simulation underestimates the z distribution of semi-inclusive hadrons at small values. For a detailed treatment of the Monte Carlo tuning procedure and more details on the performance of the Monte Carlo simulation, the reader is referred to [69].
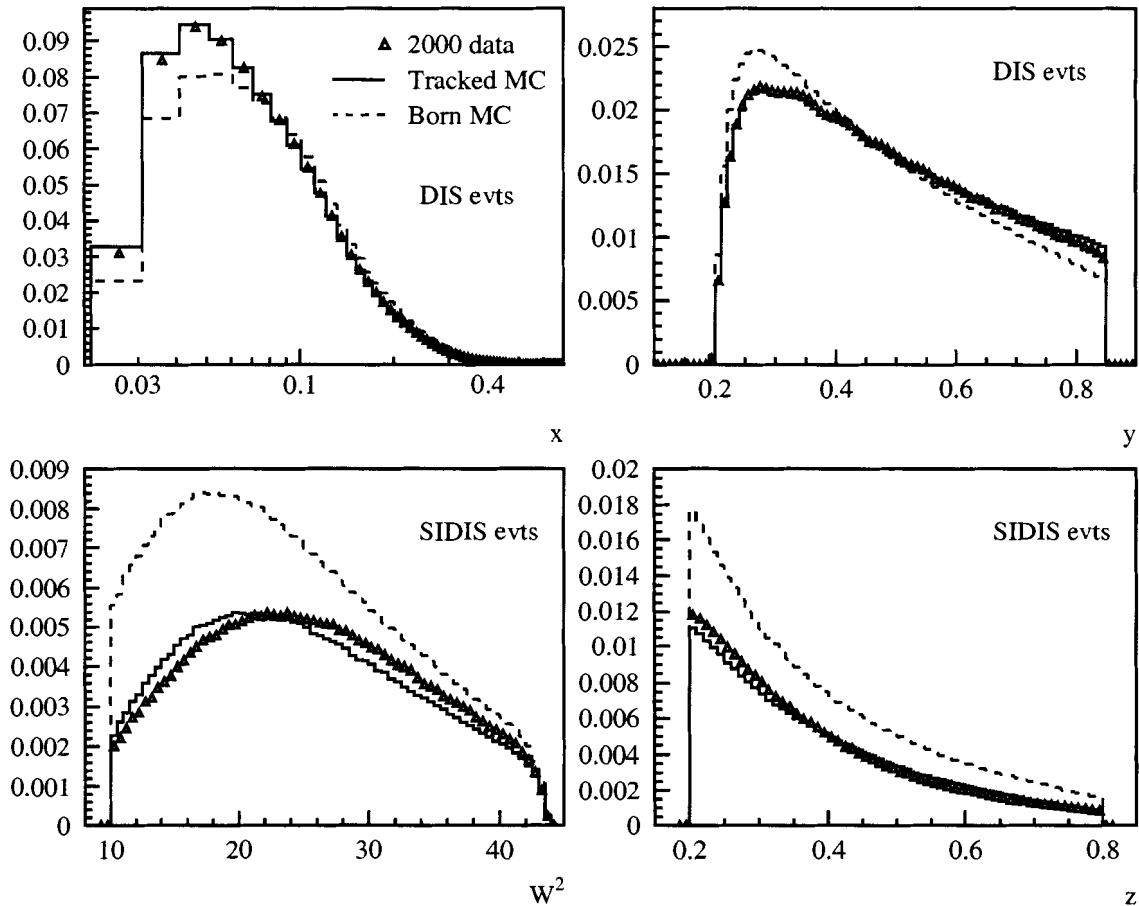
Figure 7.3: Comparison of Monte Carlo data on the deuteron with data collected in 2000.

Also shown in Fig 7.3 are the Born distributions, which exhibit the expected behaviour with respect to the experimental distributions (cf. Fig. 7.2). The Born distribution of x is shifted to larger values compared to x_X, and y_B is shifted to smaller values with respect to y_X. In the case of the semi-inclusive distributions, the mean W_B^2 is observed to be smaller than W_X^2. The mean of the z distribution is virtually unchanged. The largest difference in these distributions however is the normalization, which includes non-DIS events in the case of the experimental distribution.
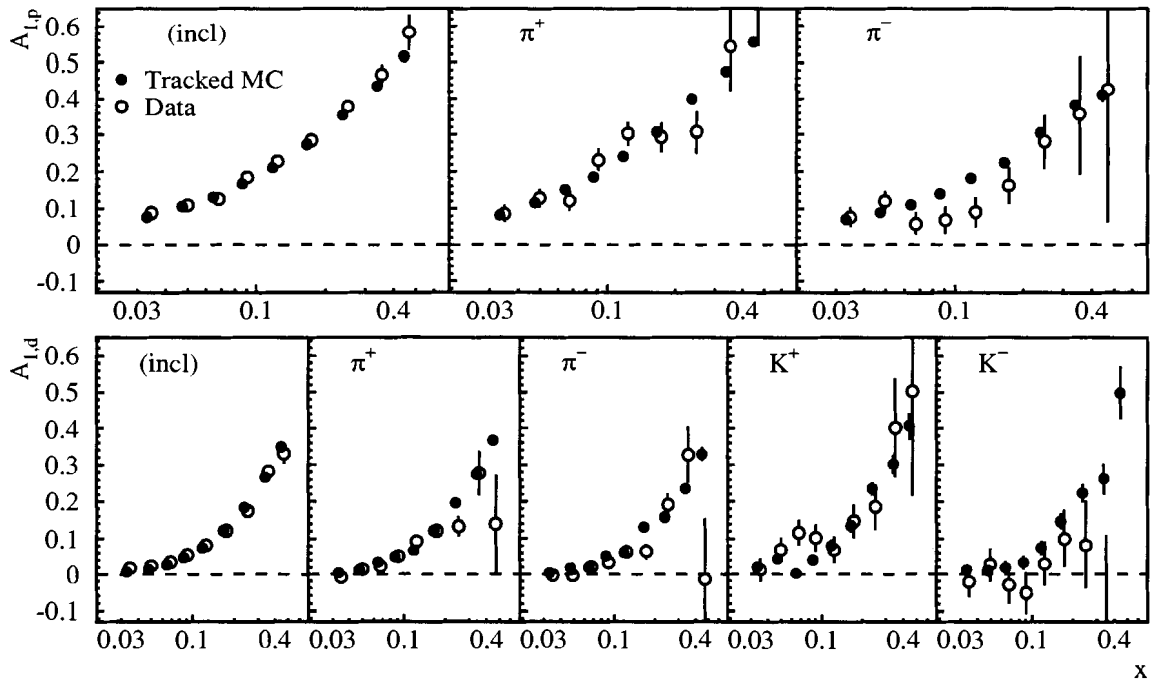
Figure 7.4: Asymmetries of the Monte Carlo simulation as function of x compared with the measured asymmetries calculated from HERMES data. The measured asymmetries are offset in x.
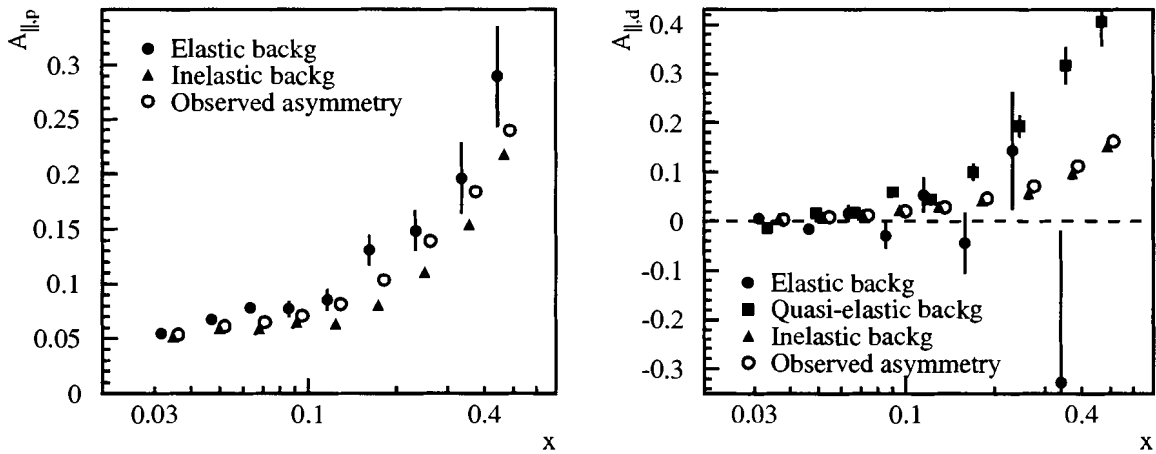
Figure 7.5: Monte Carlo asymmetries $A_{||}$ of the background processes. Left: The proton asymmetries of the elastic and inelastic background processes at apparent x. Right: The deuteron asymmetries of the elastic, quasi-elastic, and inelastic processes at apparent x. In each plot, the observed MC asymmetry is shown for comparison. All but the elastic asymmetries are offset in x.

The asymmetries calculated from the tracked Monte Carlo data are shown in Fig. 7.4. They are generally in agreement with the measured asymmetries presented in Ch. 6 that are also shown. In the case of the π^- asymmetry on the proton and the kaon asymmetries on the deuteron, some differences occur at intermediate x and also at large x in the case of $A_{1d}^{K^-}$. These differences are not understood at present. However, the unfolding procedure relies on the differences between the asymmetries of the tracked Monte Carlo data and the Born Monte Carlo data only (see Sec. 7.4). The absolute size of the Monte Carlo asymmetries is only important as an estimate of the background contribution that feeds into the acceptance. The asymmetries of these background processes are shown in Fig. 7.5. The asymmetry of the elastic tail on the proton and of the quasi-elastic tail on the deuteron is seen to be of similar size. The similarity is a result of analogous physical process — elastic scattering off a nucleon. The inelastic background asymmetry on both targets which is mostly comprised of events with low W_B^2 is of similar size as the total asymmetry. The elastic asymmetry on the deuteron is consistent with zero.
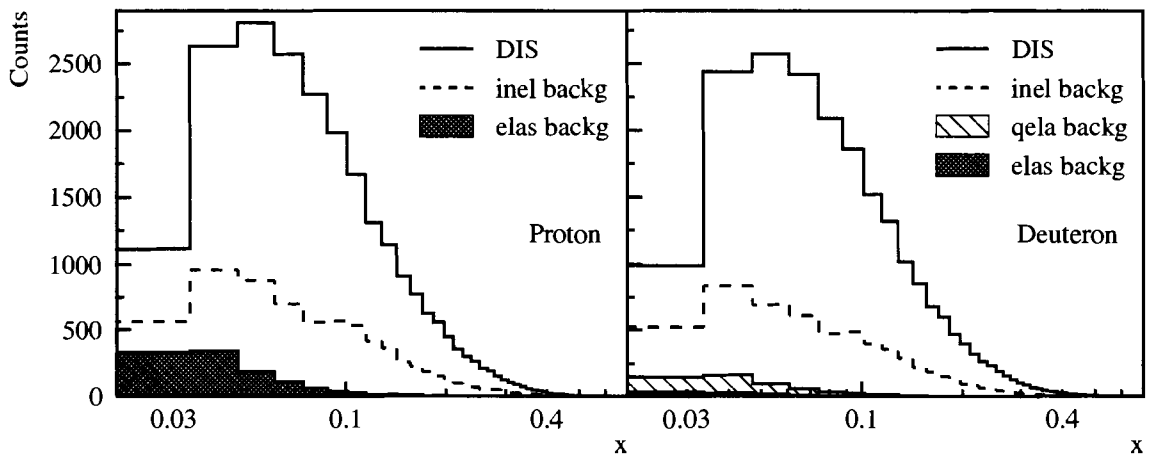
Figure 7.6: The rates of the background processes compared to the DIS rate. The left hand panel shows the rates for the proton and the right hand panel those for the deuteron as a function of x. The analyses are based on small subsamples of the MC data.

The measured unpolarized rates of the background processes and the DIS events are shown in Fig. 7.6. The inelastic rate is the largest source of background, followed by the elastic tail in the case of the proton and the quasi-elastic tail in the case of the deuteron. The elastic contribution to the deuteron cross section is very small. The figure illustrates that the largest corrections are expected at small values of x. In this region, the statistical uncertainties on the Born asymmetries are expected to

be substantially larger than those of the measured asymmetries, because only a small fraction of the measured counts are due to deep-inelastic scattering events.[2] The uncertainty increase is discussed in more detail in Sec. 7.7.1.

The tracked and the Born Monte Carlo data were used to determine the matrices $n_{\pm}(i,j)$, and the rates $n_{\pm}^{X}(i)$ and $n_{\pm}^{B}(i)$. Fig. 7.7 presents the matrices $n_u(i,j)$ for DIS events and SIDIS π^{+} events on the proton in the x-bins of the analysis presented here. The background due to higher order QED processes that migrates into the acceptance ($j = 0$) is seen to be large in the case of the DIS events. Only little background is present in the case of the SIDIS events, where the hadron-tag rejects elastic events and reduces the number of events with small W_B^2.

The inter-bin migration is of similar size in both data-samples. As expected, QED radiative effects, specifically initial and final-state bremsstrahlung, cause migration only to smaller values of observed x_X with respect to x_B. On the other hand, multiple scattering and finite resolution effects in the detector also in some cases decrease the observed x_X.

In general, the migration effects are small, *i.e.* only a small fraction of the events is migrated to neighboring bins and beyond. This result is not only important for good sensitivity to the Born asymmetries, but also crucial for the application of the unfolding algorithm (Eq. (7.10)). The algorithm relies on the numerical inversion of the migration matrix $S(i,j)$ which is in principle non-trivial, especially when migration effects are large [140]. In this case, the matrix inversion was found to yield satisfactory results, since the migration matrices are close to being diagonal.

7.6 The Born Asymmetries

7.6.1 Results

The Born asymmetries were determined from the measured asymmetries presented in Ch. 6 using the unfolding algorithm and the Monte Carlo data described in the previous subsections. The photon-nucleon asymmetries were calculated from the electron-nucleon asymmetries that follow from the unfolding using Eq. (2.66) at the Born kinematics given by Eq. (7.16). The squared statistical uncertainties are the diagonal elements of the covariance matrix given by Eq. (7.11). Fig. 7.8 shows the Born asymmetries on the proton and Fig. 7.9 those on the deuteron.

---

[2]Let N be the measured counts, N_s the desired signal, and N_b the unwanted background: $N = N_s + N_b$. The uncertainty of the signal, $\sigma(N_s) = \sqrt{(\sigma(N))^2 + (\sigma(N_b))^2}$, is larger than the uncertainty of the measured rate, $\sigma(N)$.
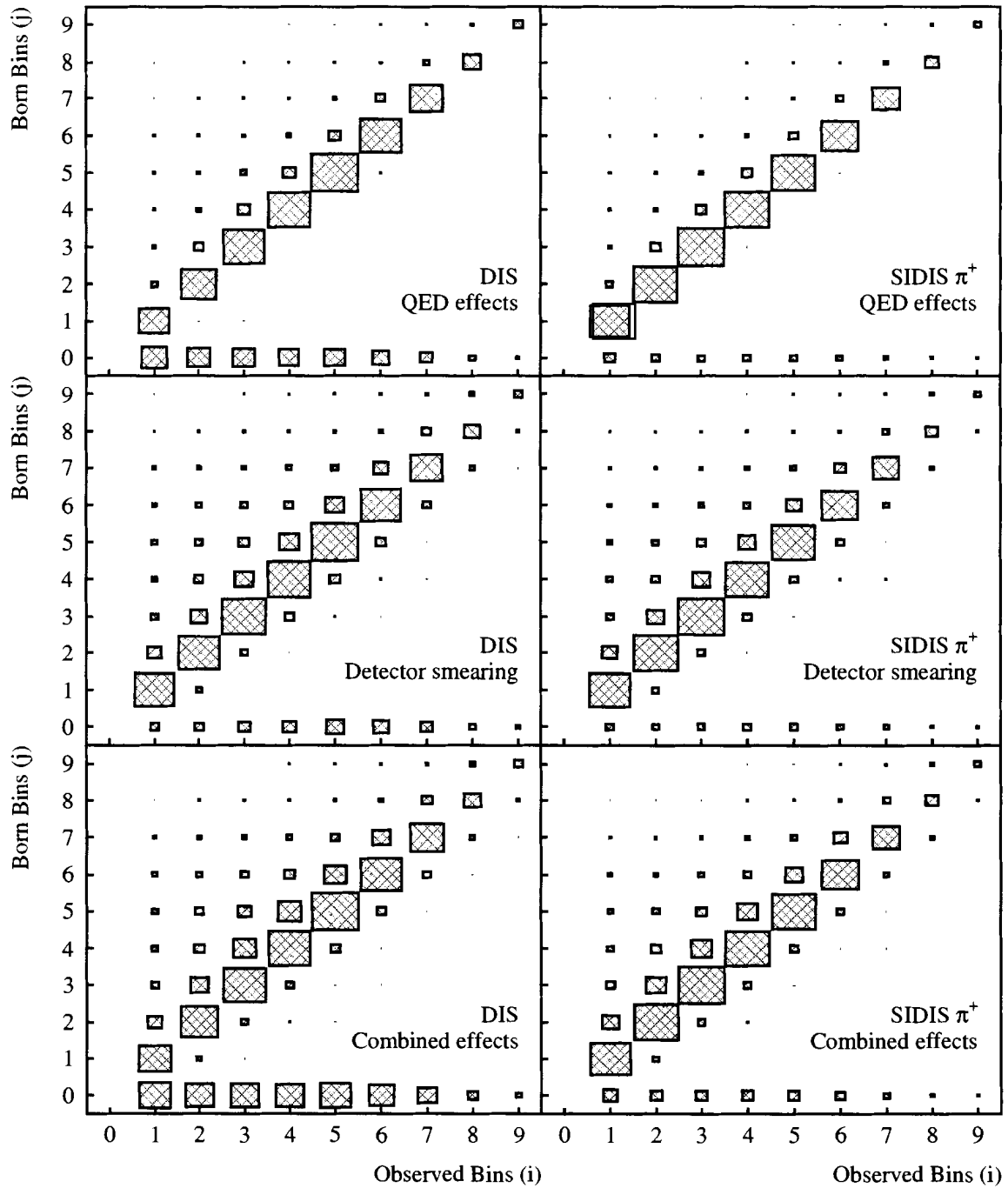
Figure 7.7: Matrices $n_u(i,j) \equiv n_-(i,j) + n_+(i,j)$ for DIS events and SIDIS π^+ events on the proton. Shown are the matrices for higher order QED processes, detector smearing, and for both effects combined. The binning shown corresponds to the 9 bins in x defined in Tab. 6.3.
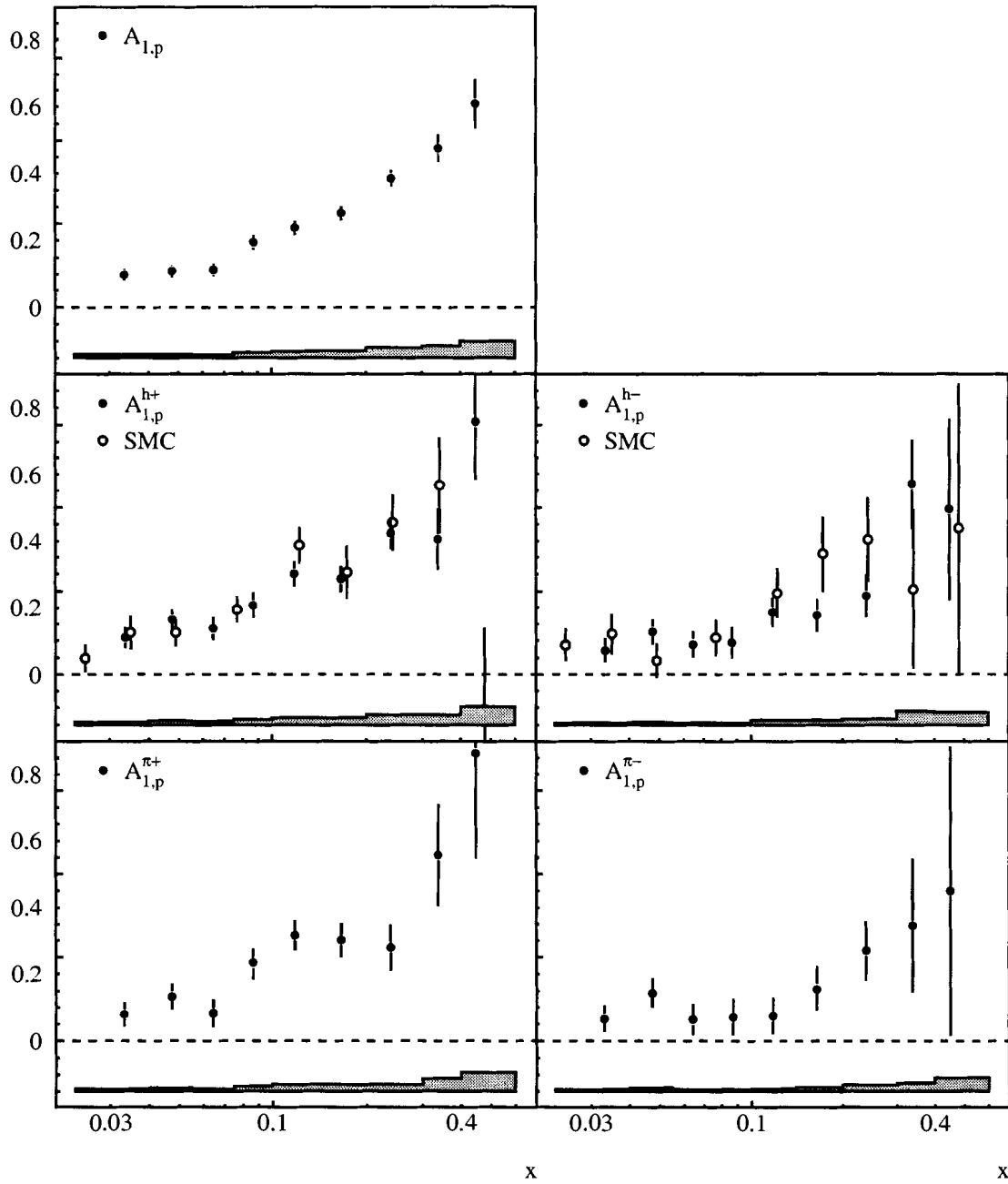
Figure 7.8: The Born asymmetries on the proton as function of x. The statistical uncertainties shown as the error bars include the uncertainties from the measured asymmetries and the very small statistical uncertainties of the Monte Carlo data. The bands illustrate the systematic error. The positive and negative hadron asymmetries measured by the SMC collaboration are also shown [141].
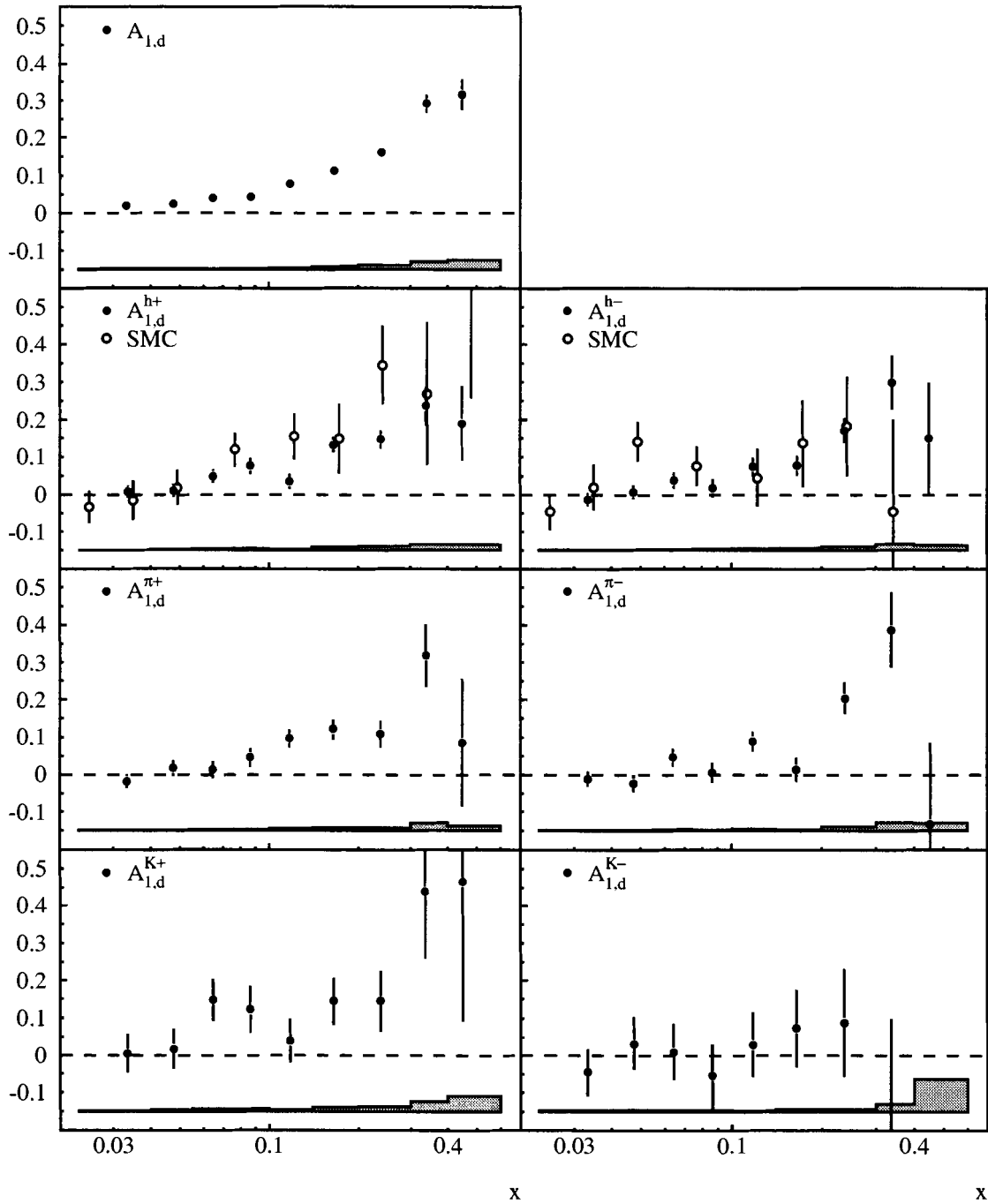
Figure 7.9: The Born asymmetries on the deuteron as function of x. One data point at $x = 0.45$ of the K^- asymmetry including its error bar is outside of the shown scale. See Fig. 7.8 for more details.

The asymmetries on the proton are all positive and increase with x. Therefore most of the spin carried by the quarks is due to the valence quarks that carry large fractions x of the nucleon momentum. The asymmetry is small at small x because a large unpolarized sea of quark/anti-quark pairs dilutes the asymmetry. All asymmetries are largely sensitive to the u-quark with fractional charge $2/3$, since the virtual photon couples proportionally to the squared fractional charges of the quarks. The varying magnitudes of the semi-inclusive asymmetries are due to the differences in the fragmentation functions. This property and the differences to the deuteron asymmetries will be exploited in the calculation of the polarized quark densities described in Ch. 8.

The asymmetries on the deuteron show in general the same trends as the proton asymmetries. However, they are smaller in size, which is an indication for a different distribution of the quark spins in the neutron. Of particular interest for the measurement of the polarization of the quark sea is the semi-inclusive negative kaon asymmetry. This asymmetry is more sensitive to the sea polarization than the other semi-inclusive asymmetries, because the final state K^- — a $\bar{u}s$-meson — does not contain any nucleon valence quarks. The typical rise with x as a consequence of sensitivity to the u-quark is not observed in $A_1^{K^-}$.

The asymmetries of undifferentiated hadrons are compared with results obtained by the Spin Muon Collaboration [141]. The asymmetries are in good agreement but the HERMES data have better precision. The agreement verifies that any instrumental effects do not bias the asymmetries. It also confirms the scaling behaviour of the asymmetries discussed in Sec. 2.3.2, because the SMC data were collected at a larger scale of $Q^2 = 10\,\mathrm{GeV}^2$ compared to an average value of $Q^2 = 2.5\,\mathrm{GeV}^2$ in this analysis.

A comparison of the inclusive asymmetry with data collected with other experiments is omitted, because the inclusive asymmetry obtained in this analysis is determined for application in the Δq decomposition. For inclusive analysis, less stringent criteria for the identification of the DIS lepton make more data available [36, 142]. The asymmetries of pions on the proton and the asymmetries of pions and kaons on the deuteron were measured for the first time by the HERMES collaboration.

7.6.2 Systematic Uncertainties

The measured asymmetries $A_{||}^X$. Systematic uncertainties were assigned to the measured asymmetries due to the beam and target polarization measurements and for the azimuthal acceptance correction. Similarly to the statistical covariance on the Born asymmetries, the systematic covari-

ances due to these sources follow via the dilution matrix. For the beam and target polarization measurements, the uncertainty on the Born asymmetries is

$$V_{P_{T(B)}}\left(A_{\|}^{B}(j), A_{\|}^{B}(k)\right) = \sum_{i_1=1}^{n_X}\sum_{i_2=1}^{n_X} \mathcal{D}(j,i_1)\mathcal{D}(k,i_2)\, \sigma_{P_{T(B)}}\left(A_{\|}^{X}(i_1)\right)\, \sigma_{P_{T(B)}}\left(A_{\|}^{X}(i_2)\right). \quad (7.17)$$

Here the double sum over the experimental uncertainties is a consequence of the complete correlation of the beam and target polarization measurement among the x-bins. In the case of the azimuthal acceptance correction, the systematic uncertainty was assumed uncorrelated between the bins. The corresponding systematic covariance on the Born asymmetries is thus

$$V_{\phi}\left(A_{\|}^{B}(j), A_{\|}^{B}(k)\right) = \sum_{i=1}^{n_X} \mathcal{D}(j,i)\mathcal{D}(k,i)\, \sigma_{\phi}\left(A_{\|}^{X}(i)\right)\, \sigma_{\phi}\left(A_{\|}^{X}(i)\right). \quad (7.18)$$

The appropriate covariances on the photon-nucleon asymmetries scale with the factor involving the depolarization factor,

$$V_{P_T,P_B,\phi}\left(A_1^{B}(j), A_1^{B}(k)\right) = \left|\frac{1}{[(1+\eta\gamma)D]_j}\,\frac{1}{[(1+\eta\gamma)D]_k}\right| V_{P_T,P_B,\phi}\left(A_{\|}^{B}(j), A_{\|}^{B}(k)\right), \quad (7.19)$$

where the kinematic factors η, γ and D are calculated at the Born kinematics in the bins j and k as indicated. The covariances due to the polarization measurements apply to all inclusive and semi-inclusive Born asymmetries. The covariance due to the azimuthal acceptance correction applies to the semi-inclusive Born asymmetries only.

The Monte Carlo simulation. The use of Monte Carlo data in the unfolding algorithm gives rise to statistical uncertainties due to the finite Monte Carlo datasets and systematic uncertainties due to the modelling of the higher order QED effects and the detector simulation.

The statistical uncertainties of the Monte Carlo data enter in the determination of $n_{\pm}(i,j)$, $n_{\pm}^{B}(j)$, and thus $S_{\pm}(i,j)$ needed in Eq. (7.10). The determination of the corresponding uncertainties on the inverted matrix and subsequently on the unfolded asymmetry is in principle straight forward, but involves a large number of terms. The count rates were propagated using a variational technique to avoid this difficulty. The count rates $N = \sum_i \omega_i$ in each entry of $n_{\pm}(i,j)$ and $n_{\pm}^{B}(j)$ are uncorrelated and Poisson distributed with uncertainties given by Eq. (6.2). The Poisson distribution of each rate can be approximated by a Gaussian distribution with mean N and standard deviation $\sigma(N)$, because of the large number of counts. The rates were independently varied following their

respective distribution using a standard random number generator. The set of varied rates was used in the unfolding algorithm and the unfolded asymmetries were stored in a histogram for each bin. This procedure was repeated $10,000$ times for each asymmetry, which was found to be sufficient for an estimate of the Monte Carlo statistical uncertainties on the asymmetries. The uncertainties were then obtained as the standard deviations of the accumulated histograms. This variational technique has the additional advantage that it can be used for any number of bins n_X and n_B. The resulting statistical uncertainties are included in the error bars shown in Figs. 7.8 and 7.9 and they are listed in a separate column in Tabs. B.5 and B.6 in App. B. A separation of the uncertainties in the figures was omitted, because the Monte Carlo statistical uncertainties are negligible with respect to the experimental statistical uncertainties. The statistical uncertainties are maximally correlated for the same target, because the same Monte Carlo data are used. They were assumed uncorrelated between Born x-bins.

The second source of uncertainty is due to possible systematic deviations of the Monte Carlo simulation from the true distributions. In the case of higher order QED effects, the uncertainties on the asymmetries were found to be smaller than 5% for $x < 0.3$ and smaller than 2% at larger x [143]. They arise from finite bin size effects ($< 2\%$), the unpolarized structure functions ($\sim 1\%$), and the quasi-elastic and elastic tails ($< 2\%$). Based on this study, the uncertainties due to QED radiative corrections on the inclusive asymmetries were estimated to be 2%. The smaller value is motivated by the applied bin-centering correction that was carried out and the decreased sensitivity of the unfolding procedure to the unpolarized structure functions with regard to the iterative method used in Ref. [143]. The uncertainty on the semi-inclusive asymmetries was estimated with 1%, since no elastic and quasi-elastic tails are present.

In the case of the detector simulation, an uncertainty of 2% was assigned to the asymmetry. A systematic deviation is not expected to be larger, because of the good agreement of the Monte Carlo asymmetries with those measured. Furthermore any systematic effects only impact the asymmetries if spin-dependent effects or large spin-independent effects leading to a dilution of the asymmetry are present. The systematic uncertainties of the Monte Carlo simulation were assumed to be maximally correlated for the same target and uncorrelated otherwise. They were assumed uncorrelated between x-bins.

The ratio R and the structure function g_2. The systematic uncertainties due to R and due to the assumption $g_2 = 0$ are calculated on the Born asymmetries $A_1^{(h)}$ in an analogous way to those on the

experimental asymmetries as described in Sec. 6.2.5. The kinematics used are the Born kinematics that follow from the bin-centering-correction. These uncertainties were assumed uncorrelated between x-bins.

Total systematic uncertainty. The total systematic uncertainty was calculated using Eq. (6.24). The uncertainty on $A_1^{(h)}$ includes all the listed uncertainties. Those on $A_{\parallel}^{(h)}$ do not include the uncertainties due to R and g_2. The uncertainties on the Born asymmetries $A_{1p(d)}^{(h)}$ averaged over x and over the inclusive and the semi-inclusive asymmetries are given in Tab. 7.1. The systematic uncertainties for the individual asymmetries are also listed in Tabs. B.11 and B.12 in App. B. The largest uncertainty is due to the target polarization measurement followed by the uncertainty of beam polarization measurement in the case of the inclusive asymmetries and the semi-inclusive proton asymmetries. In the case of the semi-inclusive asymmetries on the deuteron, the uncertainty of the azimuthal acceptance correction is larger than that of the beam polarization measurement.

Table 7.1: The fractional systematic uncertainties on the Born asymmetries A_1 averaged over x.

Source	Hydrogen data	Deuterium data
Beam polarization	4.2 %	2.3 %
Target polarization	5.1 %	5.2 %
Azimuthal acc. (SIDIS)	3.0 %	3.1 %
QED rad. corr. (DIS)	2.0 %	2.0 %
QED rad. corr. (SIDIS)	1.0 %	1.0 %
Detector smearing	2.0 %	2.0 %
R	1.1 %	1.1 %
g_2	0.6 %	1.4 %

7.7 Systematic Studies

7.7.1 Comparison of Born and Observed Asymmetries

A comparison of the observed asymmetries A_{1p} and $A_{1p}^{\pi^+}$ with the corresponding Born asymmetries is shown in Fig. 7.10. Within the uncertainties the observed asymmetries are in good agreement with the Born asymmetries. The corrections applied to the asymmetries in the unfolding procedure
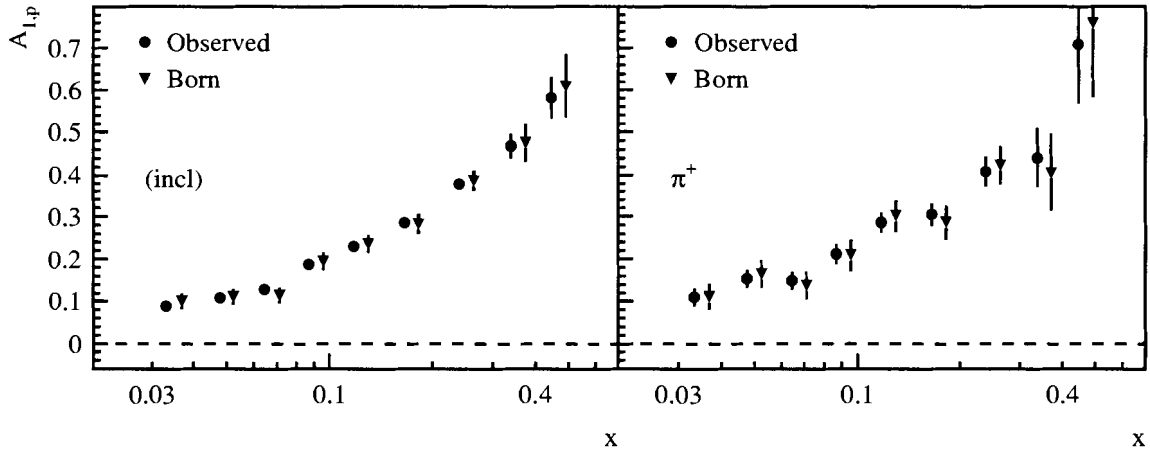
Figure 7.10: Comparison of observed and Born asymmetries on the proton. The left hand panel compares the inclusive asymmetries and the right hand panel the semi-inclusive asymmetries of positive pions. The error bars show the statistical uncertainties. Systematic uncertainties are not shown. The Born asymmetries were offset in x for presentation.

are therefore small and do not affect the measurement in a systematic way.

The figure also illustrates that the uncertainties on the Born asymmetries are increased with respect to the observed asymmetries. The ratio of these uncertainties is shown in Fig. 7.11 for the inclusive asymmetries and the positive pion asymmetries on the proton and the deuteron. The inclusive asymmetry is seen to be subject to the largest increase in uncertainty. At small values of x the increase is mostly caused by higher order QED effects, specifically by the elastic and inelastic background processes that dilute the DIS signal. The increase in the case of the inclusive asymmetry on the deuteron is not as large as that on the proton, because the quasi-elastic tail is smaller than the elastic tail for the proton (cf. Fig. 7.6). At higher values of x these processes become less important and detector smearing effects dominate the uncertainty enlargement. The increase due to these latter effects is fairly constant over the range in x. The variation is largely due to the variable width of the x-bins[3] (see Tab. 6.3 and Fig. 6.2). The maximal increase of the uncertainties due to the combined effects is larger than two.

The semi-inclusive asymmetries suffer a much smaller increase of the uncertainties. The increase due to detector effects is of similar size as in the case of the inclusive asymmetries. However,

---

[3]The logarithmic width of the bin sets the scale in this case. For example, bin 10 is broad compared to bins 9 and 11. The uncertainty increase due to detector smearing is smaller in this bin.

Proton: Inclusive

△ Detector effects   Proton: π^+
□ QED rad. effects
● Combined effects

Deuteron: Inclusive

△ Detector effects   Deuteron: π^+
□ QED rad. effects
● Combined effects

Uncert. Increase   2.4 2.2 2 1.8 1.6 1.4 1.2 1

0.03   0.1   0.4   0.03   0.1   0.4

x   x
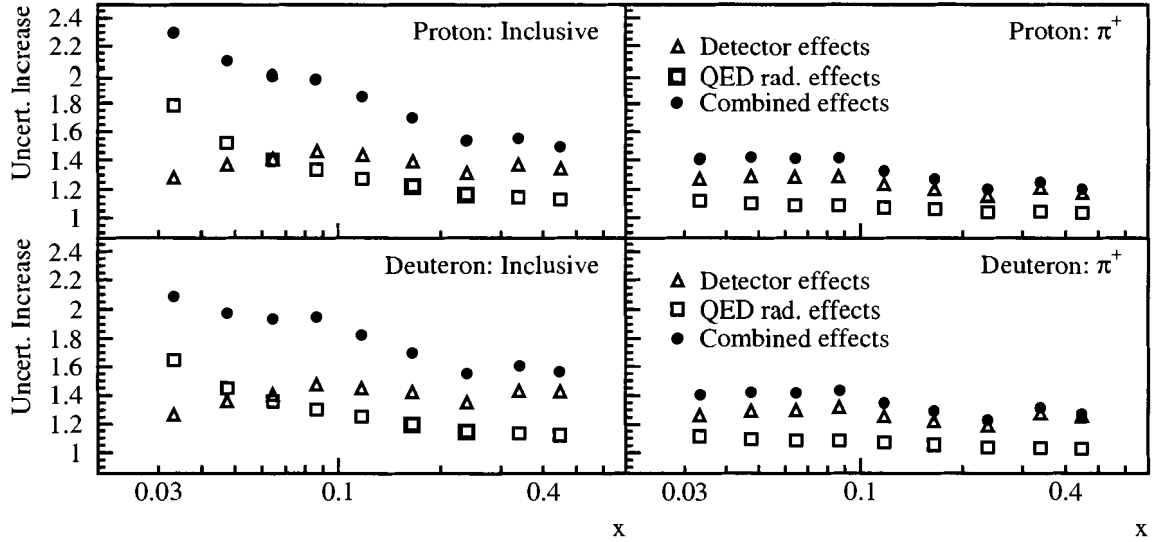
Figure 7.11: Increase of the statistical uncertainties on the inclusive Born asymmetry (left) and on the semi-inclusive π^+ Born asymmetry (right). The top panels show the increase for the proton asymmetries and the bottom panels those for the deuteron asymmetries. Shown are the total increase σ^B/σ^X and the increase due to detector smearing effects and due to higher order QED processes separately.

the impact of higher order QED effects is substantially smaller because of the hadron required in the final state.

The increase discussed here applies to the statistical uncertainties. The systematic uncertainties on the beam and target polarizations are subject to the same increase as given in Eq. (7.17). However, the complete correlation of the uncertainty between bins leads to a reduced enlargement of at most a factor of 1.7 for the proton and of 1.5 for the deuteron. The systematic uncertainty due to the azimuthal acceptance correction of the semi-inclusive asymmetries is subject to the same increase.

7.7.2 Asymmetries as a Function of z

It has been suggested [65] that polarized fragmentation functions ΔD_f^h may be non-zero and therefore play a relevant role in polarized semi-inclusive DIS. While a spin-dependent fragmentation into pseudoscalar mesons, e.g. pions and kaons, is unlikely, non-zero polarized fragmentation functions would generate terms like $q(x, Q^2) \, \Delta D_q^h(z, Q^2)$. These terms could significantly affect the polarized structure functions $g_1^h(x, Q^2, z)$ and their contribution to the semi-inclusive cross section would

vary with the fractional energy z of the produced hadron.

A z-dependence of the asymmetries could also be an indication that a large fraction of the hadrons in the semi-inclusive data sample originated from target fragmentation as opposed to current fragmentation, where the final-state hadron is directly linked to the struck quark. Hadrons from non-partonic processes such as diffractive interactions could play an important role in the semi-inclusive DIS data sample [144]. For example, at high fractional energies z, it is possible that hadrons from exclusive processes are mis-identified as SIDIS hadrons.

The semi-inclusive asymmetries were extracted in bins of z in order to study the impact of these scenarios on the SIDIS data sample. The semi-inclusive asymmetries for the proton and the deuteron are shown in Fig. 7.12. The asymmetries were calculated with the same kinematic cuts described in Sec. 6.1, except for the cut on x_F which was discarded, because x_F is highly correlated with z. The data were averaged over the range $0.023 < x < 0.6$. The Born asymmetries in z-bins were determined with the same unfolding algorithm described above. A function $A(z) = \text{constant}$ was fitted to each asymmetry and the χ^2 values are given in the panels. The data show no indication of a statistically significant z-dependence of the asymmetries. This is also true for the K^+ asymmetry on the deuteron, where although the χ^2 value of the fit is large, the data have no systematic trend.

7.7.3 Hadron Tagged Asymmetries

In the DIS regime, the quark that is knocked out of the nucleon forms a hadron in the final state. Therefore the theoretical fragmentation function to produce any hadron is unity,

$$\int_0^1 dz \, D_q^{h^+ + h^- + h^0}(z, Q^2) \equiv 1. \tag{7.20}$$

In practice, the integral deviates from unity, because the number of hadrons produced in the limited geometrical acceptance of the spectrometer is reduced. While the observed asymmetries were corrected for the asymmetric azimuthal acceptance of the spectrometer, a correction was not applied for the limited forward acceptance. The deviation of the integral from unity is also present in the case of the Born asymmetries, because the unfolding algorithm does not correct for the limited acceptance, either. In addition, the analysis presented here was restricted to charged particles, so that a contribution from neutral hadrons further reduces the integrated fragmentation function of any charged hadron. Nevertheless the inclusive Born asymmetry A_1 is expected to be in reasonable agreement with the semi-inclusive Born asymmetry $A_1^{h^+ + h^-}$ of any charged hadron, because the
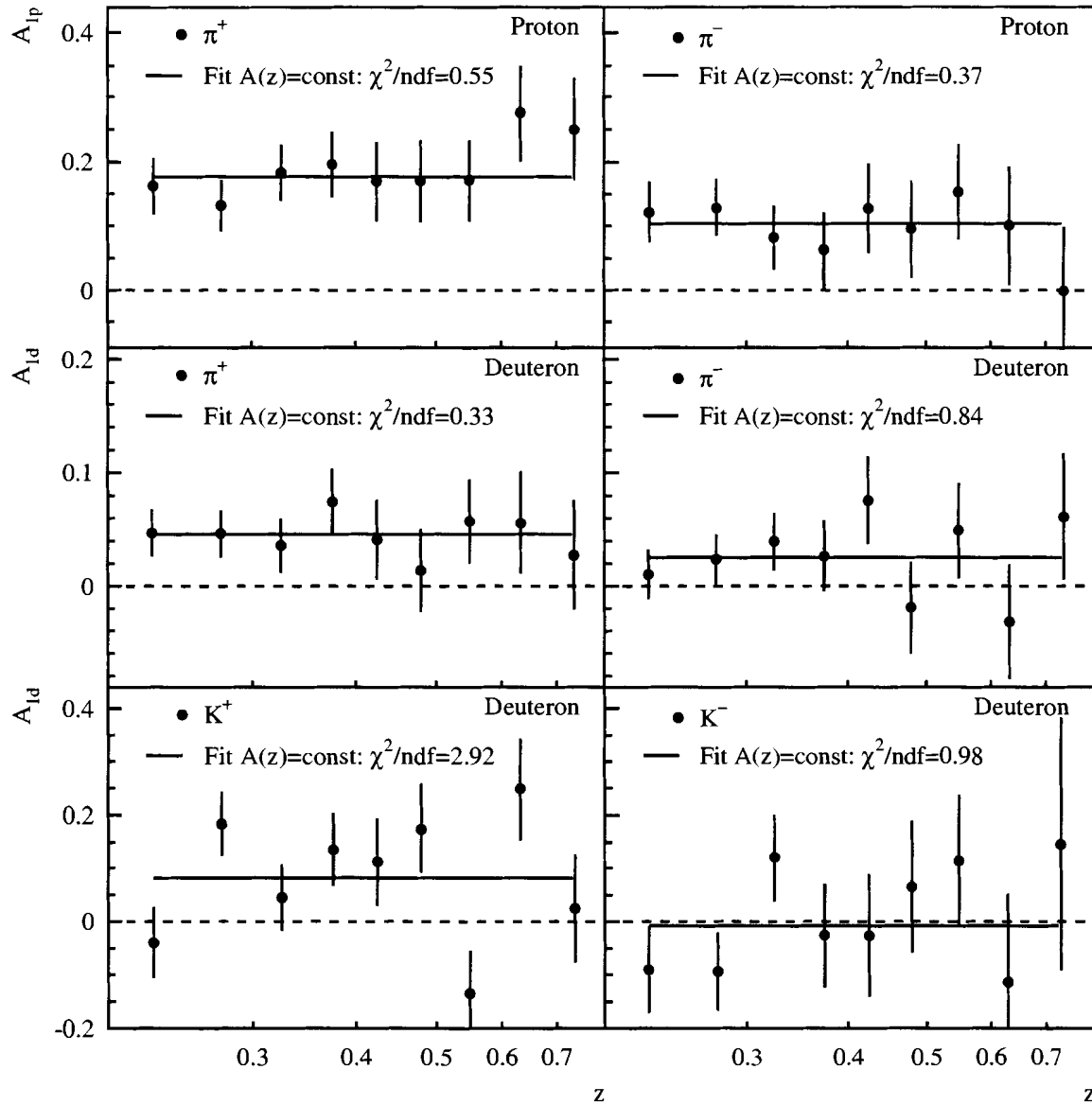
Figure 7.12: The semi-inclusive asymmetries A_1^h on the proton and the deuteron as function of z. The asymmetries were integrated over the measured range in x, $0.023 < x < 0.6$. The solid lines represent fits $A(z) = $ const to the asymmetries. The corresponding χ^2 value is given in each panel. The error bars are statistical only. Systematic uncertainties are not shown.
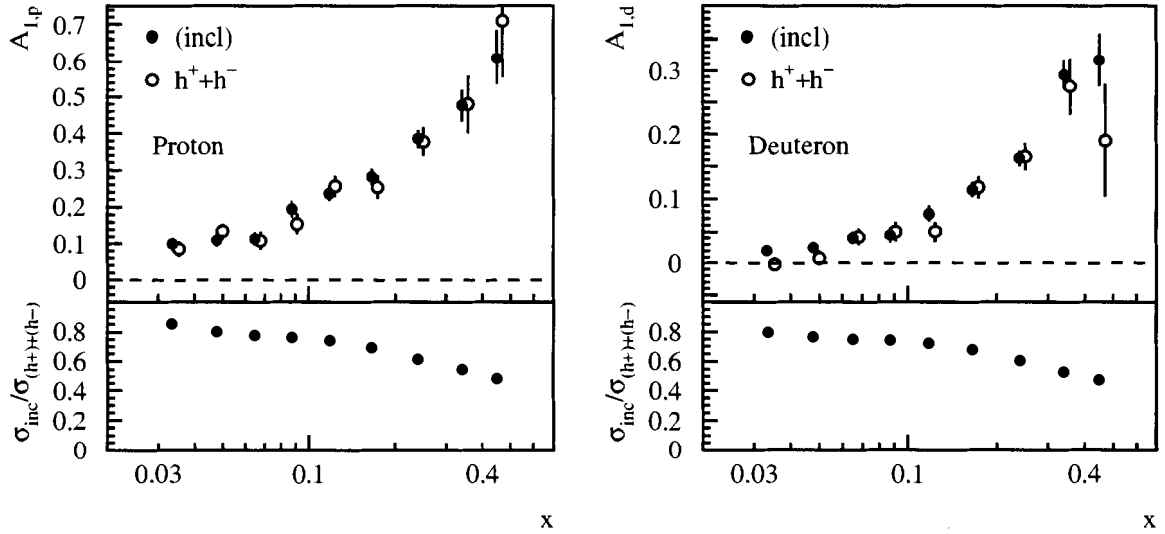
Figure 7.13: The inclusive asymmetries on the proton and the deuteron compared with the respective semi-inclusive $h^+ + h^-$ asymmetries. The top panels show the asymmetries, where the hadron tagged asymmetry is offset in x for presentation. The lower panel shows the ratio of the uncertainties, $\sigma(A_1)/\sigma(A_1^{h^+ + h^-})$.

listed limitations are polarization independent and the fragmentation into any charged hadron does not affect the flavour of the struck quark.

The inclusive asymmetries and the hadron tagged asymmetries are shown in the top panels of Fig. 7.13. The asymmetries on each target are in good agreement overall. A deviation is present at small x for the deuteron asymmetries, which is likely due to the limited acceptance effects discussed above.

The bottom panels in the figure show the ratio of the uncertainties. The uncertainties at small x are similar in size for the inclusive and the hadron-tagged asymmetries. At larger x, the inclusive asymmetries are more precise because the contribution from (quasi-)elastic and inelastic background to the inclusive rates becomes small. In addition, the phase space for the production of hadrons that can be detected in the spectrometer is reduced due to the smaller W^2 (see Fig. 6.2).
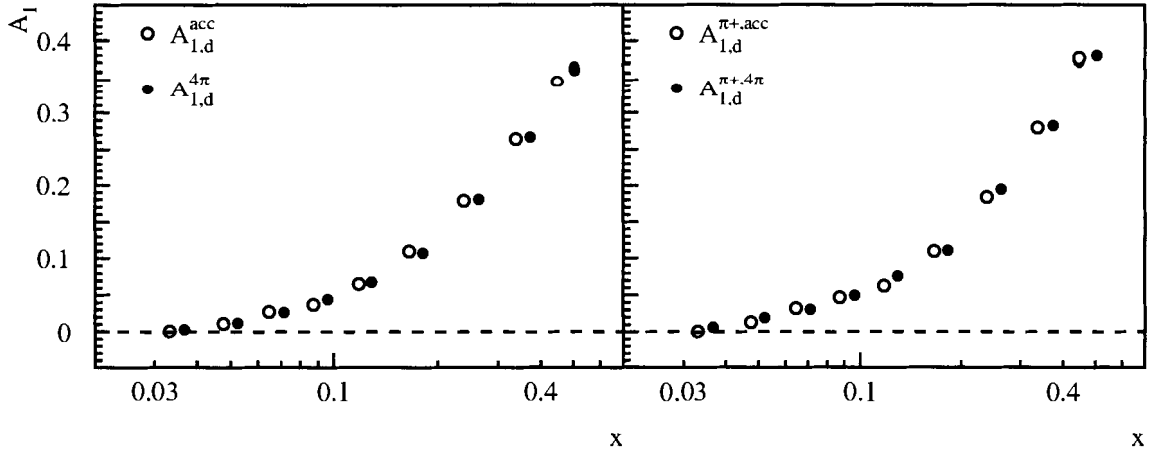
Figure 7.14: Born level Monte Carlo asymmetries on the deuteron in the acceptance and in 4π. The left hand plot compares the inclusive asymmetries $A_{1,d}$ and the right hand plot the semi-inclusive asymmetries $A_{1,d}^{\pi^+}$. In the latter case, the asymmetry in the acceptance includes the hadron momentum cut. The solid circles were shifted in x for presentation.

7.7.4 The Limited Acceptance of the Spectrometer

As mentioned in the last subsection the asymmetries were not corrected for the limited forward acceptance of the HERMES spectrometer. Acceptance effects cancel in principle in the measurement of asymmetries as opposed to total cross sections. In addition, the geometrical acceptance limits only the ranges of θ and ϕ that can be detected, but does not affect x, Q^2, or z directly. Also the large forward Lorentz boost in the laboratory frame results in a larger coverage of the phase space than the geometrical acceptance might at first convey. For these reasons, a bias of the inclusive asymmetries due to acceptance effects is not expected.

However, it is possible that the limited angular acceptance of the spectrometer biases the semi-inclusive asymmetries, because the forward geometry limits the topology of the DIS electron and the SIDIS hadron in the final state. In addition, the momentum cut ($4\,\mathrm{GeV} < p < 13.8\,\mathrm{GeV}$) on the coincident pion and kaon tracks for particle identification using the Čerenkov/RICH (cf. Sect. 5.2) could potentially bias the asymmetries of these hadron types. These acceptance effects could arise despite the azimuthal acceptance correction, that corrected for the asymmetry in the spectrometer acceptance whereas the limited polar acceptance was not accounted for.

Possible effects on the asymmetries due to these acceptance limitations were studied with the

HERMES Monte Carlo simulation. Born level data were generated and analyzed both within the acceptance and in 4π. The simulated inclusive asymmetry on the deuteron and the semi-inclusive π^+ asymmetry are shown in Fig. 7.14. The asymmetries in 4π and in the acceptance with the cuts on the hadron momentum applied are in good agreement. There is thus no indication of a bias of the asymmetries.

Chapter 8

Polarized Quark Distributions

The Born asymmetries presented in the previous chapter were used to determine the polarized quark densities $\Delta q(x, Q^2)$ in the nucleon. The determination applies the purity formalism, which is based on a leading order model. This chapter first describes the modeling of the proton and the deuteron asymmetries, followed by a discussion of the purity generation using the Born Monte Carlo simulation. The purity algorithm that leads to the polarized quark distributions is then presented. In the final part of this chapter, the results are shown and moments of the polarized quark densities are calculated.

8.1 Modeling the Proton Asymmetry

As described in Sec. 2.5 the semi-inclusive asymmetries on the nucleon can be related to the polarized and unpolarized parton densities with the aid of fragmentation functions,

$$A_1^h(x, Q^2) = \frac{g_1^h(x, Q^2)}{F_1^h(x, Q^2)} = \frac{1 + R(x, Q^2)}{1 + \gamma^2} \frac{\sum_q e_q^2 \, \Delta q(x, Q^2) \int_{z_1}^{z_2} dz \, D_q^h(Q^2, z)}{\sum_{q'} e_{q'}^2 \, q'(x, Q^2) \int_{z_1}^{z_2} dz \, D_{q'}^h(Q^2, z)} \,. \tag{8.1}$$

With respect to Eq. (2.69) which is valid in leading order QCD, an additional kinematic factor $(1 + R)/(1 + \gamma^2)$ was introduced. Eq. (8.1) is in turn valid in combination with available parameterizations of unpolarized parton densities. The parameterizations used in this analysis are the CTEQ5LO [145] parton distributions, which were computed from fits to the structure function F_2,

$$F_2(x, Q^2) = \sum_q x \, e_q^2 \, q(x, Q^2). \tag{8.2}$$

The structure function F_2 was derived from cross section measurements assuming non-zero values for the ratio R and the kinematic factor γ^2. Therefore the parameterizations of the parton densities are related to the structure function F_1 via Eq. (2.21),

$$F_1(x, Q^2) = \frac{1 + \gamma^2}{1 + R(x, Q^2)} \frac{1}{2x} F_2(x, Q^2) = \frac{1 + \gamma^2}{1 + R(x, Q^2)} \frac{1}{2} \sum_q e_q^2 q(x, Q^2). \qquad (8.3)$$

The additional factor in Eq. (8.1) is thus merely a consequence of the determination of the unpolarized parton distributions.

The measured Born asymmetries presented in Ch. 7 were determined in bins of x and integrated over $0.2 < z < 0.8$ and the Q^2-ranges $Q_{i,1}^2 < Q^2 < Q_{i,2}^2$ in each bin that follow from the kinematic cuts (see Tab. 6.1 and Fig. 6.2). Hence Eq. (8.1) becomes

$$A_1^h(x_i) = \frac{1 + R(x_i, Q_i^2)}{1 + \gamma^2} \frac{\sum_q e_q^2 \int_{Q_{i,1}^2}^{Q_{i,2}^2} dQ^2 \, \Delta q(x_i, Q^2) \int_{0.2}^{0.8} dz \, \tilde{D}_q^h(x_i, Q^2, z)}{\sum_{q'} e_{q'}^2 \int_{Q_{i,1}^2}^{Q_{i,2}^2} dQ^2 \, q'(x_i, Q^2) \int_{0.2}^{0.8} dz \, \tilde{D}_{q'}^h(x_i, Q^2, z)}, \qquad (8.4)$$

where x_i is the average value of x in bin i. The fragmentation functions $\tilde{D}_q^h(x_i, Q^2, z)$ account for the limited acceptance of the spectrometer, namely the angular acceptance of the spectrometer reflected by the allowed ranges of θ_x and θ_y (see Sec. 6.1) and the requirements on the hadron momenta for identification with the threshold Čerenkov /RICH (see Sec. 5.2). They therefore describe the conditional probability that a quark with momentum fraction x probed at a scale Q^2 will fragment into a hadron of type h within the angular acceptance and within the allowed momentum range.

The semi-inclusive asymmetry given in Eq. (8.4) can be rearranged and expressed in terms of quark polarizations $[\Delta q/q](x)$ and purities $P_q^h(x_i)$:

$$A_1^{(h)}(x_i) = \frac{1 + R(x_i)}{1 + \gamma^2} \sum_q P_q^{(h)}(x_i) \frac{\Delta q}{q}(x_i), \qquad (8.5)$$

where $R(x_i)$ is calculated at the corresponding scale Q_i^2. The polarizations are to good approximation Q^2 independent in the kinematic range under consideration (see Sec. 2.3.2). The introduced purities $P_q^h(x_i)$ give the conditional probability that a hadron in the acceptance originates from an event where a quark of flavour q was struck. In terms of the unpolarized quark densities and the fragmentation functions they are given by

$$P_q^h(x_i) = \frac{e_q^2 \int_{Q_{i,1}^2}^{Q_{i,2}^2} dQ^2 \, q(x_i, Q^2) \int_{0.2}^{0.8} dz \, \tilde{D}_q^h(x_i, Q^2, z)}{\sum_{q'} e_{q'}^2 \int_{Q_{i,1}^2}^{Q_{i,2}^2} dQ^2 \, q_{q'}(x_i, Q^2) \int_{0.2}^{0.8} dz \, \tilde{D}_{q'}^h(x_i, Q^2, z)}. \qquad (8.6)$$

The inclusive asymmetry on the proton can be included in this formalism by defining inclusive purities that describe the probability for inclusive scattering off a quark of flavour q,

$$P_q(x_i) = \frac{e_q^2 \int_{Q_{i,1}^2}^{Q_{i,2}^2} dQ^2 \, q(x_i, Q^2)}{\sum_{q'} e_{q'}^2 \int_{Q_{i,1}^2}^{Q_{i,2}^2} dQ^2 \, q_{q'}(x_i, Q^2)} . \tag{8.7}$$

The relation given in Eq. (8.6) is in essence Bayes' theorem already introduced in Eq. (5.1) for particle identification. This is seen by writing the semi-inclusive purities as $P(q|h)$, the fragmentation functions as $P(h|q)$, and the unpolarized quark densities weighted by the squared fractional charges as $P(q)$:

$$P(q|h) = \frac{P(h|q)\,P(q)}{\sum_{q'} P(h|q')\,P(q')}, \tag{8.8}$$

where the sum runs over all quark flavours q and all kinematic dependencies were dropped.

The expression for the inclusive and semi-inclusive asymmetries given by Eq. (8.5) separates the unpolarized contributions to the asymmetries from the spin-dependent contributions contained in the quark polarizations. The derivation given here relies on the assumption of factorization. That is, it is assumed that the hard scattering process parameterized by quark densities can be separated from the fragmentation process described by the fragmentation functions.

8.2 Modeling the Deuteron Asymmetry

The measured parton distribution functions used in the previous section hold for the proton. The expression for the proton asymmetries given in Eq. (8.5) model the neutron asymmetries as well, if the quark densities are replaced by the corresponding densities in the neutron. These can be deduced from the parton densities for the proton assuming isospin symmetry as shown in Eqs. (2.32) and (2.33) for the neutron structure functions F_{1n} and g_{1n}, respectively. When forming the neutron purities, the fragmentation functions are not isospin-rotated, as they are independent of the target nucleon.

Instead of a neutron target, which is experimentally difficult to realize, asymmetries were measured on a deuteron target. In the deuteron, Fermi motion and shadowing effects can be neglected. Effects due to the nuclear environment [146] on the quark fragmentation process are also negligible. Therefore the constituent nucleons contribute essentially independently to the scattering reaction. Under this assumption the deuteron asymmetry is the incoherent sum of the proton and neutron

asymmetries,

$$A_{1d}^{(h)} = f_{pd}^{(h)} \, p_{pd} \, A_{1p}^{(h)} + f_{nd}^{(h)} \, p_{nd} \, A_{1n}^{(h)}, \tag{8.9}$$

where the dilution factors $f_{pd}^{(h)}$ and $f_{nd}^{(h)}$ are the probability that the scattering took place on the proton and the neutron respectively. Naturally the factors are normalized such that $f_{pd} + f_{nd} = 1$. The dilution factor for the proton can be calculated from the unpolarized structure function F_2 and the hadron multiplicities on the proton n_p^h and the deuteron n_d^h [130],

$$f_{pd}^h = \frac{\sigma_p^h}{\sigma_d^h} = \frac{n_p^h}{n_d^h} \frac{F_{2,p}}{2 \, F_{2,d}}. \tag{8.10}$$

The factor of 2 arises, because $F_{2,d}$ is the deuteron structure function per nucleon. The multiplicity ratio is unity for the inclusive asymmetry on the deuteron.

The factors p_{pd} and p_{nd} are the effective polarizations of the proton and the neutron in the deuteron, respectively. In the deuteron ground state, the proton and the neutron have their spin aligned for a total spin projection of $S_z = 1$. However, the polarization of the nucleons in the deuteron is reduced by an admixture of the deuteron D-state with a $\omega_D = (5 \pm 1)\,\%$ probability [147, 148]. States with odd angular momentum, notably the P-state, are forbidden by parity[1] and other higher excitations are negligible. The effective polarization of the proton p_{pd} and the neutron p_{nd} in the deuteron is therefore

$$p_{pd} = p_{nd} = 1 - \frac{3}{2}\omega_D = 0.925 \pm 0.015, \tag{8.11}$$

where the factor of 3/2 is a consequence of the Clebsch-Gordan coefficients of the substates [149]. Using Eq. (8.9) and isospin symmetry it is thus possible to express the deuteron asymmetries in terms of proton and neutron purities and parton distribution functions on the proton.

8.3 Generation of the Purities

Purities on the proton and the neutron were calculated using the HERMES Monte Carlo simulation. The purities depend only on the lowest order unpolarized deep-inelastic scattering process. Detector effects and higher order QED effects therefore are not simulated, apart from the acceptance defined by the ranges of θ_x and θ_y and the cuts on the momentum of the identified hadrons.

---

[1]Admixtures of odd angular momentum states as a result of the parity-violating weak interaction are very small.

The necessary data were generated with the Born Monte Carlo simulation described in Sec. 7.5.1. The correct description of the purities relies on the model of the hard scattering reaction and the fragmentation process. The former process is well described by unpolarized parton distributions, such as the CTEQ5L parameterizations that were used in this analysis [145]. The LUND model introduced in Sec. 2.5 and implemented in JETSET was tuned to match the kinematic distributions of the final state hadrons measured at HERMES [69]. The set of tuned parameters is given in Tab. 8.1. A com-

Table 8.1: Settings of the JETSET parameters for the two LUND tunes used in this analysis. A detailed discussion of the tuning procedure is given in [69]. The parameters are explained in [67].

JETSET parameter	Default tune	Old HERMES tune
PARJ(1)	0.02	0.10
PARJ(2)	0.20	0.16
PARJ(5-7)	0.00	0.50
PARJ(21) [GeV]	0.37	0.01
PARJ(23)	0.03	0.01
PARJ(24)	2.50	2.00
PARJ(33)	0.80	0.80
PARJ(41)	1.74	0.82
PARJ(42) [GeV^{-2}]	0.23	0.24
PARL(3) [GeV]	0.44	0.44

parison of the measured and the simulated hadron multiplicities, *i.e.* the number of SIDIS hadrons normalized by the number of DIS electrons, is shown in Fig. 8.1. The tuned Monte Carlo simulation is in reasonable agreement with the positive and negative pion multiplicities and the negative kaon multiplicities. The simulated positive kaon multiplicities are smaller than those measured. This disagreement is also reported in Ref. [150]. However, the results on the polarized parton densities are not very sensitive to the positive kaon asymmetry and hence this disagreement because the large uncertainties on this asymmetry lead to only little weight in the fit.

Purities for the proton and the neutron were calculated from Monte Carlo datasets of about 10M equivalent DIS events each. The inclusive and semi-inclusive purities are shown in Fig. 8.2. The neutron purities shown in the figure were isospin rotated to illustrate the sensitivity to the quark flavours in the proton when scattering off a quark in the neutron.
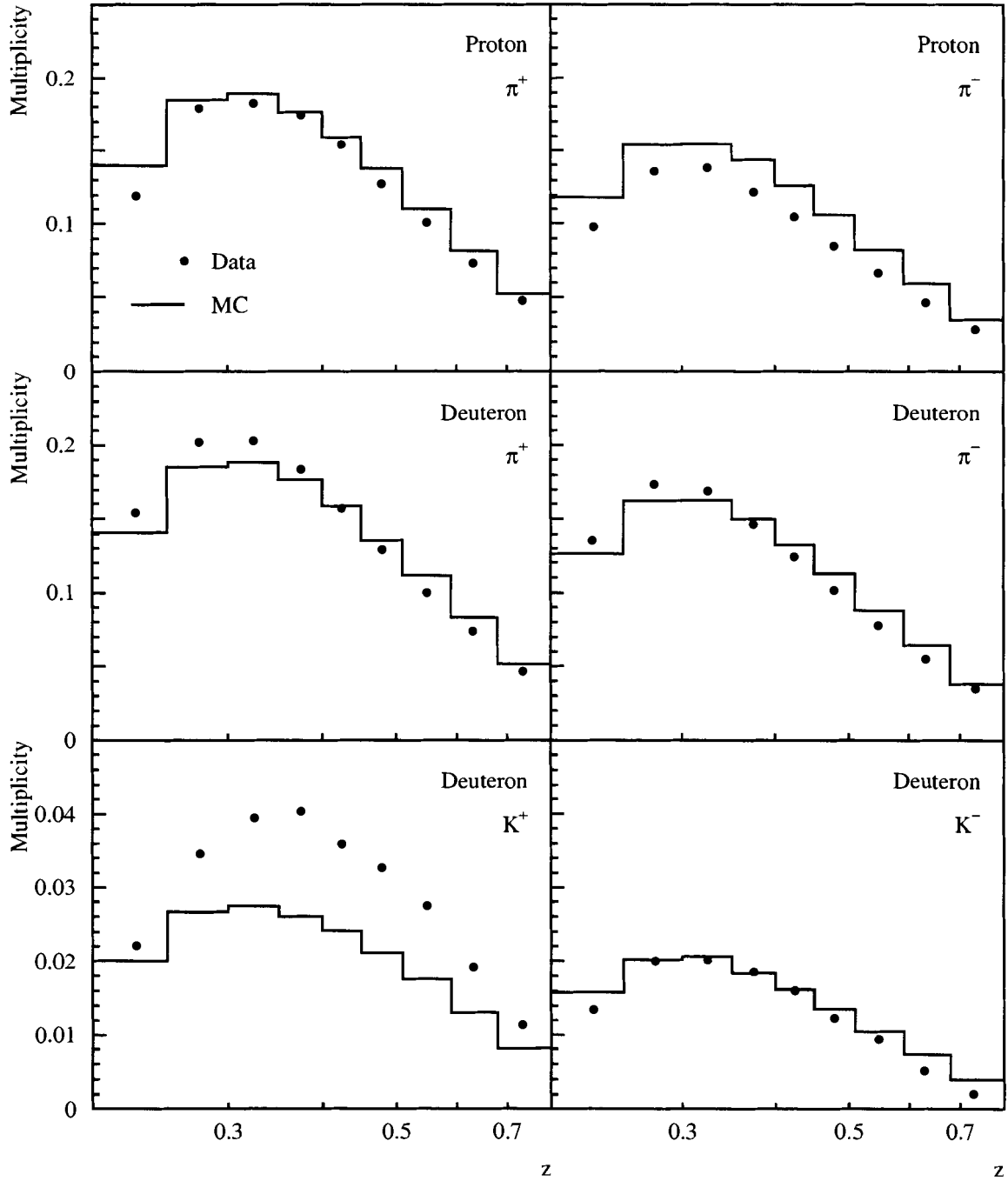
Figure 8.1: Simulated and measured hadron multiplicities as function of z. The multiplicities include higher-order QED processes and detector effects. The statistical uncertainties are negligible. Small systematic uncertainties are not shown.
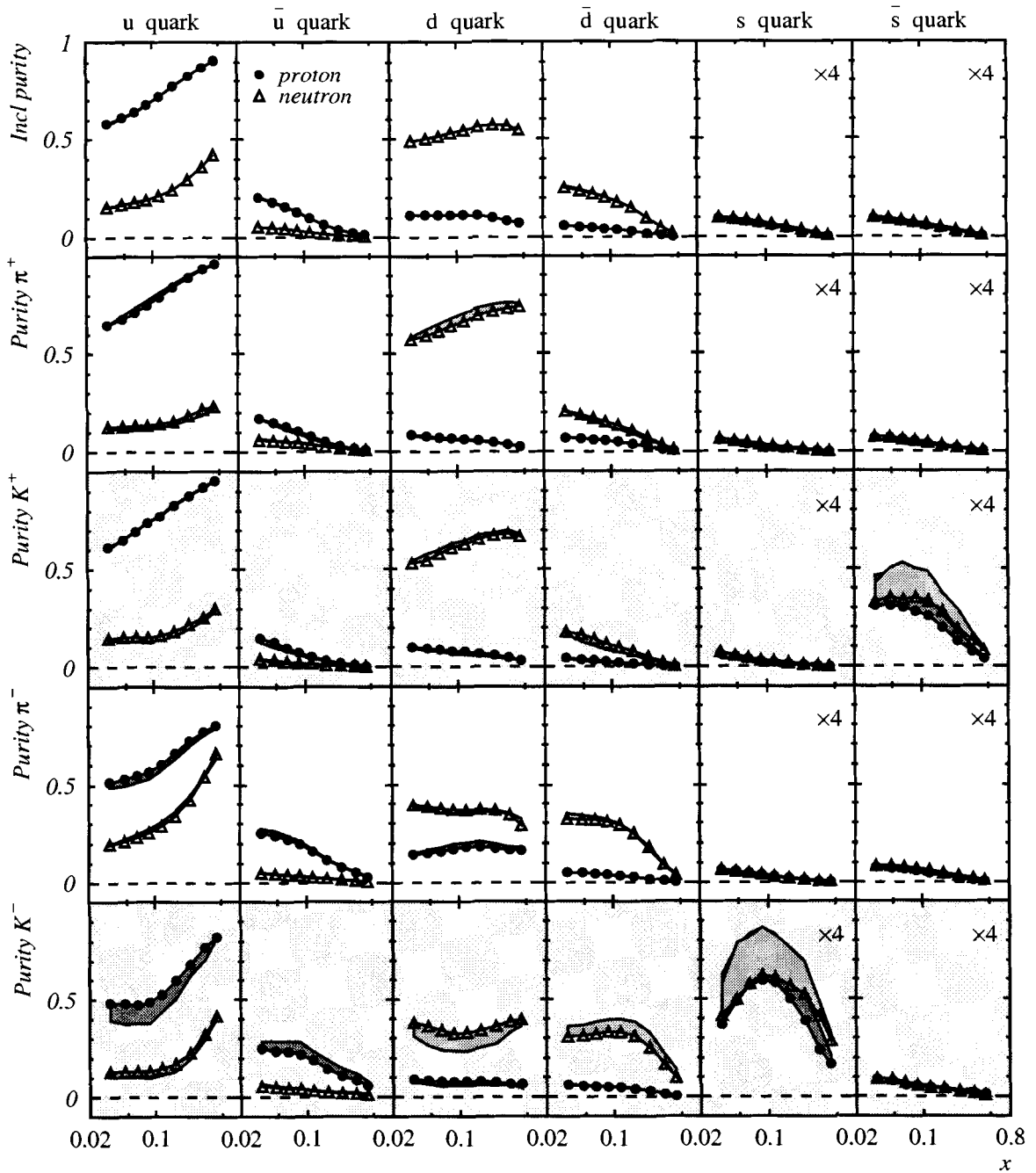
Figure 8.2: The inclusive and semi-inclusive purities on the proton and the neutron. The neutron purities were isospin rotated. The strange and anti-strange quark purities were scaled by a factor of 4 for representation. The shaded bands in each panel indicate the assigned systematic uncertainties due to the the LUND fragmentation tune. The bands overlap in some cases.

The inclusive purities and all semi-inclusive purities on the proton are largest for the u-quark, because the squared fractional charge of the u-quark increases $P_u^{(h)}$ by a factor of four with respect to the other purities $P_{q \neq u}^{(h)}$. For the same reason, the purities on the neutron are largest for the u_n-quark, shown as the d-quark by isospin rotation. This sensitivity to the u-quark is expected to yield precise results on $[\Delta u / u](x)$. On the other hand sensitivity to the other quark flavours is obtained because contributions by the u-quark cancel due to the similar size of the u-quark purities from e.g. the π^+ and the π^-. Access to the polarizations of the various quark flavours is further improved by the orthogonality of the purities for the different flavours. For example, a separation of the u and d polarizations is possible with the π^+ asymmetries on the proton and the neutron. The polarizations of the $\bar{u}$ and the $\bar{d}$ flavours are similarly identified with the π^- asymmetries. Sensitivity to the strange and anti-strange quarks is obtained through kaons in the final state. The polarization of the s flavour in the nucleon is accessed through the K^- asymmetry and the $\bar{s}$ flavour becomes accessible via the K^+ asymmetry. However, the light quark flavours also dominate these purities, so that large uncertainties on the s and $\bar{s}$ polarizations are expected.

Systematic uncertainties on the purities arise from two main sources, the unpolarized parton distributions and the fragmentation model. The CTEQ5L parameterization is provided without an estimate of the associated uncertainties. The more recent CTEQ6 parameterization [151] includes estimates of the uncertainties in the form of 40 sets of eigenvector parton distributions that parameterize the χ^2 space of the parton distributions with respect to the data. However, an implementation of the CTEQ6 parameterization in the Monte Carlo simulation was not available at the time of this thesis. In addition, the CPU-intensive estimate of the uncertainties based on the 40 eigenvector sets was not possible for this work. Consequently an uncertainty due to the unpolarized parton distributions was not assigned to the quark polarizations.

For the second source of uncertainty, a method to assess the covariance of the JETSET fragmentation parameters was recently suggested [152]. Similarly to the unpolarized parton distributions, it is based on a CPU-intensive parameterization of the χ^2 space of the fragmentation parameters, which is currently not available. Instead, uncertainties were estimated by comparing the current tune with an older tune to HERMES data [153, 154]. While this method is not strictly rigorous, it likely provides an upper estimate of the associated uncertainty. The systematic uncertainty on the purities that follows from this comparison is shown as the shaded bands in each panel. The statistical uncertainties on the purities are negligible.

8.4 The Purity Algorithm

The polarized quark distributions are determined by combining the measured Born asymmetries in a system of equations of the form

$$\vec{A}_1 = \mathcal{C}_R \mathcal{N} \mathcal{P} \, \vec{Q}, \tag{8.12}$$

where $\vec{A}_1$ is the vector of measured Born asymmetries of all types and in all bins of x, $\mathcal{C}_R$ is the matrix of the factors $(1 + R)/(1 + \gamma^2)$, the nuclear mixing matrix $\mathcal{N}$ incorporates Eq. (8.9), and the purity matrix $\mathcal{P}$ is derived from Eq. (8.4). The vector $\vec{Q}$ contains the quark polarizations $[\Delta q/q](x)$. Eq. (8.12) is solved for the vector of quark polarizations by minimizing

$$\chi^2 = \left(\vec{A}_1 - \mathcal{C}_R \mathcal{N} \mathcal{P} \, \vec{Q} \right)^T V_A^{-1} \left(\vec{A}_1 - \mathcal{C}_R \mathcal{N} \mathcal{P} \, \vec{Q} \right), \tag{8.13}$$

where V_A is the covariance matrix of the measured Born asymmetries that includes the correlations of the different types of asymmetries as well as the correlations among the x-bins.

The vector of asymmetries $\vec{A}_1$. The asymmetry vector combines the inclusive and the semi-inclusive asymmetries on the proton and the deuteron in all bins of x. In each bin, the general form of the vector is

$$\vec{A}_1(x_i) = \left(A_{1p}, A_{1p}^{\pi^+}, A_{1p}^{\pi^-}, A_{1d}, A_{1d}^{\pi^+}, A_{1d}^{\pi^-}, A_{1d}^{K^+}, A_{1d}^{K^-} \right)(x_i). \tag{8.14}$$

In the algorithm used for the minimization, the proton asymmetries are further divided into the proton asymmetries measured in 1996 and 1997, in order to account for the different systematic uncertainties of the data-taking periods,

$$\left(A_{1p}, A_{1p}^{\pi^+}, A_{1p}^{\pi^-} \right)(x_i) \longrightarrow \left(A_{1p}^{96}, A_{1p}^{96,\pi^+}, A_{1p}^{96,\pi^-}, A_{1p}^{97}, A_{1p}^{97,\pi^+}, A_{1p}^{97,\pi^-} \right)(x_i). \tag{8.15}$$

Analogously the deuteron asymmetries are divided into the asymmetries measured in 1998, 1999, and 2000. The following discussion of the algorithm disregards this subdivision, but it is trivially extended.

The final vector of measured Born asymmetries $\vec{A}_1$ combines the asymmetries measured in each x-bin consecutively,

$$\vec{A}_1 = \left(\vec{A}_1(x_1), \vec{A}_1(x_2), \dots, \vec{A}_1(x_9) \right). \tag{8.16}$$

The asymmetry vector does not include the asymmetries $A_1^{h^\pm}$ of undifferentiated hadrons shown in Figs. 7.8 and 7.9. These asymmetries add little information to the χ^2-minimization, because they are highly correlated with the pion asymmetries and to a smaller extend with the kaon asymmetries.

The matrix C_R. The matrix C_R of kinematic factors accounts for the factor $(1 + R)/(1 + \gamma^2)$ in each bin of x. The elements of C_R are

$$(C_R)_{ij} = [(1 + R)/(1 + \gamma^2)](x_i)\ \delta_{ij},\tag{8.17}$$

where δ_{ij} is the usual Kronecker symbol; $\delta_{ij} = 1$, if $i = j$ and $\delta_{ij} = 0$ otherwise.

The purity matrix $\mathcal{P}$. The matrix $\mathcal{P}$ contains as elements the purities on the proton and the neutron. In each x-bin, it can be separated in a proton and a neutron purity sub-matrix. The proton sub-matrix is

$$\mathcal{P}_p(x_i) = \begin{pmatrix} P_{up} & P_{\bar{u}p} & P_{dp} & P_{\bar{d}p} & P_{sp} & P_{\bar{s}p} \\ P_{up}^{\pi^+} & P_{\bar{u}p}^{\pi^+} & P_{dp}^{\pi^+} & P_{\bar{d}p}^{\pi^+} & P_{sp}^{\pi^+} & P_{\bar{s}p}^{\pi^+} \\ P_{up}^{\pi^-} & P_{\bar{u}p}^{\pi^-} & P_{dp}^{\pi^-} & P_{\bar{d}p}^{\pi^-} & P_{sp}^{\pi^-} & P_{\bar{s}p}^{\pi^-} \\ P_{up}^{K^+} & P_{\bar{u}p}^{K^+} & P_{dp}^{K^+} & P_{\bar{d}p}^{K^+} & P_{sp}^{K^+} & P_{\bar{s}p}^{K^+} \\ P_{up}^{K^-} & P_{\bar{u}p}^{K^-} & P_{dp}^{K^-} & P_{\bar{d}p}^{K^-} & P_{sp}^{K^-} & P_{\bar{s}p}^{K^-} \end{pmatrix}(x_i)\tag{8.18}$$

The neutron sub-matrix is given by an analogous expression using isospin rotation to identify the (anti-)up and (anti-)down flavour in the neutron with the (anti-)down and (anti-)up flavour in the proton, respectively. The total purity matrix is the block-diagonal matrix of these proton and neutron purity matrices,

$$\mathcal{P} = \begin{pmatrix} \boxed{\begin{matrix} \mathcal{P}_p(x_1) \\ \mathcal{P}_n(x_1) \end{matrix}} & & \\ & \ddots & \\ & & \boxed{\begin{matrix} \mathcal{P}_p(x_9) \\ \mathcal{P}_n(x_9) \end{matrix}} \end{pmatrix}.\tag{8.19}$$

The nuclear mixing matrix $\mathcal{N}$. The nuclear mixing matrix maps the proton and the neutron asymmetries contained in the vector $\mathcal{P}\,\vec{Q}$ onto a vector of proton and deuteron asymmetries. In each

bin, the matrix is given by

$$\mathcal{N}(x_i) = \begin{pmatrix} 1 & & & & & & & & & & & \\ & 1 & & & & & & & & & & \\ & & 1 & & & & & & & & & \\ a & & & & & & b & & & & & \\ & a^{\pi^+} & & & & & & b^{\pi^+} & & & & \\ & & a^{\pi^-} & & & & & & b^{\pi^-} & & & \\ & & & a^{K^+} & & & & & & b^{K^+} & & \\ & & & & a^{K^-} & & & & & & b^{K^-} \end{pmatrix} (x_i) , \qquad (8.20)$$

where all other elements are zero and the factors $a^{(h)}$ and $b^{(h)}$ are given by Eq. (8.9):

$$a^{(h)} = f_{pd}^h p_{pd} , \qquad b^{(h)} = f_{nd}^{(h)} p_{nd} = 1 - f_{pd}^{(h)} p_{pd} . \qquad (8.21)$$

The vertical line in Eq. (8.20) separates the sub-matrices corresponding to the proton and neutron asymmetries; the horizontal line divides the sub-matrices that correspond to the proton and deuteron asymmetries. The total nuclear mixing matrix is similar to the total purity matrix a block-diagonal matrix of the matrices $\mathcal{N}(x_i)$.

The vector of quark polarizations $\vec{Q}$. The vector $\vec{Q}(x_i)$ contains the polarizations of the six quark flavours,

$$\vec{Q}(x_i) = \left(\frac{\Delta u}{u}(x_i), \frac{\Delta \bar{u}}{\bar{u}}(x_i), \frac{\Delta d}{d}(x_i), \frac{\Delta \bar{d}}{\bar{d}}(x_i), \frac{\Delta s}{s}(x_i), \frac{\Delta \bar{s}}{\bar{s}}(x_i) \right) , \qquad (8.22)$$

where as before the total vector $\vec{Q}$ contains consecutively the values for each x-bin. The vector given here makes no additional symmetry assumptions on the quark polarizations.

The covariance matrix V_A. The covariance matrix of the asymmetries consists in general of the statistical and the systematic covariances. The statistical covariance matrix for each dataset is given

by Eq. (7.15). The total statistical covariance is the combination of these covariances,

$$
V_A^{\text{st}} =
\begin{pmatrix}
\boxed{V_{x_1 x_1}^{A_{1p}^B}} & \boxed{V_{x_1 x_2}^{A_{1p}^B}} & \cdots & & & \boxed{V_{x_1 x_9}^{A_{1d}^B}} \\
& \boxed{V_{x_1 x_1}^{A_{1d}^B}} & & & & \\
\vdots & & \ddots & & & \vdots \\
& & & & \boxed{V_{x_9 x_9}^{A_{1p}^B}} & \\
\boxed{V_{x_9 x_1}^{A_{1d}^B}} & & \cdots & & & \boxed{V_{x_9 x_9}^{A_{1d}^B}}
\end{pmatrix}
,
\tag{8.23}
$$

where the sub-matrices are the covariances of the asymmetries A_{1p}^B, A_{1p}^{B,π^+}, and A_{1p}^{B,π^-} for the proton and A_{1d}^B, A_{1d}^{B,π^+}, A_{1d}^{B,π^-}, A_{1d}^{B,K^+}, and A_{1d}^{B,K^-} for the deuteron in a given pair of x-bins.

The systematic covariance matrix V_A^{sy} on the Born asymmetries follows from the systematic uncertainties on the asymmetries and their correlations as described in Sec. 7.6.2. The minimization of Eq. (8.13), however, was carried out without the systematic covariance matrix, because the systematic covariances were found to bias the result of the minimization. The bias is likely due to the approximate singularity of V_A^{sy} caused by e.g. the maximal correlation of the beam polarization measurement for 1996 through 1998, and for 1999 and 2000. More details are given in Sec. 8.7.1.

The χ^2-minimization. The system of equations given in Eq. (8.12) is slightly over-constrained, as eight asymmetries[2] are available to determine the polarizations of six quark flavours. Additional assumptions are imposed on the quark flavours in order to improve the precision of the results on the quark polarizations. The anti-strange polarization was fixed at zero,

$$
\Delta \bar{s}(x) = 0,
\tag{8.24}
$$

because the asymmetries do not provide sufficient constraint on the polarizations of the anti-strange flavour. A discussion of this assumption is found in Sec. 8.7.2. In addition, the polarizations of the sea flavours were assumed to be zero for $x > 0.3$,

$$
\Delta \bar{u}(x) = \Delta \bar{d}(x) = \Delta s(x) = \Delta \bar{s}(x) = 0, \qquad \text{for } x > 0.3.
\tag{8.25}
$$

This assumption is motivated by the small contribution of the sea flavours to the cross section at large values of x. It is imposed because the large uncertainties on the asymmetries for $x > 0.3$ do

---

[2]As noted above, the three asymmetries on the proton are divided into those measured in 1996 and 1997, and the asymmetries on the deuteron into those measured in 1998, 1999, and 2000. Therefore the number of asymmetries in the system of equations is 21, but they represent measurements of only eight physically different asymmetries.

not allow a determination of all polarizations. These constraints are included in the minimization of Eq. (8.13) by separating these fixed parameters $\vec{Q}_{\text{fix}}$ from the free parameters,

$$\chi^2 = \left(\left[\vec{A}_1 - C_R \mathcal{N} \mathcal{P} \vec{Q}_{\text{fix}}\right] - C_R \mathcal{N} \mathcal{P} \vec{Q}\right)^T \left(V_A^{\text{st}}\right)^{-1} \left(\left[\vec{A}_1 - C_R \mathcal{N} \mathcal{P} \vec{Q}_{\text{fix}}\right] - C_R \mathcal{N} \mathcal{P} \vec{Q}\right),$$

(8.26)

where $\vec{Q}$ was identified with the remaining free parameters. The minimization of Eq. (8.26) was carried out using a linear regression [112]. The solution is

$$\vec{Q} = \left(\mathcal{P}_{\text{ef}}^T \left(V_A^{\text{st}}\right)^{-1} \mathcal{P}_{\text{ef}}\right)^{-1} \mathcal{P}_{\text{ef}}^T \left(V_A^{\text{st}}\right)^{-1} \vec{A}_1',$$

(8.27)

where the identifications $\vec{A}_1' \equiv \vec{A}_1 - C_R \mathcal{N} \mathcal{P} \vec{Q}_{\text{fix}}$ and $\mathcal{P}_{\text{ef}} \equiv C_R \mathcal{N} \mathcal{P}$ were used. The covariance matrix of the quark polarizations due to the Born asymmetries follows from Eq. (8.27) by the usual error propagation [112],

$$\begin{aligned} V\left(\vec{Q}\right) &= \left[\left(\mathcal{P}_{\text{ef}}^T \left(V_A^{\text{st}}\right)^{-1} \mathcal{P}_{\text{ef}}\right)^{-1} \mathcal{P}_{\text{ef}}^T \left(V_A^{\text{st}}\right)^{-1}\right] V_A \left[\left(\mathcal{P}_{\text{ef}}^T \left(V_A^{\text{st}}\right)^{-1} \mathcal{P}_{\text{ef}}\right)^{-1} \mathcal{P}_{\text{ef}}^T \left(V_A^{\text{st}}\right)^{-1}\right]^T \\ &= \left[\left(\mathcal{P}_{\text{ef}}^T \left(V_A^{\text{st}}\right)^{-1} \mathcal{P}_{\text{ef}}\right)^{-1} \mathcal{P}_{\text{ef}}^T \left(V_A^{\text{st}}\right)^{-1}\right] V_A \left[\left(V_A^{\text{st}}\right)^{-1} \mathcal{P}_{\text{ef}} \left(\mathcal{P}_{\text{ef}}^T \left(V_A^{\text{st}}\right)^{-1} \mathcal{P}_{\text{ef}}\right)^{-1}\right], \end{aligned}$$

(8.28)

where the covariance matrix V_A on the asymmetries includes the statistical and the systematic covariance, $V_A = V_A^{\text{st}} + V_A^{\text{sy}}$. Additional systematic uncertainties on the quark polarizations arise due to the imposed constraints, the unpolarized parton distribution functions and the fragmentation model. These uncertainties were included in the total systematic uncertainties on the quark polarizations. They are discussed in Sec. 8.6.

8.5 Results

The quark polarizations. The quark polarizations determined using the linear regression described under the assumptions of Eq. (8.24) and Eq. (8.25) are shown in Fig. 8.3 as a function of x at the measured value of Q^2 in each bin. The values of the polarizations are listed in Tab. C.1 in App. C. The value of the reduced χ^2 of the fit is $\chi^2/ndf = 0.91$. The number of degrees of freedom is $ndf = 150$ (six asymmetries on the proton, 15 asymmetries on the deuteron in nine x-bins and 39 quark polarizations). The polarization of the u-quarks is positive in the measured range of x with the largest polarizations at high x where the valence quarks dominate. The polarization of the d-quark is negative and also reaches the largest (negative) polarizations in the x-range where the
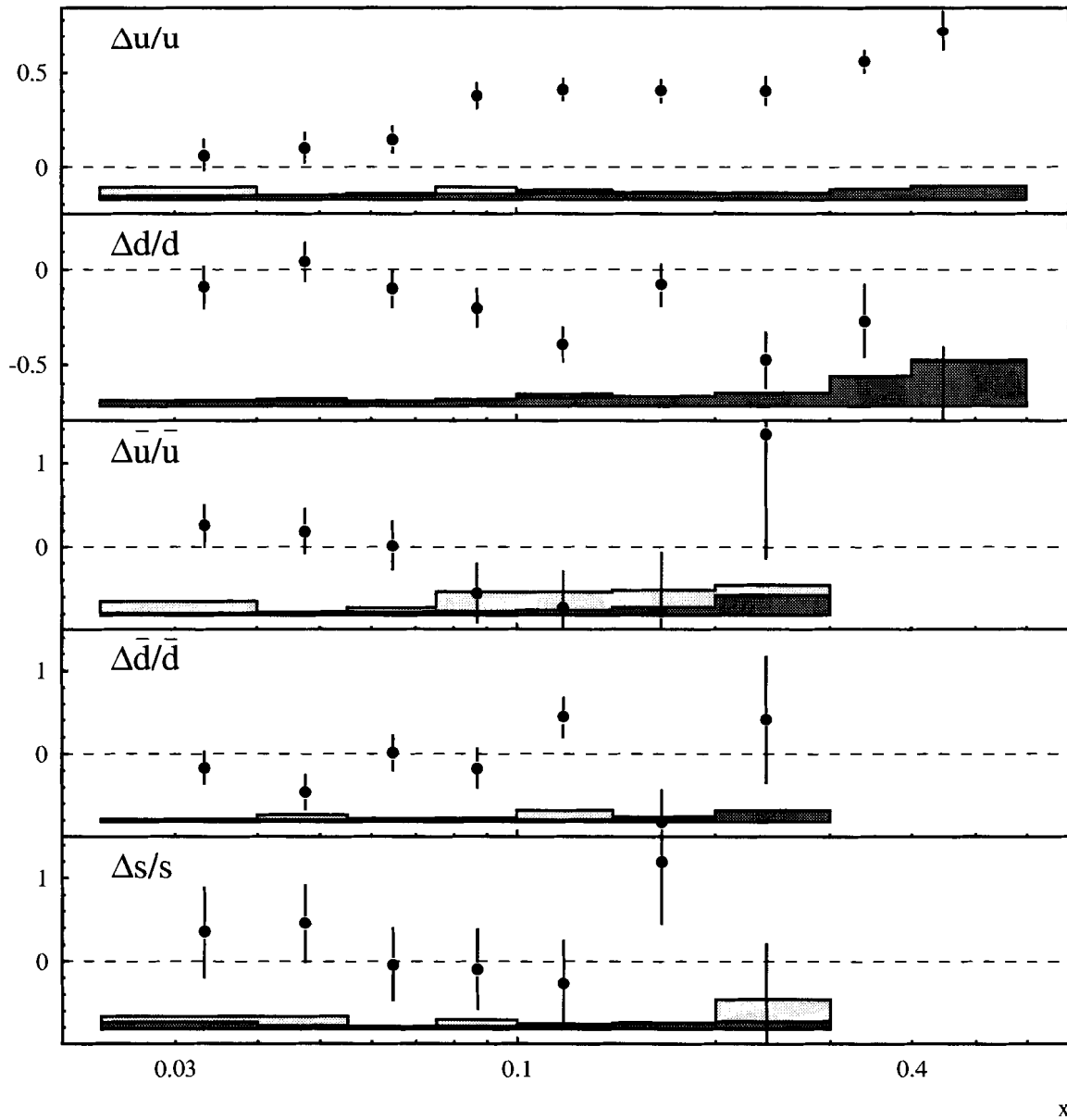
Figure 8.3: The polarizations of the quark flavours in the proton as a function of x. The error bars represent the statistical uncertainty. The dark-shaded shows the systematic uncertainty due to the Born asymmetries and the light-shaded band is the uncertainty due to the fragmentation functions, the unpolarized parton distributions and the assumptions on the polarization of the sea.
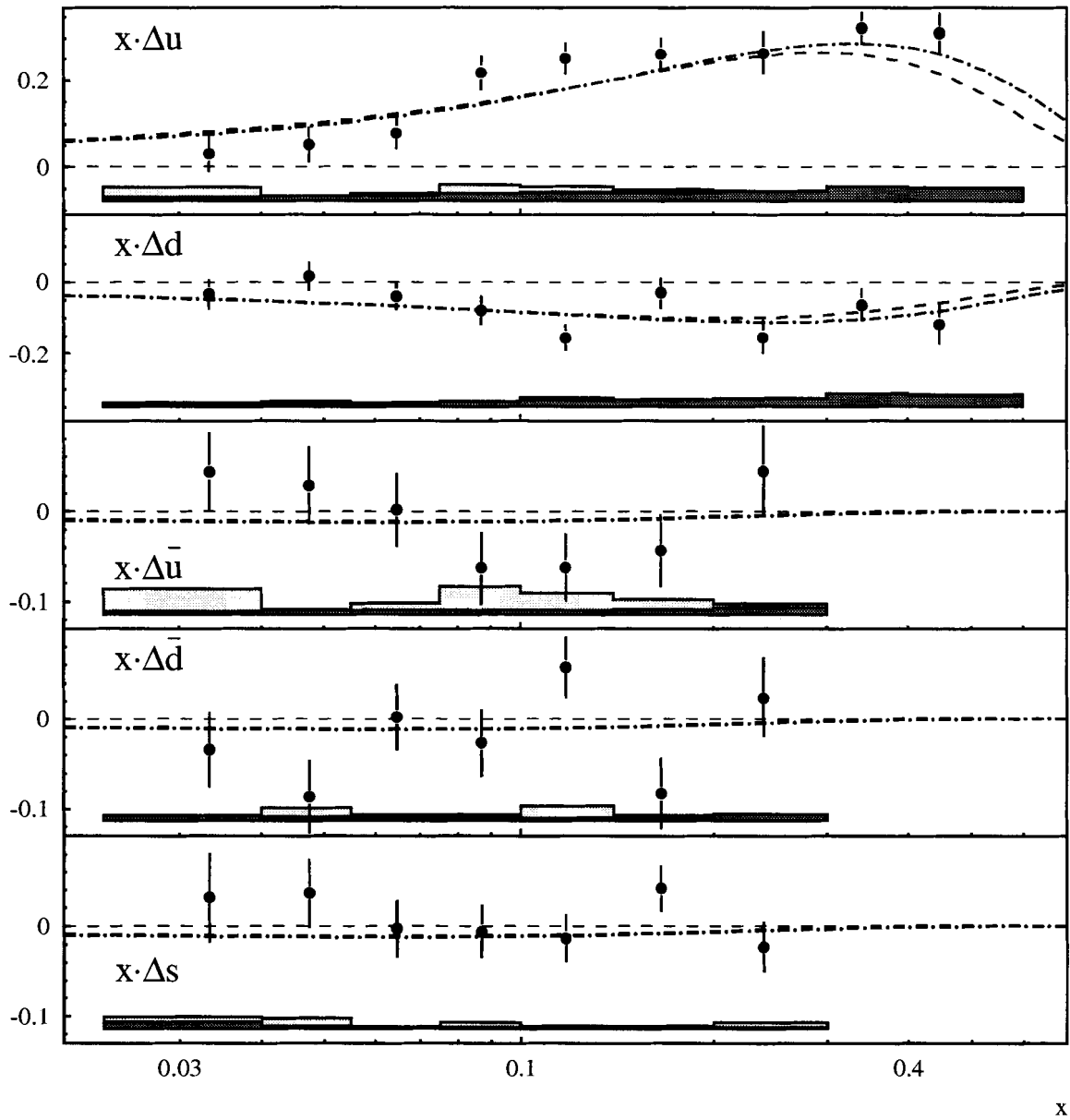
Figure 8.4: The polarized parton densities of the proton as a function of x. The distributions were evolved to common $Q_0^2 = 2.5\,\text{GeV}^2$. Also shown are the results of fits to inclusive data. The dashed line shows the GRSV2000 parameterization [64] and the dashed-dotted line the Böttcher-Blümlein parameterization [155]. The GRSV parameterization was scaled with a factor $1/(1 + R)$. For an explanation of the uncertainties, see Fig. 8.3.

valence quarks dominate. The polarization of the light sea flavours $\bar{u}$ and $\bar{d}$, and the polarization of the strange sea are consistent with zero. The values of the reduced χ^2 for the zero hypothesis are 7.4/7, 11.2/7, and 4.3/7 for the $\bar{u}$, the $\bar{d}$, and the s-flavour respectively. The $\bar{d}$-quark has therefore the highest probability for a non-zero polarization, but the data largely fluctuate about zero and do not suggest a systematic trend. Hence, the up and down flavours carry most of the spin that the quarks contribute to the nucleon spin. For both flavours, the largest contribution is due to the valence quarks.

The polarizations determined here are correlated between flavours and between x-bins. The statistical correlations are listed in Tab. C.3 in App. C. Similar to the asymmetries the correlations between x-bins are largest for neighbouring bins, reaching an absolute value of about 25 %. The correlations decrease rapidly for more distant bins. These bin-to-bin correlations are a consequence of the detector smearing and higher order QED effects in the measured asymmetries. Between flavours the measurement of u and $\bar{u}$ polarizations has a strong negative correlation. The negative correlation between the measured $[\Delta d/d](x)$ and $[\Delta \bar{d}/\bar{d}](x)$ is also large but slightly smaller in magnitude. These correlations result from the sensitivity of the inclusive DIS cross section to the sums $e_q^2(q(x) + \bar{q}(x))$ for each flavour and anti-flavour (see Eqs. (2.23) and (2.28)). For example, the anti-correlation of the u and the $\bar{u}$ flavour is due to a high probability to scatter off a $\bar{u}$ quark, if scattering off a u quark has not occurred. The inclusion of semi-inclusive asymmetries decreases this large negative correlation only by a small amount, because the differences between the semi-inclusive and the inclusive asymmetries are small. The u and d flavours are found to be sizably anti-correlated, because these flavours make up the valence content in the nucleon. The observed anti-correlation of the $\bar{u}$ and $\bar{d}$ flavour is caused by the dominance of the light sea in comparison to the strange sea.

The polarized parton densities.   The polarized quark densities $\Delta q(x, Q^2)$ were determined from the polarizations under the assumption that the polarizations scale. This assumption is based on the approximate Q^2-independence of the ratio g_1/F_1 as outlined in Sec. 2.3.2 and the observed scaling behaviour of the semi-inclusive asymmetries $A_1^{h^\pm}$ shown in Figs. 7.8 and 7.9 by comparison of the HERMES data with the SMC data. The polarized densities are thus evolved to a common Q_0^2 of $2.5\,\mathrm{GeV}^2$ using the evolution of the unpolarized parton distributions,

$$\Delta q(x, Q_0^2) = \frac{\Delta q}{q}(x)\, q(x, Q_0^2). \tag{8.29}$$

Table 8.2: Comparison of the measured polarized parton densities with parameterizations of inclusive data and with the zero hypothesis. Listed are the reduced values χ^2/ndf for each hypothesis.

	$x\Delta u(x)$	$x\Delta d(x)$	$x\Delta\bar{u}(x)$	$x\Delta\bar{d}(x)$	$x\Delta s(x)$
GRSV2000	1.41	1.12	0.97	1.34	0.91
BB	1.02	1.06	0.97	1.32	0.95
$x\Delta q(x) \equiv 0$	13.19	2.50	1.06	1.60	0.61
ndf	9	9	7	7	7

The densities, evolved using the CTEQ5L parameterization distributions, are presented in Fig. 8.4 and listed in Tab. C.1 in App. C. The data are compared with polarized parton distributions [64, 155] derived from global fits to inclusive data from other experiments. The GRSV2000 parameterization which was fitted using the assumption $R = 0$ is shown with the scaling factor $1/(1 + R)$ to match this analysis. The χ^2-values of the comparison of the measured densities with the parameterizations and the zero hypothesis are given in Tab. 8.2. The measured densities are in good agreement with the parameterizations. The data favour the BB parameterization of the u-quark, which is a result of the better agreement at large x. The small negative density of the $\bar{d}$-quark predicted by both parameterizations is preferred over the zero hypothesis. The measured strange density is within the uncertainties in agreement with the negative values of the parameterizations.

Asymmetry of the polarized light quark sea. In unpolarized deep-inelastic scattering, the flavour-symmetry of the light sea quarks is observed to be broken, $\bar{d}(x, Q^2) - \bar{u}(x, Q^2) > 0$ [86, 156, 157]. Consequently the violation of the Gottfried sum rule is experimentally well established (see Sec. 2.4). In the polarized sector, the chiral quark soliton model (χQSM) [158] similarly predicts an asymmetry in the polarized light sea densities, $\Delta\bar{u}(x) - \Delta\bar{d}(x) > 0$. The χQSM models baryons as soliton solutions of the chiral Lagrangian in the limit of infinite quark colours (large N_c) and in the limit of massless quarks (the chiral limit). The model relies on few input parameters unlike the GRSV2000 and the BB parameterizations discussed above, that use inclusive data as input. The χQSM is therefore unbiased with respect to experimental results. A statistical model [159] which describes the nucleon as a gas of massless partons and a model based on the meson cloud picture [160] also predict sizable asymmetries that agree in sign and order of magnitude with the predictions in the χQSM. On the other hand an analysis in the meson cloud model recently predicted a small
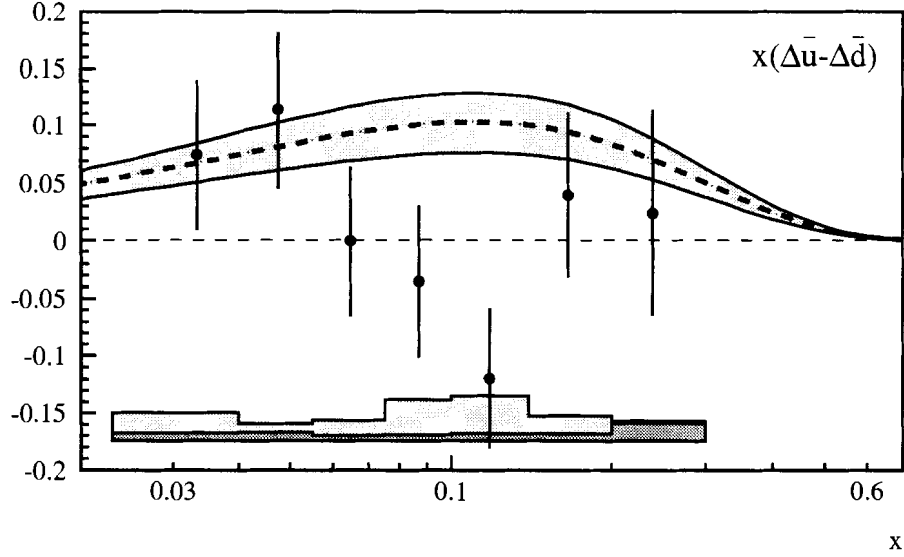
Figure 8.5: The asymmetry of the polarized light quark sea, $x(\Delta\bar{u}(x) - \Delta\bar{d}(x))$. Shown is the result of this analysis in comparison with the prediction in the chiral quark soliton model [158]. The band about the prediction illustrates its uncertainty. The presentation of the uncertainties on the measurement is analogous to Fig. 8.3.

negative asymmetry, $\Delta\bar{u}(x) - \Delta\bar{d}(x) < 0$ [161].

The measured inclusive and semi-inclusive Born asymmetries were used in a separate fit to compute this flavour asymmetry. In this fit, the parameter $[\Delta\bar{u}/\bar{u}](x)$ was replaced with $[(\Delta\bar{u} - \Delta\bar{d})/(\bar{u} - \bar{d})](x)$. The asymmetry $x(\Delta\bar{u} - \Delta\bar{d})(x)$ is presented in Fig. 8.5. For comparison, the asymmetry calculated in the χQSM [158] is also shown as an example. The value of the reduced χ^2 for the symmetry hypothesis is $7.7/7$ and the reduced χ^2 of the comparison to the χQSM is $17.6/7$. The measurement thus shows no evidence of an asymmetry in the polarized light flavour sea. The measurement is not compatible with the predictions in the χQSM. However, in view of the various predictions listed above and the large fluctuations in the data, more measurements are necessary to conclusively rule out any of the models.

8.6 Systematic Uncertainties

The Born asymmetries. The systematic covariance matrix of the Born asymmetries is constructed from the systematic uncertainties discussed in Sec. 7.6.2. The systematic covariance matrix of the

quark polarizations follows using Eq. (8.28) with the systematic covariance matrix V_A^{sy}.

The constraints on the sea quarks. Uncertainties due to the constraints given in Eq. (8.24) and Eq. (8.25) were estimated by assuming a uniform distribution of the constrained polarization within the limits defined by the unpolarized parton distributions,

$$\left| \Delta q(x, Q^2) \right| \leq \frac{1 + \gamma^2}{1 + R(x, Q^2)} \left| q(x, Q^2) \right| , \tag{8.30}$$

known as the positivity limit. The factor $(1 + \gamma^2)/(1 + R)$ arises from the definition of the CTEQ5L parameterization used here (see Sec. 8.1). Given these limits, the quark polarizations were evaluated with the positive limits of the positivity constraint and in another fit with the negative limits given by

$$\frac{\Delta \bar{s}}{\bar{s}}(x_i) = \pm \frac{1 + \gamma^2}{\sqrt{3}\,(1 + R(x_i))} ,$$

$$\frac{\Delta \bar{u}}{\bar{u}}(x_i) = \frac{\Delta \bar{d}}{\bar{d}}(x_i) = \frac{\Delta s}{s}(x_i) = \pm \frac{1 + \gamma^2}{\sqrt{3}\,(1 + R(x_i))} , \quad \text{for} \quad x_i > 0.3, \tag{8.31}$$

where the factor of $1/\sqrt{3}$ is the standard deviation of a uniform distribution in the range $[-1, +1]$ [112]. The maximum deviation of the resulting quark polarizations to those obtained using Eqs. (8.24) and (8.25) was assigned as the uncertainty.

The unpolarized parton distributions. The default parameterization of the unpolarized parton distributions used in this analysis is the CTEQ5L parameterization. It was used to calculate the purities and to evolve the polarizations in order to obtain the parton densities at a common scale. As noted in Sec. 8.3 uncertainty estimates for the CTEQ5L parameterization are not available. An uncertainty due to the unpolarized parton distributions was therefore not assigned.

The fragmentation tune. As outlined in Sec. 8.3 uncertainties on the purities due to the fragmentation tune of the Monte Carlo simulation were estimated by comparing the purities of the default tune and an older HERMES tune. The uncertainties on the quark polarizations and the densities were estimated by comparing the results of a fit based on purities using the old tune with the fit using the default purities. The difference in the polarizations and the densities was assigned as the systematic uncertainty due to the fragmentation tune.

Total systematic uncertainty. The total systematic covariance matrix of the quark polarizations is the sum of the covariances of the sources listed above. The total systematic uncertainties are shown as the error bands in Figs. 8.3, 8.4, and 8.5. The bands are divided into the uncertainty due to the purity model and the uncertainty due to the asymmetry measurement. The individual uncertainties on the quark polarizations are listed in Tab. C.4 in App. C.

8.7 Systematic Studies

8.7.1 The Systematic Covariance Matrix

The linear regression was carried out using the statistical covariance matrix only, as mentioned in Sec. 8.4. The systematic covariance matrix was omitted, because it was found to bias the result of the fit. Fig. 8.6 illustrates this effect. The panels on the left hand side show the polarizations calculated in a linear regression with V_A^{st} and those computed with $V_A^{st} + V_A^{sy}$. The latter result systematically deviates from the first, which is clearly visible in the polarizations of the u-flavour and the d-flavour. The observed bias due to the systematic covariance matrix is not expected, as the linear regression is deterministic and should not systematically depend on the covariance matrices used [162]. The panels on the right hand side confirm that the bias is due to the systematic covariances. The plot shows the default fit result and two additional fits. In the first additional fit, the statistical uncertainties were increased by a factor of 100. The second additional fit was computed with the systematic uncertainties scaled by 100. This latter fit significantly deviates from the default fit, while the linear regression is stable with respect to an increase of the statistical uncertainties. There is thus strong evidence that the systematic covariances bias the result. Consequently the fit was carried out with the statistical covariance matrix only.

8.7.2 The Assumption on the Strange Quark Polarizations

The polarization of the anti-strange quarks was fixed to zero (see Eq. (8.24)) in the linear regression. This assumption was imposed because the asymmetries, specifically the kaon asymmetries, provide little constraint on the anti-strange polarization due to their large uncertainties. In addition, the production of positive kaons in the final state is dominated by events where a u-quark was struck (see Fig. 8.2). Sensitivity to the polarization of the strange quarks is better, because the valence quarks in the negative kaon are both sea-objects in the nucleon. The assumption of zero anti-strange
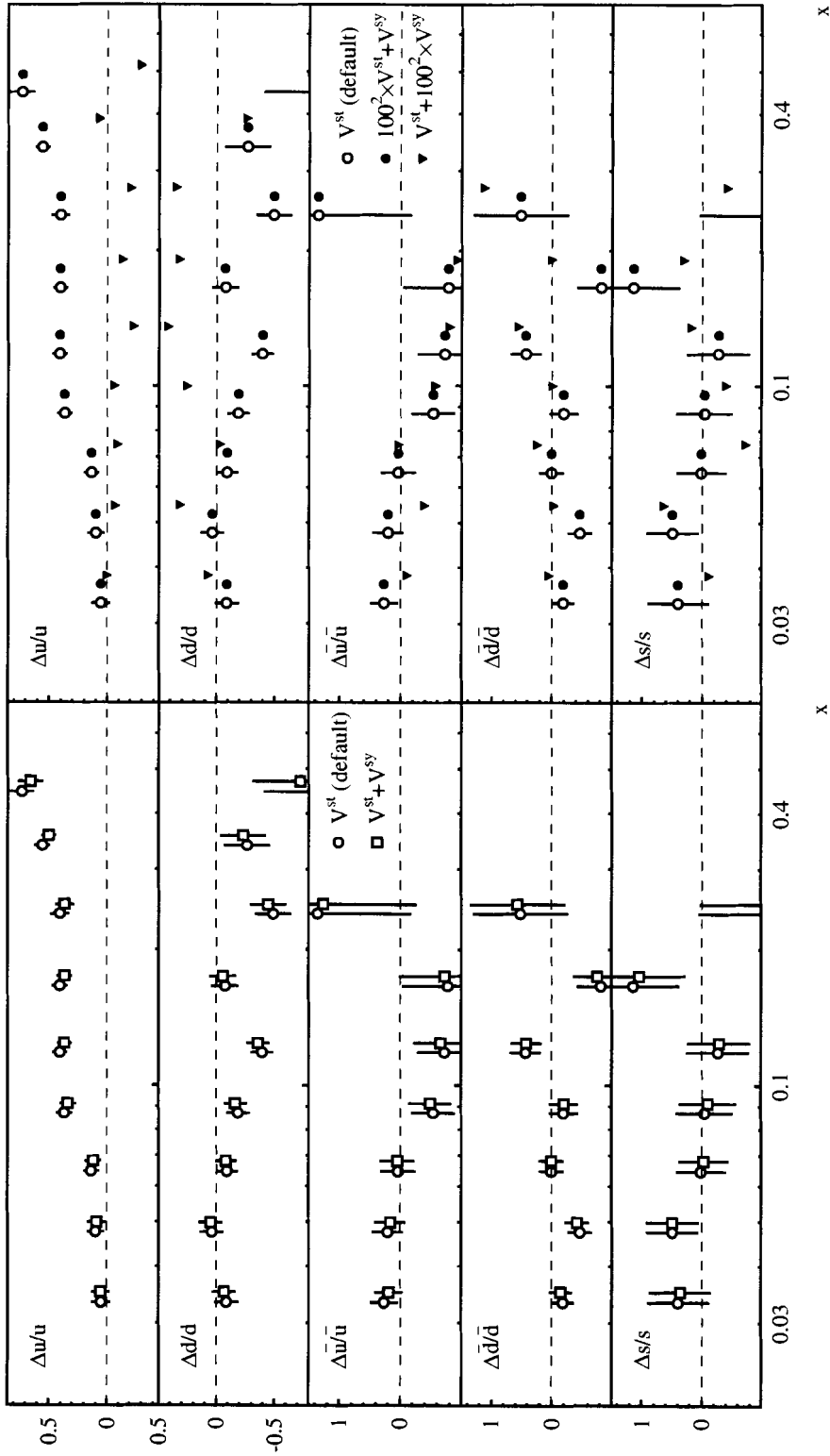
Figure 8.6: Bias of the quark polarizations caused by the systematic covariance matrix. The left hand panels show the difference between the default regression using the statistical covariances only to the regression using the statistical and systematic covariance. The right hand panels show the default results in comparison to two fits with increased covariances, $(100^2 \times V_A^{\text{st}}) + V_A^{\text{sy}}$ and $V_A^{\text{st}} + (100^2 \times V_A^{\text{sy}})$ respectively. The statistical uncertainties on these results are not shown. Data other than the default data are offset in x for presentation. Systematic errors are not shown.
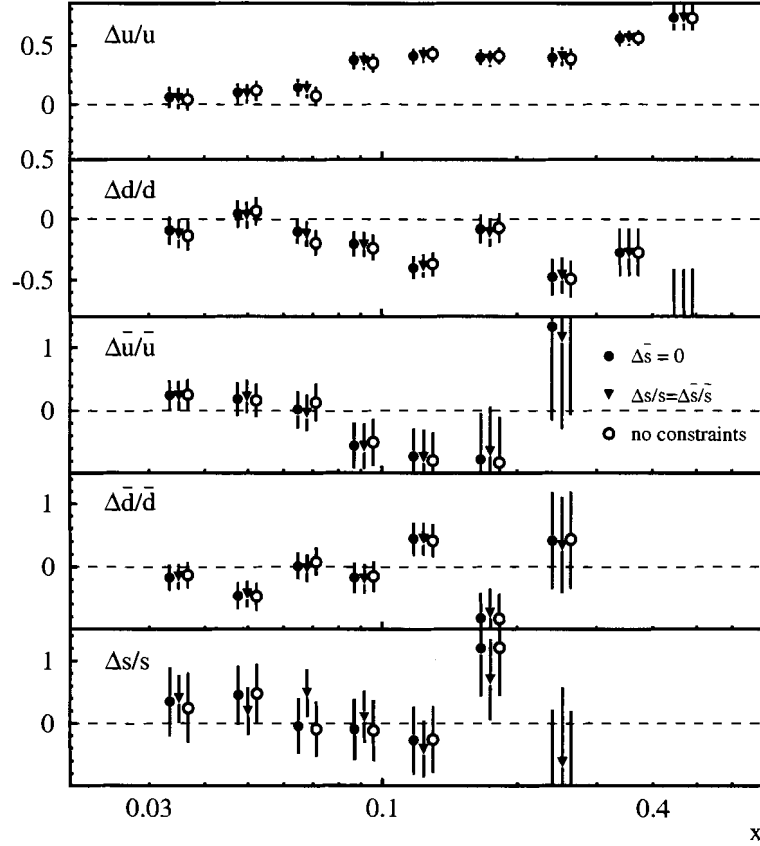
Figure 8.7: Quark polarizations computed assuming zero anti-strange polarization, $\Delta \bar{s}(x) = 0$, a symmetric strange sea, $[\Delta s/s](x) = [\Delta \bar{s}/\bar{s}](x)$, and computed with no assumption on the strange sea. The error bars show the statistical uncertainties. The inverted triangles and the open circles were offset in x for presentation. Systematic uncertainties are not shown.

polarization is further motivated by the chiral quark soliton model that suggests the polarizations of the strange and anti-strange sea are different [163].

In perturbative QCD, the polarization of the sea quarks and anti-quarks is expected to be symmetric. Therefore the polarization of the strange sea is expected to equal the polarization of the anti-strange sea,

$$\frac{\Delta s}{s}(x) = \frac{\Delta \bar{s}}{\bar{s}}(x).$$

(8.32)

This assumption is incorporated in Eq. (8.12) by replacing the vector $\vec{Q}$ given in Eq. (8.22) by a

matrix $\mathcal{M}$ that maps the remaining free parameters $\vec{Q}_f$ onto the vector $\vec{Q}$,

$$\vec{Q} = \mathcal{M}\vec{Q}_f. \tag{8.33}$$

For the assumption of symmetric strange sea polarization, the vector $\vec{Q}_f(x_i)$ in each bin is

$$\vec{Q}_f(x_i) = \left(\frac{\Delta u}{u}(x_i),\ \frac{\Delta \bar{u}}{\bar{u}}(x_i),\ \frac{\Delta d}{d}(x_i),\ \frac{\Delta \bar{d}}{\bar{d}}(x_i),\ \frac{\Delta s}{s}(x_i) = \frac{\Delta \bar{s}}{\bar{s}}(x_i) \right), \tag{8.34}$$

and the matrix $\mathcal{M}(x_i)$ is given by

$$\mathcal{M}(x_i) = \begin{pmatrix} 1 & & & & \\ & 1 & & & \\ & & 1 & & \\ & & & 1 & \\ & & & & 1 \\ & & & & 1 \end{pmatrix}, \tag{8.35}$$

where all other entries are zero. In combination with the purity matrix $\mathcal{P}$, the mapping matrix leads to an effective purity $\mathcal{PM}$ that includes the symmetry assumption.

A comparison of the quark polarizations computed with these two assumptions is shown in Fig. 8.7. Also shown are the polarizations computed without constraining the polarization of the strange or anti-strange sea. The various results are in good agreement. The sea-polarizations extracted assuming an unpolarized anti-strange sea agree with those extracted without constraints. The agreement of the sea polarizations extracted assuming Eq. (8.32) with the polarizations computed without constraints on the strange sea is not as good.

8.7.3 Influence of the Inclusive Asymmetry

The quark polarizations were computed without the inclusive symmetries in order to detect flaws in the applied models of the asymmetries or in the formalism in general. A difference of the resulting polarizations to those computed with the inclusive asymmetries could be due to several sources: The LUND model used in the Monte Carlo simulation could badly describe the fragmentation process; the limited acceptance of the spectrometer could bias the semi-inclusive asymmetries (see also Sec.7.7.4); the detector smearing corrections and in particular the higher-order QED corrections could bias the inclusive asymmetries; finally the purity ansatz in general could be flawed.

Figure 8.8: Quark polarizations computed with and without the inclusive asymmetries. The latter dataset was offset in x for presentation. The error bars shown are statistical. Systematic uncertainties are omitted.

A comparison of the quark polarizations computed with and without inclusive asymmetries is shown in Fig. 8.8. The two sets of data agree within the statistical uncertainties. There is thus no indication for any of the listed hypotheses.

The comparison also illustrates that the inclusive asymmetries improve the measurement mostly at large values of x, where there is little phase space for the generation of hadrons (see Fig. 6.2). This was already illustrated in Fig. 7.13.

8.7.4 The Pion-Charge-Difference-Asymmetry Method

The polarized valence quark distributions in the proton can also be extracted using a method [164] that does not rely on the calculation of purities with a Monte Carlo simulation. Instead the algorithm is based on the assumption that the various fragmentation functions of the pions can be classified into

favoured, disfavoured, and strange fragmentation functions labelled D_1, D_2, and D_3 respectively,

$$D_1(Q^2, z) \equiv D_u^{\pi^+}(Q^2, z) = D_d^{\pi^-}(Q^2, z) = D_d^{\pi^+}(Q^2, z) = D_{\bar{u}}^{\pi^-}(Q^2, z)$$

$$D_2(Q^2, z) \equiv D_d^{\pi^+}(Q^2, z) = D_u^{\pi^-}(Q^2, z) = D_{\bar{u}}^{\pi^+}(Q^2, z) = D_{\bar{d}}^{\pi^-}(Q^2, z) \tag{8.36}$$

$$D_3(Q^2, z) \equiv D_s^{\pi^+}(Q^2, z) = D_s^{\pi^-}(Q^2, z) = D_{\bar{s}}^{\pi^+}(Q^2, z) = D_{\bar{s}}^{\pi^-}(Q^2, z). \tag{8.37}$$

These relations follow using isospin and charge conjugation symmetry. Under the additional asssumption of factorization as given in Eq. (8.1), the asymmetry of the pion charge difference count rate $N_{\pi^+} - N_{\pi^-}$ on the proton is [164]

$$A_{1p}^{\pi^+ - \pi^-}(x, Q^2) = \frac{1 + R(x, Q^2)}{1 + \gamma^2} \frac{4\Delta u_V(x, Q^2) - \Delta d_V(x, Q^2)}{4 u_V(x, Q^2) - d_V(x, Q^2)}, \tag{8.38}$$

where the valence quark densities $(\Delta)u_V(x)$ and $(\Delta)d_V(x)$ were defined in Eq. (2.34). Similarly the asymmetry $A_{1d}^{\pi^+ - \pi^-}(x, Q^2)$ on the deuteron is

$$A_{1d}^{\pi^+ - \pi^-}(x, Q^2) = \frac{1 + R(x, Q^2)}{1 + \gamma^2} \frac{\Delta u_V(x, Q^2) + \Delta d_V(x, Q^2)}{u_V(x, Q^2) + d_V(x, Q^2)}, \tag{8.39}$$

where isospin symmetry was used to express the parton densities in the neutron in terms of those in the proton. These two equations can be solved for the polarized valence quark densities,

$$\Delta u_V(x, Q^2) = \frac{1 + \gamma^2}{5(1 + R(x, Q^2))} \Big[\big(4u_V(x, Q^2) - d_V(x, Q^2)\big) A_{1p}^{\pi^+ - \pi^-}(x, Q^2)$$

$$+ \big(u_V(x, Q^2) - d_V(x, Q^2)\big) A_{1d}^{\pi^+ - \pi^-}(x, Q^2) \Big] \tag{8.40}$$

$$\Delta d_V(x, Q^2) = \frac{1 + \gamma^2}{5(1 + R(x, Q^2))} \Big[- \big(4u_V(x, Q^2) - d_V(x, Q^2)\big) A_{1p}^{\pi^+ - \pi^-}(x, Q^2)$$

$$+ 4 \big(u_V(x, Q^2) - d_V(x, Q^2)\big) A_{1d}^{\pi^+ - \pi^-}(x, Q^2) \Big] \tag{8.41}$$

For more details on the algorithm, see e.g. Refs. [109, 113].

The Born asymmetries $A_{1p}^{\pi^+ - \pi^-}(x)$ and $A_{1d}^{\pi^+ - \pi^-}(x)$ are shown in Fig. 8.9 at the average Q^2 values in each bin. The valence quark densities $x\Delta u_V(x, Q_0^2)$ and $x\Delta d_V(x, Q_0^2)$ at $Q_0^2 = 2.5\,\text{GeV}^2$ determined using these asymmetries are presented in Fig. 8.10. The valence quark densities extracted using the purity algorithm are also shown for comparison. The uncertainties on the valence densities determined here are substantially larger than those on the densities computed with the
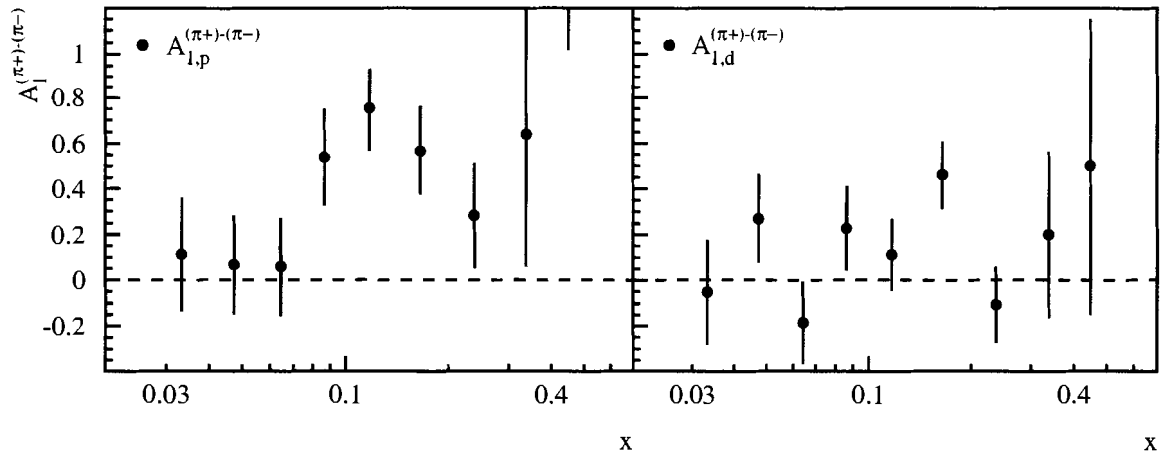
Figure 8.9: The pion charge difference asymmetries on the proton and on the deuteron. The error bars show the statistical uncertainties. Systematic uncertainties are omitted.
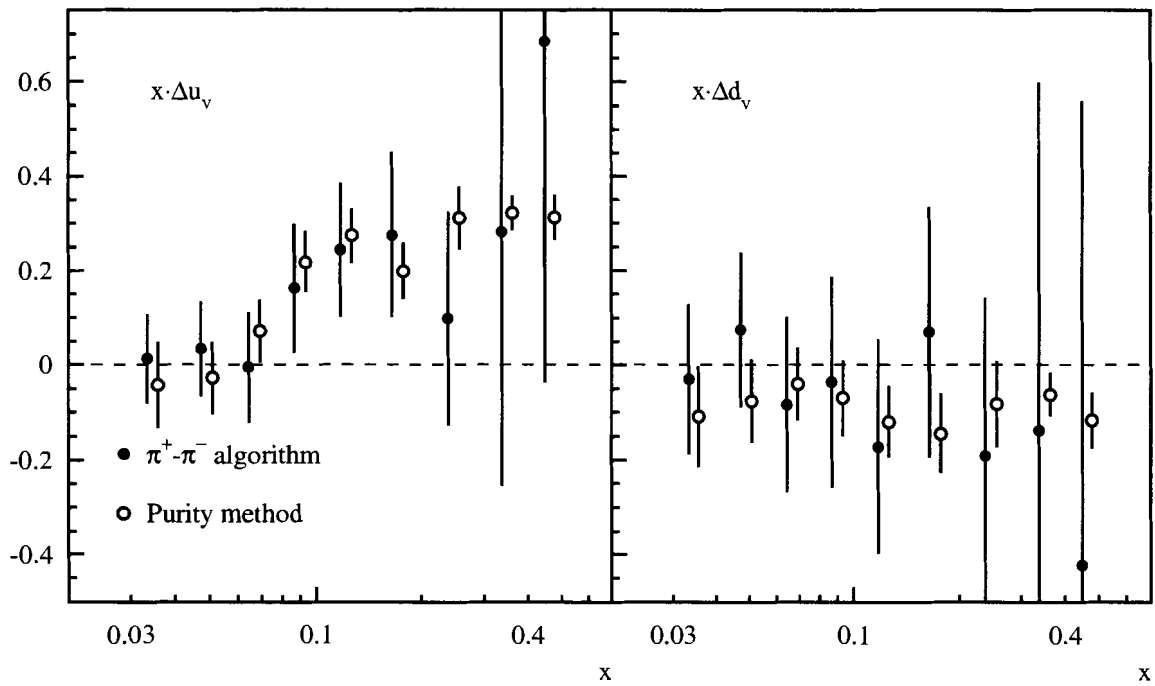
Figure 8.10: Polarized valence quark distributions computed from the charge difference asymmetries at $Q_0^2 = 2.5\,\mathrm{GeV}^2$. For comparison, the same densities extracted with the purity algorithm are shown slightly offset in x. The error bars represent the statistical uncertainties. Systematic uncertainties are omitted.

purity algorithm. Their large size is due to the computation being based on the charge difference asymmetries of pions only. Within these uncertainties the densities computed with the pion charge difference algorithm agree with the results of the purity algorithm. However, this algorithm is not sensitive to the polarization of the quark sea and therefore does not provide a cross check of the measured sea polarizations. Within these limitations the pion charge difference asymmetry algorithm confirms that the valence quark densities determined with the purity algorithm are not biased by the assumptions applied, *e.g.* the fragmentation tune.

8.8 Sum Rules

8.8.1 Determination of the Moments

The polarized parton densities can be used to test the sum rules described in Sec. 2.4. The nth moment of the parton density $\Delta q(x, Q^2)$ is given by,

$$\Delta^{(n)} q(Q_0^2) \equiv \int_0^1 dx \; x^{n-1} \, \Delta q(x, Q_0^2). \tag{8.42}$$

The polarized parton densities were measured in the range $0.023 < x < 0.6$. In this range, the moments can be determined from the measured distributions as,

$$\left(\Delta^{(n)} q(Q_0^2) \right)_{\text{meas}} = \sum_i \left[\frac{\Delta q}{q}(x_i) \int_{\xi_i}^{\xi_{i+1}} dx \; x^{n-1} \, q(x, Q_0^2) \right], \tag{8.43}$$

where the integration runs over the range $[\xi_i, \xi_{i+1}]$ in bin i and the sum runs over all bins. The quark polarization $[\Delta q/q](x_i)$ is assumed to be constant in each bin and the unpolarized parton densities $q(x, Q_0^2)$ at the scale Q_0^2 are computed using the CTEQ5L parameterization [145]. The covariances on Eq. (8.43) are

$$V_{\text{meas}}^{qq'} = \sum_{i,j} \int_{\xi_i}^{\xi_{i+1}} dx \; x^{n-1} \, q(x, Q_0^2) \int_{\xi_j}^{\xi_{j+1}} dx \; x^{n-1} \, q'(x, Q_0^2) \, V\left(\tfrac{\Delta q}{q}(x_i), \tfrac{\Delta q'}{q'}(x_j) \right) \tag{8.44}$$

where the covariance on the quark polarizations is given in Eq. (8.28) modified to include the additional systematic uncertainties discussed in Sec. 8.6.

The measurement has to be extrapolated into the unmeasured regions at small and large x in order to calculate the moments in the full range of x. Theoretical models predict various functional forms of the structure function g_1 at low x. For example, a model based on non-perturbative gluon

exchange predicts a behaviour proportional to $\log(1/x)$ [165]. In this thesis, the functional form $n_q\, x^{-\alpha}$ that stems from Regge theory [166] was used to parameterize the densities $\Delta q(x)$ at small x. A value of $\alpha = -0.07^{+0.42}_{-0.32}$ which denotes the intercept of the axial vector Regge trajectories, was obtained in fits to EMC data on g_1 [167]. Assuming a value of $\alpha = 0$, the constant n_q was fitted to each of the measured quark densities in the range $0.023 < x < 0.075$. The results extrapolated into the unmeasured region at low x were compared with the unpolarized densities that are known to smaller x and that constrain the polarized densities via the positivity limit (Eq. (8.30)). The fits were found to be well inside these limits, despite measurements that found the Regge model to badly describe the behaviour of g_{1n} at low x [28]. The integral of these fits over the unmeasured range $0 < x < 0.023$ was used as an estimate of the low-x contribution to the moments. The uncertainties on the integrals follow from the uncertainties on the fitted parameters N_q and α_q.

The behaviour of the polarized parton densities in the unmeasured region at large x was estimated by extrapolating the measured quark polarizations using the functional form

$$\frac{\Delta q}{q}(x) = N_q\, x^{\alpha_q}. \tag{8.45}$$

This behaviour is motivated by the general functional form $N_q\, x^{\alpha_q} (1 - x)^{\beta_q}$ which is a commonly used approximation in QCD fits [7, 168]. At large x the factor $(1 - x)^{\beta_q}$ becomes small, and was omitted, to improve the precision of the fit. The two remaining parameters N_q and α_q were obtained in fits to the measured quark polarizations in the full measured range $0.023 < x < 0.6$. The contributions to the moments in the range $0.6 < x < 1$ were estimated with the integrals of these extrapolations. The systematic uncertainty was conservatively estimated to be 100 % of the integral. Note that the contribution to the moments and thus the associated uncertainty is small, because the unpolarized densities and hence the polarized densities in this region are very small.

The first moments of the measured polarized parton densities are at the scale $Q_0^2 = 2.5\,\mathrm{GeV}^2$:

$$\Delta u = 0.649 \pm 0.040 \pm 0.053,$$

$$\Delta d = -0.239 \pm 0.041 \pm 0.050,$$

$$\Delta \bar{u} = 0.003 \pm 0.038 \pm 0.023, \tag{8.46}$$

$$\Delta \bar{d} = -0.070 \pm 0.035 \pm 0.011,$$

$$\Delta s = 0.032 \pm 0.034 \pm 0.010,$$

where the first uncertainty is the statistical uncertainty and the second is the systematic uncertainty. The u quarks contribute the largest amount to the nucleon spin fraction carried by the quark spins. The contribution to the nucleon spin by the spin of the d quarks is negative and the sea flavours contribute an amount consistent with zero within the combined uncertainties.

The first moments of the measured polarized parton densities are also listed in Tab. C.5 in App. C for the measured range, as well as for the low and high x extrapolations, and for the full x-range. The statistical and systematic correlations of the first moments in the measured range are given in Tab. C.6 in App. C. The results for the moments presented here are based on an implementation of the moment formalism by M. Beckmann [169].

8.8.2   The Bjørken Sum Rule

The Bjørken sum rule introduced in Sec. 2.4.1 can be rewritten in terms of the isotriplet combination Δq_3,

$$\Delta q_3(Q^2) = \left| \frac{g_A}{g_V} \right| \Delta C_{NS}(Q^2), \qquad (8.47)$$

where the non-singlet coefficient function $\Delta C_{NS}(Q^2)$ is given in Eq. (2.46). Using a value of the strong coupling constant $\alpha_s^{(n_f=3)}(2.5\,\text{GeV}^2) = 0.351 \pm 0.021$ for three active quark flavours [18], the coefficient function is $\Delta C_{NS}(Q_0^2) = 0.795 \pm 0.022$. The isotriplet combination computed from the moments of the measured parton densities at $Q_0^2 = 2.5\,\text{GeV}^2$ is

$$\Delta q_3(Q_0^2) = 0.961 \pm 0.051(\text{stat}) \pm 0.110(\text{syst}). \qquad (8.48)$$

The result deviates from the expectation of $|g_A/g_V|\,\Delta C_{NS}(Q_0^2) = 1.007 \pm 0.028$ (see Eq. (2.50)) by less than 0.4 standard deviations of the combined uncertainties. The present analysis therefore confirms the Bjørken sum rule. The results on the sum rules and the respective theoretical predictions are also summarized in Tab. 8.3.

8.8.3   The Ellis-Jaffe Sum Rule

The prediction for the Ellis-Jaffe sum can be calculated with the triplet and octet matrix elements given in Eqs. (2.50) and (2.51) using Eq. (2.53). The required non-singlet coefficient function is given in the previous section and the singlet coefficient function at $Q_0^2 = 2.5\,\text{GeV}^2$ is $\Delta C_S(Q_0^2) = 0.870 \pm 0.009$ (see Eq. (2.45)). The prediction for the Ellis-Jaffe sum is therefore $\Gamma_{1p}(Q_0^2) =$

Table 8.3: Singlet and non-singlet flavour combinations at $Q_0^2 = 2.5\,\text{GeV}^2$. Also listed is the result for the Ellis-Jaffe sum. The data are compared to theoretical predictions. The systematic uncertainties for the predictions include the uncertainties in the QCD evolution terms.

	Total integral	Prediction	Ref.
Δq_3 (BJSR)	$0.961 \pm 0.051 \pm 0.110$	1.007 ± 0.028	[18]
Δq_8	$0.280 \pm 0.084 \pm 0.050$	0.465 ± 0.024	[52]
Γ_{1p} (EJSR)	$0.129 \pm 0.006 \pm 0.012$	0.153 ± 0.004	Eq. (2.53)
$\Delta\Sigma$	$0.374 \pm 0.034 \pm 0.069$	~ 0.6	[3, 59]

0.153 ± 0.004. The value for the Ellis-Jaffe sum calculated from the moments of the polarized parton densities is

$$\Gamma_{1p}(Q_0^2) = \frac{1}{12}\left(\Delta q_3 + \frac{\Delta q_8}{3}\right) + \frac{\Delta q_0}{9} = 0.129 \pm 0.006(\text{stat}) \pm 0.012(\text{syst}). \qquad (8.49)$$

This result deviates by 1.7 standard deviations of the combined uncertainties from the expectation.

More directly, the semi-inclusive data can be used to compare the octet matrix element Δq_8 with its measurement in hyperon decay. The measured value of

$$\Delta q_8(Q_0^2) = 0.280 \pm 0.084(\text{stat}) \pm 0.050(\text{syst})$$

deviates from the expectation by 1.8 standard deviations of the combined uncertainties (see Tab. 8.3).

As outlined in Sec. 2.4.2 the Ellis-Jaffe sum rule was deduced under the assumption of vanishing strange quark and gluon polarizations and using results from hyperon β-decay where $SU(3)$ flavour symmetry was assumed. The measured deviations from the Ellis-Jaffe sum rule and from the expectation for Δq_8 provide evidence that the assumptions used in the sum rule are not well-founded. However, the present results do not allow to discriminate between these assumptions.

8.8.4 The Spin Carried by the Quarks

The sum of the first moments is a measurement of the total spin carried by the quark spins,

$$\Delta\Sigma = \Delta u + \Delta\bar{u} + \Delta d + \Delta\bar{d} + \Delta s + \Delta\bar{s}. \qquad (8.50)$$

As noted in Sec. 2.4.3, theoretical models predict a range of values for the nucleon spin fraction carried by the quarks, but favour a value of about 60%. The value $\Delta\Sigma = 0.56$ computed in the

χQSM is given at a scale of 5 GeV^2, whereas the upper limit $\Delta\Sigma \lesssim 0.3 \pm 0.26$ obtained in the QCD sum rule approach was computed at $Q^2 = 1\,\text{GeV}^2$. The E155 collaboration measured a value in inclusive DIS for the singlet current of $a_0 = 0.23 \pm 0.04(\text{stat}) \pm 0.06(\text{syst})$ at $Q^2 = 5\,\text{GeV}^2$.

The value computed from the semi-inclusive measurement presented here is

$$\Delta\Sigma(Q_0^2 = 2.5\,\text{GeV}^2) = 0.380 \pm 0.034 \pm 0.072\,. \tag{8.51}$$

The result is smaller than the prediction in the χQSM by 2.3 standard deviations of the experimental uncertainties. It is 1.4 standard deviations larger than the inclusive measurement of a_0 by the E155 collaboration. The measurement is in good agreement with the upper limit given in the QCD sum rule approach. The comparisons are based on values of $\Delta\Sigma$ at different scales of Q^2. In principle, the results need to be evolved to common Q^2, but $\Delta\Sigma$ is independent of Q^2 to first order in α_s [7]. Furthermore the evolution is slow, when including higher orders [170].

The semi-inclusive measurement of $\Delta\Sigma$ presented in this thesis, is indication that the small values of a_0 measured in inclusive DIS were a result of the axial anomaly and a non-zero gluon polarization (see Eq. (2.58)). The measurement thus does not contribute substantially to the "proton spin crisis". Nevertheless, the deviation from most model predictions towards lower values of $\Delta\Sigma$ leaves a "spin puzzle" (see also Ch. 9).

On the other hand, an assessment of the predictions of $\Delta\Sigma$ by the various models with this semi-inclusive measurement requires refinement of the models as well as a reduction of the experimental uncertainties, notably the systematics.

8.8.5   Comparison with Results by the Spin Muon Collaboration

The Spin Muon Collaboration (SMC) is the only other collaboration that has published results from semi-inclusive DIS on the polarized parton densities in the nucleon [141]. Due to limited statistics and their inability to discriminate between different hadron types, SMC extracted polarized parton densities under the assumption of $SU(3)$ flavour symmetry for the sea quark flavours, i.e. $\Delta\bar{u}(x) \equiv \Delta\bar{d}(x) \equiv \Delta s(x) \equiv \Delta\bar{s}(x)$. Therefore, when comparing to the results obtained by SMC, agreement with the sea quark flavours is not necessarily expected, in particular for flavours other than $u_{\text{sea}}(x)$ and $\bar{u}(x)$. Scattering off sea quarks predominantly occurs from up-flavour quarks and anti-quarks, because of the weighting by the square of the fractional charge in the DIS cross section (Eqs. (2.13) and (2.28)). The first moments for the polarized valence and light sea quark flavours are compared in Tab. 8.4 with the results from the SMC experiment, which were integrated over the same kinematic

Table 8.4: Comparison of the first moments in the measured range from this analysis with results from the SMC experiment. The SMC values were extrapolated to the same value of $Q_0^2 = 2.5\,\mathrm{GeV}^2$ and integrated over the HERMES x-range [154].

	HERMES	SMC
Δu_v	$0.579 \pm 0.072 \pm 0.039$	$0.59 \pm 0.08 \pm 0.07$
Δd_v	$-0.159 \pm 0.068 \pm 0.043$	$-0.33 \pm 0.11 \pm 0.09$
$\Delta \bar{u}$	$0.000 \pm 0.037 \pm 0.024$	$0.02 \pm 0.03 \pm 0.02$
$\Delta \bar{d}$	$-0.056 \pm 0.034 \pm 0.011$	$0.02 \pm 0.03 \pm 0.02$

region. The moments, computed at the scale $Q_0^2 = 2.5\,\mathrm{GeV}^2$, are given for the measured range of the HERMES data only. The results from both experiments are in agreement within their combined uncertainties. The moments determined in the present analysis have an improved precision.

Chapter 9

Summary and Outlook

The HERMES collaboration collected data on deep-inelastic scattering of polarized positrons/electrons from polarized hydrogen in 1996 and 1997 and from polarized deuterium in 1998, 1999, and 2000. For this thesis, technical work was done on data quality and on particle identification. These tools were used in the determination of Born level asymmetries with respect to the alignment of the virtual photon and the nucleon spins. Polarized parton distributions were computed from these asymmetries. The results presented here were submitted for publication in Physical Review Letters [171]. A longer paper is in preparation for publication in Physical Review D.

For the determination of these asymmetries, it is essential that only data when the experiment was fully operational are included, in order to prevent a bias of the physics results due to malfunctioning experimental components. For this work, the existing data quality scheme was augmented by a comprehensive package including a www-based interface that provides detailed data quality information and a means of monitoring the quality of the data. The data collection efficiencies during the 1996–2000 polarized running periods were 65 %, 79 %, 87 %, 79 %, and 83 % respectively.

Another crucial part of the asymmetry analysis is the identification of the scattered deep-inelastic electron/positron and the tagging of semi-inclusive hadrons in the final state. For this purpose, the HERMES spectrometer incorporates four particle identification detectors — a calorimeter, a preshower detector, a threshold/ring-imaging Čerenkov detector, and a transition radiation detector. The identification of DIS leptons in a probability analysis of the PID detector responses is excellent reaching efficiencies larger than 98 % and hadron contaminations smaller than 0.6 %. Likewise, SIDIS hadrons are identified with efficiencies close to 100 % and contaminations smaller than 0.1 %.

The inclusive asymmetry A_{1p} and semi-inclusive asymmetries of undifferentiated hadrons $(A_{1p}^{h^{\pm}})$

and pions ($A_{1p}^{\pi^\pm}$) were extracted from 1.7×10^6 deep-inelastic scattering events on a polarized proton target. On a polarized deuteron target, 6.7×10^6 DIS events were available to determine the inclusive asymmetry A_{1d} and semi-inclusive asymmetries of undifferentiated hadrons ($A_{1d}^{h^\pm}$), pions ($A_{1d}^{\pi^\pm}$) and kaons ($A_{1d}^{K^\pm}$). Pions in the former dataset were identified with a threshold Čerenkov detector. Pions and kaons in the deuterium dataset were identified with a ring-imaging Čerenkov detector. Both datasets cover a kinematic range of $0.023 < x < 0.6$ at an average scale of $\langle Q^2 \rangle \simeq 2.5\,\mathrm{GeV}^2$.

The asymmetries were corrected for detector smearing and higher-order QED effects using an unfolding algorithm that is new to the analysis of asymmetries. The algorithm properly accounts for the migration of DIS events among kinematic bins and for background events that are migrated into the acceptance. The final inclusive Born asymmetries were determined with high precision, and good precision was reached for the semi-inclusive asymmetries. The asymmetries of undifferentiated hadrons are in good agreement with measurements at the SMC experiment, but with better statistical precision. The agreement is an indication that the photon-nucleon asymmetries scale, because the SMC results were obtained at a higher scale of $\langle Q^2 \rangle \simeq 10\,\mathrm{GeV}^2$. The asymmetries of pions on the proton and of pions and kaons on the deuteron were measured for the first time.

Polarized parton densities were computed from the Born asymmetries at a scale of $Q^2 = 2.5\,\mathrm{GeV}^2$ using the purity formalism. This algorithm applies the probabilistic relation of the type of final state hadron to the flavour of the struck quark. The densities of the u quark and the d quark which were found to be positive and negative, respectively, were determined with high precision. The polarized densities of the $\bar{u}$, $\bar{d}$, and s flavours were separated for the first time by the HERMES collaboration. These densities are consistent with zero within the uncertainties. There is also no evidence for a flavour asymmetry in the polarized light quark sea as predicted in the χQSM. The polarized parton densities were found to be in good agreement with leading-order parameterizations of polarized inclusive data from other experiments.

The present measurement relies on the leading order description of the semi-inclusive DIS process, notably the description of the fragmentation in the LUND model. The results on the polarized parton densities obtained here confirm the analysis of inclusive data within the uncertainties. Note however, that in the case of the small polarized densities of the sea-flavours, more semi-inclusive data are desirable to support or reject the inclusive analyses.

Moments of the polarized parton densities were calculated using extrapolations of the measured densities to low and high x. The Bjørken sum rule was verified. With a deviation of 1.7 standard deviations the Ellis-Jaffe sum rule could not be confirmed by these semi-inclusive measurements.

This result is in agreement with inclusive measurements that also found results smaller than expected by the Ellis-Jaffe sum rule. The total contribution by the quark spins to the nucleon spin was measured to be $\Delta\Sigma = 0.380 \pm 0.034(\text{stat}) \pm 0.072(\text{syst})$. This value is closer to the expectation of $\Delta\Sigma \approx 0.6$ than early measurements that had led to the "proton spin crisis". The discrepancy of $\Delta\Sigma$ to measurements of the singlet axial current a_0 in inclusive DIS and the observed deviation from the Ellis-Jaffe sum rule indicate that a non-zero amount of the nucleon spin is carried by the spins of the gluons. In addition, the small value of $\Delta\Sigma$ is suggestive of a sizable contribution to the nucleon spin by the quark and gluon orbital angular momenta, as predicted in various models.

Future measurements of the nucleon spin structure therefore need to include efforts to measure the quark and gluon orbital angular momentum and the polarized density of the gluons. First measurements of the gluon polarization were carried out by the HERMES collaboration [172]. The strongly model dependent average value of the gluon polarization was measured to be $\langle\Delta G/G(x_G)\rangle = 0.41 \pm 0.18(\text{stat}) \pm 0.03(\text{syst})$ at $\langle x_G \rangle = 0.17$. The COMPASS experiment at CERN, which has been taking data since 2002 was designed to carry out more precise measurements of the gluon polarization [173, 174, 175]. The experiment uses a 100–200 GeV μ-beam ($P_B \simeq 0.8$) in combination with a ^{6}LiD solid state target ($P_T \simeq 0.5$) to measure polarized μN deep-inelastic scattering events. The gluon polarization is accessed using the photon-gluon fusion process $\gamma^* g \to q\bar{q}$, which is detected via two channels: The production of $c\bar{c}$ pairs and therefore charmed mesons in the final state and the production of hadron pairs with large transverse momentum p_T with respect to the virtual photon direction. Within the first 2.5 years of running, the COMPASS collaboration will measure $\Delta G/G$ with a precision of ~ 0.15 at one value of x_G using the former process and with a precision of ~ 0.05 at three values of x_G using the high p_T hadron pair data. COMPASS will also measure the polarized parton distributions described in this thesis. The experiment will thus provide a wealth of new and exciting data on the nucleon spin structure.

At the Brookhaven National Laboratory, a program to investigate the proton spin structure is underway using the Relativistic Heavy Ion Collider (RHIC) [176]. The spin structure is investigated via the collision of polarized proton beams at center-of-mass energies $\sqrt{s} \le 500$ GeV [177], a scale sufficiently hard to reliably perform calculations in perturbative QCD. The high energy and the pp collisions studied instead of DIS allow unique measurements of the nucleon spin structure. The gluon polarization can be accessed through a variety of processes, notably prompt photon production, where the main contributing process is gluon Compton scattering, $qg \to \gamma q$. Measurements of the polarized parton densities Δu and $\Delta \bar{d}$ (Δd and $\Delta \bar{u}$) are possible via the production of vector

bosons W^+ (W^-). The polarized parton densities measured at RHIC will thus complement data from fixed target experiments by providing results using an entirely different process. The higher scale of the reactions will also allow an investigation of the QCD evolution of the polarized densities [178]. The spin program at RHIC will therefore not only improve and verify current data, but the nucleon spin structure will be probed in kinematic regions that were previously inaccessible.

A determination of the orbital angular momentum may become possible using the theory of generalized parton distributions [179, 180]. In this framework, deeply virtual Compton scattering (DVCS) — the exclusive lepto-production of a single photon with the target nucleon remaining intact — was identified as a possibility to study the orbital angular momentum [181]. Promising first measurements were carried out by the HERMES collaboration [182], but a determination of L_q or L_g requires substantially more effort, both in experiment and theory.

In conclusion, recent experiments and theoretical results have turned the "spin crisis" into merely a puzzle. Yet, there remain open questions in the understanding of nucleon spin structure that will be addressed in the coming years.

Appendix A

Data Selection

A.1 Data Quality

Table A.1: The data quality bit-pattern for the 00c1 production. The second column specifies whether the bit was set ($-$, data bad) or not set ($+$, data analyzable) with respect to the condition given in the third column.

Bit	$+/-$	Condition
0	$+$	Target polarization parallel or anti-parallel
1	$+$	Reasonable beam polarization ($0.3 < P_B < 0.8$)
2	$+$	Live time larger than 0.5
3	$+$	Reasonable burst length (less than 11 s)
4	$+$	Reasonable beam current ($5\,\text{mA} < I_B < 50\,\text{mA}$)
5	$+$	Reasonable luminosity ($5\,\text{Hz} < \mathcal{L} < 80\,\text{Hz}$)
6	$-$	First burst in a run
7	$-$	μDST record bad
8	$-$	Calorimeter threshold setting unknown
9	$+$	Logbook: Data analyzable
10	$+$	Logbook: Target in polarized (2-state) mode
11	$-$	Logbook: Unpolarized running (part of bit 10)
12	$-$	Logbook: No data quality available (part of bit 10)

Bit	$+/-$	Condition
13	$-$	Logbook: Target in special 3-state mode (part of bit 10)
14	$-$	Logbook: Target in Bhabha scattering mode (part of bit 10)
15	$-$	UGFS valve setting: Unpolarized data-taking
16	$-$	Target data quality: Target bad
17	$-$	Dead blocks in calorimeter
18	$-$	Dead blocks in preshower or luminosity monitor
19	$-$	TRD data quality: TRD bad
20	$-$	High voltage trips in a wire chamber
21	$-$	RICH or calorimeter bad
22	$-$	High voltage trips in the RICH
23	$-$	Bad measurement of the atomic fraction in the injected target gas
24	$-$	Bad measurement of the molecular recombination rate in the target gas
25	$-$	RICH data quality: RICH bad
26	$-$	Target in tensor polarization state
27	$+$	Reasonable target polarization $(0. < P_T < 1.5)$
28	$+$	Beam polarization measured within last five minutes
30	$-$	Live time measurement bad because of DAQ problems

A.2 The Inverse of the RICH $\mathcal{P}$-Matrix

The inverse of the RICH $\mathcal{P}$-matrix is equivalent to the matrix of inverted conditional probabilities $\mathcal{Q}$ that follow from Bayes' Theorem, if both matrices are combined with the identified particle fluxes. The equivalence of these matrices is shown in the following in two dimensions, that is for two particle types 1, and 2. As usual, the quantity $P(A|B)$ is the conditional probability for the event A if the event B is true. Similarly $P(B|I)$ is the probability that B occurs, given some prior information I. In this case, $P(i_{1(2)}|I)$ is the probability to identify the particle $i_{1(2)}$, and $P(t_{1(2)}|I)$ is the probability for the true particle $t_{1(2)}$. The conditional probability $P(t_{1(2)}|I)$ is the normalized particle flux, which is often labeled $\phi_{1(2)}$ (see [183]).

With these definitions the vector of measured particles $\vec{I}$ and the vector of true particles $\vec{N}$ is

given by

$$\vec{I} = M \begin{pmatrix} P(i_1|I) \\ P(i_2|I) \end{pmatrix} \quad \text{and} \quad \vec{N} = M \begin{pmatrix} P(t_1|I) \\ P(t_2|I) \end{pmatrix}. \tag{A.1}$$

where M is the total number of particles.

The vector of identified particles is related to the vector of true particles through the matrices $\mathcal{P}$ and $\mathcal{Q}$,

$$\vec{I} = \mathcal{P} \cdot \vec{N} \quad \text{and} \quad \vec{N} = \mathcal{Q} \cdot \vec{I}. \tag{A.2}$$

In terms of the conditional probabilities $P(i_j|t_k)$ and $P(t_k|i_j)$, these matrices are

$$\mathcal{P} = \begin{pmatrix} P(i_1|t_1) & P(i_1|t_2) \\ P(i_2|t_1) & P(i_2|t_2) \end{pmatrix} \quad \text{and} \quad \mathcal{Q} = \begin{pmatrix} P(t_1|i_1) & P(t_1|i_2) \\ P(t_2|i_1) & P(t_2|i_2) \end{pmatrix}, \tag{A.3}$$

where the probabilities are related through Bayes' Theorem,

$$P(t_k|i_j) = \frac{P(i_j|t_k)\,P(t_k|I)}{\sum_{j'} P(i_{j'}|t_k)\,P(t_k|I)}. \tag{A.4}$$

The relation $\vec{N} = \mathcal{Q}\,\vec{I}$ in Eq. (A.2) is trivially shown when inserting Eq. (A.1) and Eq. (A.3),

$$\mathcal{Q} \cdot \vec{I} = M \begin{pmatrix} P(t_1|i_1)\,P(i_1|I) + P(t_1|i_2)\,P(i_2|I) \\ P(t_2|i_1)\,P(i_1|I) + P(t_2|i_2)\,P(i_2|I) \end{pmatrix} = M \begin{pmatrix} P(t_1|I) \\ P(t_2|I) \end{pmatrix} = \vec{N}. \tag{A.5}$$

Here the identity $P(i_j|I) \equiv P(i_j|t_1)\,P(t_1|I) + P(i_j|t_2)\,P(t_2|I)$ was used.

Based on the $\mathcal{Q}$-matrix it is thus possible to calculate the true hadron fluxes $\vec{N}$ from the measured or identified hadron fluxes $\vec{I}$. However, the determination of the $\mathcal{Q}$-matrix that involves knowledge of these true hadron fluxes, is only possible in an iteration. In the analysis presented in this thesis, the true fluxes were found by inversion of the $\mathcal{P}$-matrix (see Sec. 5.2). In the two-dimensional case discussed here, the inverse $\mathcal{P}$-matrix is given by

$$\mathcal{P}^{-1} = \frac{1}{\det(\mathcal{P})} \begin{pmatrix} P(i_2|t_2) & -P(i_1|t_2) \\ -P(i_2|t_1) & P(i_1|t_1) \end{pmatrix}. \tag{A.6}$$

Therefore the true number of hadrons $\vec{N}$ given by inversion of the first expression in Eq. (A.2) is

$$\begin{aligned} \mathcal{P}^{-1} \cdot \vec{I} &= \frac{M}{\det(\mathcal{P})} \begin{pmatrix} P(i_2|t_2)\,P(i_1|I) - P(i_1|t_2)\,P(i_2|I) \\ -P(i_2|t_1)\,P(i_1|I) + P(i_1|t_1)\,P(i_2|I) \end{pmatrix} \\ &= \frac{M}{\det(\mathcal{P})} \begin{pmatrix} [\,P(i_2|t_2)\,P(i_1|t_1) - P(i_1|t_2)\,P(i_2|t_1)\,]\,P(t_1|I) \\ [\,P(i_2|t_2)\,P(i_1|t_1) - P(i_1|t_2)\,P(i_2|t_1)\,]\,P(t_2|I) \end{pmatrix}, \end{aligned} \tag{A.7}$$

where in the last step the following identities were used for the first row,

$$P(i_2|t_2)\,P(i_1|I) = P(i_2|t_2)\,[\,P(i_1|t_1)P(t_1|I) + P(i_1|t_2)P(t_2|I)\,]\,, \tag{A.8}$$

$$P(i_1|t_2)\,P(i_2|I) = P(i_1|t_2)\,[\,P(i_2|t_1)P(t_1|I) + P(i_2|t_2)P(t_2|I)\,]\,, \tag{A.9}$$

and analogously for the second row. The determinant of the $\mathcal{P}$-matrix is

$$\det(\mathcal{P}) = P(i_1|t_1)\,P(i_2|t_2) - P(i_1|t_2)\,P(i_2|t_1). \tag{A.10}$$

Hence the last term in Eq (A.7) reduces to the vector $\vec{N}$.

In conclusion, inverting the $\mathcal{P}$-matrix to solve for $\vec{N}$ is formally equivalent to applying the $\mathcal{Q}$-matrix. The matrices $\mathcal{P}^{-1}$ and $\mathcal{Q}$, however, are not identical. Only the expressions $\mathcal{P}^{-1}\,\vec{I}$ and $\mathcal{Q}\,\vec{I}$, which in both cases contain the proper particle fluxes, agree. The proof given here for two hadron types extends to the three hadron types used in the analysis.

Appendix B

Results: Asymmetries

Table B.1: Coefficients of the parameterization of the azimuthal acceptance correction for the semi-inclusive proton asymmetries. The parameterizations are given in Eqs. (6.8) and (6.9).

Type	x_0^h	a_0^h	a_1^h	a_2^h	a_3^h	b_0^h	b_1^h	b_2^h	b_3^h
h^+	-1.65	-0.052	-0.180	-0.580	-0.500				
h^-	-1.65	-0.041	-0.246	-0.662	-0.486				
π^+	-1.65	-0.048	-0.233	-0.617	-0.464	1.075	-0.389	1.204	-1.127
π^-	-1.65	-0.038	-0.212	-0.559	-0.408	1.057	-0.151	0.445	-0.492

Table B.2: Coefficients of the parameterization of the azimuthal acceptance correction for the semi-inclusive deuteron asymmetries. The parameterizations are given in Eqs. (6.8) and (6.9).

Type	x_0^h	a_0^h	a_1^h	a_2^h	a_3^h	b_0^h	b_1^h	b_2^h	b_3^h
h^+	-1.65	-0.080	-0.318	-0.879	-0.667				
h^-	-1.65	-0.064	-0.358	-0.889	-0.634				
π^+	-1.65	-0.091	-0.466	-1.145	-0.785	1.188	-0.996	2.470	-1.983
π^-	-1.65	-0.075	-0.440	-1.055	-0.718	1.232	-1.304	3.208	-2.513
K^+	-1.65	-0.041	-0.042	-0.282	-0.317	1.095	-0.038	-0.330	0.253
K^-	-1.65	-0.034	-0.083	-0.322	-0.312	1.060	0.241	-0.895	0.575

Table B.3: Measured inclusive and semi-inclusive asymmetries $A_{\|p}^{(h)}$ on the proton. Listed are the combined asymmetries of the 1996 and 1997 data-taking periods.

$\langle x \rangle$	$\langle Q^2 \rangle /\mathrm{GeV}^2$		$A_{\|p}$	$\pm$stat	$\pm$syst			
0.033	1.22		0.063	0.005	0.003			
0.047	1.47		0.063	0.005	0.003			
0.065	1.71		0.062	0.004	0.003			
0.087	1.98		0.078	0.004	0.004			
0.118	2.39		0.087	0.004	0.005			
0.166	3.19		0.107	0.005	0.006			
0.239	4.55		0.148	0.006	0.008			
0.339	6.53		0.197	0.012	0.011			
0.446	9.08		0.270	0.023	0.015			
$\langle x \rangle$	$\langle Q^2 \rangle /\mathrm{GeV}^2$	$\langle z \rangle$	$A_{\|p}^{h^+}$	$\pm$stat	$\pm$syst	$A_{\|p}^{h^-}$	$\pm$stat	$\pm$syst
0.033	1.22	0.355	0.077	0.014	0.004	0.054	0.017	0.003
0.048	1.46	0.373	0.088	0.012	0.005	0.065	0.015	0.004
0.065	1.76	0.383	0.075	0.011	0.004	0.043	0.014	0.002
0.087	2.15	0.389	0.098	0.011	0.006	0.049	0.014	0.003
0.118	2.72	0.391	0.127	0.011	0.007	0.084	0.014	0.005
0.166	3.68	0.389	0.135	0.012	0.008	0.085	0.017	0.005
0.238	5.15	0.387	0.186	0.016	0.011	0.119	0.024	0.007
0.338	7.17	0.377	0.206	0.033	0.012	0.260	0.050	0.015
0.447	9.75	0.366	0.353	0.070	0.020	0.241	0.108	0.014
$\langle x \rangle$	$\langle Q^2 \rangle /\mathrm{GeV}^2$	$\langle z \rangle$	$A_{\|p}^{\pi^+}$	$\pm$stat	$\pm$syst	$A_{\|p}^{\pi^-}$	$\pm$stat	$\pm$syst
0.033	1.22	0.363	0.061	0.018	0.004	0.054	0.020	0.003
0.047	1.51	0.412	0.077	0.016	0.004	0.073	0.019	0.004
0.064	1.90	0.441	0.068	0.016	0.004	0.033	0.019	0.002
0.086	2.44	0.459	0.127	0.017	0.007	0.038	0.021	0.002
0.118	3.18	0.473	0.163	0.018	0.009	0.049	0.022	0.003
0.165	4.32	0.479	0.159	0.022	0.009	0.089	0.028	0.005
0.237	5.92	0.495	0.165	0.031	0.010	0.152	0.040	0.009
0.337	8.03	0.502	0.289	0.065	0.017	0.189	0.086	0.011
0.448	10.50	0.494	0.436	0.142	0.025	0.218	0.188	0.014

Table B.4: Measured inclusive and semi-inclusive asymmetries $A_{\|d}^{(h)}$ on the deuteron. Listed are the combined asymmetries of the 1998, 1999, and 2000 data-taking periods.

$\langle x \rangle$	$\langle Q^2 \rangle /\mathrm{GeV}^2$		$A_{\|d}$	$\pm$stat	$\pm$syst			
0.033	1.22		0.013	0.003	0.001			
0.047	1.47		0.014	0.002	0.001			
0.065	1.72		0.017	0.002	0.001			
0.087	2.00		0.023	0.002	0.001			
0.118	2.40		0.031	0.002	0.002			
0.166	3.21		0.046	0.002	0.002			
0.239	4.56		0.068	0.003	0.003			
0.339	6.54		0.119	0.006	0.006			
0.445	9.08		0.154	0.012	0.007			
$\langle x \rangle$	$\langle Q^2 \rangle /\mathrm{GeV}^2$	$\langle z \rangle$	$A_{\|d}^{h^+}$	$\pm$stat	$\pm$syst	$A_{\|d}^{h^-}$	$\pm$stat	$\pm$syst
0.033	1.22	0.354	0.007	0.007	0.000	−0.001	0.008	0.001
0.048	1.46	0.373	0.011	0.006	0.001	0.007	0.007	0.001
0.065	1.76	0.383	0.020	0.005	0.001	0.012	0.006	0.001
0.087	2.16	0.390	0.029	0.005	0.001	0.015	0.007	0.001
0.118	2.74	0.393	0.028	0.005	0.002	0.026	0.007	0.001
0.165	3.70	0.392	0.057	0.006	0.003	0.050	0.008	0.003
0.238	5.17	0.389	0.072	0.008	0.004	0.081	0.011	0.004
0.338	7.19	0.384	0.109	0.017	0.006	0.131	0.025	0.006
0.445	9.61	0.383	0.111	0.037	0.006	0.104	0.055	0.005
$\langle x \rangle$	$\langle Q^2 \rangle /\mathrm{GeV}^2$	$\langle z \rangle$	$A_{\|d}^{\pi^+}$	$\pm$stat	$\pm$syst	$A_{\|d}^{\pi^-}$	$\pm$stat	$\pm$syst
0.033	1.22	0.352	−0.006	0.009	0.001	−0.003	0.009	0.001
0.047	1.51	0.402	0.009	0.008	0.001	−0.003	0.009	0.001
0.064	1.90	0.431	0.012	0.008	0.001	0.012	0.009	0.001
0.086	2.42	0.448	0.028	0.008	0.001	0.018	0.009	0.001
0.118	3.17	0.460	0.050	0.009	0.003	0.035	0.010	0.002
0.165	4.28	0.470	0.065	0.010	0.003	0.035	0.012	0.002
0.237	5.88	0.481	0.071	0.015	0.004	0.101	0.018	0.005
0.338	7.96	0.491	0.146	0.033	0.008	0.171	0.040	0.008
0.446	10.22	0.503	0.073	0.070	0.005	−0.007	0.088	0.008

$\langle x \rangle$	$\langle Q^2 \rangle /\mathrm{GeV}^2$	$\langle z \rangle$	$A^{K^+}_{\|d}$	$\pm$stat	$\pm$syst	$A^{K^-}_{\|d}$	$\pm$stat	$\pm$syst
0.033	1.22	0.382	0.009	0.024	0.001	-0.015	0.031	0.002
0.047	1.51	0.424	0.042	0.021	0.002	0.017	0.030	0.002
0.064	1.90	0.449	0.065	0.019	0.004	-0.017	0.029	0.002
0.086	2.42	0.469	0.056	0.020	0.003	-0.029	0.033	0.002
0.118	3.19	0.477	0.037	0.021	0.002	0.017	0.035	0.001
0.165	4.33	0.487	0.080	0.024	0.005	0.057	0.044	0.003
0.238	5.91	0.500	0.099	0.033	0.006	0.046	0.067	0.003
0.335	7.84	0.517	0.210	0.071	0.012	-0.084	0.146	0.009
0.447	10.16	0.513	0.268	0.151	0.018	0.695	0.298	0.035

Table B.5: Inclusive and semi-inclusive Born asymmetries $A^{(h)}_{1p}$ on the proton. Listed are the combined asymmetries of the 1996 and 1997 data-taking periods.

$\langle x \rangle$	$\langle Q^2 \rangle /\mathrm{GeV}^2$	A_{1p}	$\pm$stat	$\pm$syst	$\pm$MC
0.033	1.22	0.100	0.018	0.009	0.004
0.048	1.45	0.110	0.017	0.009	0.004
0.065	1.68	0.113	0.018	0.009	0.005
0.087	1.93	0.194	0.021	0.015	0.006
0.118	2.34	0.237	0.020	0.018	0.006
0.166	3.16	0.282	0.022	0.021	0.005
0.240	4.54	0.385	0.024	0.029	0.004
0.340	6.56	0.476	0.043	0.036	0.005
0.447	9.18	0.610	0.075	0.049	0.006

$\langle x \rangle$	$\langle Q^2 \rangle /\mathrm{GeV}^2$	$\langle z \rangle$	$A^{h^+}_{1p}$	$\pm$stat	$\pm$syst	$\pm$MC	$A^{h^-}_{1p}$	$\pm$stat	$\pm$syst	$\pm$MC
0.034	1.21	0.356	0.110	0.030	0.008	0.007	0.072	0.034	0.005	0.007
0.048	1.44	0.375	0.164	0.032	0.011	0.008	0.126	0.036	0.009	0.008
0.065	1.72	0.386	0.136	0.033	0.010	0.008	0.090	0.038	0.006	0.009
0.087	2.06	0.393	0.207	0.037	0.015	0.010	0.095	0.044	0.007	0.011
0.118	2.58	0.395	0.301	0.036	0.021	0.009	0.186	0.044	0.014	0.011
0.166	3.52	0.390	0.285	0.038	0.021	0.008	0.177	0.050	0.013	0.010
0.239	5.03	0.388	0.422	0.046	0.030	0.007	0.236	0.064	0.017	0.010
0.338	7.09	0.377	0.405	0.091	0.030	0.010	0.570	0.134	0.040	0.016
0.448	9.76	0.364	0.759	0.176	0.054	0.012	0.496	0.272	0.037	0.023

$\langle x \rangle$	$\langle Q^2 \rangle /\text{GeV}^2$	$\langle z \rangle$	$A_{1p}^{\pi^+}$	±stat	±syst	±MC	$A_{1p}^{\pi^-}$	±stat	±syst	±MC
0.033	1.22	0.364	0.080	0.035	0.006	0.008	0.068	0.039	0.005	0.008
0.047	1.50	0.416	0.134	0.039	0.009	0.009	0.145	0.043	0.010	0.009
0.064	1.87	0.449	0.083	0.041	0.007	0.009	0.065	0.046	0.004	0.010
0.087	2.38	0.471	0.231	0.046	0.016	0.010	0.071	0.054	0.005	0.011
0.118	3.08	0.487	0.316	0.046	0.021	0.009	0.075	0.055	0.006	0.010
0.166	4.22	0.490	0.302	0.053	0.020	0.009	0.157	0.065	0.011	0.010
0.238	5.83	0.504	0.278	0.070	0.020	0.009	0.270	0.089	0.019	0.011
0.337	7.97	0.506	0.557	0.153	0.038	0.014	0.346	0.200	0.025	0.018
0.449	10.49	0.496	0.865	0.318	0.057	0.017	0.449	0.434	0.041	0.027

Table B.6: Inclusive and semi-inclusive Born asymmetries $A_{1d}^{(h)}$ on the deuteron. Listed are the combined asymmetries of the 1998, 1999, and 2000 data-taking periods.

$\langle x \rangle$	$\langle Q^2 \rangle /\text{GeV}^2$		A_{1d}	±stat	±syst	±MC
0.033	1.22		0.020	0.008	0.001	0.003
0.048	1.45		0.025	0.008	0.002	0.004
0.065	1.69		0.040	0.008	0.002	0.005
0.087	1.95		0.044	0.010	0.003	0.006
0.118	2.35		0.078	0.010	0.006	0.006
0.166	3.18		0.114	0.011	0.008	0.005
0.240	4.55		0.162	0.012	0.012	0.005
0.339	6.58		0.293	0.023	0.020	0.006
0.446	9.16		0.316	0.041	0.025	0.007

$\langle x \rangle$	$\langle Q^2 \rangle /\text{GeV}^2$	$\langle z \rangle$	$A_{1d}^{h^+}$	±stat	±syst	±MC	$A_{1d}^{h^-}$	±stat	±syst	±MC
0.033	1.21	0.355	0.008	0.015	0.001	0.007	−0.012	0.016	0.001	0.007
0.048	1.44	0.374	0.011	0.016	0.002	0.008	0.007	0.017	0.001	0.008
0.065	1.73	0.384	0.048	0.016	0.003	0.009	0.038	0.019	0.002	0.009
0.087	2.07	0.391	0.075	0.018	0.004	0.010	0.018	0.021	0.003	0.011
0.118	2.60	0.394	0.035	0.018	0.004	0.009	0.074	0.021	0.004	0.011
0.166	3.56	0.392	0.133	0.019	0.009	0.009	0.077	0.024	0.007	0.011
0.238	5.04	0.388	0.147	0.024	0.011	0.008	0.171	0.031	0.011	0.011
0.338	7.12	0.382	0.237	0.050	0.016	0.012	0.300	0.070	0.018	0.017
0.446	9.61	0.380	0.190	0.100	0.016	0.015	0.150	0.148	0.015	0.024

$\langle x \rangle$	$\langle Q^2 \rangle / \mathrm{GeV}^2$	$\langle z \rangle$	$A_{1d}^{\pi^+}$	$\pm$stat	$\pm$syst	$\pm$MC	$A_{1d}^{\pi^-}$	$\pm$stat	$\pm$syst	$\pm$MC
0.033	1.22	0.353	−0.017	0.017	0.001	0.008	−0.011	0.018	0.001	0.008
0.047	1.50	0.405	0.018	0.019	0.002	0.009	−0.023	0.020	0.001	0.009
0.064	1.87	0.437	0.013	0.020	0.002	0.010	0.046	0.022	0.003	0.010
0.087	2.36	0.458	0.045	0.023	0.003	0.010	0.006	0.025	0.002	0.011
0.118	3.07	0.472	0.097	0.022	0.006	0.010	0.088	0.025	0.005	0.010
0.165	4.18	0.479	0.121	0.026	0.008	0.009	0.014	0.030	0.004	0.010
0.238	5.80	0.488	0.109	0.034	0.008	0.010	0.204	0.041	0.012	0.011
0.338	7.93	0.494	0.318	0.082	0.021	0.016	0.386	0.099	0.021	0.018
0.446	10.24	0.503	0.086	0.169	0.013	0.022	−0.132	0.216	0.020	0.028

$\langle x \rangle$	$\langle Q^2 \rangle / \mathrm{GeV}^2$	$\langle z \rangle$	$A_{1d}^{K^+}$	$\pm$stat	$\pm$syst	$\pm$MC	$A_{1d}^{K^-}$	$\pm$stat	$\pm$syst	$\pm$MC
0.033	1.22	0.383	0.005	0.048	0.002	0.020	−0.047	0.060	0.004	0.021
0.048	1.50	0.424	0.017	0.050	0.004	0.023	0.031	0.066	0.004	0.024
0.065	1.86	0.457	0.147	0.050	0.008	0.025	0.010	0.070	0.005	0.026
0.086	2.33	0.484	0.122	0.056	0.008	0.027	−0.055	0.081	0.005	0.029
0.118	3.08	0.489	0.040	0.053	0.005	0.024	0.029	0.083	0.003	0.027
0.165	4.23	0.493	0.144	0.059	0.010	0.023	0.072	0.099	0.007	0.028
0.238	5.81	0.503	0.144	0.077	0.012	0.024	0.087	0.141	0.007	0.032
0.336	7.76	0.516	0.439	0.175	0.027	0.037	−0.250	0.342	0.021	0.062
0.448	10.20	0.510	0.464	0.369	0.041	0.054	1.458	0.700	0.086	0.101

Table B.7: Statistical correlations of the measured asymmetries $A_{\|p}^{(h)}$ on the proton. The values are calculated from the measured multiplicities and averaged over spin-states.

$\langle x \rangle$	$\rho(e, \pi^+)$	$\rho(e, \pi^-)$	$\rho(\pi^+, \pi^-)$
0.033	0.400	0.354	0.112
0.047	0.392	0.339	0.084
0.065	0.364	0.309	0.077
0.087	0.325	0.269	0.072
0.118	0.290	0.233	0.062
0.166	0.269	0.213	0.061
0.239	0.246	0.190	0.039
0.339	0.224	0.170	0.022
0.446	0.200	0.158	0.011

Table B.8: Statistical correlations of the measured asymmetries on $A_{\parallel d}^{(h)}$ the deuteron. The values are calculated from the measured multiplicities and averaged over spin-states. The negative correlations are a consequence of weighting with negative elements of the inverse RICH $\mathcal{P}$-matrix.

$\langle x \rangle$	ρ $e\pi^+$	ρ $e\pi^-$	ρ eK^+	ρ eK^-	ρ $\pi^+\pi^-$	ρ π^+K^+	ρ π^+K^-	ρ π^-K^+	ρ π^-K^-	ρ K^+K^-
0.033	0.404	0.380	0.151	0.112	0.113	0.000	0.019	0.028	0.004	0.073
0.047	0.399	0.368	0.157	0.108	0.095	−0.003	0.012	0.022	0.003	0.076
0.065	0.368	0.336	0.151	0.099	0.084	−0.004	0.012	0.018	0.002	0.079
0.087	0.331	0.297	0.140	0.087	0.076	−0.004	0.010	0.018	0.003	0.071
0.118	0.295	0.261	0.129	0.076	0.069	−0.005	0.009	0.017	0.003	0.068
0.166	0.274	0.236	0.122	0.068	0.059	−0.005	0.008	0.016	0.003	0.057
0.239	0.251	0.212	0.114	0.058	0.044	−0.006	0.006	0.010	0.004	0.045
0.339	0.225	0.186	0.104	0.052	0.026	−0.009	0.005	0.008	0.003	0.035
0.445	0.215	0.176	0.099	0.049	0.018	−0.004	−0.001	0.003	0.001	0.046

Table B.9: Statistical correlations of the Born asymmetries on the proton. Listed are the correlations in the nine x-bins of the for each combination of asymmetries.

$\rho(e,e)$	1	2	3	4	5	6	7	8	9
1	1.000	−0.164	0.002	−0.009	−0.006	−0.006	−0.002	0.001	0.000
2	−0.164	1.000	−0.229	0.010	−0.016	−0.006	−0.002	0.000	0.000
3	0.002	−0.229	1.000	−0.285	0.013	−0.013	−0.003	0.000	0.000
4	−0.009	0.010	−0.285	1.000	−0.312	0.030	−0.011	0.001	0.000
5	−0.006	−0.016	0.013	−0.312	1.000	−0.285	0.029	−0.007	0.001
6	−0.006	−0.006	−0.013	0.030	−0.285	1.000	−0.255	0.031	−0.005
7	−0.002	−0.002	−0.003	−0.011	0.029	−0.255	1.000	−0.235	0.031
8	0.001	0.000	0.000	0.001	−0.007	0.031	−0.235	1.000	−0.236
9	0.000	0.000	0.000	0.000	0.001	−0.005	0.031	−0.236	1.000

$\rho(e,\pi^+)$	1	2	3	4	5	6	7	8	9
1	0.399	−0.064	0.000	−0.003	−0.002	−0.002	−0.001	0.000	0.000
2	−0.069	0.391	−0.084	0.003	−0.005	−0.002	−0.001	0.000	0.000
3	0.000	−0.080	0.361	−0.093	0.003	−0.003	−0.001	0.000	0.000
4	−0.004	0.003	−0.082	0.323	−0.089	0.007	−0.003	0.000	0.000
5	−0.002	−0.003	0.004	−0.075	0.289	−0.074	0.006	−0.001	0.000
6	−0.001	−0.001	−0.002	0.005	−0.063	0.267	−0.061	0.007	−0.001
7	0.000	0.000	0.000	−0.002	0.004	−0.053	0.245	−0.052	0.006
8	0.000	0.000	0.000	0.000	−0.001	0.005	−0.044	0.223	−0.046
9	0.000	0.000	0.000	0.000	0.000	−0.001	0.005	−0.044	0.200

$\rho(e,\pi^-)$	1	2	3	4	5	6	7	8	9
1	0.353	−0.056	0.000	−0.003	−0.002	−0.001	0.000	0.000	0.000
2	−0.060	0.338	−0.072	0.002	−0.004	−0.001	0.000	0.000	0.000
3	0.000	−0.066	0.307	−0.078	0.002	−0.003	−0.001	0.000	0.000
4	−0.002	0.002	−0.067	0.266	−0.070	0.005	−0.002	0.000	0.000
5	−0.001	−0.003	0.004	−0.058	0.232	−0.058	0.005	−0.001	0.000
6	−0.001	−0.001	−0.002	0.003	−0.048	0.212	−0.047	0.005	−0.001
7	0.000	0.000	0.000	−0.001	0.003	−0.040	0.189	−0.040	0.005
8	0.000	0.000	0.000	0.000	−0.001	0.003	−0.032	0.169	−0.037
9	0.000	0.000	0.000	0.000	0.000	0.000	0.003	−0.030	0.158

$\rho(\pi^+,\pi^+)$	1	2	3	4	5	6	7	8	9
1	1.000	−0.173	−0.001	−0.011	−0.006	−0.003	−0.001	0.000	0.000
2	−0.173	1.000	−0.216	0.006	−0.011	−0.004	−0.001	0.000	0.000
3	−0.001	−0.216	1.000	−0.244	0.009	−0.009	−0.001	0.000	0.000
4	−0.011	0.006	−0.244	1.000	−0.241	0.014	−0.006	0.000	0.000
5	−0.006	−0.011	0.009	−0.241	1.000	−0.219	0.014	−0.003	0.000
6	−0.003	−0.004	−0.009	0.014	−0.219	1.000	−0.201	0.019	−0.003
7	−0.001	−0.001	−0.001	−0.006	0.014	−0.201	1.000	−0.186	0.020
8	0.000	0.000	0.000	0.000	−0.003	0.019	−0.186	1.000	−0.206
9	0.000	0.000	0.000	0.000	0.000	−0.003	0.020	−0.206	1.000

$\rho(\pi^+,\pi^-)$	1	2	3	4	5	6	7	8	9
1	0.112	−0.015	0.000	−0.001	0.000	0.000	0.000	0.000	0.000
2	−0.015	0.084	−0.017	0.000	−0.001	0.000	0.000	0.000	0.000
3	0.000	−0.016	0.076	−0.018	0.001	−0.001	0.000	0.000	0.000
4	−0.001	0.000	−0.017	0.071	−0.015	0.001	0.000	0.000	0.000
5	0.000	−0.001	0.001	−0.015	0.062	−0.013	0.001	0.000	0.000
6	0.000	0.000	0.000	0.001	−0.013	0.060	−0.009	0.001	0.000
7	0.000	0.000	0.000	0.000	0.001	−0.008	0.039	−0.005	0.000
8	0.000	0.000	0.000	0.000	0.000	0.001	−0.004	0.022	−0.003
9	0.000	0.000	0.000	0.000	0.000	0.000	0.000	−0.002	0.011

$\rho(\pi^-,\pi^-)$	1	2	3	4	5	6	7	8	9
1	1.000	−0.175	−0.003	−0.009	−0.005	−0.003	0.000	0.000	0.000
2	−0.175	1.000	−0.212	0.005	−0.011	−0.003	−0.001	0.000	0.000
3	−0.003	−0.212	1.000	−0.241	0.009	−0.008	−0.001	0.000	0.000
4	−0.009	0.005	−0.241	1.000	−0.225	0.010	−0.004	0.000	0.000
5	−0.005	−0.011	0.009	−0.225	1.000	−0.207	0.014	−0.003	0.000
6	−0.003	−0.003	−0.008	0.010	−0.207	1.000	−0.196	0.018	−0.002
7	0.000	−0.001	−0.001	−0.004	0.014	−0.196	1.000	−0.178	0.018
8	0.000	0.000	0.000	0.000	−0.003	0.018	−0.178	1.000	−0.176
9	0.000	0.000	0.000	0.000	0.000	−0.002	0.018	−0.176	1.000

Table B.10: Statistical correlations of the Born asymmetries on the deuteron. Listed are the correlations in the nine x-bins of the for each combination of asymmetries.

$\rho(e,e)$	1	2	3	4	5	6	7	8	9
1	1.000	−0.175	0.009	−0.010	−0.004	−0.006	−0.002	0.000	0.000
2	−0.175	1.000	−0.245	0.023	−0.016	−0.004	−0.002	0.000	0.000
3	0.009	−0.245	1.000	−0.308	0.031	−0.014	−0.001	0.000	0.000
4	−0.010	0.023	−0.308	1.000	−0.336	0.045	−0.011	0.001	0.000
5	−0.004	−0.016	0.031	−0.336	1.000	−0.304	0.040	−0.008	0.001
6	−0.006	−0.004	−0.014	0.045	−0.304	1.000	−0.272	0.041	−0.007
7	−0.002	−0.002	−0.001	−0.011	0.040	−0.272	1.000	−0.256	0.042
8	0.000	0.000	0.000	0.001	−0.008	0.041	−0.256	1.000	−0.265
9	0.000	0.000	0.000	0.000	0.001	−0.007	0.042	−0.265	1.000

$\rho(e,\pi^+)$	1	2	3	4	5	6	7	8	9
1	0.404	−0.069	0.003	−0.003	−0.001	−0.002	0.000	0.000	0.000
2	−0.072	0.398	−0.091	0.007	−0.005	−0.001	0.000	0.000	0.000
3	0.003	−0.085	0.366	−0.103	0.008	−0.004	0.000	0.000	0.000
4	−0.003	0.007	−0.088	0.329	−0.097	0.011	−0.003	0.000	0.000
5	−0.001	−0.004	0.009	−0.083	0.294	−0.081	0.009	−0.002	0.000
6	−0.001	0.000	−0.003	0.009	−0.069	0.273	−0.066	0.009	−0.001
7	0.000	0.000	0.000	−0.002	0.007	−0.058	0.250	−0.057	0.009
8	0.000	0.000	0.000	0.000	−0.001	0.007	−0.050	0.224	−0.056
9	0.000	0.000	0.000	0.000	0.000	−0.001	0.007	−0.052	0.215

$\rho(e,\pi^-)$	1	2	3	4	5	6	7	8	9
1	0.380	−0.064	0.003	−0.003	−0.001	−0.001	0.000	0.000	0.000
2	−0.067	0.367	−0.084	0.006	−0.004	−0.001	0.000	0.000	0.000
3	0.003	−0.077	0.334	−0.092	0.007	−0.003	0.000	0.000	0.000
4	−0.003	0.006	−0.078	0.294	−0.085	0.009	−0.002	0.000	0.000
5	−0.001	−0.003	0.007	−0.070	0.259	−0.070	0.008	−0.001	0.000
6	0.000	0.000	−0.002	0.007	−0.058	0.235	−0.056	0.007	−0.001
7	0.000	0.000	0.000	−0.001	0.005	−0.047	0.211	−0.047	0.007
8	0.000	0.000	0.000	0.000	−0.001	0.005	−0.039	0.186	−0.047
9	0.000	0.000	0.000	0.000	0.000	−0.001	0.005	−0.040	0.176

$\rho(e,K^+)$	1	2	3	4	5	6	7	8	9
1	0.151	−0.027	0.001	−0.001	−0.001	−0.001	0.000	0.000	0.000
2	−0.029	0.157	−0.037	0.003	−0.002	−0.001	0.000	0.000	0.000
3	0.001	−0.035	0.150	−0.043	0.003	−0.002	0.000	0.000	0.000
4	−0.001	0.003	−0.038	0.139	−0.042	0.005	−0.001	0.000	0.000
5	0.000	−0.002	0.005	−0.036	0.128	−0.036	0.004	−0.001	0.000
6	0.000	0.000	−0.001	0.004	−0.031	0.122	−0.030	0.004	−0.001
7	0.000	0.000	0.000	−0.001	0.003	−0.026	0.113	−0.027	0.004
8	0.000	0.000	0.000	0.000	0.000	0.003	−0.022	0.104	−0.027
9	0.000	0.000	0.000	0.000	0.000	0.000	0.003	−0.023	0.099

$\rho(e, K^-)$	1	2	3	4	5	6	7	8	9
1	0.112	−0.019	0.001	−0.001	0.000	0.000	0.000	0.000	0.000
2	−0.019	0.108	−0.025	0.002	−0.001	0.000	0.000	0.000	0.000
3	0.000	−0.022	0.098	−0.027	0.002	−0.001	0.000	0.000	0.000
4	−0.001	0.002	−0.022	0.086	−0.025	0.003	−0.001	0.000	0.000
5	0.000	−0.001	0.002	−0.020	0.075	−0.020	0.002	0.000	0.000
6	0.000	0.000	−0.001	0.002	−0.016	0.068	−0.016	0.002	0.000
7	0.000	0.000	0.000	0.000	0.001	−0.013	0.058	−0.014	0.002
8	0.000	0.000	0.000	0.000	0.000	0.001	−0.009	0.051	−0.013
9	0.000	0.000	0.000	0.000	0.000	0.000	0.001	−0.009	0.049
$\rho(\pi^+, \pi^+)$	1	2	3	4	5	6	7	8	9
1	1.000	−0.180	0.007	−0.010	−0.004	−0.002	−0.001	0.000	0.000
2	−0.180	1.000	−0.228	0.017	−0.012	−0.001	0.000	0.000	0.000
3	0.007	−0.228	1.000	−0.257	0.021	−0.009	0.000	0.000	0.000
4	−0.010	0.017	−0.257	1.000	−0.257	0.024	−0.006	0.001	0.000
5	−0.004	−0.012	0.021	−0.257	1.000	−0.234	0.021	−0.004	0.001
6	−0.002	−0.001	−0.009	0.024	−0.234	1.000	−0.213	0.025	−0.004
7	−0.001	0.000	0.000	−0.006	0.021	−0.213	1.000	−0.208	0.029
8	0.000	0.000	0.000	0.001	−0.004	0.025	−0.208	1.000	−0.228
9	0.000	0.000	0.000	0.000	0.001	−0.004	0.029	−0.228	1.000
$\rho(\pi^+, \pi^-)$	1	2	3	4	5	6	7	8	9
1	0.112	−0.018	0.001	−0.001	0.000	0.000	0.000	0.000	0.000
2	−0.018	0.095	−0.020	0.001	−0.001	0.000	0.000	0.000	0.000
3	0.001	−0.019	0.084	−0.020	0.001	−0.001	0.000	0.000	0.000
4	−0.001	0.001	−0.020	0.076	−0.018	0.002	0.000	0.000	0.000
5	0.000	−0.001	0.001	−0.017	0.069	−0.014	0.001	0.000	0.000
6	0.000	0.000	0.000	0.001	−0.014	0.059	−0.010	0.001	0.000
7	0.000	0.000	0.000	0.000	0.001	−0.010	0.044	−0.006	0.001
8	0.000	0.000	0.000	0.000	0.000	0.001	−0.006	0.026	−0.005
9	0.000	0.000	0.000	0.000	0.000	0.000	0.001	−0.004	0.018

$\rho(\pi^+, K^+)$	1	2	3	4	5	6	7	8	9
1	−0.001	0.000	0.000	0.000	0.000	0.000	0.000	0.000	0.000
2	0.000	−0.003	0.001	0.000	0.000	0.000	0.000	0.000	0.000
3	0.000	0.001	−0.004	0.001	0.000	0.000	0.000	0.000	0.000
4	0.000	0.000	0.001	−0.004	0.001	0.000	0.000	0.000	0.000
5	0.000	0.000	0.000	0.001	−0.005	0.001	0.000	0.000	0.000
6	0.000	0.000	0.000	0.000	0.001	−0.005	0.001	0.000	0.000
7	0.000	0.000	0.000	0.000	0.000	0.001	−0.006	0.002	0.000
8	0.000	0.000	0.000	0.000	0.000	0.000	0.002	−0.009	0.001
9	0.000	0.000	0.000	0.000	0.000	0.000	0.000	0.001	−0.004

$\rho(\pi^+, K^-)$	1	2	3	4	5	6	7	8	9
1	0.019	−0.002	0.000	0.000	0.000	0.000	0.000	0.000	0.000
2	−0.002	0.012	−0.003	0.000	0.000	0.000	0.000	0.000	0.000
3	0.000	−0.003	0.012	−0.003	0.000	0.000	0.000	0.000	0.000
4	0.000	0.000	−0.003	0.010	−0.003	0.000	0.000	0.000	0.000
5	0.000	0.000	0.000	−0.002	0.009	−0.002	0.000	0.000	0.000
6	0.000	0.000	0.000	0.000	−0.002	0.008	−0.001	0.000	0.000
7	0.000	0.000	0.000	0.000	0.000	−0.001	0.006	−0.001	0.000
8	0.000	0.000	0.000	0.000	0.000	0.000	−0.001	0.005	0.000
9	0.000	0.000	0.000	0.000	0.000	0.000	0.000	0.000	−0.001

$\rho(\pi^-, \pi^-)$	1	2	3	4	5	6	7	8	9
1	1.000	−0.180	0.007	−0.010	−0.003	−0.002	0.000	0.000	0.000
2	−0.180	1.000	−0.226	0.016	−0.010	−0.002	−0.001	0.000	0.000
3	0.007	−0.226	1.000	−0.253	0.018	−0.008	−0.001	0.000	0.000
4	−0.010	0.016	−0.253	1.000	−0.243	0.021	−0.005	0.000	0.000
5	−0.003	−0.010	0.018	−0.243	1.000	−0.226	0.020	−0.003	0.000
6	−0.002	−0.002	−0.008	0.021	−0.226	1.000	−0.205	0.023	−0.003
7	0.000	−0.001	−0.001	−0.005	0.020	−0.205	1.000	−0.194	0.025
8	0.000	0.000	0.000	0.000	−0.003	0.023	−0.194	1.000	−0.218
9	0.000	0.000	0.000	0.000	0.000	−0.003	0.025	−0.218	1.000

$\rho(\pi^-,K^+)$	1	2	3	4	5	6	7	8	9
1	0.028	−0.004	0.000	0.000	0.000	0.000	0.000	0.000	0.000
2	−0.004	0.022	−0.004	0.000	0.000	0.000	0.000	0.000	0.000
3	0.000	−0.004	0.018	−0.005	0.000	0.000	0.000	0.000	0.000
4	0.000	0.000	−0.005	0.018	−0.004	0.000	0.000	0.000	0.000
5	0.000	0.000	0.000	−0.004	0.017	−0.004	0.000	0.000	0.000
6	0.000	0.000	0.000	0.000	−0.004	0.016	−0.002	0.000	0.000
7	0.000	0.000	0.000	0.000	0.000	−0.002	0.010	−0.002	0.000
8	0.000	0.000	0.000	0.000	0.000	0.000	−0.002	0.008	−0.001
9	0.000	0.000	0.000	0.000	0.000	0.000	0.000	−0.001	0.003

$\rho(\pi^-,K^-)$	1	2	3	4	5	6	7	8	9
1	0.004	−0.001	0.000	0.000	0.000	0.000	0.000	0.000	0.000
2	−0.001	0.003	−0.001	0.000	0.000	0.000	0.000	0.000	0.000
3	0.000	0.000	0.002	−0.001	0.000	0.000	0.000	0.000	0.000
4	0.000	0.000	−0.001	0.003	−0.001	0.000	0.000	0.000	0.000
5	0.000	0.000	0.000	−0.001	0.003	−0.001	0.000	0.000	0.000
6	0.000	0.000	0.000	0.000	−0.001	0.003	−0.001	0.000	0.000
7	0.000	0.000	0.000	0.000	0.000	−0.001	0.004	−0.001	0.000
8	0.000	0.000	0.000	0.000	0.000	0.000	−0.001	0.003	0.000
9	0.000	0.000	0.000	0.000	0.000	0.000	0.000	0.000	0.001

$\rho(K^+,K^+)$	1	2	3	4	5	6	7	8	9
1	1.000	−0.185	0.008	−0.010	−0.002	−0.004	0.000	0.000	0.000
2	−0.185	1.000	−0.229	0.018	−0.011	−0.002	0.000	0.000	0.000
3	0.008	−0.229	1.000	−0.266	0.029	−0.010	0.000	−0.001	0.000
4	−0.010	0.018	−0.266	1.000	−0.258	0.026	−0.004	0.000	0.000
5	−0.002	−0.011	0.029	−0.258	1.000	−0.242	0.023	−0.003	0.000
6	−0.004	−0.002	−0.010	0.026	−0.242	1.000	−0.216	0.026	−0.004
7	0.000	0.000	0.000	−0.004	0.023	−0.216	1.000	−0.202	0.028
8	0.000	0.000	−0.001	0.000	−0.003	0.026	−0.202	1.000	−0.225
9	0.000	0.000	0.000	0.000	0.000	−0.004	0.028	−0.225	1.000

$\rho(K^+,K^-)$	1	2	3	4	5	6	7	8	9
1	0.073	−0.014	0.001	−0.001	0.000	0.000	0.000	0.000	0.000
2	−0.013	0.076	−0.018	0.001	−0.001	0.000	0.000	0.000	0.000
3	0.000	−0.017	0.079	−0.019	0.002	−0.001	0.000	0.000	0.000
4	−0.001	0.001	−0.017	0.071	−0.018	0.002	0.000	0.000	0.000
5	0.000	−0.001	0.001	−0.017	0.068	−0.014	0.001	0.000	0.000
6	0.000	0.000	0.000	0.001	−0.013	0.057	−0.010	0.001	0.000
7	0.000	0.000	0.000	0.000	0.001	−0.010	0.044	−0.008	0.001
8	0.000	0.000	0.000	0.000	0.000	0.001	−0.006	0.035	−0.010
9	0.000	0.000	0.000	0.000	0.000	0.000	0.001	−0.007	0.046
$\rho(K^-,K^-)$	1	2	3	4	5	6	7	8	9
1	1.000	−0.170	0.003	−0.009	−0.001	−0.002	0.000	0.000	0.000
2	−0.170	1.000	−0.221	0.016	−0.013	−0.001	−0.001	0.000	0.000
3	0.003	−0.221	1.000	−0.236	0.019	−0.008	0.001	0.000	0.000
4	−0.009	0.016	−0.236	1.000	−0.246	0.021	−0.005	0.001	0.000
5	−0.001	−0.013	0.019	−0.246	1.000	−0.214	0.018	−0.002	0.000
6	−0.002	−0.001	−0.008	0.021	−0.214	1.000	−0.196	0.022	−0.003
7	0.000	−0.001	0.001	−0.005	0.018	−0.196	1.000	−0.169	0.022
8	0.000	0.000	0.000	0.001	−0.002	0.022	−0.169	1.000	−0.186
9	0.000	0.000	0.000	0.000	0.000	−0.003	0.022	−0.186	1.000

Table B.11: Systematic uncertainties of the Born asymmeties on the proton. The systematic uncertainties are the weighted averages of 1996 and 1997 data-taking periods. The total systematic uncertainty given in the second column is the quadratic sum of the individual contributions.

				Systematic Uncertainties on $A_{1,p}$				
$\langle x \rangle$	Total	P_B	P_T	ϕ	$R(x,Q^2)$	$g_2(x,Q^2)$	QED	Det.
0.033	0.0091	0.0053	0.0067	0.0000	0.0012	0.0004	0.0020	0.0020
0.048	0.0093	0.0054	0.0067	0.0000	0.0015	0.0009	0.0022	0.0022
0.065	0.0089	0.0051	0.0061	0.0000	0.0015	0.0015	0.0023	0.0023
0.087	0.0145	0.0081	0.0101	0.0000	0.0024	0.0024	0.0039	0.0039
0.118	0.0181	0.0102	0.0125	0.0000	0.0025	0.0036	0.0047	0.0047
0.166	0.0213	0.0120	0.0147	0.0000	0.0023	0.0049	0.0056	0.0056
0.240	0.0290	0.0162	0.0201	0.0000	0.0022	0.0068	0.0077	0.0077
0.340	0.0357	0.0196	0.0244	0.0000	0.0022	0.0100	0.0095	0.0095
0.447	0.0489	0.0271	0.0332	0.0000	0.0026	0.0153	0.0122	0.0122

Systematic Uncertainties on $A_{1,p}^{h^+}$								
$\langle x \rangle$	Total	P_B	P_T	ϕ	$R(x,Q^2)$	$g_2(x,Q^2)$	QED	Det.
0.034	0.0077	0.0040	0.0050	0.0033	0.0014	0.0004	0.0011	0.0022
0.048	0.0113	0.0059	0.0073	0.0046	0.0022	0.0009	0.0016	0.0033
0.065	0.0097	0.0049	0.0057	0.0047	0.0018	0.0014	0.0014	0.0027
0.087	0.0148	0.0074	0.0092	0.0068	0.0024	0.0022	0.0021	0.0041
0.118	0.0214	0.0113	0.0138	0.0086	0.0030	0.0031	0.0030	0.0060
0.166	0.0213	0.0112	0.0137	0.0086	0.0022	0.0042	0.0029	0.0057
0.239	0.0298	0.0156	0.0199	0.0104	0.0024	0.0058	0.0042	0.0084
0.338	0.0304	0.0155	0.0194	0.0115	0.0018	0.0089	0.0040	0.0081
0.448	0.0535	0.0286	0.0348	0.0179	0.0031	0.0142	0.0076	0.0152

Systematic Uncertainties on $A_{1,p}^{h^-}$								
$\langle x \rangle$	Total	P_B	P_T	ϕ	$R(x,Q^2)$	$g_2(x,Q^2)$	QED	Det.
0.033	0.0054	0.0028	0.0036	0.0022	0.0009	0.0004	0.0007	0.0014
0.048	0.0087	0.0044	0.0058	0.0032	0.0017	0.0009	0.0013	0.0025
0.065	0.0058	0.0029	0.0033	0.0025	0.0012	0.0014	0.0009	0.0018
0.087	0.0068	0.0031	0.0041	0.0031	0.0011	0.0021	0.0010	0.0019
0.118	0.0137	0.0071	0.0090	0.0052	0.0018	0.0030	0.0019	0.0037
0.165	0.0132	0.0067	0.0085	0.0049	0.0013	0.0040	0.0018	0.0035
0.239	0.0173	0.0088	0.0109	0.0063	0.0013	0.0056	0.0024	0.0047
0.339	0.0396	0.0211	0.0261	0.0137	0.0025	0.0087	0.0057	0.0114
0.447	0.0367	0.0182	0.0228	0.0122	0.0021	0.0145	0.0050	0.0099

Systematic Uncertainties on $A_{1,p}^{\pi^+}$								
$\langle x \rangle$	Total	P_B	P_T	ϕ	$R(x,Q^2)$	$g_2(x,Q^2)$	QED	Det.
0.033	0.0058	0.0029	0.0038	0.0025	0.0010	0.0004	0.0008	0.0016
0.047	0.0091	0.0047	0.0059	0.0037	0.0017	0.0008	0.0013	0.0027
0.064	0.0068	0.0033	0.0040	0.0037	0.0010	0.0012	0.0008	0.0017
0.087	0.0158	0.0081	0.0099	0.0069	0.0025	0.0017	0.0023	0.0046
0.118	0.0214	0.0114	0.0138	0.0083	0.0028	0.0023	0.0032	0.0063
0.166	0.0203	0.0107	0.0133	0.0076	0.0021	0.0031	0.0030	0.0060
0.238	0.0201	0.0106	0.0131	0.0075	0.0014	0.0046	0.0028	0.0056
0.338	0.0379	0.0196	0.0252	0.0136	0.0023	0.0075	0.0056	0.0111
0.449	0.0571	0.0311	0.0365	0.0195	0.0034	0.0130	0.0087	0.0173

⟨x⟩	Total	P_B	P_T	ϕ	$R(x,Q^2)$	$g_2(x,Q^2)$	QED	Det.
			Systematic Uncertainties on $A^{\tau^-}_{1,p}$					
0.033	0.0053	0.0027	0.0035	0.0022	0.0008	0.0004	0.0007	0.0014
0.047	0.0095	0.0049	0.0063	0.0033	0.0019	0.0008	0.0014	0.0029
0.064	0.0040	0.0019	0.0023	0.0016	0.0008	0.0012	0.0006	0.0013
0.087	0.0049	0.0023	0.0030	0.0020	0.0008	0.0017	0.0007	0.0014
0.117	0.0060	0.0029	0.0036	0.0025	0.0007	0.0022	0.0008	0.0015
0.165	0.0109	0.0055	0.0068	0.0042	0.0011	0.0030	0.0016	0.0031
0.238	0.0191	0.0102	0.0125	0.0067	0.0014	0.0045	0.0027	0.0054
0.338	0.0245	0.0129	0.0148	0.0088	0.0014	0.0076	0.0035	0.0069
0.450	0.0409	0.0159	0.0250	0.0103	0.0018	0.0137	0.0045	0.0090

Table B.12: Systematic uncertainties of the Born asymmeties on the deuteron. The systematic uncertainties are the weighted averages of 1998, 1999, and 2000 data-taking periods. The total systematic uncertainty given in the second column is the quadratic sum of the individual contributions.

⟨x⟩	Total	P_B	P_T	ϕ	$R(x,Q^2)$	$g_2(x,Q^2)$	QED	Det.
			Systematic Uncertainties on $A_{1,d}$					
0.033	0.0015	0.0005	0.0012	0.0000	0.0002	0.0002	0.0004	0.0004
0.048	0.0017	0.0006	0.0013	0.0000	0.0003	0.0004	0.0005	0.0005
0.065	0.0023	0.0008	0.0016	0.0000	0.0005	0.0007	0.0008	0.0008
0.087	0.0032	0.0012	0.0024	0.0000	0.0005	0.0011	0.0009	0.0009
0.118	0.0056	0.0020	0.0043	0.0000	0.0008	0.0016	0.0016	0.0016
0.166	0.0084	0.0031	0.0066	0.0000	0.0009	0.0023	0.0023	0.0023
0.240	0.0118	0.0043	0.0093	0.0000	0.0009	0.0032	0.0032	0.0032
0.339	0.0200	0.0072	0.0157	0.0000	0.0013	0.0048	0.0059	0.0059
0.446	0.0247	0.0092	0.0194	0.0000	0.0014	0.0075	0.0063	0.0063

⟨x⟩	Total	P_B	P_T	ϕ	$R(x,Q^2)$	$g_2(x,Q^2)$	QED	Det.
			Systematic Uncertainties on $A^{h^+}_{1,d}$					
0.033	0.0007	0.0002	0.0004	0.0003	0.0001	0.0002	0.0001	0.0002
0.048	0.0018	0.0005	0.0012	0.0008	0.0003	0.0004	0.0002	0.0005
0.065	0.0028	0.0008	0.0016	0.0014	0.0007	0.0006	0.0006	0.0011
0.087	0.0045	0.0014	0.0029	0.0020	0.0009	0.0010	0.0008	0.0015
0.118	0.0040	0.0012	0.0027	0.0020	0.0003	0.0014	0.0003	0.0007
0.166	0.0088	0.0031	0.0064	0.0036	0.0010	0.0019	0.0013	0.0027
0.238	0.0107	0.0037	0.0079	0.0041	0.0008	0.0027	0.0015	0.0029
0.339	0.0157	0.0051	0.0111	0.0064	0.0010	0.0043	0.0024	0.0047
0.446	0.0164	0.0053	0.0113	0.0060	0.0008	0.0070	0.0019	0.0038

$\langle x \rangle$	Total	P_B	P_T	ϕ	$R(x, Q^2)$	$g_2(x, Q^2)$	QED	Det.
			Systematic Uncertainties on $A_{1,d}^{h^-}$					
0.033	0.0013	0.0003	0.0008	0.0003	0.0003	0.0002	0.0002	0.0005
0.047	0.0014	0.0004	0.0009	0.0006	0.0003	0.0004	0.0002	0.0004
0.065	0.0023	0.0007	0.0014	0.0010	0.0006	0.0006	0.0004	0.0009
0.087	0.0034	0.0011	0.0024	0.0014	0.0005	0.0009	0.0005	0.0009
0.118	0.0041	0.0011	0.0027	0.0017	0.0007	0.0013	0.0007	0.0015
0.165	0.0068	0.0024	0.0048	0.0030	0.0006	0.0018	0.0008	0.0015
0.238	0.0106	0.0036	0.0075	0.0044	0.0009	0.0027	0.0017	0.0034
0.338	0.0180	0.0061	0.0126	0.0074	0.0013	0.0043	0.0030	0.0060
0.446	0.0146	0.0046	0.0086	0.0061	0.0008	0.0070	0.0020	0.0040

$\langle x \rangle$	Total	P_B	P_T	ϕ	$R(x, Q^2)$	$g_2(x, Q^2)$	QED	Det.
			Systematic Uncertainties on $A_{1,d}^{\pi^+}$					
0.033	0.0011	0.0003	0.0006	0.0004	0.0003	0.0002	0.0003	0.0005
0.047	0.0022	0.0007	0.0016	0.0008	0.0005	0.0004	0.0004	0.0007
0.064	0.0017	0.0005	0.0010	0.0009	0.0003	0.0005	0.0003	0.0005
0.087	0.0030	0.0009	0.0019	0.0016	0.0005	0.0008	0.0004	0.0009
0.118	0.0062	0.0020	0.0045	0.0026	0.0009	0.0010	0.0010	0.0019
0.165	0.0080	0.0027	0.0060	0.0032	0.0008	0.0014	0.0012	0.0024
0.238	0.0075	0.0026	0.0051	0.0033	0.0006	0.0022	0.0011	0.0022
0.339	0.0205	0.0068	0.0149	0.0079	0.0015	0.0037	0.0036	0.0072
0.446	0.0133	0.0039	0.0082	0.0046	0.0006	0.0065	0.0016	0.0032

$\langle x \rangle$	Total	P_B	P_T	ϕ	$R(x, Q^2)$	$g_2(x, Q^2)$	QED	Det.
			Systematic Uncertainties on $A_{1,d}^{\pi^-}$					
0.033	0.0014	0.0004	0.0010	0.0004	0.0003	0.0002	0.0003	0.0005
0.047	0.0012	0.0002	0.0007	0.0004	0.0003	0.0004	0.0002	0.0005
0.064	0.0028	0.0009	0.0018	0.0010	0.0007	0.0005	0.0006	0.0012
0.086	0.0021	0.0006	0.0013	0.0011	0.0002	0.0007	0.0002	0.0004
0.118	0.0046	0.0015	0.0031	0.0018	0.0008	0.0010	0.0009	0.0018
0.165	0.0037	0.0012	0.0024	0.0018	0.0002	0.0014	0.0003	0.0006
0.237	0.0118	0.0040	0.0084	0.0047	0.0011	0.0022	0.0020	0.0041
0.337	0.0213	0.0077	0.0148	0.0085	0.0016	0.0037	0.0039	0.0077
0.451	0.0200	0.0051	0.0142	0.0065	0.0009	0.0067	0.0023	0.0046

$\langle x \rangle$	Total	P_B	P_T	ϕ	$R(x, Q^2)$	$g_2(x, Q^2)$	QED	Det.
Systematic Uncertainties on $A_{1,d}^{K^+}$								
0.033	0.0021	0.0005	0.0014	0.0009	0.0003	0.0002	0.0002	0.0005
0.048	0.0043	0.0015	0.0029	0.0022	0.0007	0.0004	0.0005	0.0011
0.065	0.0083	0.0025	0.0058	0.0034	0.0018	0.0005	0.0015	0.0029
0.086	0.0079	0.0028	0.0058	0.0030	0.0013	0.0008	0.0012	0.0024
0.118	0.0047	0.0016	0.0033	0.0022	0.0006	0.0010	0.0007	0.0013
0.165	0.0105	0.0036	0.0081	0.0039	0.0010	0.0014	0.0014	0.0029
0.238	0.0123	0.0039	0.0096	0.0046	0.0007	0.0022	0.0014	0.0029
0.336	0.0273	0.0100	0.0201	0.0103	0.0018	0.0037	0.0044	0.0088
0.448	0.0411	0.0111	0.0337	0.0130	0.0019	0.0066	0.0046	0.0093

$\langle x \rangle$	Total	P_B	P_T	ϕ	$R(x, Q^2)$	$g_2(x, Q^2)$	QED	Det.
Systematic Uncertainties on $A_{1,d}^{K^-}$								
0.033	0.0039	0.0013	0.0031	0.0012	0.0006	0.0002	0.0005	0.0009
0.047	0.0041	0.0015	0.0030	0.0015	0.0008	0.0003	0.0007	0.0013
0.064	0.0051	0.0010	0.0035	0.0013	0.0011	0.0005	0.0009	0.0019
0.086	0.0046	0.0016	0.0033	0.0016	0.0008	0.0007	0.0008	0.0015
0.118	0.0033	0.0010	0.0022	0.0009	0.0003	0.0010	0.0003	0.0007
0.165	0.0070	0.0025	0.0055	0.0025	0.0005	0.0013	0.0007	0.0014
0.236	0.0070	0.0024	0.0047	0.0027	0.0006	0.0020	0.0012	0.0025
0.336	0.0206	0.0059	0.0142	0.0073	0.0016	0.0036	0.0040	0.0079
0.444	0.0861	0.0317	0.0640	0.0325	0.0056	0.0062	0.0146	0.0292

Appendix C

Results: Polarized Quark Distributions

Table C.1: Quark polarizations $(\Delta q/q)(x)$, and polarized quark densities $x \cdot \Delta q(x, Q_0^2)$ evolved to $Q_0^2 = 2.5\,\mathrm{GeV}^2$. The systematic uncertainty due to the purities and parton distribution functions ($[\pm Pur]$) is included in the total systematic uncertainty ($\pm$sys).

$\langle x \rangle$	$\Delta u/u$	$\pm$stat	$\pm$sys	$[\pm Pur]$	$\pm$MC	$x \cdot \Delta u$	$\pm$stat	$\pm$sys	$[\pm Pur]$	$\pm$MC
0.033	0.063	0.087	0.064	0.062	0.009	0.030	0.041	0.030	0.029	0.004
0.048	0.102	0.082	0.020	0.003	0.006	0.052	0.042	0.010	0.001	0.003
0.065	0.145	0.074	0.030	0.020	0.004	0.078	0.040	0.016	0.011	0.002
0.087	0.379	0.071	0.062	0.055	0.004	0.219	0.041	0.036	0.032	0.003
0.118	0.411	0.063	0.052	0.041	0.005	0.253	0.038	0.032	0.025	0.003
0.166	0.404	0.065	0.038	0.023	0.004	0.262	0.042	0.024	0.015	0.003
0.239	0.404	0.078	0.033	0.010	0.003	0.265	0.051	0.022	0.007	0.002
0.339	0.559	0.063	0.054	0.005	0.009	0.324	0.036	0.031	0.003	0.005
0.447	0.729	0.109	0.069	0.014	0.008	0.312	0.047	0.029	0.006	0.004

$\langle x \rangle$	$\Delta d/d$	$\pm$stat	$\pm$sys	$[\pm Pur]$	$\pm$MC	$x \cdot \Delta d$	$\pm$stat	$\pm$sys	$[\pm Pur]$	$\pm$MC
0.033	-0.091	0.112	0.035	0.015	0.011	-0.034	0.042	0.013	0.005	0.004
0.048	0.044	0.108	0.044	0.032	0.009	0.017	0.041	0.017	0.012	0.003
0.065	-0.101	0.099	0.031	0.014	0.009	-0.039	0.039	0.012	0.006	0.004
0.087	-0.200	0.101	0.040	0.013	0.015	-0.079	0.040	0.016	0.005	0.006
0.118	-0.394	0.096	0.069	0.048	0.017	-0.155	0.038	0.027	0.019	0.007
0.166	-0.078	0.114	0.058	0.008	0.014	-0.030	0.043	0.022	0.003	0.005
0.239	-0.475	0.150	0.075	0.001	0.011	-0.154	0.048	0.024	0.000	0.004
0.339	-0.269	0.191	0.164	0.016	0.038	-0.063	0.045	0.038	0.004	0.009
0.447	-0.815	0.408	0.246	0.057	0.040	-0.116	0.058	0.035	0.008	0.006

$\langle x \rangle$	$\Delta \bar{u}/\bar{u}$	$\pm$stat	$\pm$sys	$[\pm Pur]$	$\pm$MC	$x \cdot \Delta \bar{u}$	$\pm$stat	$\pm$sys	$[\pm Pur]$	$\pm$MC

0.033	0.249	0.246	0.161	0.160	0.038	0.044	0.043	0.028	0.028	0.007
0.048	0.185	0.274	0.037	0.006	0.033	0.029	0.043	0.006	0.001	0.005
0.065	0.013	0.299	0.093	0.086	0.039	0.002	0.040	0.013	0.012	0.005
0.087	−0.557	0.357	0.274	0.270	0.043	−0.062	0.040	0.031	0.030	0.005
0.118	−0.727	0.436	0.276	0.269	0.051	−0.062	0.037	0.024	0.023	0.004
0.166	−0.771	0.718	0.300	0.283	0.070	−0.043	0.040	0.017	0.016	0.004
0.239	1.341	1.493	0.352	0.259	0.118	0.045	0.050	0.012	0.009	0.004
$\langle x \rangle$	$\Delta \bar{d}/\bar{d}$	±stat	±sys	[±Pur]	±MC	$x \cdot \Delta \bar{d}$	±stat	±sys	[±Pur]	±MC
0.033	−0.168	0.207	0.033	0.015	0.015	−0.034	0.042	0.007	0.003	0.003
0.048	−0.464	0.217	0.081	0.077	0.029	−0.086	0.040	0.015	0.014	0.005
0.065	0.013	0.216	0.040	0.035	0.034	0.002	0.037	0.007	0.006	0.006
0.087	−0.174	0.242	0.048	0.043	0.038	−0.027	0.037	0.007	0.007	0.006
0.118	0.438	0.254	0.131	0.128	0.036	0.058	0.034	0.017	0.017	0.005
0.166	−0.816	0.390	0.063	0.047	0.050	−0.083	0.040	0.006	0.005	0.005
0.239	0.412	0.762	0.134	0.029	0.098	0.024	0.044	0.008	0.002	0.006
$\langle x \rangle$	$\Delta s/s$	±stat	±sys	[±Pur]	±MC	$x \cdot \Delta s$	±stat	±sys	[±Pur]	±MC
0.033	0.348	0.551	0.147	0.122	0.044	0.032	0.050	0.013	0.011	0.004
0.048	0.452	0.474	0.146	0.142	0.034	0.037	0.038	0.012	0.011	0.003
0.065	−0.041	0.440	0.034	0.025	0.042	−0.003	0.031	0.002	0.002	0.003
0.087	−0.097	0.486	0.111	0.106	0.051	−0.006	0.030	0.007	0.006	0.003
0.118	−0.272	0.527	0.061	0.056	0.062	−0.013	0.026	0.003	0.003	0.003
0.166	1.193	0.756	0.078	0.022	0.067	0.042	0.026	0.003	0.001	0.002
0.239	−1.153	1.368	0.356	0.344	0.111	−0.023	0.027	0.007	0.007	0.002

Table C.2: The polarized light sea flavour asymmetry evolved to $Q_0^2 = 2.5\,\text{GeV}^2$. The systematic uncertainty due to the purities and parton distribution function ($[\pm Pur]$) is included in the total systematic uncertainty ($\pm$sys).

$\langle x \rangle$	$x \cdot (\Delta \bar{u} - \Delta \bar{d})$	$\pm$stat	$\pm$sys	$[\pm Pur]$	$\pm$MC
0.033	0.075	0.065	0.025	0.024	0.009
0.048	0.113	0.067	0.015	0.013	0.010
0.065	−0.001	0.064	0.018	0.017	0.011
0.087	−0.036	0.065	0.037	0.037	0.010
0.118	−0.120	0.061	0.040	0.040	0.009
0.166	0.040	0.071	0.022	0.021	0.009
0.239	0.024	0.089	0.018	0.008	0.010

Table C.3: Statistical correlations of the quark polarizations. Listed are the correlations the nine x-bins for all flavour combinations. In the case of the sea flavours, the correlations are zero in the two highest bins, because these flavours were fixed at zero in those bins.

$\rho\left(\frac{\Delta u}{u}, \frac{\Delta u}{u}\right)$	1	2	3	4	5	6	7	8	9
1	1.000	−0.174	0.000	−0.010	−0.005	−0.003	0.000	0.000	0.000
2	−0.174	1.000	−0.215	0.007	−0.011	−0.003	−0.001	0.000	0.000
3	0.000	−0.215	1.000	−0.246	0.010	−0.009	−0.001	0.000	0.000
4	−0.010	0.007	−0.246	1.000	−0.242	0.014	−0.005	0.000	0.000
5	−0.005	−0.011	0.010	−0.242	1.000	−0.221	0.016	−0.003	0.000
6	−0.003	−0.003	−0.009	0.014	−0.221	1.000	−0.206	0.013	−0.002
7	0.000	−0.001	−0.001	−0.005	0.016	−0.206	1.000	−0.099	0.012
8	0.000	0.000	0.000	0.000	−0.003	0.013	−0.099	1.000	−0.231
9	0.000	0.000	0.000	0.000	0.000	−0.002	0.012	−0.231	1.000
$\rho\left(\frac{\Delta u}{u}, \frac{\Delta d}{d}\right)$	1	2	3	4	5	6	7	8	9
1	−0.377	0.075	0.002	0.005	0.003	0.002	0.000	0.000	0.000
2	0.065	−0.424	0.098	−0.002	0.006	0.002	0.001	0.000	0.000
3	0.002	0.093	−0.475	0.126	−0.003	0.005	0.001	0.000	0.000
4	0.004	−0.001	0.123	−0.529	0.132	−0.008	0.004	0.000	0.000
5	0.003	0.005	−0.004	0.132	−0.542	0.128	−0.009	0.002	0.000
6	0.002	0.002	0.005	−0.007	0.125	−0.586	0.127	−0.011	0.002
7	0.000	0.000	0.001	0.003	−0.009	0.122	−0.600	0.086	−0.011
8	0.000	0.000	0.000	0.000	0.003	−0.015	0.120	−0.894	0.208
9	0.000	0.000	0.000	0.000	0.000	0.003	−0.016	0.207	−0.894
$\rho\left(\frac{\Delta u}{u}, \frac{\Delta \bar{u}}{\bar{u}}\right)$	1	2	3	4	5	6	7	8	9
1	−0.919	0.161	0.001	0.008	0.004	0.003	0.000	0.000	0.000

	1	2	3	4	5	6	7	8	9
2	0.162	−0.924	0.196	−0.006	0.010	0.003	0.001	0.000	0.000
3	0.001	0.196	−0.913	0.219	−0.009	0.007	0.001	0.000	0.000
4	0.009	−0.006	0.217	−0.887	0.202	−0.010	0.004	0.000	0.000
5	0.004	0.009	−0.009	0.201	−0.871	0.181	−0.012	0.000	0.000
6	0.002	0.003	0.007	−0.010	0.182	−0.869	0.172	0.000	0.000
7	0.000	0.001	0.001	0.004	−0.012	0.175	−0.889	0.000	0.000
8	0.000	0.000	0.000	0.000	0.000	0.001	−0.004	0.000	0.000
9	0.000	0.000	0.000	0.000	0.000	0.000	0.001	0.000	0.000
$\rho\left(\frac{\Delta u}{u}, \frac{\Delta \bar{d}}{\bar{d}}\right)$	1	2	3	4	5	6	7	8	9
1	0.284	−0.062	−0.002	−0.004	−0.003	−0.002	0.000	0.000	0.000
2	−0.048	0.346	−0.079	0.001	−0.005	−0.002	0.000	0.000	0.000
3	−0.002	−0.072	0.383	−0.098	0.002	−0.003	0.000	0.000	0.000
4	−0.003	0.000	−0.091	0.419	−0.092	0.003	−0.002	0.000	0.000
5	−0.002	−0.004	0.002	−0.091	0.416	−0.089	0.005	0.000	0.000
6	−0.001	−0.001	−0.003	0.003	−0.085	0.458	−0.090	0.000	0.000
7	0.000	0.000	0.000	−0.002	0.005	−0.090	0.480	0.000	0.000
8	0.000	0.000	0.000	0.000	0.000	−0.001	0.000	0.000	0.000
9	0.000	0.000	0.000	0.000	0.000	0.000	0.000	0.000	0.000
$\rho\left(\frac{\Delta u}{u}, \frac{\Delta s}{s}\right)$	1	2	3	4	5	6	7	8	9
1	0.115	−0.008	0.000	0.000	0.000	0.000	0.000	0.000	0.000
2	−0.026	0.063	−0.012	0.000	0.000	0.000	0.000	0.000	0.000
3	0.000	−0.017	0.073	−0.009	0.000	0.000	0.000	0.000	0.000
4	−0.001	0.000	−0.019	0.029	−0.009	0.000	0.000	0.000	0.000
5	−0.001	−0.001	0.000	−0.006	0.038	0.000	0.001	0.000	0.000
6	−0.001	−0.001	−0.001	0.000	−0.011	0.003	−0.017	0.000	0.000
7	0.000	0.000	0.000	0.000	0.001	−0.005	0.104	0.000	0.000
8	0.000	0.000	0.000	0.000	0.000	0.001	0.000	0.000	0.000
9	0.000	0.000	0.000	0.000	0.000	0.000	0.000	0.000	0.000

$\rho\left(\frac{\Delta d}{d}, \frac{\Delta d}{d}\right)$	1	2	3	4	5	6	7	8	9
1	1.000	−0.177	0.004	−0.010	−0.004	−0.003	0.000	0.000	0.000
2	−0.177	1.000	−0.224	0.013	−0.011	−0.003	−0.001	0.000	0.000
3	0.004	−0.224	1.000	−0.258	0.016	−0.009	−0.001	0.000	0.000
4	−0.010	0.013	−0.258	1.000	−0.260	0.022	−0.006	0.000	0.000
5	−0.004	−0.011	0.016	−0.260	1.000	−0.239	0.021	−0.004	0.001
6	−0.003	−0.003	−0.009	0.022	−0.239	1.000	−0.217	0.019	−0.003
7	0.000	−0.001	−0.001	−0.006	0.021	−0.217	1.000	−0.141	0.020
8	0.000	0.000	0.000	0.000	−0.004	0.019	−0.141	1.000	−0.239
9	0.000	0.000	0.000	0.000	0.001	−0.003	0.020	−0.239	1.000

$\rho\left(\frac{\Delta d}{d}, \frac{\Delta \bar{u}}{\bar{u}}\right)$	1	2	3	4	5	6	7	8	9
1	0.273	−0.047	−0.003	−0.003	−0.002	−0.001	0.000	0.000	0.000
2	−0.055	0.311	−0.064	0.000	−0.003	−0.001	0.000	0.000	0.000
3	−0.002	−0.069	0.335	−0.077	0.001	−0.002	0.000	0.000	0.000
4	−0.004	0.000	−0.082	0.354	−0.073	0.001	−0.001	0.000	0.000
5	−0.002	−0.003	0.001	−0.072	0.335	−0.064	0.003	0.000	0.000
6	−0.001	−0.002	−0.003	0.002	−0.073	0.387	−0.075	0.000	0.000
7	0.000	0.000	0.000	−0.002	0.003	−0.074	0.408	0.000	0.000
8	0.000	0.000	0.000	0.000	0.001	−0.002	0.007	0.000	0.000
9	0.000	0.000	0.000	0.000	0.000	0.000	−0.002	0.000	0.000

$\rho\left(\frac{\Delta d}{d}, \frac{\Delta \bar{d}}{d}\right)$	1	2	3	4	5	6	7	8	9
1	−0.893	0.158	−0.004	0.009	0.003	0.002	0.000	0.000	0.000
2	0.160	−0.887	0.194	−0.010	0.009	0.002	0.001	0.000	0.000
3	−0.004	0.193	−0.859	0.211	−0.013	0.007	0.000	0.000	0.000
4	0.009	−0.011	0.208	−0.822	0.195	−0.013	0.004	0.000	0.000
5	0.003	0.009	−0.012	0.191	−0.792	0.170	−0.013	0.000	0.000
6	0.002	0.002	0.007	−0.014	0.179	−0.805	0.162	0.000	0.000
7	0.000	0.000	0.000	0.004	−0.014	0.162	−0.809	0.000	0.000
8	0.000	0.000	0.000	0.000	0.000	0.000	0.004	0.000	0.000
9	0.000	0.000	0.000	0.000	0.000	0.000	−0.001	0.000	0.000

$\rho\left(\frac{\Delta d}{d}, \frac{\Delta s}{s}\right)$	1	2	3	4	5	6	7	8	9
1	0.014	−0.002	0.001	−0.001	0.000	0.000	0.000	0.000	0.000
2	−0.010	0.038	−0.010	0.001	0.000	0.000	0.000	0.000	0.000
3	0.002	−0.014	0.052	−0.023	0.002	−0.001	0.000	0.000	0.000
4	−0.001	0.002	−0.017	0.076	−0.021	0.003	−0.001	0.000	0.000
5	0.000	0.000	0.001	−0.022	0.076	−0.031	0.002	0.000	0.000
6	0.000	0.000	0.000	0.003	−0.023	0.128	−0.017	0.000	0.000
7	0.000	0.000	0.000	−0.001	0.003	−0.031	0.076	0.000	0.000
8	0.000	0.000	0.000	0.000	0.000	0.001	−0.006	0.000	0.000
9	0.000	0.000	0.000	0.000	0.000	0.000	0.001	0.000	0.000

$\rho\left(\frac{\Delta \bar{u}}{\bar{u}}, \frac{\Delta \bar{u}}{\bar{u}}\right)$	1	2	3	4	5	6	7	8	9
1	1.000	−0.175	−0.001	−0.009	−0.005	−0.003	0.000	0.000	0.000
2	−0.175	1.000	−0.214	0.007	−0.011	−0.003	−0.001	0.000	0.000
3	−0.001	−0.214	1.000	−0.243	0.010	−0.008	−0.001	0.000	0.000
4	−0.009	0.007	−0.243	1.000	−0.231	0.012	−0.005	0.000	0.000
5	−0.005	−0.011	0.010	−0.231	1.000	−0.211	0.014	0.000	0.000
6	−0.003	−0.003	−0.008	0.012	−0.211	1.000	−0.199	0.000	0.000
7	0.000	−0.001	−0.001	−0.005	0.014	−0.199	1.000	0.000	0.000
8	0.000	0.000	0.000	0.000	0.000	0.000	0.000	0.000	0.000
9	0.000	0.000	0.000	0.000	0.000	0.000	0.000	0.000	0.000

$\rho\left(\frac{\Delta \bar{u}}{\bar{u}}, \frac{\Delta \bar{d}}{\bar{d}}\right)$	1	2	3	4	5	6	7	8	9
1	−0.270	0.060	0.002	0.004	0.003	0.002	0.000	0.000	0.000
2	0.047	−0.346	0.080	0.000	0.005	0.002	0.000	0.000	0.000
3	0.003	0.074	−0.396	0.105	−0.002	0.004	0.000	0.000	0.000
4	0.003	0.000	0.098	−0.456	0.103	−0.004	0.002	0.000	0.000
5	0.002	0.004	−0.002	0.104	−0.462	0.103	−0.006	0.000	0.000
6	0.001	0.002	0.003	−0.004	0.096	−0.510	0.101	0.000	0.000
7	0.000	0.000	0.000	0.002	−0.006	0.102	−0.520	0.000	0.000
8	0.000	0.000	0.000	0.000	0.000	0.000	0.000	0.000	0.000
9	0.000	0.000	0.000	0.000	0.000	0.000	0.000	0.000	0.000

$\rho\left(\frac{\Delta\bar{u}}{\bar{u}}, \frac{\Delta s}{s}\right)$	1	2	3	4	5	6	7	8	9
1	−0.323	0.055	0.000	0.003	0.001	0.001	0.000	0.000	0.000
2	0.043	−0.232	0.050	−0.002	0.002	0.001	0.000	0.000	0.000
3	0.000	0.049	−0.223	0.052	−0.002	0.002	0.000	0.000	0.000
4	0.002	−0.002	0.045	−0.175	0.038	−0.002	0.001	0.000	0.000
5	0.000	0.002	−0.003	0.044	−0.180	0.039	−0.003	0.000	0.000
6	0.000	0.000	0.001	−0.002	0.028	−0.131	0.025	0.000	0.000
7	0.000	0.000	0.000	0.001	−0.004	0.047	−0.230	0.000	0.000
8	0.000	0.000	0.000	0.000	0.000	0.000	0.000	0.000	0.000
9	0.000	0.000	0.000	0.000	0.000	0.000	0.000	0.000	0.000

$\rho\left(\frac{\Delta\bar{d}}{\bar{d}}, \frac{\Delta\bar{d}}{\bar{d}}\right)$	1	2	3	4	5	6	7	8	9
1	1.000	−0.178	0.004	−0.010	−0.004	−0.003	0.000	0.000	0.000
2	−0.178	1.000	−0.222	0.012	−0.011	−0.002	−0.001	0.000	0.000
3	0.004	−0.222	1.000	−0.250	0.015	−0.008	−0.001	0.000	0.000
4	−0.010	0.012	−0.250	1.000	−0.240	0.017	−0.005	0.000	0.000
5	−0.004	−0.011	0.015	−0.240	1.000	−0.220	0.017	0.000	0.000
6	−0.003	−0.002	−0.008	0.017	−0.220	1.000	−0.203	0.000	0.000
7	0.000	−0.001	−0.001	−0.005	0.017	−0.203	1.000	0.000	0.000
8	0.000	0.000	0.000	0.000	0.000	0.000	0.000	0.000	0.000
9	0.000	0.000	0.000	0.000	0.000	0.000	0.000	0.000	0.000

$\rho\left(\frac{\Delta\bar{d}}{\bar{d}}, \frac{\Delta s}{s}\right)$	1	2	3	4	5	6	7	8	9
1	−0.202	0.036	−0.003	0.002	0.000	0.000	0.000	0.000	0.000
2	0.036	−0.199	0.047	−0.004	0.002	0.000	0.000	0.000	0.000
3	−0.002	0.046	−0.202	0.051	−0.004	0.001	0.000	0.000	0.000
4	0.002	−0.004	0.058	−0.216	0.054	−0.005	0.001	0.000	0.000
5	0.001	0.002	−0.004	0.053	−0.209	0.047	−0.004	0.000	0.000
6	0.001	0.001	0.002	−0.006	0.064	−0.265	0.057	0.000	0.000
7	0.000	0.000	0.000	0.001	−0.005	0.039	−0.189	0.000	0.000
8	0.000	0.000	0.000	0.000	0.000	0.000	0.000	0.000	0.000
9	0.000	0.000	0.000	0.000	0.000	0.000	0.000	0.000	0.000

$\rho\left(\frac{\Delta s}{s},\frac{\Delta s}{s}\right)$	1	2	3	4	5	6	7	8	9
1	1.000	−0.172	0.004	−0.009	−0.002	−0.002	0.000	0.000	0.000
2	−0.172	1.000	−0.222	0.015	−0.012	−0.001	−0.001	0.000	0.000
3	0.004	−0.222	1.000	−0.242	0.018	−0.008	0.000	0.000	0.000
4	−0.009	0.015	−0.242	1.000	−0.247	0.021	−0.005	0.000	0.000
5	−0.002	−0.012	0.018	−0.247	1.000	−0.217	0.018	0.000	0.000
6	−0.002	−0.001	−0.008	0.021	−0.217	1.000	−0.197	0.000	0.000
7	0.000	−0.001	0.000	−0.005	0.018	−0.197	1.000	0.000	0.000
8	0.000	0.000	0.000	0.000	0.000	0.000	0.000	0.000	0.000
9	0.000	0.000	0.000	0.000	0.000	0.000	0.000	0.000	0.000

Table C.4: Systematic uncertainties on the quark polarizations. The total systematic uncertainty given in the second column is the quadratic sum of the individual contributions.

Systematic uncertainties on $[\Delta u/u](x)$										
$\langle x \rangle$	Total	P_B	P_T	ϕ	R	g_2	QED	Det.	Sea	Pur.
0.033	0.0637	0.0043	0.0055	0.0041	0.0013	0.0005	0.0015	0.0021	0.0139	0.0615
0.048	0.0199	0.0044	0.0053	0.0054	0.0014	0.0006	0.0018	0.0018	0.0174	0.0027
0.065	0.0295	0.0066	0.0080	0.0038	0.0018	0.0007	0.0025	0.0026	0.0183	0.0200
0.087	0.0618	0.0138	0.0167	0.0051	0.0041	0.0008	0.0055	0.0068	0.0156	0.0547
0.118	0.0517	0.0170	0.0208	0.0053	0.0041	0.0010	0.0068	0.0085	0.0119	0.0405
0.166	0.0377	0.0163	0.0197	0.0047	0.0032	0.0014	0.0071	0.0077	0.0101	0.0229
0.239	0.0332	0.0178	0.0220	0.0052	0.0023	0.0020	0.0088	0.0083	0.0045	0.0099
0.339	0.0540	0.0282	0.0362	0.0008	0.0025	0.0043	0.0137	0.0140	0.0196	0.0048
0.447	0.0686	0.0381	0.0478	0.0008	0.0031	0.0072	0.0174	0.0176	0.0097	0.0140

Systematic uncertainties on $[\Delta d/d](x)$										
$\langle x \rangle$	Total	P_B	P_T	ϕ	R	g_2	QED	Det.	Sea	Pur.
0.033	0.0347	0.0071	0.0089	0.0034	0.0014	0.0010	0.0027	0.0032	0.0288	0.0147
0.048	0.0437	0.0080	0.0112	0.0048	0.0011	0.0012	0.0035	0.0039	0.0248	0.0324
0.065	0.0309	0.0093	0.0116	0.0044	0.0018	0.0015	0.0041	0.0039	0.0216	0.0144
0.087	0.0404	0.0176	0.0237	0.0066	0.0029	0.0018	0.0080	0.0098	0.0195	0.0128
0.118	0.0689	0.0245	0.0337	0.0077	0.0036	0.0024	0.0110	0.0129	0.0187	0.0479
0.166	0.0581	0.0260	0.0433	0.0079	0.0009	0.0034	0.0150	0.0169	0.0132	0.0078
0.239	0.0748	0.0363	0.0568	0.0113	0.0025	0.0057	0.0218	0.0203	0.0024	0.0014
0.339	0.1637	0.0734	0.1182	0.0026	0.0010	0.0128	0.0439	0.0452	0.0552	0.0160
0.447	0.2458	0.1179	0.1833	0.0030	0.0034	0.0259	0.0642	0.0649	0.0267	0.0565

Systematic uncertainties on $[\Delta \bar{u}/\bar{u}](x)$										
$\langle x \rangle$	Total	P_B	P_T	ϕ	R	g_2	QED	Det.	Sea	Pur.
0.033	0.1611	0.0102	0.0136	0.0111	0.0013	0.0011	0.0039	0.0032	0.0074	0.1596
0.048	0.0373	0.0144	0.0199	0.0176	0.0029	0.0016	0.0056	0.0071	0.0189	0.0055
0.065	0.0934	0.0049	0.0085	0.0141	0.0002	0.0022	0.0038	0.0045	0.0319	0.0858
0.087	0.2740	0.0108	0.0156	0.0225	0.0052	0.0031	0.0043	0.0070	0.0353	0.2699
0.118	0.2755	0.0178	0.0245	0.0318	0.0070	0.0050	0.0067	0.0115	0.0384	0.2688
0.166	0.2996	0.0192	0.0576	0.0486	0.0056	0.0092	0.0202	0.0205	0.0541	0.2826
0.239	0.3522	0.1041	0.1702	0.1023	0.0072	0.0204	0.0470	0.0586	0.0252	0.2588

Systematic uncertainties on $[\Delta \bar{d}/\bar{d}](x)$										
$\langle x \rangle$	Total	P_B	P_T	ϕ	R	g_2	QED	Det.	Sea	Pur.
0.033	0.0331	0.0068	0.0098	0.0060	0.0006	0.0007	0.0030	0.0023	0.0262	0.0146
0.048	0.0812	0.0083	0.0103	0.0095	0.0020	0.0009	0.0036	0.0027	0.0194	0.0769
0.065	0.0401	0.0027	0.0064	0.0100	0.0010	0.0012	0.0031	0.0050	0.0149	0.0346
0.087	0.0479	0.0009	0.0028	0.0151	0.0014	0.0017	0.0034	0.0029	0.0142	0.0428
0.118	0.1314	0.0048	0.0043	0.0198	0.0030	0.0023	0.0015	0.0061	0.0169	0.1285
0.166	0.0631	0.0140	0.0208	0.0269	0.0054	0.0042	0.0106	0.0096	0.0146	0.0466
0.239	0.1338	0.0587	0.0811	0.0677	0.0004	0.0082	0.0238	0.0385	0.0178	0.0294

Systematic uncertainties on $[\Delta s/s](x)$										
$\langle x \rangle$	Total	P_B	P_T	ϕ	R	g_2	QED	Det.	Sea	Pur.
0.033	0.1469	0.0117	0.0255	0.0099	0.0014	0.0011	0.0064	0.0024	0.0757	0.1221
0.048	0.1465	0.0068	0.0161	0.0113	0.0003	0.0007	0.0059	0.0064	0.0277	0.1421
0.065	0.0345	0.0063	0.0131	0.0108	0.0035	0.0007	0.0071	0.0034	0.0127	0.0249
0.087	0.1108	0.0102	0.0197	0.0142	0.0063	0.0009	0.0102	0.0085	0.0076	0.1064
0.118	0.0614	0.0075	0.0089	0.0188	0.0002	0.0013	0.0078	0.0054	0.0089	0.0557
0.166	0.0781	0.0242	0.0575	0.0274	0.0088	0.0009	0.0238	0.0172	0.0076	0.0216
0.239	0.3560	0.0034	0.0318	0.0702	0.0002	0.0051	0.0255	0.0065	0.0419	0.3440

Table C.5: First moments of the polarized parton densities at a scale of $Q_0^2 = 2.5\,\mathrm{GeV}^2$, using the CTEQ5L unpolarized parton densities [145].

	Measured range	Low-x	High-x	Total integral
Δu	$0.601 \pm 0.039 \pm 0.049$	0.026 ± 0.012	0.021 ± 0.021	$0.649 \pm 0.040 \pm 0.053$
$\Delta \bar{u}$	$-0.002 \pm 0.036 \pm 0.023$	0.008 ± 0.012	-0.003 ± 0.003	$0.003 \pm 0.038 \pm 0.023$
Δd	$-0.226 \pm 0.039 \pm 0.050$	-0.009 ± 0.011	-0.004 ± 0.004	$-0.239 \pm 0.041 \pm 0.050$
$\Delta \bar{d}$	$-0.054 \pm 0.033 \pm 0.011$	-0.013 ± 0.011	-0.003 ± 0.003	$-0.070 \pm 0.035 \pm 0.011$
Δs	$0.028 \pm 0.033 \pm 0.009$	0.005 ± 0.009	-0.002 ± 0.002	$0.032 \pm 0.034 \pm 0.010$
$\Delta u + \Delta \bar{u}$	$0.599 \pm 0.022 \pm 0.065$	0.034 ± 0.007	0.018 ± 0.024	$0.652 \pm 0.023 \pm 0.069$
$\Delta d + \Delta \bar{d}$	$-0.280 \pm 0.026 \pm 0.057$	-0.022 ± 0.008	-0.006 ± 0.006	$-0.309 \pm 0.027 \pm 0.057$
Δu_v	$0.603 \pm 0.071 \pm 0.040$	0.018 ± 0.022	0.024 ± 0.018	$0.646 \pm 0.075 \pm 0.044$
Δd_v	$-0.172 \pm 0.068 \pm 0.045$	0.004 ± 0.020	-0.001 ± 0.001	$-0.169 \pm 0.071 \pm 0.045$
Δq_0	$0.347 \pm 0.024 \pm 0.066$	0.016 ± 0.024	0.011 ± 0.022	$0.374 \pm 0.034 \pm 0.069$
Δq_3	$0.880 \pm 0.045 \pm 0.107$	0.056 ± 0.022	0.025 ± 0.022	$0.961 \pm 0.051 \pm 0.110$
Δq_8	$0.262 \pm 0.078 \pm 0.045$	0.002 ± 0.029	0.016 ± 0.022	$0.280 \pm 0.084 \pm 0.050$

Table C.6: Statistical (ρ_stat) and systematic (ρ_syst) correlations of the first moments of the polarized parton densities in the measured x-range.

ρ_stat	Δu	Δd	$\Delta \bar{u}$	$\Delta \bar{d}$	Δs
Δu	1.000	-0.564	-0.827	0.346	0.075
Δd	-0.564	1.000	0.301	-0.758	0.032
$\Delta \bar{u}$	-0.827	0.301	1.000	-0.385	-0.257
$\Delta \bar{d}$	0.346	-0.758	-0.385	1.000	-0.196
Δs	0.075	0.032	-0.257	-0.196	1.000

ρ_syst	Δu	Δd	$\Delta \bar{u}$	$\Delta \bar{d}$	Δs
Δu	1.000	-0.732	0.577	-0.176	0.388
Δd	-0.732	1.000	-0.170	0.548	0.190
$\Delta \bar{u}$	0.577	-0.170	1.000	0.228	0.524
$\Delta \bar{d}$	-0.176	0.548	0.228	1.000	0.450
Δs	0.388	0.190	0.524	0.450	1.000

Appendix D

Contributions to HERMES

Particle physics experiments require the collaboration of many people. The HERMES collaboration consists of close to 200 collaborators from 10 countries. This appendix summarizes my personal contributions to the experiment.

I began working on my PhD by joining the efforts to improve the existing HERMES data quality scheme. In collaboration with Thore Lindemann, I wrote a software package that accumulated the necessary data in histograms. I developed a comprehensive www-based interface that displays these histograms and transparently archives all additional data quality information.

During my Master's degree I had worked on the particle identification scheme. Throughout my PhD, I continued this effort by providing parent distributions for all datasets. I also optimized the algorithms and eventually implemented a complete package for PID analysis, which includes a user-callable library that provides the most up-to-date particle identification information. Both, the data quality software and the PID package, are now inherent to the HERMES data analysis scheme.

I was involved in the HERMES Monte Carlo group and helped to debug the DIS event generator and the implementation of the radiative correction algorithms. For the HERMES Canada group, I maintained a 5 CPU PC cluster and a number of desktop PC's running Linux. I transferred and synchronized the μDST datasets for local analysis at TRIUMF.

For the data analysis, I wrote and implemented an analysis code to extract the measured asymmetries from the μDST data. In collaboration with Andy Miller, I developed an unfolding algorithm to correct the asymmetries for detector effects and higher order QED processes. For the Δq analysis, I wrote a program to extract the polarized parton distributions from the Born level asymmetries. These latter codes properly account for the statistical and systematic covariances of the asymmetries.

I took shifts during the data taking periods being responsible for the spectrometer. In recent years, I assumed the shift leader position. I contributed to the maintenance of the TRD with safety walks during shutdown periods and by occasionally helping with hardware problems.

Bibliography

[1] M. J. Alguard *et al.*, Phys. Rev. Lett. **37**, 1261 (1976).

[2] J. Ashman *et al.*, **EMC**, Phys. Lett. **B 206**, 364 (1988).

[3] R. L. Jaffe and A. Manohar, Nucl. Phys. **B 337**, 509 (1990).

[4] P. L. Anthony *et al.*, **E155**, Phys. Lett. **B 493**, 19 (2000), [hep-ph/0007248].

[5] M. Düren, *The HERMES Experiment: From the Design to the First Results*, Habilitation, Universität Erlangen-Nürnberg, 1995, HERMES-95-02.

[6] F. Halzen and A. Martin, *Quarks and Leptons: An Introductory Course in Modern Particle Physics* (John Wiley and Sons, 1984).

[7] R. Ellis, W. Stirling and B. Webber, *QCD and Collider Physics* (Cambridge Monographs on Particle Physics, Nuclear Physics and Cosmology 8, 1996).

[8] A. Thomas and W. Weise, *The Structure of the Nucleon* (Wiley-VCH, 2001).

[9] E. Leader, *Spin in Particle Physics* (Cambridge Monographs on Particle Physics, Nuclear Physics and Cosmology 15, 2001).

[10] R. Hofstadter and R. McAllister, Phys. Rev. **98**, 217 (1955).

[11] R. McAllister and R. Hofstadter, Phys. Rev. **102**, 851 (1956).

[12] M. Rosenbluth, Phys. Rev. **79**, 497 (1950).

[13] G. Höhler *et al.*, Nucl. Phys. **B 114**, 505 (1976).

[14] R. C. Walker *et al.*, Phys. Rev. **D 49**, 5671 (1994).

[15] E. D. Bloom *et al.*, *Determination of the total photon-proton cross-section from high-energy inelastic electron scattering*, SLAC-PUB-653, 1969.

[16] K. Abe *et al.*, **E143**, Phys. Lett. **B 452**, 194 (1999), [hep-ex/9808028].

[17] C. Callan and D. Gross, Phys. Rev. Lett. **21**, 311 (1968).

[18] K. Hagiwara *et al.*, Phys. Rev. **D 66**, 010001 (2002).

[19] A. C. Benvenuti *et al.*, **BCDMS**, Phys. Lett. **B 223**, 485 (1989).

[20] L. W. Whitlow, E. M. Riordan, S. Dasu, S. Rock and A. Bodek, Phys. Lett. **B 282**, 475 (1992).

[21] M. Arneodo *et al.*, **NMC**, Nucl. Phys. **B 483**, 3 (1997), [hep-ph/9610231].

[22] M. R. Adams *et al.*, **E665**, Phys. Rev. **D 54**, 3006 (1996).

[23] C. Adloff *et al.*, **H1**, Eur. Phys. J. **C 13**, 609 (2000), [hep-ex/9908059].

[24] C. Adloff *et al.*, **H1**, Eur. Phys. J. **C 21**, 33 (2001), [hep-ex/0012053].

[25] S. Chekanov *et al.*, **ZEUS**, Eur. Phys. J. **C 21**, 443 (2001), [hep-ex/0105090].

[26] J. D. Bjørken and E. A. Paschos, Phys. Rev. **185**, 1975

[27] K. Abe *et al.*, **E154**, Phys. Lett. **B 405**, 180 (1997), [hep-ph/9705344].

[28] K. Abe *et al.*, **E154**, Phys. Rev. Lett. **79**, 26 (1997), [hep-ex/9705012].

[29] P. L. Anthony *et al.*, **E155**, Phys. Lett. **B 458**, 529 (1999), [hep-ex/9901006].

[30] P. L. Anthony *et al.*, **E142**, Phys. Rev. **D 54**, 6620 (1996), [hep-ex/9610007].

[31] K. Abe *et al.*, **E143**, Phys. Rev. **D 58**, 112003 (1998), [hep-ph/9802357].

[32] P. L. Anthony *et al.*, **E155**, Phys. Lett. **B 463**, 339 (1999), [hep-ex/9904002].

[33] J. Ashman *et al.*, **EMC**, Nucl. Phys. **B 328**, 1 (1989).

[34] B. Adeva *et al.*, **SMC**, Phys. Rev. **D 58**, 112001 (1998).

[35] B. Adeva *et al.*, **SMC**, Phys. Rev. **D 60**, 072004 (1999), Erratum-ibidum **D 62**, 079902 (2000).

[36] A. Airapetian *et al.*, **HERMES**, Phys. Lett. **B 442**, 484 (1998), [hep-ex/9807015].

[37] K. Ackerstaff *et al.*, **HERMES**, Phys. Lett. **B 404**, 383 (1997), [hep-ex/9703005].

[38] P. L. Anthony *et al.*, **E155**, Phys. Lett. **B 553**, 18 (2003), [hep-ex/0204028].

[39] K. Abe *et al.*, **E154**, Phys. Lett. **B 404**, 377 (1997), [hep-ex/9705017].

[40] K. Abe *et al.*, **E143**, Phys. Rev. Lett. **76**, 587 (1996), [hep-ex/9511013].

[41] R. P. Feynman, Phys. Rev. Lett. **23**, 1415 (1969).

[42] V. N. Gribov and L. N. Lipatov, Sov. J. Nucl. Phys. **15**, 438

[43] V. N. Gribov and L. N. Lipatov, Sov. J. Nucl. Phys. **15**, 675

[44] G. Altarelli and G. Parisi, Nucl. Phys. **B 126**, 298 (1977).

[45] M. Anselmino, A. Efremov and E. Leader, Phys. Rept. **261**, 1 (1995), [hep-ph/9501369], Erratum-ibidum **281**, 399 (1997).

[46] M. Glück, E. Reya and W. Vogelsang, Phys. Lett. **B 359**, 201 (1995), [hep-ph/9507354].

[47] T. Gehrmann and W. J. Stirling, Z. Phys. **C 65**, 461 (1995), [hep-ph/9406212].

[48] K. Gottfried, Phys. Rev. Lett. **18**, 1174 (1967).

[49] D. A. Ross and C. T. Sachrajda, Nucl. Phys. **B 149**, 497 (1979).

[50] P. Amaudruz *et al.*, **NMC**, Phys. Rev. Lett. **66**, 2712 (1991).

[51] S. A. Larin, Phys. Lett. **B 334**, 192 (1994), [hep-ph/9403383].

[52] Y. Goto *et al.*, Phys. Rev. **D 62**, 034017 (2000), [hep-ph/0001046].

[53] P. G. Ratcliffe, Phys. Rev. **D 59**, 014038 (1999), [hep-ph/9806381].

[54] J. D. Bjørken, Phys. Rev. **148**, 1467 (1966).

[55] J. R. Ellis and R. L. Jaffe, Phys. Rev. **D 9**, 1444 (1974), Erratum-ibidum **D 10**, 1669 (1974).

[56] I. Balitsky and X.-D. Ji, Phys. Rev. Lett. **79**, 1225 (1997), [hep-ph/9702277].

[57] F. Close, *An Introduction to Quarks and Partons* (Academic Press, 1979).

[58] C. V. Christov *et al.*, Prog. Part. Nucl. Phys. **37**, 91 (1996), [hep-ph/9604441].

[59] K. Suzuki and W. Weise, Nucl. Phys. **A 634**, 141 (1998), [hep-ph/9711368].

[60] A. V. Kolesnichenko, Sov. J. Nucl. Phys. **39**, 968 (1984).

[61] V. M. Belyaev and B. Y. Blok, Z. Phys. **C 30**, 279 (1986).

[62] N. F. Nasrallah, Phys. Rev. **D 61**, 056002 (2000), [hep-ph/9903225].

[63] S. L. Adler, Phys. Rev. **177**, 2426 (1969).

[64] M. Glück, E. Reya, M. Stratmann and W. Vogelsang, Phys. Rev. **D 63**, 094005 (2001), [hep-ph/0011215].

[65] M. Glück and E. Reya, hep-ph/0203063.

[66] B. Andersson, G. Gustafson, G. Ingelman and T. Sjostrand, Phys. Rept. **97**, 31 (1983).

[67] T. Sjostrand, Comp. Phys. Comm. **82**, 74 (1994).

[68] B. Andersson, G. Gustafson and T. Sjostrand, Phys. Scripta **32**, 574 (1985).

[69] F. Menden, *Determination of the Gluon Polarization in the Nucleon*, Dissertation, Albert-Ludwigs-Universität Freiburg im Breisgau, 2001, HERMES-01-073. One parameter of the described all-W^2-tune was changed: PARL(3) = 0.44 [104].

[70] DESY Website, http://www.desy.de/.

[71] A. Sokolov and I. Ternov, Sov. Phys. Dokl. **8**, 1203 (1964).

[72] J. Buon and K. Steffen, Nucl. Instrum. Meth. **A 245**, 248 (1986).

[73] D. P. Barber *et al.*, Nucl. Instrum. Meth. **A 329**, 79 (1993).

[74] D. P. Barber *et al.*, Nucl. Instrum. Meth. **A 338**, 166 (1994).

[75] B. Tipton, *Measurement of Polarized Parton Distributions With Spin-Dependent Deep-inelastic Scattering*, PhD thesis, Massachusetts Institute of Technology, 1999, HERMES-99-034.

[76] M. Beckmann *et al.*, Nucl. Instrum. Meth. **A 479**, 334 (2002), [physics/0009047].

[77] C. Baumgarten *et al.*, **HERMES Target Group**, Nucl. Inst. Meth. **A 496**, 277 (2003), HERMES-02-041.

[78] D. DeSchepper *et al.*, Nucl. Instrum. Meth. **A 419**, 16 (1998).

[79] M. Henoch, *Absolute Calibration of a Polarized Deuterium Gas Target*, Dissertation, Friedrich-Alexander-Universität Erlangen-Nürnberg, 2002, HERMES-02-026.

[80] C. Baumgarten *et al.*, **HERMES Target Group**, Nucl. Instrum. Meth. **A 482**, 606 (2002).

[81] C. Baumgarten, *Aufbau und Kalibration eines Gasanalysators für das HERMES-Wasserstofftarget*, Diplomarbeit, Universität Hamburg, 1996, HERMES-96-068.

[82] H. Kolster, *The HERMES Gaseous Internal Polarized Proton Target and its use in the HERA Positron Storage Ring*, Dissertation, Ludwig-Maximilians-Universität München, 1998, HERMES-98-009.

[83] T. Lindemann, *Extraktion der polarisierten Quarkverteilungen des Nukleons mit besonderer Berücksichtigung der Seequarks im HERMES-Experiment*, Dissertation, Universität Hamburg, 2001, HERMES-01-069.

[84] The HERMES Target Group, *The polarization of HERMES target and its error for the deuterium running in 2000*, HERMES-02-010.

[85] M. Beckmann, *Target polarization values and their uncertainties used by the Δq analysis group for the 1996 to 2000 running periods*, HERMES-03-005.

[86] K. Ackerstaff *et al.*, **HERMES**, Phys. Rev. Lett. **81**, 5519 (1998), [hep-ex/9807013].

[87] A. Airapetian *et al.*, **HERMES**, Eur. Phys. J. **C 21**, 599 (2001), [hep-ex/0104004].

[88] A. Airapetian *et al.*, **HERMES**, Phys. Rev. **D 64**, 112005 (2001), [hep-ex/9911017].

[89] T. Benisch *et al.*, Nucl. Instrum. Meth. **A 471**, 314 (2001).

[90] K. Ackerstaff *et al.*, **HERMES**, Nucl. Instrum. Meth. **A 417**, 230 (1998), [hep-ex/9806008].

[91] M. G. van Beuzekom *et al.*, Nucl. Instrum. Meth. **A 409**, 255 (1998).

[92] J. Blouw *et al.*, Nucl. Instrum. Meth. **A 434**, 227 (1999).

[93] J. T. Brack *et al.*, Nucl. Instrum. Meth. **A 469**, 47 (2001).

[94] A. Andreev *et al.*, Nucl. Instrum. Meth. **A 465**, 482 (2001).

[95] S. Bernreuther *et al.*, Nucl. Instrum. Meth. **A 367**, 96 (1995).

[96] S. Bernreuther *et al.*, Nucl. Instrum. Meth. **A 416**, 45 (1998), [hep-ex/9803005].

[97] W. Wander, *Reconstruction of High Energy Scattering Events in the HERMES Experiment*, Dissertation, Friedrich-Alexander-Universität Erlangen-Nürnberg, 1996, HERMES-97-031.

[98] A. Hillenbrandt, private communication, 2002.

[99] H. Avakian *et al.*, Nucl. Instrum. Meth. **A 417**, 69 (1998), [hep-ex/9810004].

[100] H. Avakian *et al.*, Nucl. Instrum. Meth. **A 378**, 155 (1996).

[101] J. D. Jackson, *Classical Electrodynamics* (John Wiley and Sons, 1975).

[102] X. Artru, G. B. Yodh and G. Mennessier, Phys. Rev. **D 12**, 1289 (1975).

[103] N. Akopov *et al.*, Nucl. Instrum. Meth. **A 479**, 511 (2002), [physics/0104033].

[104] E. C. Aschenauer, private communication, 2002.

[105] CERN-CN Division, *EPIO — Experimental Physics Input Output Package*, CERN Program Library Long Writeup I101, 1993.

[106] CERN Programming Techniques Group, *ADAMO — Entity-Relationship Programming System, Users Guide, Version 3.3*, 1993.

[107] M. Hartig and K. Garrow, private communications, 2001/2002.

[108] HERMES Data Quality Website, http://www-hermes.desy.de/groups/daqlgrp/, 2003.

[109] J. Wendland, *Improved Particle Identification at HERMES and Polarised Valence Quark Distributions in the Proton*, Master's thesis, Simon Fraser University, 1999, HERMES-99-016.

[110] J. Wendland, *Particle Identification for HERMES Run I*, HERMES-01-067, 2001.

[111] HERMES Particle Identification Website, http://www-hermes.desy.de/PID/, 2003.

[112] R. J. Barlow, *Statistics, a Guide to the Use of Statistical Methods in the Physical Sciences* (John Wiley & Sons, 1989).

[113] F. Menden, *Measurement of the Valence Quark Spin Distributions of the Nucleon Using Deep Inelastic Scattering at HERMES*, Diplomarbeit, Universität Hamburg, 1997, HERMES-98-001.

[114] Y. Gärber, *Messung der Proton-Spinstrukturfuntion g_1 bis zu kleinstmöglichen Bjørken-x mit dem HERMES Experiment*, Dissertation, Humboldt-Universität Berlin, 2001, HERMES-01-048.

[115] P. Jung, *Pion-Kaon Separation mit dem HERMES-RICH-Detektor*, Diplomarbeit, Humboldt-Universität Berlin, 2000, HERMES-01-025.

[116] K. Negodaeva, *The PID Efficiency of the HERMES RICH and the IRT Method*, HERMES-00-028, 2000.

[117] HERMES RICH Website, http://www-hermes.desy.de/groups/richgrp/rich/, 2003.

[118] E. L. Berger, *Semi-inclusive Inelastic Electron Scattering from Nuclei*, ANL-HEP-CP-87-45.

[119] P. J. Mulders, AIP Conf. Proc. **588**, 75 (2001), [hep-ph/0010199].

[120] S. J. Brodsky, L. Frankfurt, J. F. Gunion, A. H. Mueller and M. Strikman, Phys. Rev. **D 50**, 3134 (1994), [hep-ph/9402283].

[121] S. Goertz *et al.*, *Recent Developments in Polarized Solid Deuteron Targets*, Workshop on Testing QCD through Spin Observables in Nuclear Targets, Charlottesville, Virginia, 2002.

[122] R. N. Cahn, Phys. Lett. **B 78**, 269 (1978).

[123] P. J. Mulders and R. D. Tangerman, Nucl. Phys. **B 461**, 197 (1996), [hep-ph/9510301].

[124] A. Airapetian *et al.*, **HERMES**, Phys. Lett. **B 562**, 182 (2003), [hep-ex/0212039].

[125] K. A. Oganessyan, P. J. Mulders and E. De Sanctis, Phys. Lett. **B 532**, 87 (2002), [hep-ph/0201061].

[126] K. A. Oganessyan, L. S. Asilyan, M. Anselmino and E. De Sanctis, Phys. Lett. **B 564**, 60 (2003), [hep-ph/0208208].

[127] A. Jgoun and A. Miller, private communication, 2003.

[128] A. Jgoun, *Measurement of Hadronic Azimuthal Distributions in Deep Inelastic Scattering*, HERMES-03-001, 2003.

[129] J. Pretz, *Messung der polarisierten Quarkverteilungen in semi-inklusiver Myon-Nukleon-Streuung*, Dissertation, Johannes-Gutenberg Universität Mainz, 1997.

[130] M. Funk, *A Measurement of the Polarized Parton Densities of the Nucleon in Deep-Inelastic Scattering at HERMES*, Dissertation, Universität Hamburg, 1998, HERMES-98-034.

[131] M. C. Simani, *Flavour Decomposition of the Nucleon Spin*, Dissertation, Vrije Universiteit Amsterdam, 2002, HERMES-02-046.

[132] R. Kaiser, *Measurement of the Spin Structure of the Neutron using Polarised Deep Inelastic Scattering*, PhD thesis, Simon Fraser University, 1997, HERMES-97-017.

[133] M. Arneodo *et al.*, NMC, Phys. Lett. **B 364**, 107 (1995), [hep-ph/9509406].

[134] I. V. Akushevich and N. M. Shumeiko, J. Phys. **G 20**, 513 (1994).

[135] I. Akushevich, A. Ilichev, N. Shumeiko, A. Soroko and A. Tolkachev, Acta Phys. Polon. **B 28**, 563 (1997).

[136] I. Akushevich, H. Böttcher and D. Ryckbosch, hep-ph/9906408.

[137] HERMES Monte Carlo Website, http://www-hermes.desy.de/hmc/, 2003.

[138] R. Brun, R. Hagelberg, M. Hansroul and J. Lassalle, (1978), CERN-DD-78-2-REV, see also http://geant4.web.cern.ch/geant4/.

[139] A. Miller, *Applying Radiative Corrections to Polarisation Asymmetries for Deeply Inelastic Scattering*, unpublished, 2002.

[140] V. Blobel, hep-ex/0208022.

[141] B. Adeva *et al.*, **SMC**, Phys. Lett. **B 420**, 180 (1998), [hep-ex/9711008].

[142] L. De Nardo, *Measurement of the Structure Function g_{1d} at HERMES and Extraction of Polarized Parton Distributions*, PhD thesis, University of Alberta, 2002, HERMES-02-038.

[143] I. Akushevich and A. Nagaitsev, *The Systematical Uncertainties in Measurements of the Spin-Dependent Structure Function g_{1n} with ^{3}He Target due to Radiative Correction Procedure*, HERMES-97-027, 1997.

[144] A. Szczurek, V. Uleshchenko and J. Speth, Phys. Rev. **D 63**, 114005 (2001), [hep-ph/0009318].

[145] H. L. Lai *et al.*, **CTEQ**, Eur. Phys. J. **C 12**, 375 (2000), [hep-ph/9903282].

[146] K. Ackerstaff *et al.*, **HERMES**, Phys. Rev. Lett. **82**, 3025 (1999), [hep-ex/9811011].

[147] B. Desplanques, Phys. Lett. **B 203**, 200 (1988).

[148] R. Machleidt, K. Holinde and C. Elster, Phys. Rept. **149**, 1 (1987).

[149] O. A. Rondon, *Effective nucleon polarization in polarized targets*, Workshop on Testing QCD through Spin Observables in Nuclear Targets, Charlottesville, Virginia, 2002.

[150] M. Arneodo *et al.*, **EMC**, Phys. Lett. **B 150**, 458 (1985).

[151] J. Pumplin *et al.*, JHEP **07**, 012 (2002), [hep-ph/0201195].

[152] N. Makins, private communication, 2002.

[153] H. Tallini, *A measurement of the quark spin distribution of the nucleon at HERMES*, PhD thesis, Oliver Lodge Laboratory, University of Liverpool, 1998, HERMES-98-024.

[154] K. Ackerstaff *et al.*, **HERMES**, Phys. Lett. **B 464**, 123 (1999), [hep-ex/9906035].

[155] J. Blümlein and H. Böttcher, Nucl. Phys. **B 636**, 225 (2002), [hep-ph/0203155].

[156] A. Baldit *et al.*, **NA51**, Phys. Lett. **B 332**, 244 (1994).

[157] R. S. Towell *et al.*, **FNAL E866/NuSea**, Phys. Rev. **D 64**, 052002 (2001), [hep-ex/0103030].

[158] B. Dressler, K. Goeke, M. V. Polyakov and C. Weiss, Eur. Phys. J. **C 14**, 147 (2000), [hep-ph/9909541].

[159] C. Bourrely, J. Soffer and F. Buccella, Eur. Phys. J. **C 23**, 487 (2002).

[160] R. J. Fries, A. Schäfer and C. Weiss, hep-ph/0204060.

[161] F.-G. Cao and A. I. Signal, hep-ph/0306033.

[162] R. Lockhardt, Dept. of Statistics & Actuarial Science, SFU, private communication, 2003.

[163] M. Wakamatsu, hep-ph/0209011.

[164] L. L. Frankfurt *et al.*, Phys. Lett. **B 230**, 141 (1989).

[165] S. D. Bass and P. V. Landshoff, Phys. Lett. **B 336**, 537 (1994), [hep-ph/9406350].

[166] R. L. Heimann, Nucl. Phys. **B 64**, 429 (1973).

[167] J. R. Ellis and M. Karliner, Phys. Lett. **B 213**, 73 (1988).

[168] M. Glück, E. Reya and A. Vogt, Eur. Phys. J. **C 5**, 461 (1998), [hep-ph/9806404].

[169] M. Beckmann, private communication, 2003.

[170] M. Stratmann, private communication, 2003.

[171] A. Airapetian, **HERMES**, hep-ex/0307064.

[172] A. Airapetian *et al.*, **HERMES**, Phys. Rev. Lett. **84**, 2584 (2000), [hep-ex/9907020].

[173] G. Baum *et al.*, **COMPASS**, CERN-SPSLC-96-14.

[174] M. Lamanna, **COMPASS**, Nucl. Phys. **A 711**, 50 (2002).

[175] S. Hedicke, **COMPASS**, Prog. Part. Nucl. Phys. **50**, 499 (2003).

[176] RHIC Website, http://www.bnl.gov/RHIC/.

[177] N. Saito, Nucl. Phys. **A 698**, 275 (2001).

[178] M. Stratmann, hep-ph/0211317.

[179] F. M. Dittes, D. Muller, D. Robaschik, B. Geyer and J. Horejsi, Phys. Lett. **B 209**, 325 (1988).

[180] X.-D. Ji, Phys. Rev. **D 55**, 7114 (1997), [hep-ph/9609381].

[181] X.-D. Ji, Phys. Rev. Lett. **78**, 610 (1997), [hep-ph/9603249].

[182] A. Airapetian *et al.*, **HERMES**, Phys. Rev. Lett. **87**, 182001 (2001), [hep-ex/0106068].

[183] R. Kaiser, *Unfolding of Hadron Distributions and Asymmetries*, HERMES-00-027, 2000.